

CRANFIELD UNIVERSITY

CHEE WANG LIM

DYNAMIC ANALYSIS OF AEROSTATIC GUIDEWAY AND FEA
MODEL DEVELOPMENT

SCHOOL OF APPLIED SCIENCES

EngD THESIS
Academic Year 2008-2009

Supervisors: Professor Paul Shore
Mr Paul Morantz

CRANFIELD UNIVERSITY

SCHOOL OF APPLIED SCIENCES

EngD THESIS

Academic Year 2008-2009

CHEE WANG LIM

DYNAMIC ANALYSIS OF AEROSTATIC GUIDEWAY AND FEA
MODEL DEVELOPMENT

Supervisors: Professor Paul Shore
Mr Paul Morantz

15 December 2009

This thesis is submitted in partial fulfilment of the requirements for the degree of
Engineering Doctorate.

© Cranfield University 2009. All rights reserved. No part of this publication may be
reproduced without the written permission of the copyright owner.

Abstract

A dynamically optimal design is essential for a motion system to perform high speed operation without compromising its accuracy, settling time and vibration specification. Good design practice which accounts for dynamic characteristics in the modelling of a motion system warrants higher performance precision machines and cuts down redevelopment effort to ‘patch’ inherent shortcoming of the machine dynamics.

This research aimed to accurately describe the non-linear dynamics of a non-mechanical contact aerostatic guideway system in order to achieve an accurate FEA model of the design stage. The single axis aerostatic guideway is comprised of several machine interfaces that impact the dynamic behaviour of the guideway. Modelling each air bearing pad by a single stiffness element is not adequate to predict the guideway modal behaviour accurately. The aerostatic guideway has been broken down into several key machine interface elements. In-depth investigation of the air film and the air bearing mounting mechanism was carried out. A dedicated air film test rig was designed and built to acquire insight of the air film dynamic characteristics.

It is observed that the mounting mechanism of the air bearing constitutes to a significant dynamic effect to the entire air bearing setup. Based on the findings of the mounting mechanism’s stiffness properties, a method was developed to estimate ‘true’ air gap heights which cannot be easily assessed and measured directly in most aerostatic guideway carriages. The estimation method enables a more rigorous FE model of the aerostatic guideway system. The comprehensive dynamic analysis methodology proposed in this research greatly increases the confidence and accuracy of the aerostatic guideway’s FE model.

Acknowledgements

First of all, I would like to thank my two supervisors, Professor Paul Shore and Mr Paul Morantz for their guidance and encouragement throughout the course of this research. I have gained valuable knowledge in the field of precision machine design from these two experts in the precision engineering arena. I would like to express my appreciation to my Industrial supervisors, Dr Lin Wei and Mr William (Bill) J. Wills-Moren. Dr Lin was my Group Manager during the first four years of this programme. His support and technical advice on my research made managing work and research much easier. Bill is a great engineer with boundless experience to tap on, and a nice friend to have. Special thanks to my Business supervisor, Dr Alan Cousens from School of Management for his advice and suggestion on the business context of this thesis. I am also appreciative to Kath Tipping, our EngD Programme coordinator, whom has eased the administrative aspect of this programme for all the Cranfield EngD students.

I would like to thank my employer, the Singapore Institute of Manufacturing Technology (SIMTech) for sponsoring and supporting this EngD programme. I would also like to extend my gratitude to several individuals who have helped and supported me during my endeavour for this Doctorate. It is not possible to complete this thesis without the understanding and support from my bosses, Dr Yang Guilin (Group Manager, Mechatronics) and Dr Lim Ser Yong (Executive Director, SIMTech). I am also grateful to colleagues who have helped me in one way or another. There are too many of them to be named here. They are mainly colleagues from SIMTech, Mechatronics Group, Precision Measurement Group and Machining Technology Group, as well as from Cranfield University, Precision Engineering Centre. I would also like to thank members of MBA Team Green 1 whom have given me a great learning experience

during the first year of the Executive MBA modules.

Finally and perhaps most importantly, one person that I should never forget in this acknowledgement is my wife, Isabella Soh. Without her moral support and encouragement, this journey would be much harder to pursue. Isabella has also given me a beautiful baby boy, Josiah who has given me so much joy and is also partially responsible for the late submission of this thesis.

Table of contents

Abstract	i
1 Introduction	1
1.1 Background	1
1.2 Motivation of Research	2
1.3 Research Objectives	2
1.4 Thesis Overview	3
2 Literature Review	7
2.1 Introduction	7
2.2 Mechatronic Approach to Machine Design	7
2.3 Dynamic Modelling of Machine Interfaces	13
2.4 Aerostatic Bearing Static and Dynamic Characteristics	19
2.5 Discussion	26
3 Industrial Context and Technology Adoption Issues	28
3.1 Background of Precision Engineering in Singapore	28
3.2 Proposed Approach to Precision Machine Design	30
3.2.1 Current Industrial Practice	30
3.2.2 Potential Solution	33
3.3 Technology Adoption	34
3.3.1 Planning	34
3.3.2 Acquisition	36
3.3.3 Assessment	37
3.4 Conclusions	39
4 Theory and Application of Modal Analysis	41
4.1 Basic Concept of Modal Analysis	41
4.1.1 Single Degree of Freedom (SDOF) System	42
4.1.2 Multi-degree of Freedom (MDOF) Systems	48
4.2 Modal Testing	57
4.2.1 Preparation and Test Planning	57
4.2.2 Measurement Process	58
4.2.3 Post-processing - Modal Parameters Extraction	60

5	Experimental Methodology, Procedure and Equipment	64
5.1	Introduction	64
5.2	Experimental Methodologies	66
5.2.1	The Experimental Platform	67
5.2.2	Assessment of System Interfaces	69
5.3	Experimental Setup and Equipment	74
5.3.1	Modal Testing Equipment	74
5.3.2	Stiffness Testing Equipments	76
5.4	Dedicated Air Bearing Test Rig	78
5.4.1	Design Consideration of the Air Bearing Test Rig	78
5.4.2	Design of the Opposing Air Bearing Test Rig	79
5.4.3	Flexure Mechanism	81
5.4.4	Fabrication, Assembly and Other Practical Issues	84
5.4.5	Height Measurement of the Air Gaps	86
5.5	Conclusions	88
6	Dynamic Analysis of Aerostatic Bearing Interfaces	90
6.1	Introduction	90
6.2	Static Stiffness of Air Film	91
6.2.1	Stiffness Modelling of Air Film	91
6.2.2	Experimental Results for Air Film Stiffness	94
6.3	Dynamic Analysis of the Dedicated Air Bearing Test Rig	96
6.3.1	Dynamic Modelling of Air Film Test Rig Using FEA	96
6.3.2	Experimental Modal Testing Results of the Dedicated Test Rig	98
6.3.3	Error Estimates of the Test Rig Dynamic Analysis	103
6.3.4	Corrected Analytical Model of Test Rig	110
6.3.5	non-linearity of the Air Film Model	111
6.4	Discussion on Modal Analysis of the Dedicated Test Rig	115
6.4.1	Dynamics of the Test Rig	115
6.4.2	Errors and Uncertainties of the Analysis	116
7	Dynamic Analysis of an Aerostatic Guideway System	117
7.1	Introduction	117
7.2	Key Potential Errors in Modelling	118
7.2.1	Errors and Assumptions in the Mounting Mechanism	118
7.2.2	Discussion on Errors Contributed by the Mounting Mechanism	126
7.2.3	Potential Geometrical Error in the Air Bearing	127
7.2.4	Air Gap Height Measurement and Estimation	128
7.3	Analytical Dynamic Modelling and Results	130
7.3.1	Stiffness Model of the Air Bearing	133
7.3.2	Dynamic FE Model of the Air Bearing	133
7.3.3	Isolated Dynamics of the Air Bearing Carriage	136
7.3.4	Analytical Modal Results of the Overall Aerostatic Guideway	142
7.3.5	Uncertainties in Analytical Modal Results of the Guideway	145

7.4	Validation using Experimental Modal Testing Results	147
7.4.1	Experimental Modal Testing Setup for the Aerostatic Guideway	147
7.4.2	Experimental Results and Validation of the Guideway Structure	149
7.4.3	Experimental Results and Validation of the Overall Guideway	149
7.5	Discussion on Experimental Results and Validation	151
8	Overall Discussion	155
8.1	Breaking Down the Problem	155
8.2	Dedicated Air Film Dynamic Analysis	156
8.3	Minimising the Uncertainties	157
8.4	Accurate FE Model for Dynamic Simulation	158
9	Conclusion and Further Work	161
9.1	Research Overview and Contributions	161
9.2	Further work	163
	References	177
A	Technical data of New Way Air Bearing	178
A.1	Specifications of 25 mm Diameter Air Bearing	179
A.2	Load lift curves of 25 mm Diameter Air Bearing	180
A.3	Engineering drawings of 25 mm Diameter Air Bearing	181
A.4	Specifications of 65 mm Diameter Air Bearing	182
A.5	Load lift curves of 65 mm Diameter Air Bearing	183
A.6	Engineering drawings of 65 mm Diameter Air Bearing	184
B	Air gap height measurement procedure	185
C	ANSYS Element Description	187
C.1	COMBIN39 Element Description	187
C.2	SHELL93 Element Description	188
D	Flatness Measurement of Critical Surfaces using Interferometer	190
E	Experimental results of guideway modal testing	192

List of Figures

1.1	Summary of the the flow of chapters 5 to 7	6
2.1	Two type of Coupled Simulation	10
2.2	Coupled Simulation - Co-Simulation	13
2.3	Types of Machine Interfaces	15
2.4	Spring model of bolted joint	15
2.5	Dynamic model of the tool-side structure	17
2.6	Finite Element Model of Ball Bearing	18
2.7	Flowchart of FRF-based Identification Scheme	18
2.8	Types of air bearing	20
2.9	Schematic diagram of an orifice air bearing	21
2.10	Experimental and theoretical comparison of the mass vs air gap curve	23
2.11	Schematic diagram of a porous aerostatic	24
2.12	Comparison of air pressure distribution of orifice and porous type air bearings	24
3.1	Examples of high precision machines	30
3.2	Benefits Dependency Network for an HR IT management plan	35
3.3	Relationship between factors and modes	37
4.1	A simple SDOF mass and spring system	43
4.2	FRF plots of undamped SDOF system	45
4.3	A SDOF mass, spring and damper system	46
4.4	Free Damped Oscillation	47
4.5	Effect on FRF plots by changing spatial properties of the system	49
4.6	Model geometry with measurement points of the guideway structure	58
4.7	A typical modal impact testing setup	59
4.8	Three possible rigid body modes due to the spring stiffness	59
4.9	Force and acceleration time data to frequency response function.	60
4.10	Peak picking method	61
4.11	Imaginary plots	63
5.1	Flow of chapter 5 to 7.	64
5.2	Modal Analysis Validation Process	66
5.3	Aerostatic guideway system as the experimental platform	68

5.4	25 mm diameter New Way Air Bearing	69
5.5	Air bearing layout used in this test rig	69
5.6	Air bearings layout and enclosure assembly	70
5.7	Stiffness chain of the air bearing guideway	72
5.8	Porous Air Bearing Mounting Mechanism	72
5.9	Modal Testing Setup of Guideway Structure	76
5.10	Instron 4505 with 1 kN load cell	77
5.11	Test setup for air film stiffness	77
5.12	Dedicated air bearing test rig	79
5.13	Determination of air gap heights	80
5.14	Centre Mass	80
5.15	Leaf-spring flexure mechanism	81
5.16	Schematic of a leaf spring flexure mechanism	82
5.17	Schematic mass spring model of the centre mass held by three flexure mechanisms	83
5.18	Parts and air bearings for the test rig	84
5.19	Flexure mechanisms on three sides of the centre mass	85
5.20	Assembled test rig	85
5.21	Measurement software screen-shot of the top plate surface	86
5.22	Measurement of air gaps using two Mahr LVDT probes	87
5.23	Three soft springs were used to push the mass upward when air is turn off	88
6.1	Flow of chapters 5 to 7.	90
6.2	1D generalised air flow from the physical system to the 1D model differential element	92
6.3	Comparison between computed curve and manufacturer data of a 65mm diameter aerostatic porous bearing at 5.5bar	93
6.4	Stiffness curve of a 65mm diameter aerostatic porous bearing at 5.5bar	94
6.5	Schematic diagram of the air film stiffness test setup	95
6.6	Load-lift Curve of 65mm diameter air bearing at 5.5 bar and 4.5 bar supply pressure	95
6.7	Different Load-lift Curves of 65mm diameter air bearing at 5.5 bar supply pressure	96
6.8	Air gap model using 10 different non-linear springs based on their radial positions	97
6.9	Load-lift curves of 10 segments of the air film slice	98
6.10	Sensors setup and impact points for the modal testing	99
6.11	Parallelism measurement between the two fly cut surfaces	104
6.12	The flatness error contributes to the parallelism error.	105
6.13	Air bearings parallelism	105
6.14	Computing transient time data of an opposing springs and centre mass system	114

6.15	FRFs obtained from the linear spring system comparing against the non-linear ones with varying input force	115
7.1	Flow of chapters 5 to 7.	117
7.2	Aerostatic Bearing Mounting Mechanism	119
7.3	Typical Hertzian contact of a sphere on a curve surface	121
7.4	Stiffness testing for Test Setup 1	124
7.5	Stiffness testing for Test Setup 2	125
7.6	Interferometer flatness measurement of a 25mm diameter air bearing porous surface	127
7.7	Schematic illustration of air gap measurement methods	128
7.8	Graphical method for estimation of actual air bearing displacement . .	130
7.9	Carriage coordinate and orientation convention	132
7.10	Comparison of the computed, experimental and manufacturer's load versus air gap curve for 25 mm diameter air bearing	134
7.11	FE Model of a single air bearing pad	134
7.12	Actual air gap and joint displacement estimation	135
7.13	FE computed structural mode shapes	137
7.14	Expected isolated carriage mode shapes	138
7.15	Simplified model of air bearing carriage into two decoupled planes . .	139
7.16	FEA results of overall aerostatic guideway for Setup 1: 5 μm stud setting	143
7.17	FEA results of overall aerostatic guideway for Setup 2: 9 μm stud setting	144
7.18	Accelerometers positions	148
7.19	FRFs from two carriage responses in Z and Y axis, and one base plate response in Z axis	151
7.20	Schematic representation of a rotational mode of the guideway carriage	154
A.1	New Way air bearing 25 mm diameter specification	179
A.2	New Way air bearing 25 mm diameter manufacturer's load-lift curve .	180
A.3	New Way air bearing 25 mm diameter engineering drawing	181
A.4	New Way air bearing 65 mm diameter specification	182
A.5	New Way air bearing 65 mm diameter manufacturer's load-lift curve .	183
A.6	New Way air bearing 65 mm diameter engineering drawing	184
B.1	Air Gap Measurement Setup	185
C.1	COMBIN39 Geometry	188
C.2	SHELL93 Geometry	189
D.1	Flatness of Top Air Bearing Porous Surface	190
D.2	Flatness of Bottom Air Bearing Porous Surface	191
D.3	Flatness of Centre Mass Top 'Fly-cut' Surface	191
D.4	Flatness of Centre Mass Bottom 'Fly-cut' Surface	191

E.1	Experimental modal testing results of overall aerostatic guideway for Setup 1: 5 μm stud setting	193
E.2	Experimental modal testing results of overall aerostatic guideway for Setup 2: 9 μm stud setting	194

Chapter 1

Introduction

1.1 Background

Higher position accuracy and higher acceleration with minimum transient responses are increasingly stringent requirements for precision motion systems. This trend can be easily witnessed in electronics industry, where components become smaller and yield rate demand increases. One example is the wire bonder machines which need the bonder to connect pins at smaller than $30\ \mu\text{m}$ pitch with $\pm 2\ \mu\text{m}$ accuracy. To stay above the competition, machine throughput is also of prime importance, thus pushing the bonder motion speed higher. The machine tool industry pursues a similar trend. Higher speed machining and sub-micrometre position accuracy are specifications that motivate more machine tools builders to revise their motion system design. These requirements have compelled machine manufacturers to take radical design approaches in order to meet the industry needs.

Due to the ever growing demand on performance and accuracy, the design methodologies of precision machines remain a widely studied subject. For machines with rapid response, the characteristics of motion system guideways greatly influence the performance of a precision machine, in terms of its speed and accuracy. Consequently, 'near' frictionless non-contact guideways for precision motion systems have been gaining in popularity in the recent years. The use of aerostatic guideways is noticeably more prevalent in precision machines in order to realise higher motion resolution.

1.2 Motivation of Research

1.2 Motivation of Research

For high-speed precision machines, dynamic characteristics dominate performance in terms of motion system settling time and accuracy. Thus, dynamic analysis becomes an important aspect of work while designing such precision machines. Today's commercial modelling software is capable of simulating machine behaviour through Finite Element Analysis (FEA) and other types of Multi-body Dynamic Engines. The validity of results obtain from these simulation packages is based on a machine model defined by the user. Hence, the key to a robust analysis still lies in an accurate model. Dynamic and static models of structure are well-established. Most of the structural dynamic behaviour can be accurately computed using FEA. The model for machine interfaces, such as joints and guideways, is commonly defined using compliance contacts in FEA. These interface models use stiffness and damping parameters that are often inadequately accurate. Hence in most instances, these models are ineffective in predicting realistic dynamic behaviour of the machine. Although many design methodologies have adopted the Mechatronics integrated design approaches (to be discussed in Chapter 2), a dynamic modelling method for machine guide systems is yet to be established.

It is possible that having a unified modelling method for a wide range of different guide systems may not be feasible. However, a systematic model identification method is essential in achieving accurate model to enable a realistic machine modelling during the design phase. A robustly identified dynamic model of the machine enhances the rigour of the design process, thus allowing substantial cost saving and increases competitiveness (to be discussed in Chapter 3).

1.3 Research Objectives

The main objective of this research is to accurately describe the non-linear dynamics of a non-contact guideway system in order to achieve a good FEA model in the design stage. This objective can be broken down into the following sub-objectives:

Chapter 1. Introduction

Identification of key interfaces in the guideway system A guideway system can be made up of several serially connected interfaces that may contribute to the overall dynamic behaviour of the system. Many of these connected interfaces create coupling effects, which are difficult to model. It is important to identify these key interface elements and evaluate their individual significance in influencing the accuracy of the entire dynamic model of the guideway system.

Formulate a systematic identification method to obtain an accurate set of dynamic model parameters Most machine interfaces can be described analytically by model parameters such as stiffness and damping. Some of these interfaces possess non-linearity, which presents difficulties in identification. This non-linearity issue also leads to problems in dynamic analysis of the guideway system, in particular, using FEA.

Validation of design methodology that incorporates interfaces dynamics A case study of a precision motion system using a non-contact guide will be employed as a demonstrator for the proposed design methodology. This will provide insight into the method and the importance of dynamic modelling of machine interfaces.

1.4 Thesis Overview

This EngD research aims to address the issues of precision machine design methodology, in particular, the incorporation of machine interfaces dynamic model within an FEA environment. To understand the dynamics of a non-contact guideway, the research narrowed down its focus to the investigation of the aerostatic bearing guideway system (the rationale for the choice of aerostatic guideway is discussed in Chapter 2 and 5). In the course of this research, a complex problem of dynamic modelling for the aerostatic guideway was broken down into several aspects for investigation. The subsequent chapters of this thesis present the work in achieving the above aim, and are organised as follows:

1.4 Thesis Overview

Chapter 2 presents broadly the state-of-the-art approaches in precision machine design, mainly using the Mechatronic design approach. This review leads to the research arena of machine dynamic modelling methods and an in-depth discussion in modelling of machine interfaces. Particular attention was paid to the analytical modelling methods for an aerostatic bearing.

Chapter 3 is included as part of the differentiating element of an EngD to a PhD programme. An EngD programme carries out research work with a certain business/industrial agenda. The industrial context and motivation for this research work is articulated in this chapter. It is important that research outcome can be transferred to the industry in a strategic manner. Various technology adoption methods of the research outcome are discussed and suggested here.

Chapter 4 gives a broad overview of the theory and application of dynamic/modal analysis of machines. This chapter is useful in understanding the analytical and experimental work that will be presented in the remaining part of the thesis.

Figure 1.1 gives a summarised illustration of the flow of chapters from 5 to 7, which corresponds closely with the actual research work. The illustration gives an account of the flow of work carried out in this research.

Chapter 5 discusses how a complex aerostatic guideway system is broken down into various aspects of interfaces that contribute to the dynamic behaviour of the system. A systematic experimental methodology to analyse the dynamic behaviour of an aerostatic guideway system is deliberated. The individual interfaces need to be dealt with separately. Thus, a dedicated air bearing test rig is designed to carry isolated and controlled investigation of the air film. The design consideration and outcome of this test rig is discussed and presented.

Chapter 6 focuses on the dynamic analysis of solely the aerostatic bearing pads, using the developed dedicated air bearing test rig. Insight into the air film dynamics is observed using the dedicated test rig. A thorough analysis and investigation to identify

Chapter 1. Introduction

the air film dynamics parameters is illustrated in this chapter.

Chapter 7 discusses the work of synthesising the findings from the above two chapters, and validates the dynamic identification and modelling methodology using the existing aerostatic guideway, which initiated the investigation in Chapter 5.

Chapter 8 presents an overall discussion pertaining to the findings and contributions of this research.

Chapter 9 concludes this research programme and suggests further work aiming to close up more gaps between research and industrial implementation in dynamic modelling of machine interfaces.

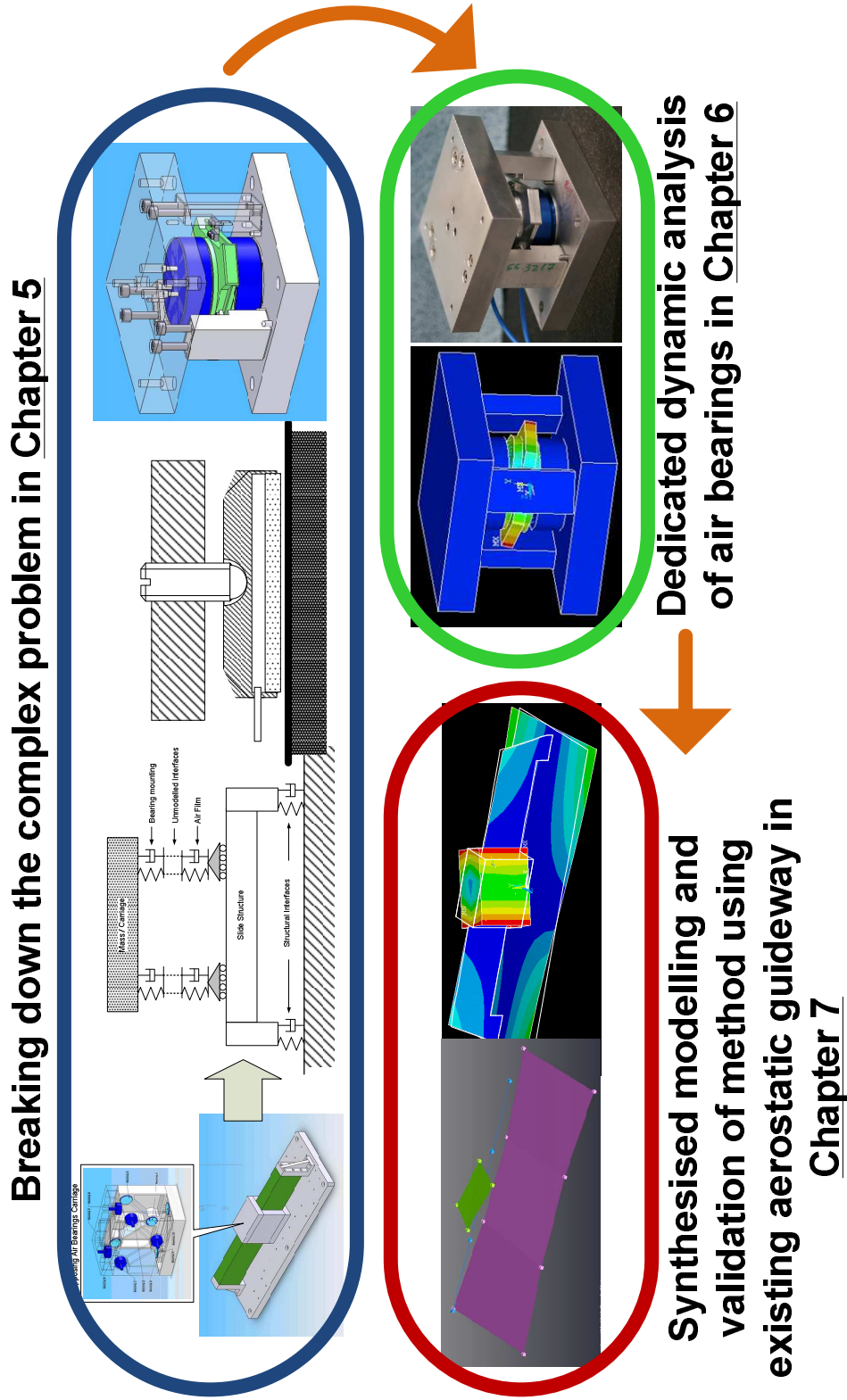


Figure 1.1: Summary of the flow of chapters 5 to 7

Chapter 2

Literature Review

2.1 Introduction

A major attribute to stay competitive in the industry is to cut down design flaws, thus reducing the cost involved in patching and/or redevelopment. The first-time-right approach in precision machine design requires a rigorous modelling effort in the design phase. Prediction only of machine's static or kinematic performance has long been viewed inadequate in designing high speed precision machines. The modelling of precision machines needs to be approached in totality. That is to say, the controller performance of the motion system needs to be taken into consideration during the design stage. In addition, accurate dynamic model of the motion system needs to be formulated to benefit from this integrated design approach. The following sections will cover a literature review of the various design approaches for precision machines, as well as relevant modelling techniques adopted.

2.2 Mechatronic Approach to Machine Design

The 'first-time-right' machine design approach warrants a more integrated prediction of the different aspects of the machine. These include the behaviour of the machine mechanical structure, motion system, controller, as well as sensors. In fact, the machine characteristics form a typical Mechatronic problem. Many proposed works for Mechatronic system attempts to solve the problem after the machine has been built,

2.2 Mechatronic Approach to Machine Design

by means of identifying and modelling the motion system behaviour [1–5] or by compensating for any unknown systematic behaviour within the control scheme [6–9]. A substantial amount of effort and time is thus spent on achieving an optimal performing motion controller. Although these methods were able to achieve some good results, the performance was always limited by the machine inherent shortcomings, thus the motion control results were always less than optimal. Many of these machine characteristics exhibit non-linear dynamic behaviour, which is difficult to compensate for. Therefore, it is useful at the design phase to develop the mechanical system that is optimised for a simple controller, i.e. both mechanical and controller aspects are evaluated simultaneously. The key notion is that a badly designed mechanical system is hard to achieve good performance even by using the most sophisticated controller [10].

During the late eighties, the European Union-sponsored Industrial Research and Development Advisory Committee (IRDAC) working group came up with following definition for Mechatronics:

“Mechatronics is the synergetic combination of precision engineering, electronic control technology and systems thinking in the design of products and processes.”

Van Brussel [11] has proposed a definition of Mechatronics that is more relevant to this thesis context:

“Mechatronics encompasses the knowledge base and the technologies required for the flexible generation of controlled motion.”

Not every electronically controlled mechanical system is a Mechatronic system because in many cases the control is just an add-on to the mechanical system in a sequential design procedure. A real Mechatronic approach requires that an optimal choice be made with respect to the realisation of the design specifications in the different domains, i.e. mechanical, electronic and computer-based control system [10, 12]. Bond graph [13] modelling method was one of the earlier modelling techniques for dynamic systems. The modelling method simplifies complex dynamic systems into components connected by multiports of energy transfer. It provides a starting platform for many

Chapter 2. Literature Review

later works in the area of dynamic system modelling. However, many of the bond graph based modelling techniques do not handle classification of system components well [14]. De Varies et al. [10, 12, 14, 15] proposed a concept, named polymorphic modelling which resolved this classification limitation. The concept of polymorphic modelling is useful, because [16, 17]:

- It enables the component library to be organised in a kind-of hierarchy, such that components are specialised incrementally downwards
- It improves classification of components by means of generic as well as specific types
- It improves understanding of models by separating essential and incidental characteristics
- It supports the iterative and evolutionary nature of modelling more directly
- It improves the possibilities for creating and maintaining (mutually consistent) alternative models

Bond graph and the later polymorphic modelling techniques provide a systematic modelling approach for multi-domain dynamic systems. However, these methods do not facilitate the process to identify key characteristics of the system, which dominate machine performance. These may lead to overlooking of significant dynamic effects within machine components that may contribute to the machine motion behaviour. Hence, a unified methodology is still lacking in offering more insight into the various machine components and their contributions to the overall system characteristics.

As mentioned, it is good practice to start the development of the controller concurrently with the machine structure design. Finite element modelling of the machine structure is commonly used to compute the structural characteristic parameters such as stiffness and damping. These parameters will form part of the transfer function in the design of the control loop. Coupled modelling of structural dynamics and control loop [18] were considered a unified way of designing a Mechatronic system. The coupled simulation can be generally classified into two types: *model parameters exchange* and *co-simulation* [19, 20]. In both of these types, Computer Aided Design (CAD) pack-

2.2 Mechatronic Approach to Machine Design

ages with Finite Element Analysis (FEA) are popular and key simulation tools. Figures 2.1(a) and 2.1(b) show illustrations of the two approaches of coupled simulations.

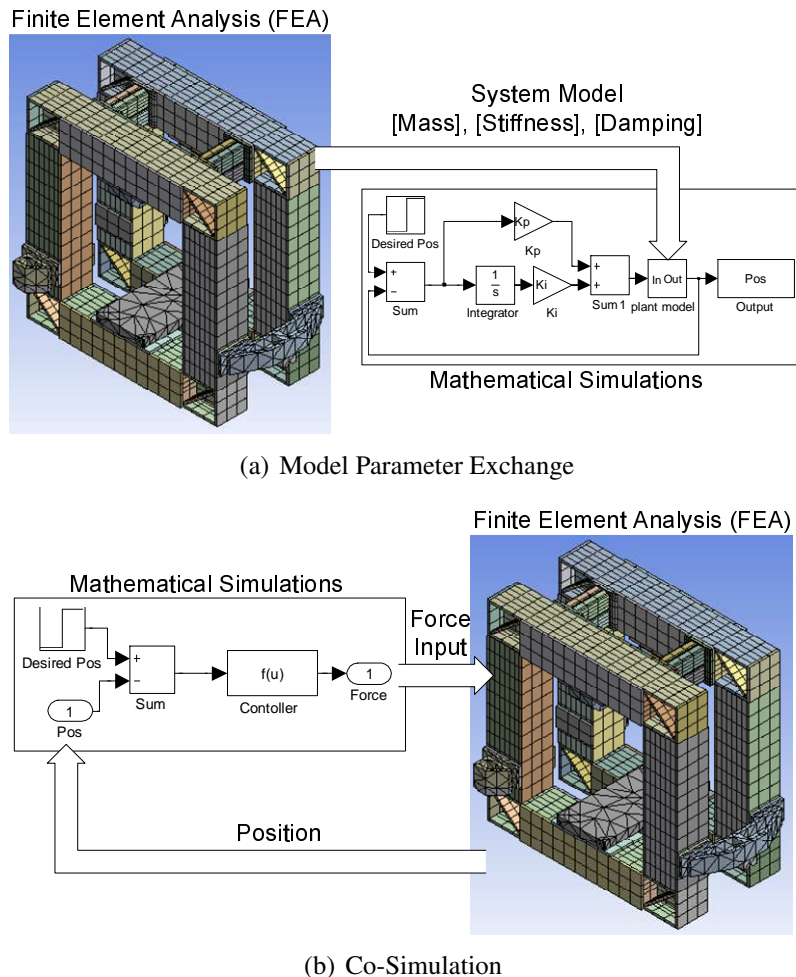


Figure 2.1: Two types of Coupled Simulation (After [19, 20])

The approach of model parameter exchange usually involves two or more simulation tools for different modelling aspects of the system. Model parameters are obtained from one simulation and transferred to the other, with each of the simulations running separately. In the context of a Mechatronic system, the predicted machine structural dynamic parameters such as the mass, stiffness and damping are transferred and used in the mathematical formulation of the controller scheme. The controller performance is evaluated and improvements can be made to the mechanical system to achieve an optimal design. In [21, 22], the transfer functions from motor torque to the tool dis-

Chapter 2. Literature Review

placement for different spatial configurations of the machine tools were computed. Using these transfer functions, a sliding mode control scheme was designed to handle the tool motion control for all configurations. The authors [21, 22] also proposed a dynamic model reduction scheme. Each axis of a three-axis mill machine was analysed separately using FEA. The proposed scheme was presented using a mill machine as a case study. The machine information in terms of the transfer function allows the designer to adjust and optimise the individual axis spatial properties, i.e. mass, stiffness and damping. This assumes that the axes are the main components that influence the motion performance of the machine. It may be valid for a heavy machine tool, which the structural characteristics constitute the bulk of the machine dynamics. In the cases of fast responding machines or lighter positioning systems, the study of its overall system transfer function may not be adequate to isolate key dynamic elements that affect the machine behaviour. Identifying and modelling the key dynamics elements becomes an apparent phase of precision machine design which is currently lacking.

Many Mechatronic design approaches used Modal Analysis as the fundamental technique to model mechanical dynamic behaviour of the system. Rankers [23] used *Modal Decomposition* method to break down the system into various machine elements. He considered the following key dynamics that may affect the machine motion performance as:

- actuator flexibility,
- guiding system flexibility, and
- limited mass and stiffness of stationary part of a machine.

Rankers' work proposed how a system could be decomposed into the above key dynamics which are represented in simpler series of mass-spring-damper systems in order to carry out modal analysis. The various machine elements were combined to predict the overall system modal model, and later derived into their state-variable representation of relevant modes and degrees of freedom. The relevant dynamic properties in the form of a state-variable representation are exported to control system modelling tools, such as MATLAB/Simulink[®]. In Rankers' doctoral thesis, modelling and validation of the major dynamic elements such as the actuator and guiding system flexibility

2.2 Mechatronic Approach to Machine Design

were not dealt with in depth. Although a general modelling technique using modal decomposition was proposed, the individual elements still require further investigation in order to realise a more accurate dynamic model for the system. Many commercial computer aided engineering (CAE) packages such as *ADAMS*[®], *DADS*[®], and *Recur-Dyn*[®] are able to provide multi-physics and multi-body dynamic solutions. However, engineers are still unable to model the dynamics of precision machine accurately. This is largely due to the lack of insight of the individual machine interfaces dynamics and hence the poorly defined models used in such CAE software.

The recent growing interest in Adaptronic components development for machine tool has witnessed more Mechatronic design approaches being applied. In a design of an Adaptronic drill tool axes, Brecher et al. [24] adopted the model parameter exchange technique to model and simulate the control performance. The author calculated the static and dynamic model using FEA simulation and used these parameters to formulate the linear state-space model equations for the control.

Model Parameters Exchange is probably the more commonly used method for coupled simulations. This may be due to its simple implementation, whereby there are minimum issues of software and parameter compatibility between simulation tools. However, such simulation techniques do not handle machine element non-linearity well. Most machine dynamic behaviour obtained from FEA results assumes that the system is linear about a particular operating point. Hence, the controller designed, which is based on this linearised model may not be able to perform well over the entire workspace of the system. Co-simulation approaches on the other hand are carried out simultaneously, and in a more integrated manner. The simulation output of the mechanical system is linked to another mathematical software that computes the controller output. Both the simulations run together synchronously in time domain. Brecher et al. [25, 26] used a Computer Aided Control Engineering (CACE) environment to couple the multi body simulation of a z-slider structure to a control block diagram in MATLAB/Simulink[®]. Figure 2.2 shows an illustration of how the structural dynamic and control simulations are linked. In [25, 26], the dynamic behaviour of the mechanical structures are simulated in FEA environment.

2.3 Dynamic Modelling of Machine Interfaces

tion. A typical motion system for a precision machine is comprised of the following components: structure/frame, machine bed, guideways, actuators, and transmission (if actuators are not direct-drive). In this thesis, the connections between these machine components are referred to as *machine interfaces*. The characteristics of these machine interfaces are very different, and can be generally categorised into three types, as listed below:

- *Structural joints*, for example, bolted, welded and adhesive based, as shown in Figure 2.3(a)
- *Moving contact interfaces*, for example, sliding contact and rolling element bearings, as shown in Figure 2.3(b)
- *Moving non-contact interfaces*, such as, hydrostatic, aerostatic and magnetic levitation bearing, as shown in Figure 2.3(c).

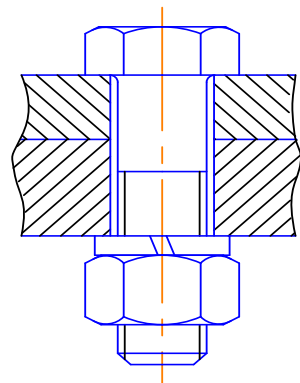
The characteristics of *structural joints* have been studied by many researchers in the field of machine simulation and design over the past few decades [27–30]. For *structural joints*, the stiffness and damping parameters can be described by the material strength of the joining components. For instance, the effective stiffness of a single bolted joint can be described by the model shown in Figure 2.4, in terms of the combined stiffness of its flange compression, flange shear, bolted base shear, the bolt itself as well as the joint interface stiffness [28, 29]. This can be simply estimated by:

$$K = K_{interface} + \frac{1}{K_{flangecompression} + K_{flangeshear} + K_{baseshear} + K_{bolt}} \quad (2.1)$$

To obtain the joint stiffness and damping matrices of structural joints, Lee [30] proposed a dynamic modelling technique by using modal testing, condensation method of FE Model and sensitivity analysis. The author has carried out thorough dynamic modelling and experimental work on structures with bolted and bearing joints. Good validation of his modelling method was achieved.

There is also considerable research effort in the modelling of *moving contact interfaces*. Moving contact interfaces deal with the mechanical interaction between relatively moving parts, such as sliding contacts and rolling elements. Differing from

Chapter 2. Literature Review



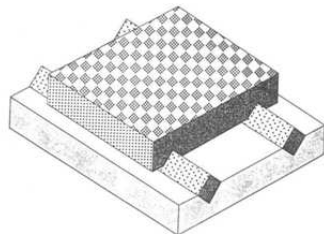
Bolted Joint



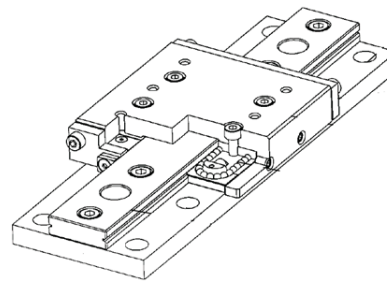
Photo by Yannick Trottier

Welded Joints

(a) Examples of Structural Joints

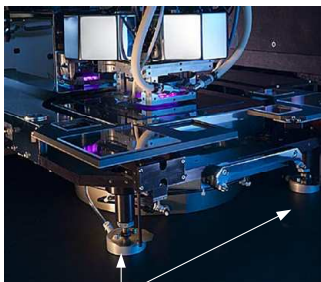


Sliding Contact bearing
(source: A. Slocum)



Rolling Element bearing
(source: PM bearings)

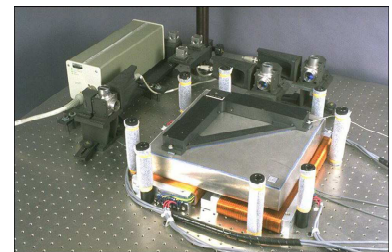
(b) Examples of Moving contact interfaces



Aerostatic bearing
(Source: Suss MicroTec)



Aerostatic bearing
(Source: ABTech inc)



Magnetic levitation bearing
(Source: Kim & Trumper, MIT)

(c) Examples of Moving contact interfaces

Figure 2.3: Types of Machine Interfaces

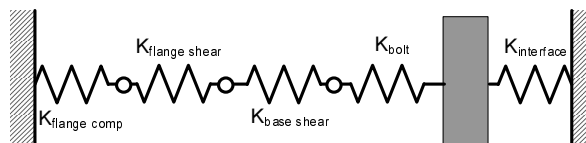


Figure 2.4: Spring model of bolted joint (Slocum [29])

2.3 Dynamic Modelling of Machine Interfaces

structural joints that constrain all degrees of freedom (DOFs), the moving contact interfaces attempt to free some DOFs and constrain the rest. Theoretically the freed DOFs can be assumed to have negligible stiffness and damping, however, this is not true in real interfaces with mechanical contacts, particularly in contact interfaces with higher friction such as sliding guideways. Owing to this consideration, Chlebus [31] modelled the sliding contact using FEA as a “third body” between the two sliding elements. This “third body” element was made up of a set of “normal” and “tangential” rod elements. These rods simulate the stiffness of the interface normal and tangent to the sliding direction, respectively. The proposed modelling method provides a more valid and simple way of evaluating the static performance of the sliding guideway. The dynamic characteristics of the interface, especially the tangential stiffness may differ significantly while the system is in motion. The dynamic aspect of the interface was not discussed in [31]. The dynamic characteristic parameters of an interface in a machine structure, namely the stiffness and damping, are determined by several factors, such as the material of the interfaces, lubricative state on the interface surfaces, machining method of the interface surfaces, etc [32]. The normal and tangential dynamic stiffness and damping of the guideway interface can be obtained experimentally based on the above factors [32, 33]. Figure 2.5 illustrates how Zhang [32] modelled the machine interfaces as elastic beams and complex springs. The measured and computed dynamic results were very close. This is mainly due to the fact that most of the joint stiffness and damping characteristics were obtained experimentally and employed in the analytical computation. In the context of a machine design phase, one may not have the luxury to obtain stiffness and damping characteristics of the machine interfaces experimentally. A general set of machine interface models in the form of finite elements would be very useful in achieving a more realistic machine model. Unfortunately, these elements are not available in most commercial FEA software packages.

There are extensive literatures in the area of static and dynamic modelling of rolling element bearing [34–39]. A rolling bearing simulation model called BEAST (BEARING Simulation Tool) [35] has been developed by SKF and used daily by their engineers to improve their insight into the bearing dynamic behaviour, thus enhancing the design process. Like sliding contact guideways, rolling element interfaces are often modelled

Chapter 2. Literature Review

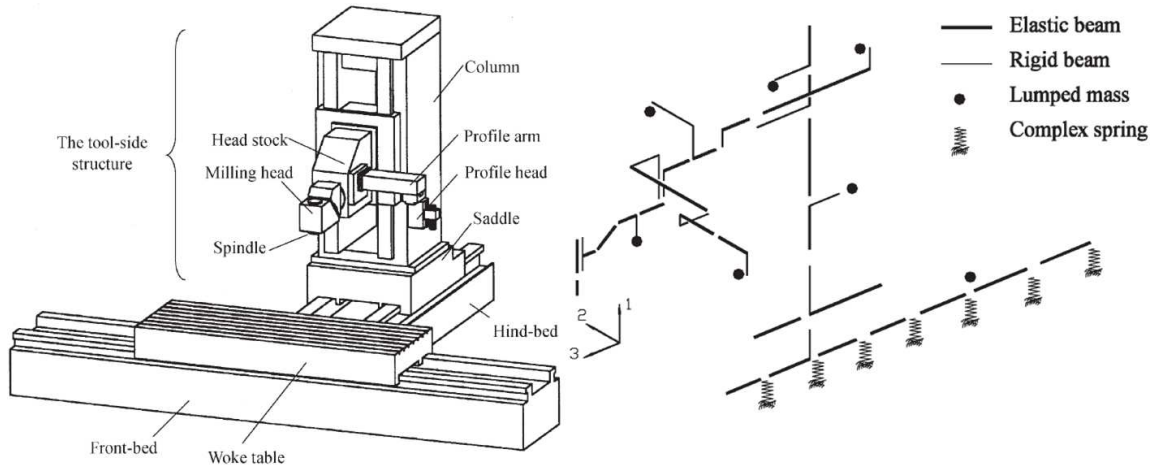


Figure 2.5: Left: ANC profile-machining centre and right: dynamic model of the tool-side structure (Zhang [32])

as spring elements in FEA. Ohta et al. modelled the ball bearing in a recirculating linear guideway carriage as two spring elements and a point mass [37]. As illustrated in Figure 2.6, each ball within the load zone l_L , was described by a point mass, m_b , corresponding to the mass of the ball. The interface between the ball and the carriage, and between the ball and the guide rail were represented by spring elements K_C and K_R , respectively. The FEA results were compared with an experimental modal test. The rigid-body natural frequencies agreed with the experimental results (with approximately 8-13% agreement).

Modal analysis, a Frequency Response Function (FRF) based method, is considered to be an effective method to evaluate dynamic models of machine interfaces. The common procedure for dynamic model parameter identification of machine interfaces can be summarised by Figure 2.7. Sharmin et al. [36] used this model identification scheme to determine dynamic model parameters of rolling element bearings in machine tools. A similar model identification approach was adopted in this work, and Chapter 5 shall present the detailed analytical and experimental procedures carried out in this research. Despite the fact that dynamic model parameters can be identified using various proposed approaches as discussed above, it is essential to understand that most machine interfaces behave in a non-linear fashion which are very much influenced by

2.3 Dynamic Modelling of Machine Interfaces

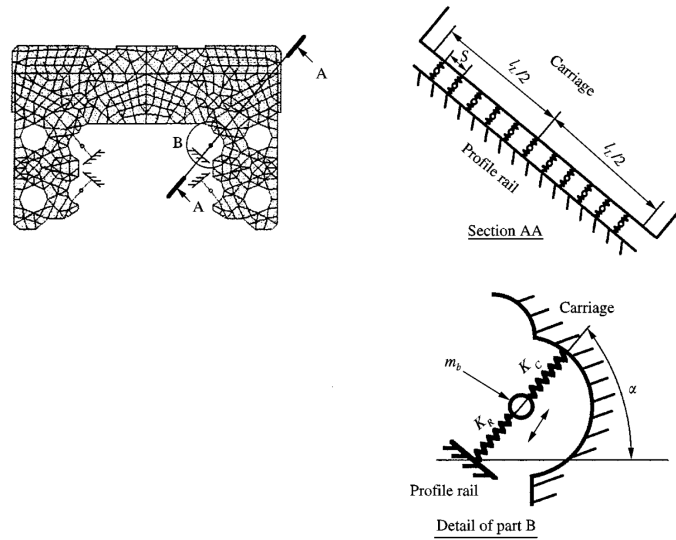


Figure 2.6: Finite Element Model of Ball Bearing (Ohta [37])

factors such as pre-loading, guide surface quality, assembly quality (alignment), etc. However, the fundamental modal analysis approach assumes the system to be linear [40]. This assumption can be relatively crude for some machine interfaces. Although there are several proposed methods [41–45] to address non-linearities in modal analysis, the practice of accounting for them in dynamic model identification is still not wide spread. This may be due to the demanding mathematical formulation involved.

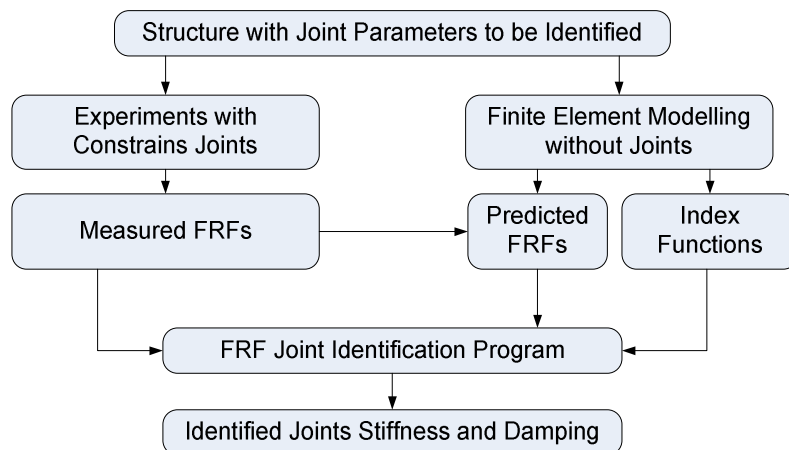


Figure 2.7: Flowchart of FRF-based Identification Scheme (Sharmin [36])

Chapter 2. Literature Review

Moving contact interfaces such as those guideways discussed formed a significant number found in motion systems of precision machines. Nonetheless, in recent years, more non-mechanical contact type of guideways was used to achieve sub-micrometre precision. These type of non-mechanical contact guideways constitute to the type of *moving non-contact interfaces*. Some examples of non-contact interfaces found in precision machines are hydrostatic, aerostatic and magnetic levitational bearings. A substantial amount of attention has been given to modelling of *structural joints* and *moving contact interfaces* over the past decades. Conversely, the understanding in dynamic modelling of non-contact interfaces was lacking. For instance, the earlier and more common non-contact guideways used in precision machine, particularly in machine tools, are hydrostatic bearings. Many good references over the last three decades have discussed the design and modelling of hydrostatic bearing guideways [29, 46–48]. Still, discussions on the dynamic characteristics of such guideways were scarce. For this reason, one of the work scopes for this research was to carry out in-depth investigation of dynamic modelling of these non-contact interfaces. Chapter 5 discusses how and why an aerostatic bearing guideway was chosen as an experimental set up for this research work. The following section shall discuss some of the related work in static and dynamic characterisation of aerostatic bearings.

2.4 Aerostatic Bearing Static and Dynamic Characteristics

In recent years, the term ‘air bearing’ has been used loosely and referred generally to as any type of air-lubricated bearing. However, the application and characteristics of the different type of air-lubricated bearings vary considerably. Air-lubricated bearings can be classified into three main types [49], as shown in Figure 2.8.

Aerodynamic bearings use a similar mechanism of viscous shearing as with hydrodynamic oil bearings. The air lubrication happens when two surfaces move relative to each other and generate a pressure between convergences of the two surfaces. In the case of a squeeze film as shown in Figure 2.8(b), the pressure is generated by one of the surface vibratory motion normal to itself. This vibration, normally at several kHz is produced by electro-mechanical or piezo-electric actuators. Due to its low load carry-

2.4 Aerostatic Bearing Static and Dynamic Characteristics

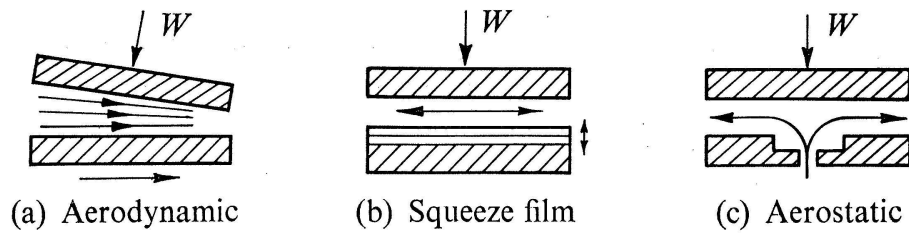


Figure 2.8: Types of air bearing (Powell[49])

ing capacity, squeeze film air bearings are more commonly used in low mass carrying applications such as hard disk drives and precision motion systems for wafer steppers. The study of squeeze films has been carried since 1950's [50]. It is receiving more attention in recent years due the development of Micro-Electro-Mechanical Systems (MEMS) [51, 52], hard disk drive read-head [53] and Tribology of air fluid [54–58]. Aerostatic bearings are also known as 'externally pressurised' air bearings owing to the fact that unlike the above two air bearings, external air supply is required to create the air film between the two sliding surfaces. Due to high load carrying capacity, aerostatic bearings are the most widely used among the three types of air bearing systems. For this reason, this research has focused investigation on aerostatic bearing systems.

In recent years, aerostatic bearings have gained in popularity in precision linear motion systems. Aerostatic bearings possess several characteristics that make them popular. Some of the advantages of aerostatic bearing as compared to contact type bearings and even hydrostatic bearings can be summarised as follows [49]:

1. Extremely low friction;
2. Capability of operating at very high speeds;
3. Precise axis definition and good averaging;
4. Little or no need for periodic maintenance;
5. Performance is less sensitive to operating temperatures; and
6. Low noise and vibration levels;

Aerostatic bearings basically utilise pressurised air to separate two sliding surfaces. The small air gaps (ranging from 5 to 10 μm) between the air bearings and the guide

Chapter 2. Literature Review

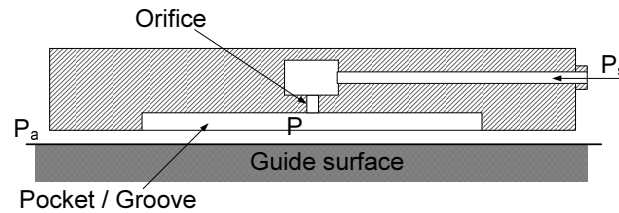


Figure 2.9: Schematic diagram of an orifice air bearing

surface enable the levitated carriage to slide along the guide surface in a “near-frictionless” manner. Two main types of aerostatic bearings are available commercially, namely the *orifice* type and *porous media* type.

The earlier form of ‘externally pressurised’ air bearings are mainly the orifice type. The orifice types of aerostatic bearings are made up of one or more small and precise holes through a bearing enclosure, as illustrated by the schematic diagram in Figure 2.9. Air at pressure P_s is supplied through the orifice and the air pressure, P in the pocket or groove regulate a stable air gap between the bearing and guide surfaces. The designs of the bearing’s orifices and pockets configuration was studied by [49, 59–61]. The static characteristics and performance of orifice aerostatics bearings were also investigated in depth by many researchers [49, 59, 61–66]. In essence, the air film in the gap is modelled as flow between two parallel surfaces, where viscous flow exists in this region. Reynolds’ theory of thin fluid film flow is used here to compute the performance of these orifice aerostatic bearings. The Reynolds equation is the differential equation governing the pressure distribution in the air film. This equation can be derived from the Navier-Stokes equation and the continuity equation under the following assumptions [49, 54]:

1. Newtonian flow and air acts as an ideal gas
2. Laminar and isothermal flow
3. Smooth surfaces
4. The gas film thickness is much smaller than the bearing dimensions so that the velocity gradients in the radial and tangential direction are negligible compared with the velocity gradients in the normal direction.

2.4 Aerostatic Bearing Static and Dynamic Characteristics

For a compressible isothermal air film of constant gap height in an aerostatic bearing, the Reynolds equation can be expressed as [60, 62]:

$$\frac{\partial^2 p^2}{\partial x^2} + \frac{\partial^2 p^2}{\partial y^2} = 0 \quad (2.2)$$

which is the Laplace field equation of p^2 , where p is the air film pressure and x and y are the perpendicular coordinates in the plane of the film. Most of the proposed methods solve the air film pressure p , numerically, using iterative methods [60, 62]. The static characteristics such as the loading capacity and stiffness can be obtained by integrating the pressure drop across the bearing surface or air film area. The load capacity, W , and static stiffness, K , of a porous aerostatic bearing air film can be expressed in terms of its air film pressure, p and ambient pressure, p_a [49, 62]:

$$W = \int_A (p - p_a) dA \quad (2.3)$$

where A is the surface area of the porous media that is sliding along the guide surface; and

$$K = -\frac{dW}{dh} \quad (2.4)$$

where h is the height of the air film. The analytical predictions were acceptable when compared with experimental results. Figure 2.10 shows the comparison of the load-lift curve (mass vs air gap) between the theoretical and experimental results obtained by Boffey [60].

The *porous media* aerostatic bearings work in a similar way except that instead of using orifice as the air pressure restrictor, porous material is used. Figure 2.11 shows a typical porous aerostatic bearing. The porous type of aerostatic bearings is more popular than the orifice type, due to their superior performance and characteristics. One major strength of porous air bearings is that the pressure within the air film is more evenly distributed. A comparison of air pressure distribution among a number of orifice type air bearings and a porous air bearing is presented in Figure 2.12.

There are more advantages of porous air bearings over conventional orifice types, such

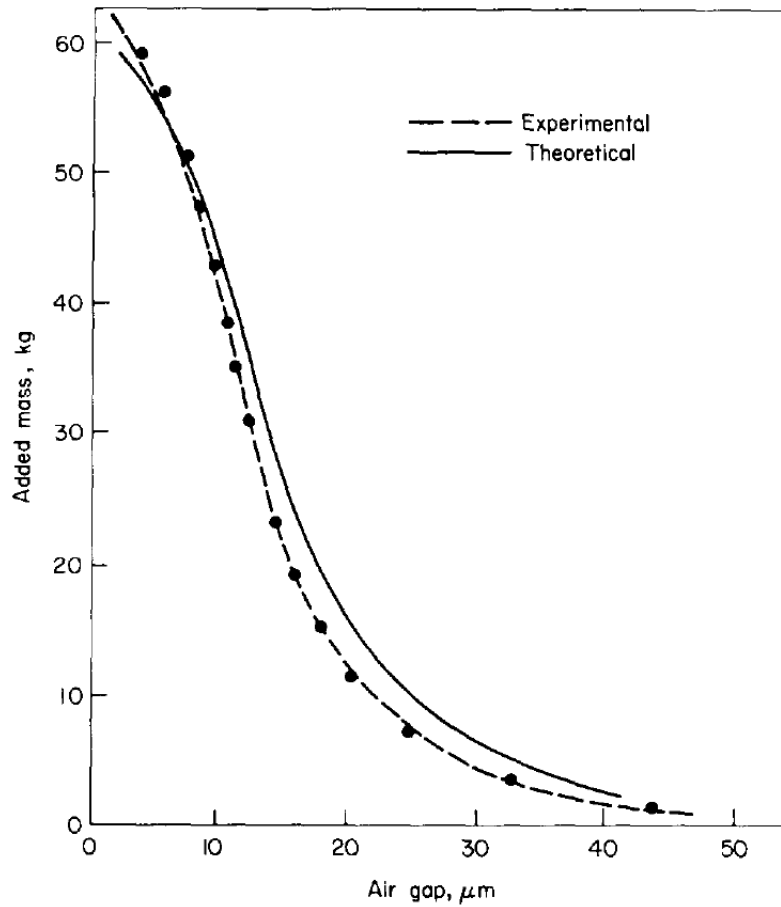


Figure 2.10: Experimental and theoretical comparison of the mass vs air gap curve (Boffey [60])

as the improved load capacity, simple construction, less sensitive to air cleanliness, as well as the superior stiffness and damping characteristics [67–70].

More research work was later directed towards the static characterisation of the porous media aerostatic bearing. Static performance such as the air film load capacity and stiffness of porous carbon aerostatics can be predicted using the pressure p of the air film, similar to the method used for orifice type of bearings. The earlier work was proposed by Rao and Majumdar et al [63, 71]. Several improvements and variations of the technique [72–77] were established after Rao and Majumdar's work. The primary target of the modelling method was to compute the pressure build up at the air film region. The pressure drop of the air supply across the porous media of the bearing is

2.4 Aerostatic Bearing Static and Dynamic Characteristics

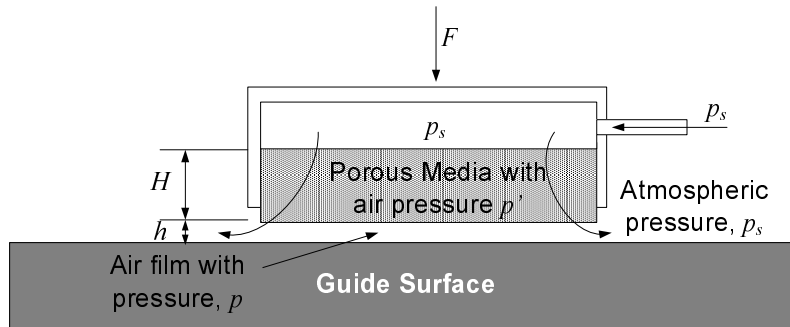


Figure 2.11: Schematic diagram of a porous aerostatic

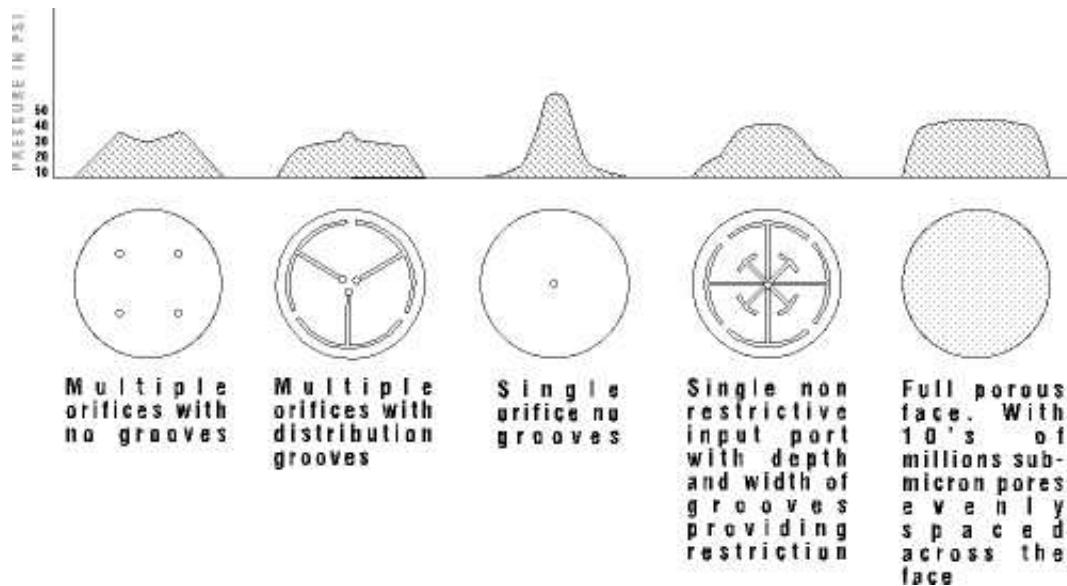


Figure 2.12: Comparison of air pressure distribution of orifice and porous type air bearings (from [67])

Chapter 2. Literature Review

computed by Darcy's Equation. In addition, the air flow within the thin air gap (which is governed by the Reynolds Equation) from the porous surface to the atmosphere is also taken into consideration. This air flow modelling is illustrated in Figure 2.11.

In the computation of air pressure for a porous aerostatic bearing, Equation (2.2) is modified to take into account the flow through the porous media, i.e. the pressure drops from supply pressure p_s to p' as it enters the porous media, then to p in the air film, and finally out to the atmosphere at pressure p_a . The pressure distribution in the porous media can be described by Darcy's Law,

$$k_x \frac{\partial^2 p'^2}{\partial x^2} + k_y \frac{\partial^2 p'^2}{\partial y^2} + k_z \frac{\partial^2 p'^2}{\partial z^2} = 0 \quad (2.5)$$

where $k_{x,y,z}$ is the permeability coefficients of the porous material in x, y and z directions respectively. The modified Reynolds equation governing the pressure in the air film can be expressed as:

$$\frac{\partial}{\partial x} \left(h^3 \frac{\partial p^2}{\partial x} \right) + \frac{\partial}{\partial y} \left(h^3 \frac{\partial p^2}{\partial y} \right) = 12k_z \left| \frac{\partial p'^2}{\partial z} \right|_{z=H} \quad (2.6)$$

By defining some boundary conditions for the model, the solution for p is solved numerically using iteration method [71, 73]. Like orifice type of bearings, the load capacity, W and static stiffness, K of a porous aerostatic bearing air film can be expressed in terms of its air film pressure, p and ambient pressure, p_a , as shown in Equations (2.3) and (2.4).

A slightly different approach for porous to compute the air film pressure, p was proposed by Plante et al [78]. Plante uses generalised one dimensional air flow method to predict the pressure distribution of circular aerostatics. As compared to former methods using Darcy's Law and Reynolds equation [63, 71–77], this method is much efficient and fast in computing the pressure p needed to evaluate the air film characteristics. Hence, Plante's method is adopted here in the air film modelling. More elaborated discussion of this method is presented in Chapter 6.

2.5 Discussion

The proposed work establishes the methods to predict static behaviour of aerostatic bearings. However, investigation of dynamic properties of an air bearing and its influence on the entire guide system behaviour is lacking. A linear motion system using non-contact aerostatics was developed in Massachusetts Institute of Technology [79]. Cortesi modelled the air film as a simple disc element in ANSYS. Though his analytical and experimental comparisons may not seem very scientific and conclusive, the work did, however, suggest a preliminary and practical approach to modelling porous aerostatic using FEA in a simple manner. This simple FEA model of the air film was evaluated in the preliminary stage of this EngD research. The prediction results of an aerostatic bearing guide system using Cortesi FEA model were not satisfactory. This evaluation is discussed in Chapter 7.

2.5 Discussion

This chapter has reviewed the previous work in the field of precision machine design, and showed the need for a Mechatronic approach in the design methodology. The need to take into account machine dynamics during the machine design phase were emphasised by prominent researchers [18, 22, 23, 25] in the field of precision engineering. It was considered that machine interfaces substantially influence the dynamic behaviour of machine system. References on modelling of various types of machine interfaces were discussed. The review progressed to focus on non-contact machine interfaces modelling. These non-contact interfaces were considered to be more complex and comprise of significant non-linearity that were more difficult to predict. A number of papers on aerostatic bearings were also presented. Several weaknesses and technology gaps were observed within the above mentioned literature review. The following statements summarise the major observations.

- Mechatronic design approach which incorporates machine dynamics is of paramount importance in developing fast responding precision machines. The success of these design methodologies warrant a general set of valid machine interface models in order to accomplish an optimal design.

Chapter 2. Literature Review

- Non-contact type machine interface models are not commercially available using finite elements, thus engineers are unable to achieve realistic model of their machines.
- A significant number of techniques [27–30, 32, 33, 35–37] have been proposed for static and dynamic modelling of joints and contact type of machine interfaces within the academics/research community. However, many researchers still choose to obtain the dynamic model of such interfaces experimentally rather than analytically.
- Due to the demand for higher resolutions, level of accuracy and operating speeds in motion systems, non-contact type guideways such as aerostatic bearings have become widely used.
- Static modelling of non-contact aerostatic bearings have been proposed [72–77], but the dynamic modelling work in such interfaces is lacking.
- The technology gap in dynamic modelling of non-contact interfaces exists and the challenges lie in the modelling and prediction of non-linear dynamic characteristics of aerostatic bearings.

It would be difficult to address all the issues of the above findings within this EngD research. Therefore this research mainly focuses on dynamic investigation of non-contact air bearings interfaces. This work aims to develop a valid aerostatic interface model that can be used to improve the accuracy of machine FEA models, so as to achieve a dynamically optimal design. The dynamic effects of an aerostatic guideways within a motion system are discussed in detail in Chapter 7. The dynamic modelling and validation of the interfaces model are presented in Chapter 6 and 7.

Chapter 3

Industrial Context and Technology Adoption Issues

3.1 Background of Precision Engineering in Singapore

Precision engineering (PE) was identified as the main manufacturing cluster in Singapore [80]. Singapore's PE industry began in the 1970s as a capability to support the first manufacturing investments. The PE industry is made up of manufacturers of precision components and machinery, as well as providers of related manufacturing services. It is a key supporting pillar to a wide range of industry sectors such as electronics, aerospace and medical technology. In 2005, the PE industry generated an output of S\$20 billion and contributed to 12% of manufacturing value add. It is also one of the largest contributors of manufacturing employment, accounting for one out of every four jobs in the sector. The industry is expected to generate an output of S\$28 billion and double its value added to S\$10 billion by 2018.

To achieve this target, one of the major efforts is to boost research and development in PE technologies [80]. This is heavily undertaken by the 10 government-supported research institutes under the Agency for Science, Technology and Research (A*STAR) and a cohort of research departments within the national universities.

The Singapore Institute of Manufacturing Technology (SIMTech), one of A*STAR's

Chapter 3. Industrial Context and Technology Adoption Issues

research institutes, is committed to enhancing Singapore's competitiveness through the generation and application of advanced manufacturing technologies. Its core competencies range from precision mechatronics, real-time control and signal processing, to product design/development and manufacturing processes. SIMTech has made good progress in developing leading edge technologies. Its Mechatronics Group is continuously acquiring new capabilities, especially in the area of high precision motion system for equipment manufacturers. The end-user applications are high precision motion applications, such as wafer inspection in the semiconductor industry, high-speed wire bonding machines in electronics industry and micro-arraying in the medical industry.

Motion accuracy in precision machines has been one of the core issues in the PE industry. In this thesis, precision machines refer to machines which are able to achieve an accuracy of at least $5 \mu\text{m}$ and resolution in the nanometre scale. These machines range from the macro type for grinding and diamond turning functions, instruments for diagnosis and lithography applications (such as wafer inspection) to the miniature "Feynman" machines for Fibre Bragg Grating applications. Figure 3.1 shows some examples where motion or positioning systems are used in high precision machines. Although the motion system of the above mentioned precision machines vary in terms of their actuation and measurement system, their design methodology and control are very much similar.

Over the last decade, advancement in technologies, such as laser interferometry, direct-drive linear motors, and higher bandwidth controllers have enabled most precision positioning system in the industry to achieve sub-micrometre accuracy. However, moving to the next phase of ultra-precision technology, achieving higher accuracy over a longer range of travel becomes the order-qualifying¹ capabilities of most manufacturers. These are especially needed in the Gen-10² large flat-panel display operation, manufacturing of the next generation large telescope optics, as well as the increasing semiconductor wafer size. The ever demanding manufacturing industry continues to

¹Order-qualifying is a term coined by Hill to describe essential criteria an organisation required to stay in the industry [81].

²10th Generation LCD display which measure 2,850 x 3,050mm, or 50 to 65 inch range.

3.2 Proposed Approach to Precision Machine Design



Figure 3.1: Examples of high precision machines

push their machine's performance indicator limit such as Unit-per-Hour (UPH) beyond its current capability. Inevitably, this desires the machine's motion system to travel at higher acceleration and velocity, yet maintaining short settling time of the end-effector tools. In order to achieve the above capabilities for precision motion system, a pragmatic approach to precision machine development is essential.

3.2 Proposed Approach to Precision Machine Design

3.2.1 Current Industrial Practice

Precision Machine Design has a long history and the process is considered very established, particularly in the machine tool industry. Most precision motion systems were designed based on their functional and performance specifications. Some of these design considerations are listed [29]:

1. *Geometry*: What is the overall size and footprint? Should consideration be separated into macro and micro geometry?

Chapter 3. Industrial Context and Technology Adoption Issues

2. *Kinematics*: What are the required maximum speed, repeatability, accuracy and resolution?
3. *Dynamics*: What forces are generated? What type of machining or operation? What are their potential effects on the system and its components? How rigid must the machine be to resist processing forces while maintaining surface finish and part accuracy?
4. *Power requirement*: What types of actuators can be used, and what systems are needed to control the operating environment (e.g. cleanroom facilities)?
5. *Sensory capability*: What is the resolution and accuracy? This often correspond to the cost of investment.
6. *Control*: What type of control system and control scheme are we using? This factor is very much related to the kinematic and dynamics of the system, which the report will discuss in the later sections.

The majority of precision motion systems are predominantly mechanical, i.e. with the above design considerations in mind, the mechanical engineer will be the key person who starts the process on the drawing board. Besides ensuring the motion system meets the geometric and kinematic requirements, such as range, speed, accuracy and resolution, dynamics (which consists of the amount of forces that will be generated) are also considered. The common practice is to ensure that the structure is able to within the reaction forces created by the acceleration of carriage and workpiece. The structure should also be rigid enough so that its first natural frequency is above the machine operating bandwidth. Many of Singapore's machine builders, especially those belonging to the small and medium enterprises (SMEs) do not have sufficient capabilities and resources to carry out extensive analytical work on their machine during the designing phase. Simple structural modelling using commercial FEA packages is usually carried out. The simple FEA helps the engineers to identify the structural stress and deformation, as well as its modal behaviour. However, as discussed in Chapter 2 many of these FE-models are not accurate, as models of the machine interfaces are either not considered or invalid. Through experience, most engineers are aware of this problem, and over-designing the system to accommodate for the uncertainties is a straight forward

3.2 Proposed Approach to Precision Machine Design

solution.

Though this mechanically conservative approach of developing precision machines may achieve acceptable performance, it introduces issues that affect the developed machines as well as the company's long term competitiveness. The following summarises some of these problems.

Excessively Bulky Machine As discussed, due to the need for higher UPH performing machines, thus higher acceleration, the machine structure is required to withstand higher reaction force. To avoid excitation of the resonance frequencies of the motion system during machine operation, machine structure and interfaces are designed to be stiff in the required DOFs. The 'brute force' approach is to select a stiffer material and guideways; and increase the moment of inertia for the structure design in the required DOFs. This designing method usually results in larger-than-essential machine. Factory space is expensive in most developed countries like Singapore. Bigger machine footprint means less space for other machinery and activities. More companies, especially those in the semiconductor and electronics industries, are seeing smaller machine footprint as an added advantage.

Motion Control Issue System modelling is essential in motion controller tuning. Lack of consideration of the motion controller capabilities during the design stage, commonly leads to an inaccurate system model. Much effort has been spent on developing and tuning the motion controller, after the machine (mainly the mechanical components) has been built. A simple controller in many cases is not sufficient to compensate for the poorly-modelled machine interfaces dynamics. Undesirable time and resources are spent on achieving good motion performance.

Cost Incurred Uncertainties in machine performance impacts the initial budget allocated for the developmental work. Unforeseen motion control issues clearly contribute to the additional cost when time and resources are consumed to tackle these unmodelled machine dynamics. During development of the motion controller, particular machine behaviour may warrant some major changes in the mechanical design

Chapter 3. Industrial Context and Technology Adoption Issues

of the system. In some cases, it may even require better or more advanced controller system, or additional devices such as anti-vibration device in order to realise the desired motion/positioning performance. All these additional cost in development are commonly underestimated.

Time-to-Market In this era of a fast moving computing and electronics world, *Time-to-Market* becomes an essential indicator for a product manufacturer to stay above the competition. *Time-to-Market* is the time taken for a product from being conceived until its being available for sale. Time spent on a poorly planned machine development will usually translate to longer time to commercialise it. To achieve faster *Time-to-Market*, some companies may resolve to commissioning a less superior machine that inherent some performance deficiency, and attempt to patch them after sale. Many iterate their machine design cycle and reintroduced improved version of their existing machines. These in many ways, affect the companies long term competitiveness and reputation.

A ‘first time right’ mindset in machine development is important to ensure the company sustainability in this ever demanding knowledge-based economy. The subsequent subsection briefly presents a holistic approach of machine design and modelling, which takes into consideration key dynamics of the machine which will influence the motion system performance.

3.2.2 Potential Solution

A mismatch in the precision machine development process exists between the mechanical design phase and the controller design phase. The aim of this EngD research project is to develop a method to model the key machine dynamics of a precision motion system, so as to bridge the gap between design and control of a mechatronic system. The research outcomes and proposed methodologies from this doctoral project are summarised in Chapter 8. These results lays the foundation to enable a design tool for analysing complex precision systems. The design tool shall facilitate engineers to model and predict accurately machine dynamic behaviour in a FEA environment.

3.3 Technology Adoption

The technology gap is in dynamic modelling of non-contact machine interfaces, as discussed in Chapter 2. Though research effort was in pursue to address this knowledge gap, many research outcomes are still not implemented in industry. The main difficulty is that many modelling techniques are considerably mathematical, thus creating some resistance among engineers. There is a need for a mechatronic design tool, which integrates with commercial FEA packages. Moreover, a unified and comprehensive design tool that consider all aspects of machine interfaces dynamics is difficult to realise and may not be feasible. A specific level of knowledge in machine dynamics and modelling is still required of the design engineers in order for him to find this proposed design tool useful. From a pragmatic standpoint, development of this technology though challenging, the adoption and diffusion of it in a company and through an industry posts equally tricky issues. The following section shall discuss the issues in and methods of *technology adoption*.

3.3 Technology Adoption

Manufacturing facilities are moving out of Singapore and attracted to lower cost countries within the Asia region. Essentially, this implies that Singapore manufacturing industry needs to direct its focus on high value added activities and competencies. These activities ought to be knowledge-base. However, Singapore industry, in particular SMEs companies have been slow in adopting cutting-edge technologies. Research and Development (R&D) effort is also not considered as an essential investment. The following subsections shall investigate the subject of technology adoption, and discuss how a systematic adoption methodology can be applied for the proposed mechatronic design tool. The methodology can be broadly grouped into: *planning*, *acquisition* and *assessment*. These groups are generally carried out in sequence and in most case iterative in nature.

3.3.1 Planning

In order to gain sustainable competitive advantage, companies have to continuously identify, build and renew its own unique core competencies. For a precision ma-

Chapter 3. Industrial Context and Technology Adoption Issues

chine/equipment builder this is of utmost importance. The process of technology adoption becomes a growing interest among academics as well as industrial practitioners.

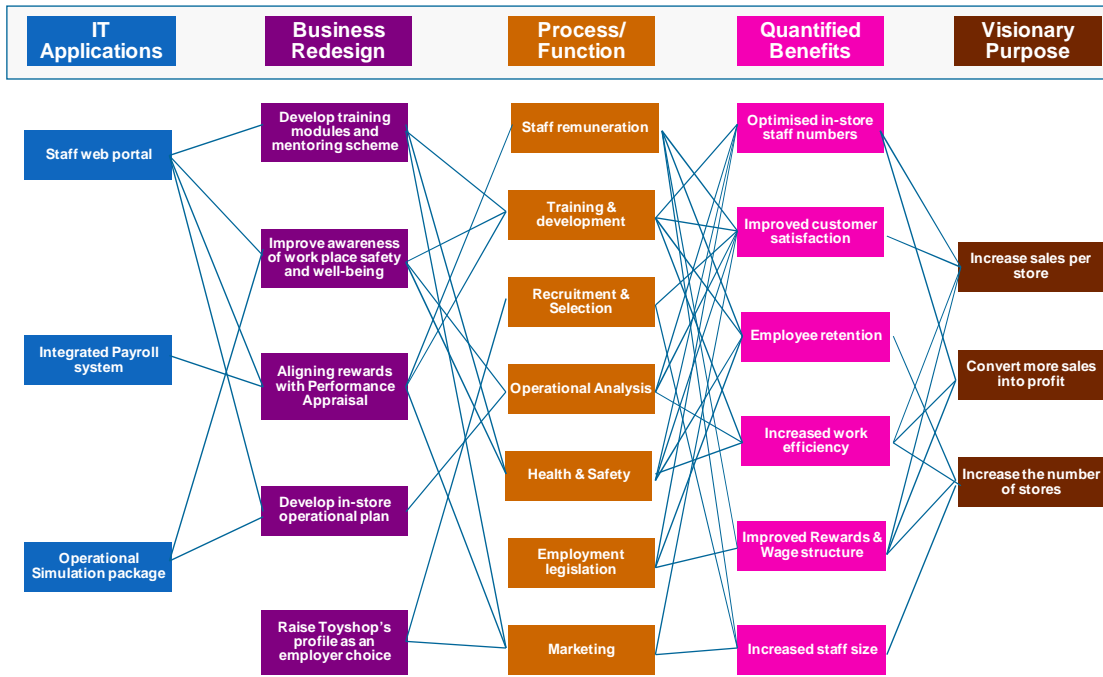


Figure 3.2: Benefits Dependency Network for an HR IT management plan

Technology adoption should be a holistic approach in gaining technological advantage to stay competitive. Consequently the technology adoption process should involve problem or objective definition, technology sourcing, implementation, monitoring and auditing. A good technology adoption process usually combines a few techniques to address the wide spectrum of issues - from problem definition, to solution formulation and implementation. From the management point of view, technology adoption should be aligned to the organization’s mission and objectives. Ward et al. [82, 83] proposed a framework called *Benefits Dependency Network (BDN)* for adopting IT solution for businesses. Although Figure 3.2 shows a BDN for IT applications proposed for HR management, one can easily apply this directly to a machine manufacturer environment. This can be done by replacing the *visionary purpose* with objectives such as *reduce cost per unit machine, increase product quality and increase time-to-market*. Subsequently, the organisation shall identify and propagate the network from right to left the *Quantified Benefits, Process/ Function, Business Redesign* that link to the adop-

3.3 Technology Adoption

tion of the new technology. The BDN allows the management to have a clear overview of how the technology adoption is linked with its business function, and how it benefits the organisation in achieving its vision.

A very common method to support technology strategy and planning is the technology roadmapping approach. The approach was originally developed by Motorola more than 25 years ago, to support integrated product-technology planning. Since then the technique has been adapted and applied in a wide variety of industrial contexts, at the company and sector levels (for example, the International Semiconductor and UK Foresight Vehicle technology roadmaps). Technology roadmaps can take many forms, but generally comprise multi-layered time-based charts that enable technology developments to be aligned with market trends and drivers [84].

3.3.2 Acquisition

The above two approaches are considered as technological gap analyses or planning, which allow companies to gain understanding of what technologies they need to embark on. The next phase is naturally technology sourcing, which also involves the common make-or-buy question. Lanctota et al. [85] and Cho et al. [86] both suggested similar consideration factors that will influence the decision making of internal technology development or external technology acquisition. Figure 3.3 summarises the relationship between the various influencing factors as well as the mode of acquisition [86].

The implementation, monitoring and auditing of the (internally/externally) acquired technology is the next major phase after the decision have been made. Baines et al. [87] proposed a nine-step technology acquisition process, which includes the implementation and post-investment audit steps. This phase of performance assessment of the newly acquired technology is important. It should be an iterative and ongoing process to continue the technology enhancement of the company competencies. There seems to be a lack of in-depth discussion in this area of technology adoption. This offer a misguided suggestion that structured and sound decision making phase is suffi-

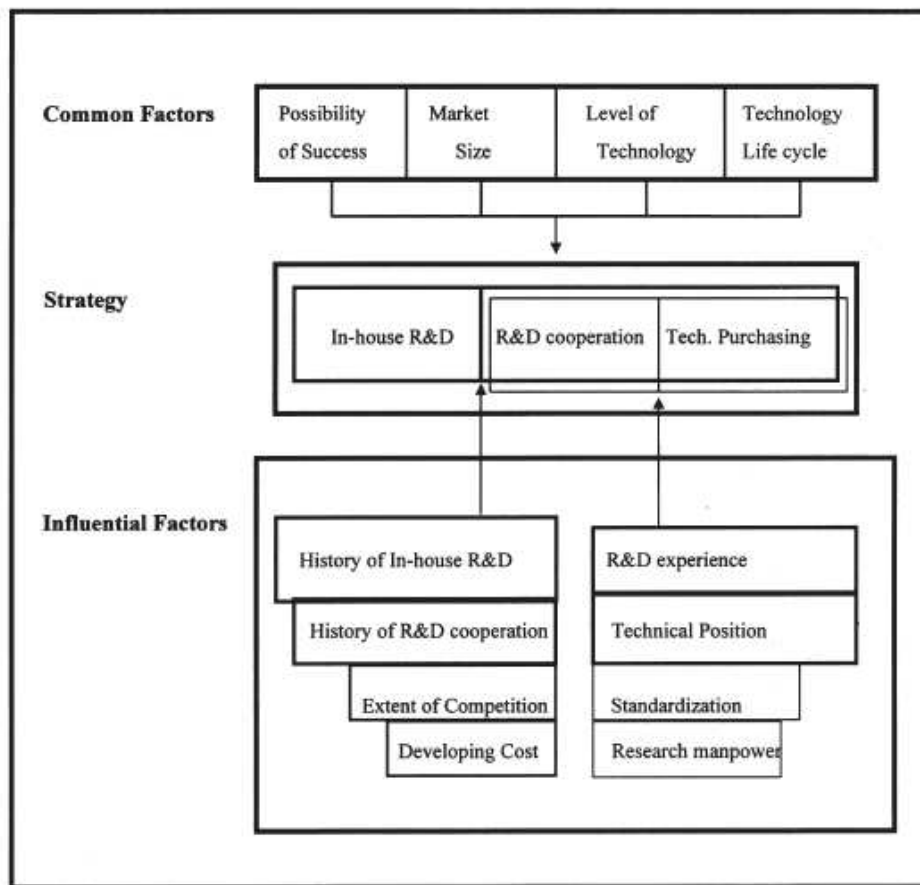


Figure 3.3: Relationship between factors and modes

cient to warrant a successful technology adoption.

Although much research has been done in the field of technology adoption or acquisition process, these structure frameworks are not widely practised in the manufacturing industries. Most companies have a rather implicit process when acquiring new technology. This implicit practice is common in the Singapore precision machine manufacturing industry.

3.3.3 Assessment

In order for this proposed mechatronic design tool to realise a successful adoption in the industries, one should recognise the adoption criterion for this technology. This section shall discuss about these criterion and the development guidelines to ensure a

3.3 Technology Adoption

more promising industrial adoption.

Many research institutes and R&D centres within multi-national companies employ an assessment method called the *Technology Readiness Level (TRL)*. TRL was initiated and used by NASA to assess the maturity of their developing/developed technologies [88]. The original definition only consisted of seven readiness levels, and later expanded to nine levels. The nine TRLs include:

1. Basic principles observed and reported
2. Technology concept and/or application formulated
3. Analytical and experimental critical function and/or characteristic proof of concept
4. Component and/or breadboard validation in laboratory environment
5. Component and/or breadboard validation in relevant environment
6. System/subsystem model or prototype demonstration in a relevant environment
7. System prototype demonstration in a real environment
8. Actual system completed through test and demonstration
9. Actual system through successful mission operations

These different levels allow the researchers and/or developers to have a clear assessment of the technology progression. It helps to direct the focus towards realising practical application, rather than just striving for scientific outcomes. However, that does not mean that the developed design tool will be readily adopted by the industry after level 6 or 7. Several factors still need to be put in place during the development of the mechatronic design tool. The tool should contribute to attaining the objective(s) defined by the end user or task(s). Speser [89] described this contribution as utility, i.e. the more contribution, the higher the utility. The metrics that define utility of a technology can be broadly categories as *performance* and *ease-of-use*.

Besides attempting to fulfil the functionality or *performance* of the design tool to predict unmodelled dynamics in precision motion system, the researcher should not lose

Chapter 3. Industrial Context and Technology Adoption Issues

sight of the *ease-of-use* characteristics of the technology. We can have a rough sense of utility of the technology by giving weight to both performance and ease-of-use to reflect their importance to end users. This can be understood by the following equation [89]:

$$\text{Performance}(\sum p_{1\dots n} \times w_{1\dots n}) + \text{Ease of Use}(\sum e_{1\dots n} \times w_{1\dots n}) = \text{Utility}(u) \quad (3.1)$$

where w is the weighting, and there can be multiple metrics of performance, p and ease of use, e .

The weighting system can be rather subjective. It is very important that the researcher does not merely based on personal judgement to infer the weight of these metrics. An industrial survey should be carried out to sample the actual metrics variable and values. Characteristics of the design tool that contributes to utility value can be incorporated into the developmental work at different TRL of the technology. The researcher developing this technology should understand the concept of matching scientific outcome with industrial and end user expectations.

Within SIMTech, *Research Planning Exercise (RPE)* is carried out yearly to chart the research direction for individual research groups. As a research institute, most of the new technologies are internally acquired (as described by Baines et al. [87]). The RPE process is a combination of a technology roadmapping approach and a TRL assessment method. This allows the research group to visualise and track the research direction and progression over a period of time, usually within 3 to 5 years.

3.4 Conclusions

Precision Engineering is an important pillar in Singapore's manufacturing industry. The country needs to develop high value added activities and competencies in order to stay ahead of the stiff competition in Asia. The initial part of this chapter discusses the deficiencies in the practice of precision machine design in the industry. The main

3.4 Conclusions

knowledge gap is in the prediction of machine dynamics, in particular machine interfaces. The rest of this thesis (particularly, Chapter 5 to 8) addresses the technical challenges and discusses various potential solutions to bridge the technological gap. However, it is recognised that scientific solutions alone do not always guarantee a successful industrial adoption of the technology. In view of that, this chapter investigates potential technology adoption methodologies that could be use to drive the development of this work and even beyond the EngD research.

Technology adoption process can be done systematically in the following phases: *planning*, *acquisition* and *assessment*. The widely used *Technology Roadmapping* approach is suggested for the planning phase. Although there are several proposed methods of decision making for technology acquisition mode, these methods are yet to be widely practised. It is observed that decision-making mechanisms in many organisations remain rather implicit. Assessment is essential to ensure that the technology development and adoption is carried out rigourously and effectively. TRL is one of the most well-established and recognised standard in assessing the readiness level of a technology. In most situations, the above 3 phases are carried out iteratively. To sum up, a good technology transfer mindset is required to be in place, even at the early stage of the research work.

Chapter 4

Theory and Application of Modal Analysis

4.1 Basic Concept of Modal Analysis

The dynamic modelling and analysis work carried out in this research was based on the modal analysis technique. Modal analysis is a methodology to investigate the dynamic characteristics of a (mechanical) system. The earlier work and objectives of modal analysis were primarily intended for the analysis of structural (in terms of their shapes, construction and material properties) behaviour; and many of the established texts were also written mainly covering aspects pertaining to it. The field of modal analysis were later extended to the area of machine tool design to better understand the dynamics of these machines. Nevertheless, the fundamental theory governing structural and machine dynamic behaviour is almost identical. This chapter shall establish some basic theoretical background of modal analysis which are applicable to dynamic analysis of machine interfaces. Many of the discussions here are represented within a number of established texts [40, 90–92].

The dynamic characteristics in the context of this research refer to the natural frequencies, damping factor and mode shapes of a system, which is also referred to as the *Modal Model*. The system model can be generally represented in the form of mass, stiffness and damping; and is referred to as the *Spatial Model*. Modal analysis encom-

4.1 Basic Concept of Modal Analysis

passes two processes: theoretical formulation and experimental testing. The theoretical formulation, also known as the analytical process, involves the identification of the system's Spatial Model. The properties of the Spatial Model can be represented in the form of a partial differential equation. The solution of the equation provides the Modal Model, i.e. the natural frequencies and mode shapes of the system. Based on the solution, the relationship of the system responses under given force excitation conditions are explicitly described using frequency domain expression. This relationship is commonly known as the *Response Model* of the system. The Response Model consists of a set of *Frequency Response Functions (FRFs)* within a specified range of frequency.

The experimental testing, also referred to as *modal testing*, is basically the process to obtain the Modal Model of an existing mechanical system experimentally. Experimental modal testing can be understood as the reverse of the above analytical process. Using a set of force and motion (accelerometers or other displacement probe) transducers, the FRFs of the system can be measured. Numerical analysis methods are used to derive the modal properties of the system from measured FRF by means of curve fitting. The detailed experimental process is presented in Chapter 5.

4.1.1 Single Degree of Freedom (SDOF) System

Almost all practical mechanical systems exhibit multi-degree of freedom (MDOF) behaviour. However, it is important to establish the fundamental understanding of a SDOF system before embarking on MDOF systems. The system model can be generally classified into: *undamped* and *damped* systems.

4.1.1.1 Undamped Systems

Figure 4.1 shows a classical undamped mass and spring system. $f(t)$ and $x(t)$ are time-varying force and displacement variables, and the spatial model here only consists of a mass (m) and a spring (k).

Using Newton's second law of motion, the SDOF system can be described in the form:

$$m\ddot{x} + kx = f(t) \quad (4.1)$$

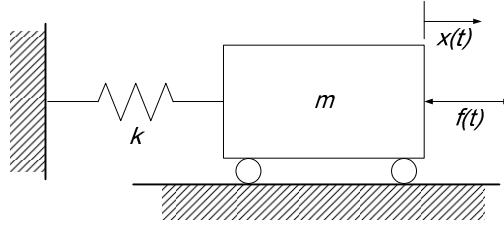


Figure 4.1: A simple SDOF mass and spring system

Applying Laplace transformation, Equation (4.1) can be rewritten in the form of a transfer function of the system, as:

$$G(s) = \frac{X(s)}{F(s)} = \frac{1}{ms^2 + k} \quad (4.2)$$

and the *response model* can be derived in the same way as Equation (4.2) in the form of a frequency response function (FRF) $H(\omega)$.

$$H(\omega) = \alpha(\omega) = \frac{X}{F} = \frac{1}{-m\omega^2 + k} \quad (4.3)$$

When excitation force is not present, i.e. $f(t) = 0$, the modal model becomes a simple solution of the natural frequency, $\bar{\omega}_0$ of a free undamped vibration.

$$\bar{\omega}_0 = \sqrt{\frac{k}{m}} \quad (4.4)$$

Note that the natural frequency of a simple SDOF system is the ratio of its mass and stiffness, and its FRF in Equation (4.3) is independent of the excitation. The response parameter X above represents displacement of the mass. FRF with displacement response is also known as *Receptance*. The term receptance is more commonly used in the study of structural behaviour. From the perspective of machine design, a more common and well-understood term to use would probably be *compliance*. Thus, this thesis shall adopt the term *compliance*. Compliance of a system is usually represented by $\alpha(\omega)$, and $H(\omega)$ is more of a general FRF representation. Depending on the application of analysis, the response may also be presented in the form of velocity or acceleration, whereby the FRFs are referred to as Mobility (V/F) or Inertance (A/F), respectively. Table 4.1 shows the different variation of FRFs and their corresponding

4.1 Basic Concept of Modal Analysis

Response Parameter, R (unit)	Standard FRF, R/F (unit)	Inverse FRF, F/R (unit)
Displacement (m)	Receptance Dynamic Compliance Dynamic Flexibility (m/N)	Dynamic Stiffness (N/m)
Velocity (m/s)	Mobility (m/Ns)	Mechanical Impedance (Ns/m)
Acceleration (m/s ²)	Accelerance Inertance (m/Ns ²)	Apparent Mass (Ns ² /m)

Table 4.1: Definition of Frequency Response Functions (after [40])

SI units. Figure 4.2 shows the frequency plots of the three different types of FRFs. For a SDOF system, the fundamental natural frequency is where the maximum response occurs. One can easily identify the natural frequency by locating the peak of the curve. Note that these frequency plots can provide useful information about the mass and stiffness of the SDOF system by superimposing the relationship between the FRF and its spatial model properties (i.e. Equation (4.3)) onto the (log-log scale) plot.

4.1.1.2 Damped Systems

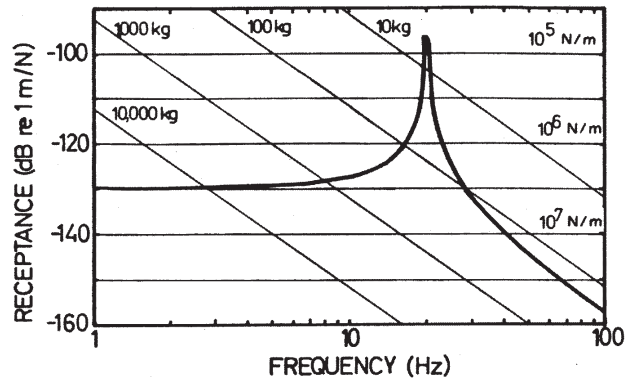
Damping exists in all mechanical systems in the form of friction, structural properties and/or energy dissipating dampers. The more commonly used damping model is the viscous damping. This section shall confine the discussion to viscously damped systems¹.

Figure 4.3 shows a mass, spring and damper system. Now, the equations of motion that govern this system has an additional viscous damper term, c .

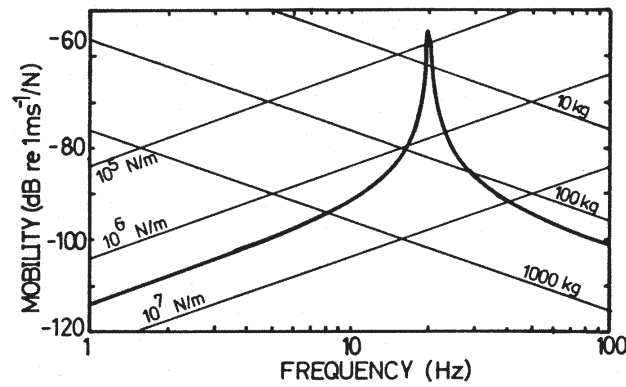
$$m\ddot{x} + c\dot{x} + kx = f(t) \quad (4.5)$$

If no excitation force is present, i.e. $f(t) = 0$, the system will correspond to a free

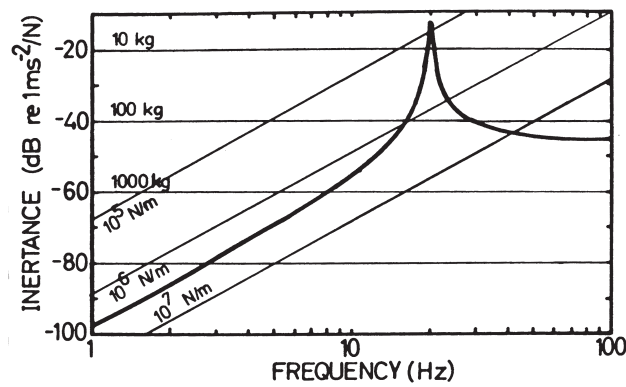
¹The study of other damping models such as the hysteretic and structural damper are beyond the scope of this thesis, thus will not be covered here. More elaborated discussions on damping models can be found in [40, 93–95].



(a) Receptance or Compliance FRF



(b) Mobility FRF



(c) Inertance FRF

Figure 4.2: FRF plots of undamped SDOF system (from [40])

4.1 Basic Concept of Modal Analysis

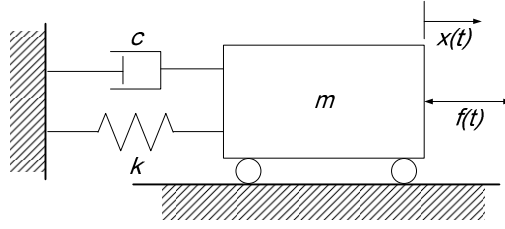


Figure 4.3: A SDOF mass, spring and damper system

damped system, expressed as:

$$m\ddot{x} + c\dot{x} + kx = 0 \quad (4.6)$$

To solve Equation (4.6), a solution can be assumed of the form:

$$x(t) = X e^{st} \quad (4.7)$$

where s is complex, and by substituting $X e^{st}$ into the equation, Equation (4.6) can be expressed in an algebraic form.

$$(ms^2 + cs + k) = 0 \quad (4.8)$$

Thus, the solution will consist of two roots:

$$s_{1,2} = -\frac{c}{2m} \pm \sqrt{\left(\frac{c}{2m}\right)^2 - \frac{k}{m}} \quad (4.9)$$

When a system is critically damped, the critical damping coefficient can be represented by the term c_0 , whereby

$$c_0 = 2m\sqrt{\frac{k}{m}} = 2\sqrt{km} \quad (4.10)$$

It is common to express damping in terms of the critical damping coefficient in a nondimensional variable, known as the damping ratio, ζ .

$$\zeta = \frac{c}{c_0} = \left(\frac{c}{2\sqrt{km}}\right) \quad (4.11)$$

Chapter 4. Theory and Application of Modal Analysis

Hence, Equation (4.9) can be rewritten as:

$$s_{1,2} = \left(-\zeta \pm i\sqrt{1 - \zeta^2} \right) \bar{\omega}_0 \quad (4.12)$$

By substituting Equation (4.12) into (4.7), the general solution for the equation of motion for free damped vibration becomes:

$$x(t) = X e^{-\bar{\omega}_0 \zeta t} e^{i(\bar{\omega}_0 \sqrt{1 - \zeta^2}) t} \quad (4.13)$$

This general modal solution has a complex natural frequency which contains the imaginary oscillatory part of frequency, $\omega'_0 = \bar{\omega}_0 \sqrt{1 - \zeta^2}$, and a real decay part of damping rate, $a = \zeta \bar{\omega}_0$, as illustrated in Figure 4.4.

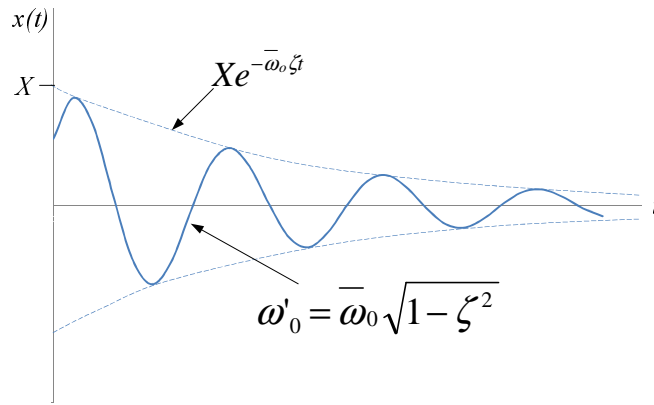


Figure 4.4: Free Damped Oscillation

Using a similar approach of Laplace transformation as carried out on an undamped system, the compliance FRF can be expressed as:

$$H(\omega) = \alpha(\omega) = \frac{X}{F} = \frac{1}{(-m\omega^2 + k) + i(c\omega)} \quad (4.14)$$

$H(\omega)$ is now a complex function, which comprises of both magnitude and phase information.

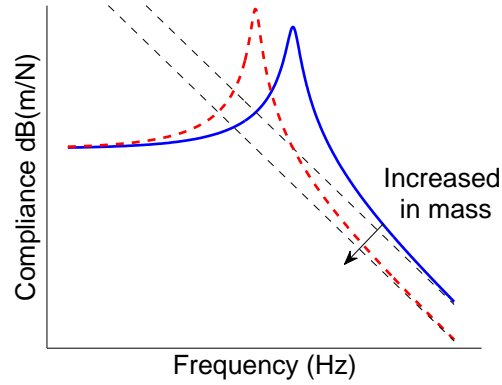
Subsections 4.1.1.1 and 4.1.1.2 discussed the mathematical relationship between the spatial properties (mass, stiffness and damping) and the modal properties, natural frequencies and mode shapes. It would be useful to understand how the spatial properties

4.1 Basic Concept of Modal Analysis

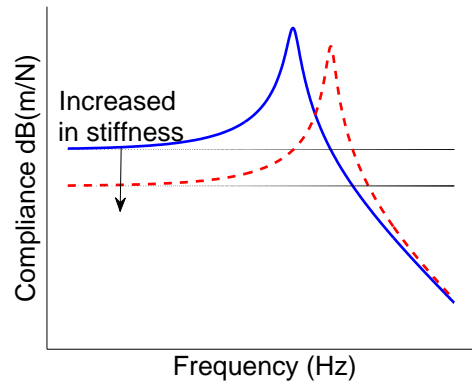
of a system influence its frequency response (FRF) plot. Figure 4.5 shows how the increased of the individual spatial properties: mass, stiffness and damping affects the frequency response of a SDOF system. Figure 4.5(a) shows that by increasing the mass without changing the other properties, the peak (i.e. the natural frequency) of the FRF curve shifted to the left, indicating a decreased in natural frequency. Note that the use of the superimposed *mass line* as discussed above and shown in Figure 4.2(a) was also illustrated by the two parallel black dashed mass lines. Figure 4.5(b) demonstrates that by increasing the stiffness, the natural frequency is increased as well. A similar use of the superimposed lines was also shown in the plot, where the horizontal black lines represent the stiffness of the system. Damping does not have any effect on the natural frequency of the system. However, the response magnitude will be reduced if the system has higher damping, as illustrated in Figure 4.5(c). This interpretation method of the FRF plots help to perform a quick evaluation of a simple system by inspecting its measured FRFs. As the system becomes more complex (with higher DOFs and non-linearity effects), understanding the system through visual inspection of its FRFs becomes much harder. The subsequent section shall extend the above theoretical formulations to MDOF systems.

4.1.2 Multi-degree of Freedom (MDOF) Systems

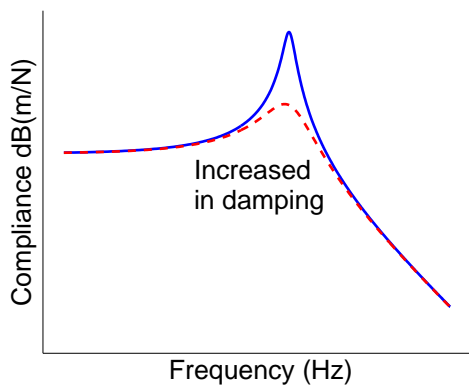
Section 4.1.1 introduced the concept of dynamic analysis in SDOF systems. However, almost all practical mechanical systems are multi-degree-of-freedom. Like a SDOF system, the fundamental elements in a MDOF system are still its mass, stiffness and damping. The principle of analytical procedure is very much similar to the SDOF system as well. The only major difference is that the system is now a combination, and in many cases, coupled effect of multiple inertia, stiffness and damping corresponding to each degree of freedom. The description of the dynamics of such systems would inevitably be in matrix form.



(a) Effect of increasing mass



(b) Effect of increasing stiffness



(c) Effect of increasing damping

Figure 4.5: Effect on FRF plots by changing spatial properties of the system. (Blue solid lines indicate original FRF and red dashed lines indicate FRF with increased in property value)

4.1 Basic Concept of Modal Analysis

4.1.2.1 Undamped Systems

An undamped MDOF system, with n degrees of freedom can be described in the same way as a SDOF system, using the equations of motion.

$$[M]\{\ddot{x}(t)\} + [K]\{x(t)\} = \{f(t)\} \quad (4.15)$$

Note that in a MDOF case, the mass, $[M]$ and stiffness, $[K]$ are $n \times n$ (symmetric) matrices. The time-varying displacement, $x(t)$ and force, $f(t)$ delimited by the braces $\{\}$ are $n \times 1$ vectors. In order to obtain the natural modal properties of the system, the free vibration solution shall be taken, i.e. $\{f(t)\} = \{0\}$, and by assuming a solution of $\{x(t)\} = \{X\}e^{i\omega t}$, the equation of motion will become:

$$([K] - \omega^2[M])\{X\}e^{i\omega t} = 0 \quad (4.16)$$

Based on linear algebra, for a homogeneous equation, like Equation (4.16), the non-trivial solutions only exist if and only if its determinant is zero. Hence, this will lead to a set of n numbers of undamped natural frequencies, $\bar{\omega}_r^2$, and a corresponding set of mode shapes, $\{\Psi\}_r$. The equation of motion can thus be expressed as an eigenvalue problem:

$$([K] - \bar{\omega}_r^2[M])\{\Psi\}_r = \{0\} \quad (4.17)$$

where $\bar{\omega}_r^2$ are the eigenvalues and $\{\Psi\}_r$ are the corresponding eigenvectors. Note that, attributable to the Orthogonality properties of the modal model, the eigenvalues matrix can also be obtained from: $[\bar{\omega}_r^2] = [m_r]^{-1}[k_r]$, whereby *modal mass*, m_r and *modal stiffness*, k_r are defined respectively as follow:

$$[\Psi]^T[M][\Psi] = [m_r] \quad (4.18a)$$

$$[\Psi]^T[K][\Psi] = [k_r] \quad (4.18b)$$

Modal mass matrix, $[m_r]$ and modal stiffness matrix, $[k_r]$ can be understood as a set of SDOF spatial models for a given r mode of the MDOF system. Effectively, a MDOF system can be ‘decomposed’ and analysed numerically as n number of SDOF systems which corresponds to the individual modes of the MDOF system.

Chapter 4. Theory and Application of Modal Analysis

To establish the response model of the undamped MDOF system, a set of sinusoidal forces $\{f(t)\} = \{F\}e^{i\omega t}$ are considered to be acting on the system. These harmonic forces are assumed to have the same frequency, ω , but with different amplitudes and phases. Equation (7.7) can be simply rewritten as:

$$([K] - \omega^2[M]) \{X\}e^{i\omega t} = \{F\}e^{i\omega t} \quad (4.19)$$

or may be written in this form:

$$\{X\} = [\alpha(\omega)]\{F\} \quad (4.20)$$

where *the response model*, $[\alpha(\omega)]$ for this system is a $n \times n$ compliance matrix. $[\alpha(\omega)]^{-1}$ or $([K] - \omega^2[M])$ are also known as the *dynamic stiffness matrix* of the MDOF system. It is useful to note that both the dynamic stiffness matrix and the compliance FRF matrix are symmetrical. This describes the reciprocity characteristic of a linear MDOF system. The compliance FRF matrix can be broken down into each element to have a clearer interpretation of this physical meaning. A response element, X_j at coordinate j can be interpreted as:

$$X_j = \alpha(\omega)_{j1}F_1 + \alpha(\omega)_{j2}F_2 + \dots + \alpha(\omega)_{jn}F_n \quad (4.21)$$

Assuming only one force, F_k is applied to the system, then Equation (4.21) will be simplified to:

$$\alpha(\omega)_{jk} = \frac{X_j}{F_k}; \quad F_r = 0, r = 1, 2, \dots, n \text{ and } r \neq k \quad (4.22)$$

Thus, the reciprocity nature of a linear MDOF system suggests that a response at coordinate, j due to a single force input at coordinate, k is the same as the response at coordinate, k due to the same force input at coordinate, j . It would not be difficult for one to realise that the values for the compliance matrix $[\alpha(\omega)]$ can be obtained by substituting the frequency values of interest into the inverse of the dynamic stiffness matrix, $([K] - \omega^2[M])$. However, this has several drawbacks, namely [40]:

4.1 Basic Concept of Modal Analysis

- it is computationally costly for large-order degrees of freedom systems;
- it is inefficient if only a few FRF expressions are required;
- it provides no insight into the form of the various FRF properties.

A more effective method of deriving the various FRF parameters is to use the system's modal properties, rather than the spatial properties, i.e. the *dynamic stiffness matrix*. To achieve that, the dynamic stiffness matrix is used as the basis.

$$([K] - \omega^2[M]) = [\alpha(\omega)]^{-1} \quad (4.23)$$

By inserting $[\Phi]^T \dots [\Phi]$ to both sides of the equation, Equation (4.23) can be rewritten as:

$$[\Phi]^T ([K] - \omega^2[M]) [\Phi] = [\Phi]^T [\alpha(\omega)]^{-1} [\Phi] \quad (4.24a)$$

$$\text{or } [(\bar{\omega}_r^2 - \omega^2)] = [\Phi]^T [\alpha(\omega)]^{-1} [\Phi] \quad (4.24b)$$

$$\text{resulting in } [\alpha(\omega)] = [\Phi] [(\bar{\omega}_r^2 - \omega^2)]^{-1} [\Phi]^T \quad (4.24c)$$

where $[\Phi]$ is the *mass-normalised mode shape* of the system, i.e.

$$[\Phi] = [\Psi][m_r]^{-1/2} \quad (4.25)$$

Again, $[\alpha(\omega)]$ is symmetric, thus agreeing to the principle of reciprocity, as mentioned above. From Equation (4.24c), any single compliance FRF element can be obtained as follow:

$$\alpha_{jk}(\omega) = \frac{\phi_{j1}\phi_{k1}}{\bar{\omega}_1^2 - \omega^2} + \frac{\phi_{j2}\phi_{k2}}{\bar{\omega}_2^2 - \omega^2} + \dots + \frac{\phi_{jn}\phi_{kn}}{\bar{\omega}_n^2 - \omega^2} \quad (4.26)$$

Equation (4.26) is more meaningful and informative than Equation (4.22). The FRF is now expressed in terms of the system's modal parameters, and reveal its composition of all the individual modes. The FRF equation can be further simplified in the form:

$$\alpha_{jk}(\omega) = \sum_{r=1}^N \frac{{}_r A_{jk}}{\bar{\omega}_r^2 - \omega^2} \quad (4.27)$$

where ${}_r A_{jk}$ is referred to as the *Modal Constant*, and sometimes also known as the

Chapter 4. Theory and Application of Modal Analysis

Residue. The formulation discussed in this sub-section established the basis for the next section on damped MDOF systems.

4.1.2.2 Damped Systems

Like mass and stiffness properties, damping of a system is an important aspect in a practical analysis of a mechanical system. Unfortunately, in most cases, damping cannot be modelled in a straightforward manner like mass and stiffness [96–98]. *Proportional* damping was considered to be an acceptable means to carry out damped MDOF systems analysis [40, 90–92]. In the context of modal analysis, incorporating proportional damping into the analysis of a damped MDOF system becomes apparent as the resulting modal properties are very similar to an undamped system, in particular the mode shapes.

Proportional Viscous Damping The general equation of motion for an MDOF system is expressed in the same way as Equation (4.5), but in matrix form. The viscous damping term is denoted as matrix $[C]$, as shown in Equation (4.28).

$$[M]\{\ddot{x}(t)\} + [C]\{\dot{x}(t)\} + [K]\{x(t)\} = \{f(t)\} \quad (4.28)$$

To enable the modal analysis of damped MDOF systems, using the same methodology of undamped system, Rayleigh [99] assumed that the viscous damping is proportional to the inertia and stiffness properties of the system (hence the name, *proportional damping*). This damping model has been widely accepted and used extensively in the area of vibration and modal analysis [40, 90–92, 97, 98]. Therefore, the damping matrix can be expressed as:

$$[C] = \gamma[M] + \beta[K] \quad (4.29)$$

Similar to the properties of the spatial model in an undamped system, defined in Equation (4.18), the *modal damping* matrix can also be defined in the same way as follow:

$$[\Psi]^T[C][\Psi] = [c_r] \quad (4.30)$$

4.1 Basic Concept of Modal Analysis

where $[c_r]$ is also a diagonal matrix, like $[m_r]$ and $[k_r]$.

Considering a free damped system, and pre and post multiplying Equation (4.28) with $[\Psi]$, the equation of motion for a damped MDOF system can be rewritten as:

$$[m_r]\{\ddot{x}_p\} + [c_r]\{\dot{x}_p\} + [k_r]\{x_p\} = \{0\} \quad (4.31)$$

where $\{x_p\} = [\Psi]^{-1}\{x\}$. As mentioned in the above subsection 4.1.2.1, this form of equation which is expressed in terms of *modal mass, stiffness and damping* can be analysed as a set of decoupled SDOF systems. Thus, it has a complex natural frequency that can be described in the similar way as a SDOF system (shown in Figure 4.4), whereby the imaginary oscillatory part, ω'_r is expressed as:

$$\omega'_r = \bar{\omega}_r \sqrt{1 - \zeta_r^2} \quad (4.32a)$$

$$\text{where its damping ratio, } \zeta_r = \frac{c_r}{2\sqrt{k_r m_r}} = \frac{\gamma}{2\bar{\omega}_r} + \frac{\beta\bar{\omega}_r}{2} \quad (4.32b)$$

$$\text{and the real decay part is } a_r = \zeta_r \bar{\omega}_r = \frac{\gamma + \beta\bar{\omega}_r^2}{2} \quad (4.33)$$

Since the above derivation from Equation (4.30) to (4.33) are based on eigenvector of the undamped system, $[\Psi]$, the assumption of proportionally damped system will still hold, i.e. the damped and undamped system mode shapes are identical.

For the same reason, the forced response analysis of a proportionally damped MDOF system can also be performed in a similar method as an undamped MDOF system. Hence, alike Equation (4.23), the general compliance FRF equation can be written in this form:

$$[\alpha(\omega)] = [K + i\omega C - \omega^2 M]^{-1} \quad (4.34)$$

and each of the FRF elements becomes a complex function, depicted as:

$$\alpha_{jk}(\omega) = \sum_{r=1}^N \frac{r A_{jk}}{\bar{\omega}_r^2 - \omega^2 + i2\zeta\omega\bar{\omega}_r} \quad (4.35)$$

Chapter 4. Theory and Application of Modal Analysis

Proportional Hysteresis Damping A practical damping modal that is also commonly used is the *hysteresis* or *structural damping* model. Besides the internal material characteristics of structure, this hysteretic behaviour also found in machine motion system in the form of contact friction, e.g. sliding contacts and roller element bearings [29, 100–102]. Instead of proportional to the velocity like viscous damping, hysteresis damping is described by a force that is proportional to the displacement. This damping force is in phase with the velocity. Thus, the general equations of motion that include the *proportional hysteresis damping* will be depicted as:

$$[M]\{\ddot{x}\} + ([K + iD])\{x\} = \{f\} \quad (4.36)$$

where $[D]$ is the proportional hysteresis damping matrix, which also has the same ‘proportional’ nature as $[C]$, whereby

$$[D] = \beta[K] + \gamma[M] \quad (4.37)$$

Again, due to its proportionality of the damping effect, the system shares the same eigenvectors with its equivalent undamped system. However, the hysteretically damped system has eigenvalues, λ_r^2 which are complex and are described as:

$$\lambda_r^2 = \bar{\omega}_r^2(1 + \eta_r) \quad (4.38a)$$

$$\text{where } \eta_r = \beta + \frac{\gamma}{\bar{\omega}_r^2} \quad (4.38b)$$

η_r is defined as the damping loss factor of the system at r th mode.

The force response solution for the hysteretically damped MDOF system follows through the same method as the above undamped and viscously damped MDOF system. Consequently, the general compliance FRF element results in an expression of this form.

$$\alpha_{jk}(\omega) = \sum_{r=1}^N \frac{rA_{jk}}{\bar{\omega}_r^2 - \omega^2 + i\eta_r\bar{\omega}_r^2} \quad (4.39)$$

4.1 Basic Concept of Modal Analysis

Non-proportional Hysteresis Damping Most would prefer the system to comprise of proportional damping, however in most instances machine damping comprising of various type of interfaces do not behaviour proportionally. It would be essential to employ a more general term for hysteresis damping in mechanical system. Due to its non-proportional nature, the complex eigenvalue equation yields a set of eigenvalues that are different from the undamped eigenvalue solution (refer to the previous undamped systems discussion in the beginning of subsection 4.1.2.1). Therefore, the eigenvalue λ_r^2 is now a complex function of the natural frequency ω_r , instead of $\bar{\omega}_r$. Note that the overline on ω_r denotes an undamped natural frequency.

$$\lambda_r^2 = \omega_r^2(1 + i\eta_r) \quad (4.40)$$

Consequently, the problem will lead to a FRF equation that is similar to Equation (4.39), but using a general natural frequency term, ω_r . The compliance FRF elements of a non-proportional hysteretically damped MDOF system is expressed as:

$$\alpha_{jk}(\omega) = \sum_{r=1}^N \frac{rA_{jk}}{\omega_r^2 - \omega^2 + i\eta_r\omega_r^2} \quad (4.41)$$

and in matrix form

$$[\alpha_{jk}(\omega)] = ([K] + i[D] - \omega^2[M])^{-1} \quad (4.42a)$$

$$\text{or} \quad [\alpha_{jk}(\omega)] = [\Phi] [(\lambda_r^2 - \omega^2)]^{-1} [\Phi]^T \quad (4.42b)$$

The above give a broad but thorough overview of the theoretical formulation of modal analysis of SDOF and MDOF systems under both undamped and damped conditions. As mentioned, the analysis is consisted of two processes: analytical and experimental. The theory of system modal behaviour will be useful in the modal parameters extraction which will be carried out during experimental modal testing. The procedure and methods for modal testing is introduced in the next section.

4.2 Modal Testing

Modal Testing as mentioned earlier, is an experimental process to obtain the actual modal characteristics of a system. This involves measurement of the frequency response of the system and post processing to extract the modal parameters, such as the natural frequencies and mode shapes. The modal testing procedure can be broadly divided into three main steps, namely, Preparation, Measurement and Post Processing. The following subsections briefly discuss each of these steps.

4.2.1 Preparation and Test Planning

Test planning for modal testing is a wide subject area, especially for large complex structures. For the modal testing performed in this research, elaborated test planning is not required. However, it is useful to have some form of plan in order to obtain sufficient measurements that describe all the dynamic behaviour which of interest to the analysis. Below are some considerations to make before the test:

- The numbers and placement of response points (position of accelerometers) are crucial in acquiring accurately the ‘expected or interested’ mode shapes.;
- The range of frequency and resolution for the measurement.;
- The size and measurement range of the impact hammer is dependent on the size and stiffness of the system.
- The hardness/softness of the impulse hammer head. This will determine the range of frequency that will be excited by impulse hammer.;
- The location of the impact point. Although it is useful to choose an impact location where impact force can be directed in three DOFs (X, Y and Z axis), it is more important that the location is effective in exciting all the response points.

Based on the above consideration of measurement points, a wireframe model was constructed in the software, which corresponds to the actual geometry of the test system (in this case, a guideway structure as shown in Figure 5.3(b)). Figure 4.6 shows the model geometry which consists of the determined measurement points.

4.2 Modal Testing

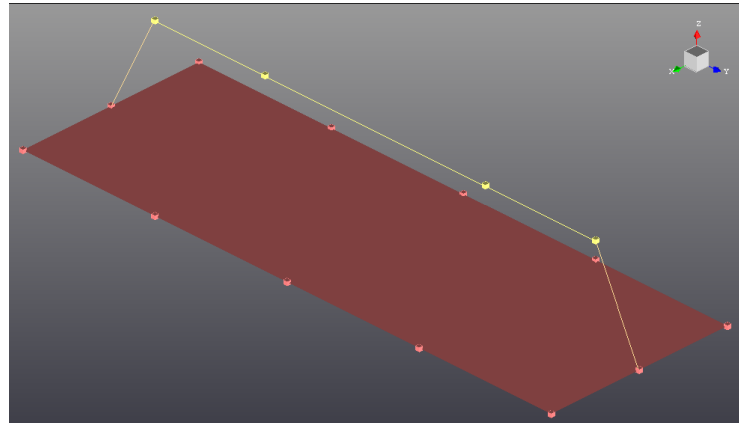


Figure 4.6: Model geometry with measurement points of the guideway structure

4.2.2 Measurement Process

The measurement steps basically obtain the frequency response of the test system. In essence, a frequency response function is the ratio between the response of a system when subject to an excitation force, normally presented and analysed in the frequency domain. There are two major class of sensors used for measuring the responses of a system, namely: acceleration transducer (accelerometer) and laser transducer. These transducers primarily measure the displacement, velocity or acceleration of the response over a specific time period. The excitation force information is obtained by means of a force transducer embedded either in a impact hammer or a shaker. This work adopted the impact testing experimental scheme with the use of a impact hammer (for force measurement) and accelerometers (for response measurements). Figure 4.7 shows a schematic of a typical experimental setup for modal impact testing.

The impact hammer excitation method is a simple and quick-to-setup experiment, and that was the main reason it was chosen for this work. In the setup as shown in Figure 4.7, three accelerometers were attached to the structure by thin layer of adhesive wax. The accelerometers were placed in locations which were considered to measure sufficient number of points so that the mode shapes can be uniquely described. A more comprehensive discussion of sensors placement for modal testing can be found in [40].

The simple illustration in Figure 4.7 shows the impact hammer exciting the structure at

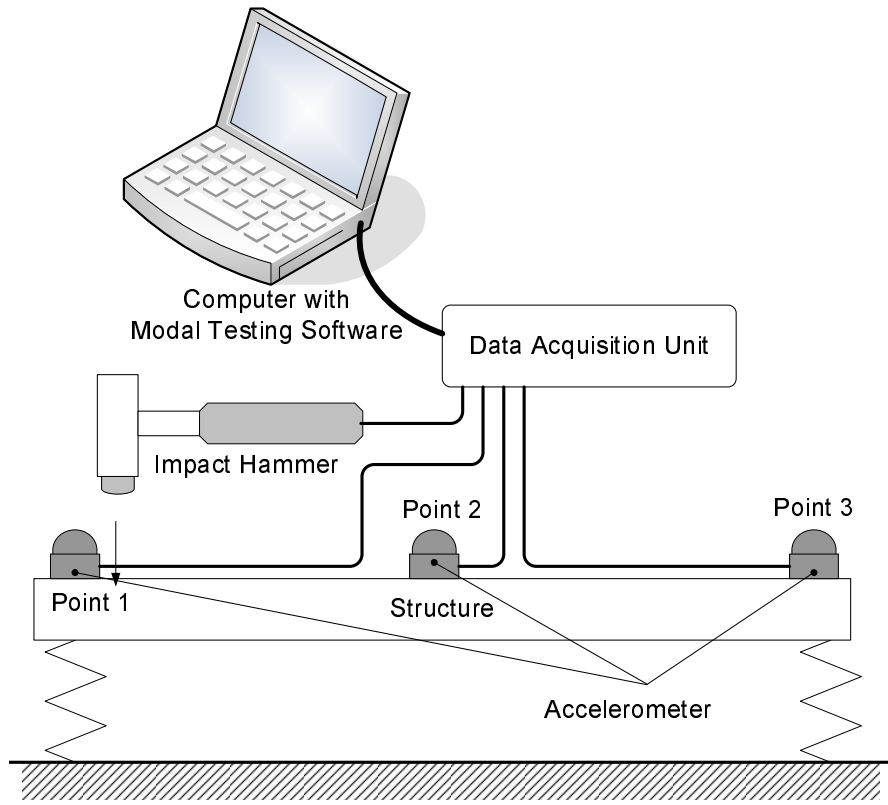


Figure 4.7: A typical modal impact testing setup

point 1 in a single (vertical) direction. In most cases, the test rig is usually hit in more than one direction in order to excite all the possible modal responses, ideally in all the three degree-of-freedom (DOFs). The position of impact is set as the *reference point*. In this research, the interest is not too much in the structural deformation modes, but rather in the rigid body modes under the influence of interfaces stiffness. For example, the test setup in Figure 4.7 may display these three rigid body modes as shown in Figure 4.8 that are of more interest in this investigation. The springs in the above example may represent the stiffness of a guideway interface.

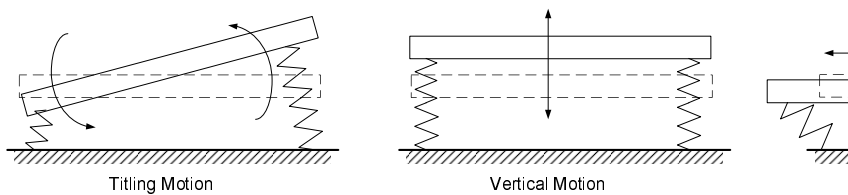


Figure 4.8: Three possible rigid body modes due to the spring stiffness

4.2 Modal Testing

Impact force and response acceleration information were captured by a data acquisition unit at a specified sampling time, i.e. in time domain. The measured time data were sent to a computer with modal testing software. The software evaluated various signal processing algorithms on the measured data, such as averaging, antialiasing filtering as well as windowing. The software then transforms the processed force and response data from time domain to frequency domain by applying Fast Fourier Transformation (FFT), producing the force signal, $F(\omega)$, and response signal, $X(\omega)$, respectively, as illustrated by Figure 4.9. The frequency response function, $F(\omega)$ having the following force and response relationship was computed.

$$H(\omega) = \frac{X(\omega)}{F(\omega)} \quad (4.43)$$

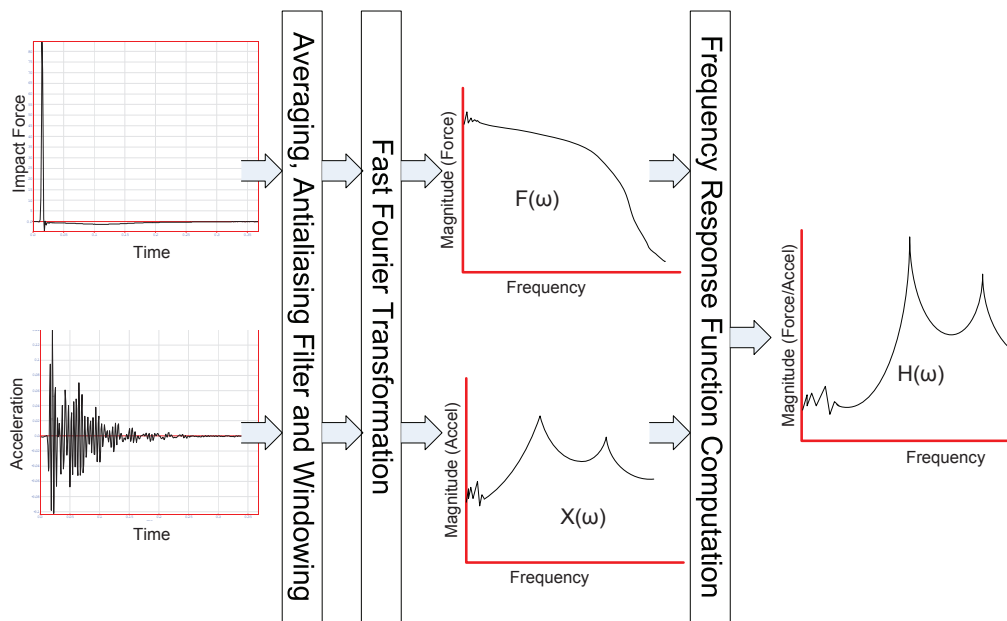


Figure 4.9: Force and acceleration time data to frequency response function.

4.2.3 Post-processing - Modal Parameters Extraction

The main aim of this modal experimental process was to understand the dynamic behaviour of the system. This can be done by analysing the modal parameters: the num-

Chapter 4. Theory and Application of Modal Analysis

ber, r , of natural frequencies $[\omega_r]$, their corresponding mode shapes $[\psi_r]$ and damping, ζ . Hence the post-processing of the measured FRFs is carried out compute these modal parameters. This post-process is known as *modal parameter extraction*. Modal parameter extraction is commonly done using *curve fitting* methods. There are a wide range of *curve fitting* methods to tackle different types of FRF signals [40, 90, 103]. The detailed discussion of these algorithms is beyond the scope of this work. Furthermore, in recent years, commercial modal analysis software packages have produced semi-automated module to compute and extract these parameters. However, it is still useful to explain briefly in this subsection how the modal parameters can be interpreted from the FRFs.

The simplest and fastest way to have a rough idea of the modal behaviour of a test rig using its measured and computed FRFs is by SDOF Peak-picking method (Figure 4.10). This method picks the r th numbers of peaks in the FRF plot and considered them as the harmonics or modes of the system. The frequency at which the maximum responses happen are identified as its natural frequency, ω_r , i.e. at $|\alpha_r(\omega)|_{max}$.

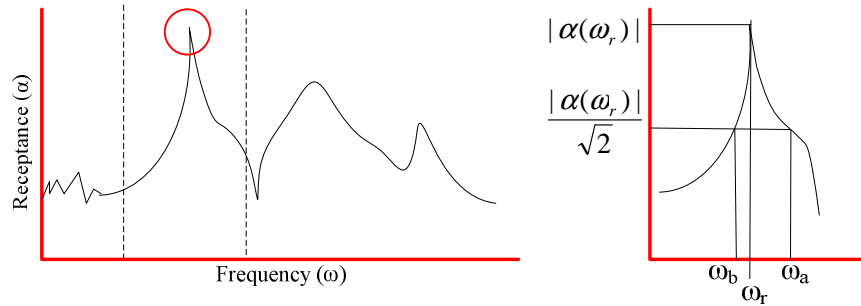


Figure 4.10: Peak picking method

The frequency bandwidth in the vicinity of the local maximum response, $|\alpha_r|$, can be defined by the bound of the half-power points, ω_b and ω_a , at response level $|\alpha_r|/\sqrt{2}$. The damping ratio and damping loss factor can then be estimated using this frequency bandwidth by:

$$\eta_r = \frac{\omega_a^2 - \omega_b^2}{2\omega_r^2} \quad (4.44)$$

$$\zeta_r = \frac{\eta_r}{2} \quad (4.45)$$

4.2 Modal Testing

From Chapter 4, we know that the FRF of a damped N DOFs system is a complex function, and the response model can be expressed as:

$$\alpha_{jk}(\omega) = \sum_{r=1}^N \frac{{}_r A_{jk}}{\lambda_r^2 - \omega^2} \quad (4.46)$$

where the eigenvalues, λ_r^2 , of the damped system takes the complex form:

$$\lambda_r^2 = \bar{\omega}_r^2(1 + i\eta_r) \quad (4.47)$$

${}_r A_{jk}$ is the *Modal Constant*, whereby ${}_r A_{jk} = \phi_{jr}\phi_{kr}$. Thus, we can relate ${}_r A_{jk}$ to the r mode shape by some scaling factor. It is difficult to visualise the mode shapes from the Modal Constant matrix. However, the imaginary plot of the FRF gives a better visualisation of the mode shape. This is its imaginary part of the FRF versus the frequency. For a damped MDOF system, the imaginary part is computed analytically using Equation (4.46):

$$Im(\alpha_{jk}(\omega)) = Imag \left(\sum_{r=1}^N \frac{{}_r A_{jk}}{\lambda_r^2 - \omega^2} \right) \quad (4.48)$$

We can use the setup shown in Figure 4.7 as an illustration example. Assuming the three accelerometers are uni-axial. Therefore, they are only capable of sensing the tilting and vertical oscillation mode, as shown in Figure 4.8 (ignoring the structural mode shapes, if any). If the impact position is point 1 and in the vertical direction, three imaginary plots of the modal test may be obtained as shown in Figure 4.11. Each of the imaginary plots represents the responses measured by the individual accelerometers when subjected to an impact excitation force at point 1.

The method shown in Figure 4.11 provides an evaluation of the mode shapes of a system. Note that there is only one peak in the imaginary plot of response 2, which corresponds to the vertical oscillation mode. This is due to the fact that point 2 is located at the node of the tilting mode, hence no or minimum response was measured in this mode. The evaluation of the FRF Imaginary Plots allows one to have a quick visualisation of the key mode shapes of the system. However, in complex machines

Chapter 4. Theory and Application of Modal Analysis

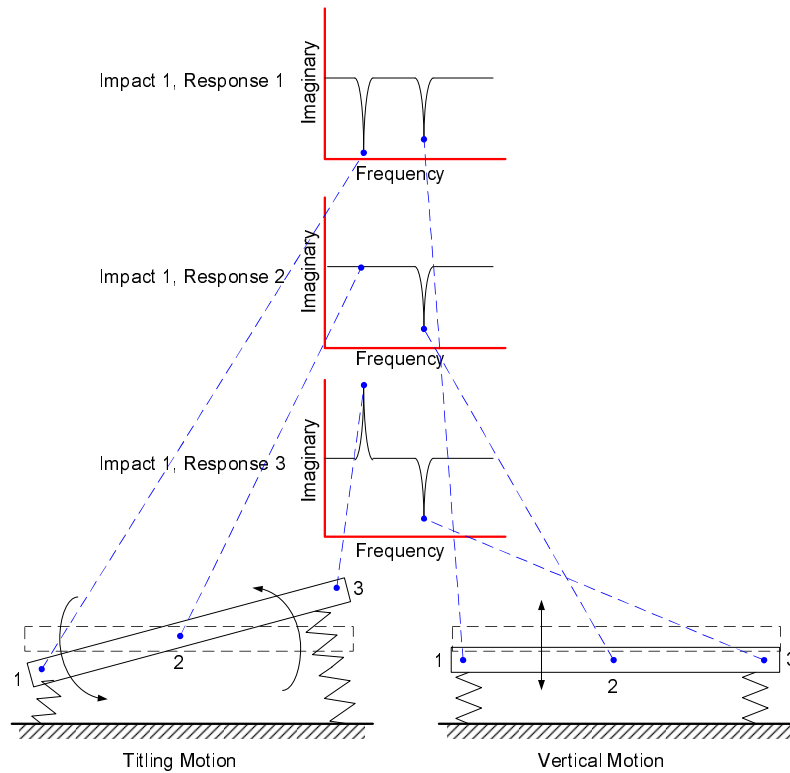


Figure 4.11: Imaginary plots obtained from the three accelerometers and one impact (reference) point

with high damping and noisy FRF data, this simple visualisation method may be insufficient. As mentioned many commercial software are able to accurately compute the mode shapes based on the selected natural frequencies. The software also provides tools to facilitate easier selection of the natural frequencies.

Chapter 5

Experimental Methodology, Procedure and Equipment

5.1 Introduction

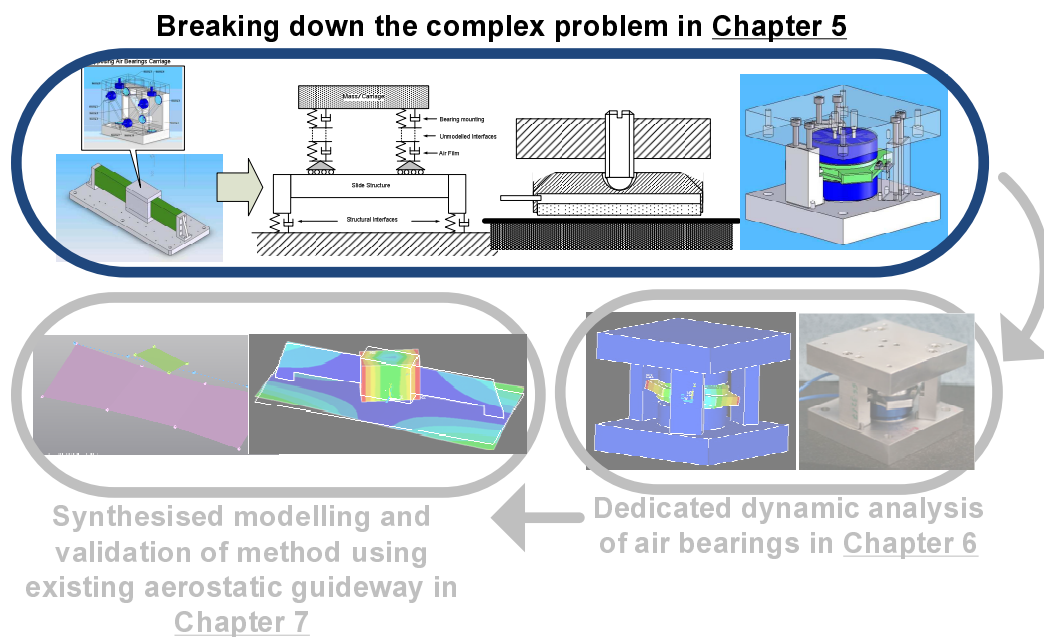


Figure 5.1: Flow of chapter 5 to 7.

This research aims to develop a valid air bearing interface model that can be used to improve the accuracy of machine FEA models, so as to achieve a dynamically optimal design. In order to realise this objective, the dynamic behaviour of air bearing based

Chapter 5. Experimental Methodology, Procedure and Equipment

motion systems needs to be investigated in a systematic and rigorous manner. This chapter discusses how a complex aerostatic guideway system is broken down into various aspects of interfaces, which influence the dynamic behaviour of the system. A systematic experimental methodology to analyse the dynamic behaviour of an aerostatic guideway system is deliberated. The dynamic characteristics of the aerostatic guideway system are contributed by several interfaces. Various analysis and experiments are set up to investigate the individual interfaces in a controlled environment. This process leads to the design of a dedicated air bearing test rig which was targeted to carry out the isolated and controlled investigation. The design consideration and outcome of this test rig is discussed and presented in this chapter. The process of identifying/designing the experiments and analyses for the various interface elements forms the initial stage of this research as illustrated in Figure 5.1. This chapter also aim to set the scene for the subsequent two chapters, and at the same time gives a good representation of the flow of work carried out in this research, which has been illustrated in Figure 1.1.

Chapter 4 presents the theory of the analytical process for dynamic modelling a general system. It discussed how modal and response models (i.e. the dynamic characteristics and performance) of a system can be computed using the system's spatial model which comprises of the mass, stiffness and damping variables. Therefore, the key dynamic parameters that need to be developed is a set of stiffness and damping which can be used to accurately describe the behaviour of the air bearing interfaces. The stiffness and/or damping models will be developed as elements (in FEA) which represent the interfaces within the machine. The modal parameters of the machine will be computed in FEA, incorporating the various spatial models of the interface elements.

In order to validate the above analytical spatial model developed, experimental data of the real system need to be used. Experimental modal tests were carried out to obtain the actual dynamic behaviour of the interfaces. The modal testing process is presented in this chapter. The validation process compares the modal parameters, i.e. the natural frequencies and mode shapes obtained from the analytical and experimental processes. Perfect agreement between the experimental and analytical results is evidently

5.2 Experimental Methodologies

impossible. The discrepancies between the two results are analysed to explore potential improvements to be made to the analytical model and/or the experimental setup. Therefore, this forms an iterative and decomposition experimental process to achieve a robust and reliable dynamic model for the machine interfaces. Figure 5.2 illustrates a single validation scheme of the process described above, in the form of a flow chart.

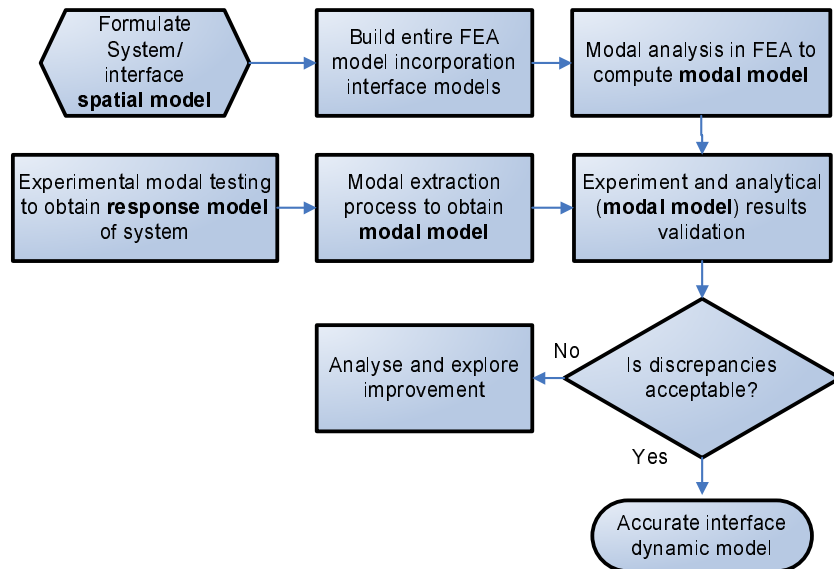


Figure 5.2: Modal Analysis Validation Process

Note that the iterative and breaking down of the experimental process are not depicted in this flow chart. The following sections shall detail the progress of decomposing a ‘more’ complicated experimental setup to isolated experiments to understand the various interfaces behaviour of an aerostatic bearing setup. In Chapter 7, the findings pertaining to the various identified interfaces are consolidated and utilised to formulate the dynamic FE model for the entire aerostatic guideway. The detailed analysis and model validation of the guideway system are also discussed.

5.2 Experimental Methodologies

This research aims to develop a valid dynamic model for non-contact type machine interfaces to realise an accurate FEA machine model. It is common and logical to start by studying a simpler experimental set up and progressively expanding the investigation towards a more complicated system. However, for a non-mechanical contact

Chapter 5. Experimental Methodology, Procedure and Equipment

guideway, e.g. an aerostatic guideway, it is difficult to pinpoint and justify an initial investigation of a specific feature or aspect within the system. Hence, it was decided upon to choose to commence experimental work with a relatively simple (which later appear to be otherwise) single axis non-mechanical contact guide system. The purpose of this attempt is to appreciate the machine interface overall behaviour and its influence on the motion system; and to categorise the various characteristics of the experimental results. By doing so, the dynamic problem of the single axis motion system is broken down into smaller isolated issues and analysed separately in a methodically manner. The discussion in the following subsections will detail the procedures and its rationale of this experimental approach.

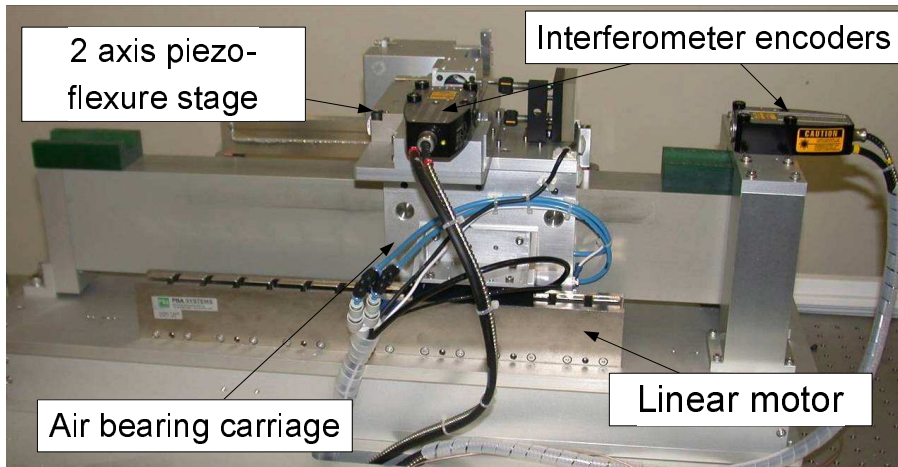
5.2.1 The Experimental Platform

As mentioned above, the aim is to gain an initial overall appreciation of the dynamic behaviour of a non-contact type interface based motion system. Though starting from a system perspective, it is still useful to begin with a relatively simple motion system. The following are selection criteria for an experimental platform based on practical and analytical reasons:

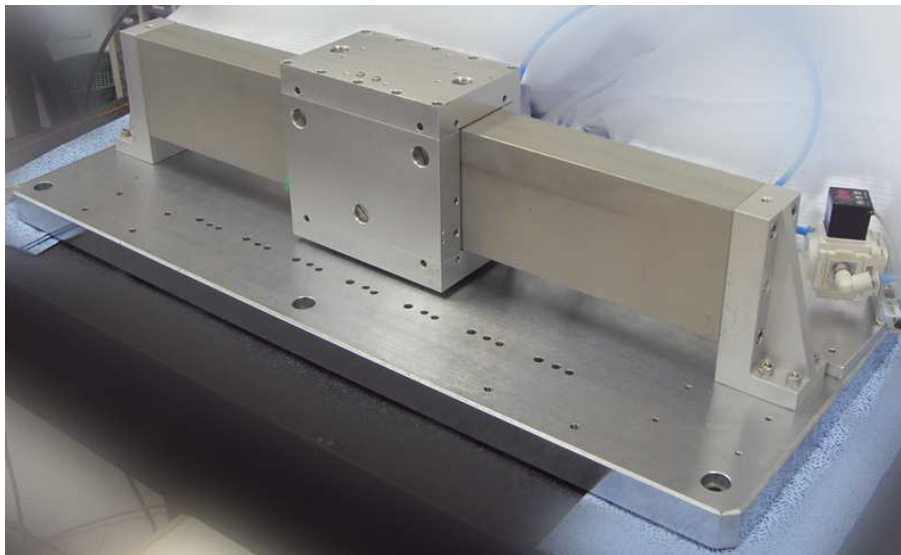
- The test rig shall be a single axis motion system
- The motion system shall be guided by aerostatic bearings, which use a common or manufacturer recommended setup.
- The motion system configuration shall be kept minimal, i.e. components/parts not relevant to the investigation will be removed.
- The motion system shall be of manageable size, due to practical reasons for the experimental process. Equipments and sensors used in this research will be introduced in the later part of this chapter, and the practical rationale will become apparent.

A single axis air bearing based motion system was selected as the experimental platform to understand machine interfaces dynamics. Figure 5.3 shows the experimental platform, which used air bearings in its axis guiding system.

5.2 Experimental Methodologies



(a) Original three axis system



(b) Single axis aerostatic guideway system

Figure 5.3: Aerostatic guideway system as the experimental platform

The motion system shown in Figure 5.3(a) was originally a three axis system, with one macro DOF motion, guided by the air bearings, and two micro DOFs from a piezo-actuated flexure stage. For simplicity, the motion system was reduced to the minimum, which only comprises of the relevant components. The major components of the scaled-down system are the guideway structure, the air bearing carriage and the structural base. Figure 5.3(b) shows the scaled-down single axis aerostatic guideway.

Chapter 5. Experimental Methodology, Procedure and Equipment

5.2.2 Assessment of System Interfaces

The air bearing carriage is made up of ten 25 mm diameter air bearing pads from New Way[®] Air Bearings, as shown in Figure 5.4. The air bearing uses a porous carbon graphite material as their air flow restrictor [67, 104]. A schematic diagram of the construction of a porous air bearing was shown in Chapter 2, Figure 2.11. The porous media restrictor offers a nearly even air pressure distribution within the air gaps, as discussed in Section 2.4. Technical specifications and drawings of the 25 mm porous air bearing can be found in Appendix A.



Figure 5.4: 25 mm diameter New Way Air Bearing

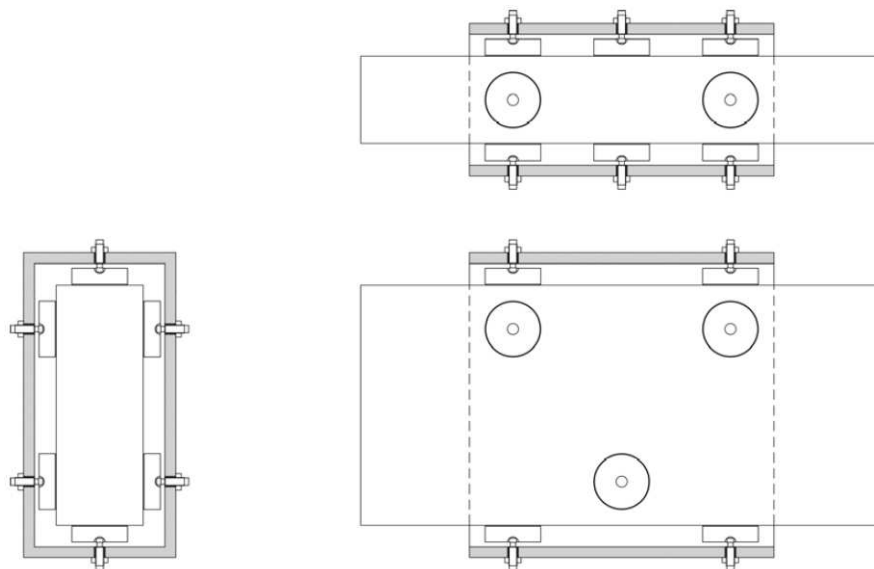


Figure 5.5: Air bearing layout used in this test rig (from [104])

The air bearing layout configuration is based on one of the manufacturer's recommendation (page 34 of [104]). It was made up of two sets of opposing bearings directly

5.2 Experimental Methodologies

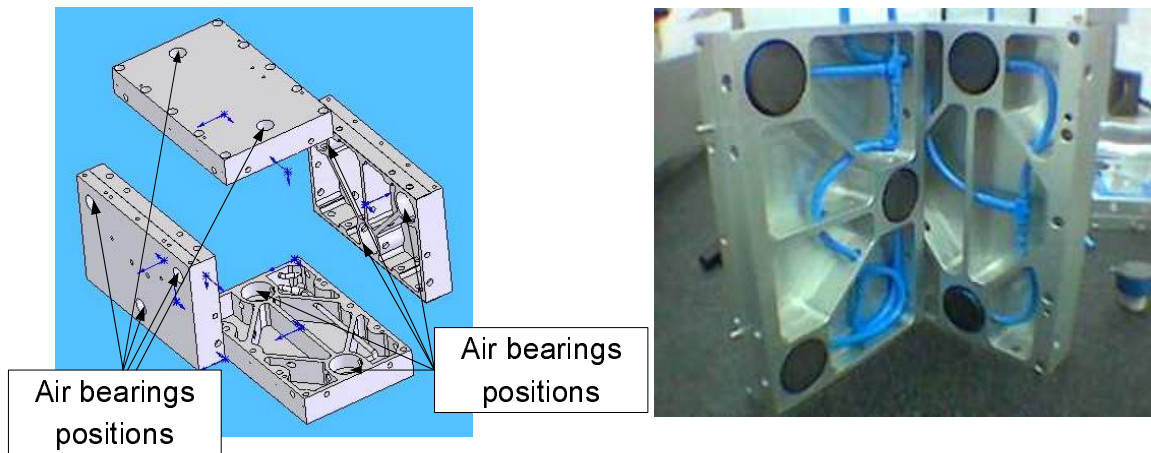


Figure 5.6: Air bearings layout and enclosure assembly

across each other in the horizontal and vertical plane. Three air bearings established a plane and two established a line, hence comprising of ten air bearings in this layout. Figure 5.5 illustrates the above described bearings configuration. The air bearings enclosure is consists of four aluminium blocks, with pockets to hold the air bearings and ribs to route the air tube. The left of Figure 5.6 shows the 3D CAD model in exploded view of the enclosure and on the right shows two perpendicular blocks (half of the enclosure) exposing the air bearings and the tubing assembly. The 2D CAD drawing of the air bearing enclosure can be found in Appendix A. Note that the air bearings layout was over constrained and *non-kinematic* [29], but this type of layout offers a higher stiffness in terms of the guideway configuration.

Similar to the concept of a structural loop [29] in machine design, stiffness chains [105, 106] are often used to evaluate machine interface compliance. The major structural components are separated and connected by a set of interfaces (with a certain stiffness and damping properties) that are perceived to possess identifiable extent of compliance. Using the single axis air bearing guideway as an example, Figure 5.7 illustrates how the chain can be constructed.

The left side of the diagram shows the CAD model of the simplified guideway and the air bearing carriage. Ten 25mm diameter round air bearing pads were used, and were

Chapter 5. Experimental Methodology, Procedure and Equipment

arranged in a configuration to create opposing preload as shown in (top left of) Figure 5.7. The right side of the diagram shows a schematic illustration of the stiffness chain of the system. Each interface is represented by a spring and damper system, which is the *spatial model* of the system. To estimate these spatial parameters of the air bearing guideway, dynamic modelling and testing were carried out on the guideway system. The details of the dynamic analysis and experiments of this air bearing guideway are discussed in Chapter 7. An initial assessment identifies several issues and queries concerning the FE modelling of the aerostatic guideway. These issues/queries provide the basis for further in-depth investigation into the various static and dynamic aspects of the air bearing interfaces. Experiments were designed to address each of the key issues/queries. This permits a more in-depth research into the various aspects of the guideway which contribute to the dynamic behaviour of the system. Consequently, these isolated analyses could be synthesised to derive a more comprehensive analytical model for the entire air bearing system. The subsequent sections discuss the key issues and the experimental methodologies to acquire more insight of the various interfaces.

5.2.2.1 *Coupling of Structural and Air Bearing Interface Dynamics*

Structural joints are considered as one of the common weak interfaces in machines. For simplicity, the joints in machine structures are usually modelled as rigid bonding in the FEA. Their contributions to the model prediction errors are often not very significant. This will be evidenced in the later chapters. However, it is still essential to characterise the deficiency of the analytical model through experimental validation of such structural interfaces. This was carried out by performing modal tests separately on just the structures (without the air bearings influence) and the entire air bearing guideway. The model test results are analysed and the dynamic behaviour of the structure and the air bearings are differentiated. The experimental setup and equipment used for modal testing is presented in Section 5.3.1. The same modal testing equipment is used throughout this research to obtain the frequency response measurement of various test setups.

5.2 Experimental Methodologies

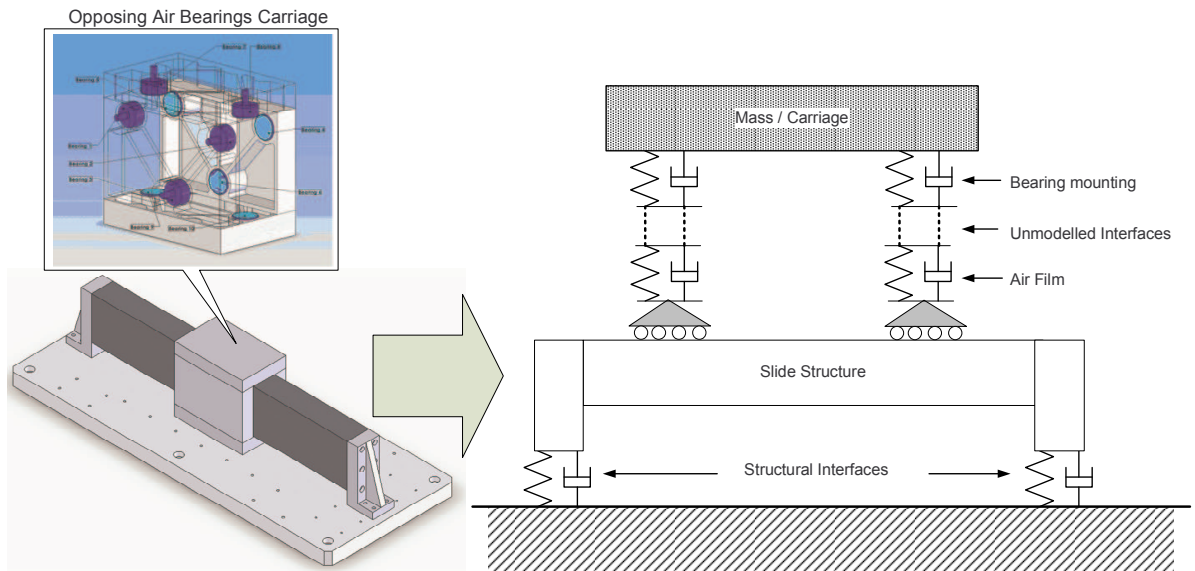


Figure 5.7: Stiffness chain of the air bearing guideway

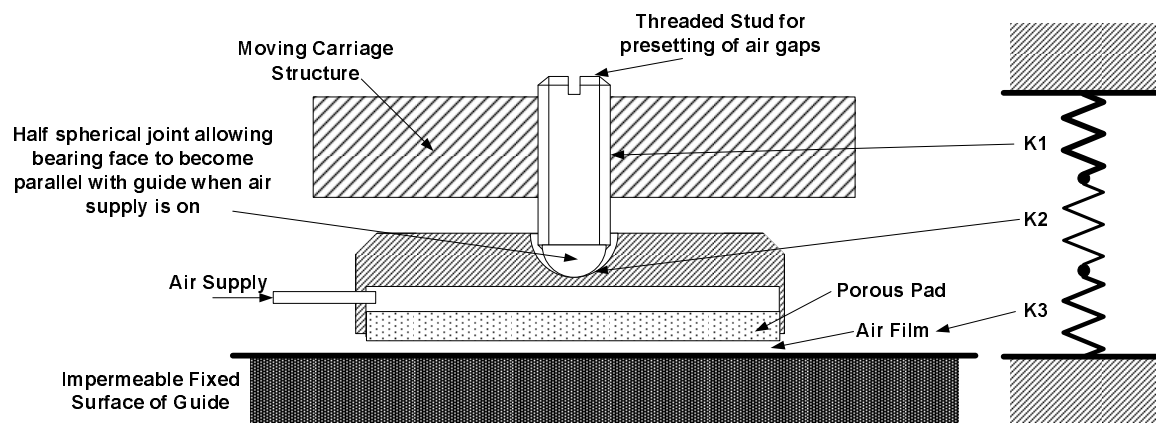


Figure 5.8: Porous Air Bearing Mounting Mechanism

Chapter 5. Experimental Methodology, Procedure and Equipment

5.2.2.2 *Effect of Air Bearing Mounting*

The air bearing pads were mounted to the carriage by threaded studs, and a ball joint to ensure the parallelism between the sliding surfaces and the air bearing pad surfaces, as illustrated in Figure 5.8. In many air bearing guideway modelling [79, 107–110], this interface was often neglected, or assumed to be as stiff as the structural joints. However, this research found that this assumption may not be acceptable. Realistically, the air bearing is made up of several interfaces, which contribute to the overall stiffness of a single bearing system. This can be considered as a number of linear or non-linear springs connected in series, as illustrated in Figure 5.8, .i.e. the overall stiffness will be substantially smaller (depending on the other interfaces stiffness) than that of only the air film. Two experiments were carried out to find out the static stiffness of ball-socket mounting of the air bearings: 1) Purely ball and socket, and 2) ball in threaded stub. The detail of the experimental setup is presented later in this Chapter and results will be elaborated in Chapter 6.

5.2.2.3 *Uncertainty of Air Gap Height*

The carriage (which was also the air bearings enclosure) hovered on air films that were between the slide structure surface and the air bearing pad surfaces, creating a “near frictionless” guide in the motion axis. Due to the construction of the carriage and mounting mechanism as discussed in the previous paragraph, the confidence on the actual air gaps within the carriage was not high. Although displacement can be measured using the top of the threaded stub (which is exposed on the surface of the carriage), it is considered to be an indirect measurement. The procedure for air gap setting and measurement via the threaded stub is presented in Appendix B. An air gap height measurement/identification method is essential to provide a more deterministic value, so as to increase the confidence of the air film model parameters and a more rigorous validation process.

5.3 Experimental Setup and Equipment

5.2.2.4 Inadequacy of Air Film Model

Air film dynamics are the least understood characteristics in this guideway test setup. Numerous research works had been carried out in characterising the static behaviour of air bearings, but there is little on the dynamic behaviour. Some of these works have been discussed in the literature review of Chapter 2. To analyse an air bearing accurately in FEA, a valid stiffness and/or damping model of the air film need to be established. Therefore, experiments were performed to measure the stiffness of the air film. In order to study the air film dynamic behaviour in a controlled environment, it is essential to design a test rig that allows dedicated investigation of the air film dynamics.

5.2.2.5 Other Unmodelled Interfaces

There are always some interfaces characteristics, which are not modelled and/or not considered. One example of such unmodelled interface is the joining between the air bearing porous material and its aluminium case. Some of the interfaces are highly non-linear, and are very difficult to include in a FEA model. Many commercial FEA tools do not consider non-linearity of elements in their modal analysis, i.e. non-linear elements are linearised to a specific set point in the computation of the modal parameters. It is therefore important to be aware of such unmodelled interfaces in a system, and appreciate their contribution to the discrepancies of the experimental validation. Chapters 6 and 7 will discuss these issues.

The next section presents the setup and equipment for the experiments designed to investigate all the above key issues.

5.3 Experimental Setup and Equipment

5.3.1 Modal Testing Equipment

Modal testing methods are well established technique in the field of structural vibration analysis. In the industry, they are classified under a common area called Noise, Vibration and Harshness (NVH). NVH testing equipment is commercially available. It

Chapter 5. Experimental Methodology, Procedure and Equipment

varies mainly in terms of signal processing and data post processing capabilities. The three major NVH testing equipment suppliers¹ are Brüel & Kjær (B&K), LMS and National Instruments (NI) [111]. In this work, Brüel & Kjær and LMS modal testing equipment was used. These gave consistent frequency response results. B&K do not come with a post processor or modal analysis software. The measured data were exported to a third-party modal analysis software called ME'scopeVES by Vibrant Technology Inc². The modal analysis of ME'scopeVES uses the imported FRF data to extract the modal parameters of the measured system, i.e. modal shapes, natural frequencies and damping ratios, as discussed in Section 4.2.3. On the other hand, LMS test equipment is bundled with modal analysis software. This allows direct analysis of the FRF measurements in a seamless manner. LMS uses a patented frequency domain method to extract modal parameters from FRF data, named PolyMax. PolyMax or polyreference least-square complex frequency-domain (LSCF) modal parameter estimation method offers a more robust and accurate estimation as compared to classical methods employed in other modal analysis software packages [112]. Its modal parameters estimation method is able to clearly identify the stable poles of a highly-damped and/or noisy system. Due to the better post processing features of LMS and for consistency, it was used in most of the experimental modal tests.

As discussed in Section 5.2.2.1, the dynamic characteristics of the structure and the air bearing interfaces were evaluated separately to isolate their behaviour and prevent coupling effect between them. Hence, Figure 5.9 shows the experimental modal testing setup of just the guideway structure without the air bearing carriage. Table 5.1 summarises the equipment used for a typical modal test.

The LMS data acquisition system was connected to a computer laptop through Ethernet. The laptop was loaded with LMS Test.Lab[114], the bundled modal testing and analysis software which was mentioned above. Tri-axial accelerometers were used in most of the experiments, as they were able to acquire three DOF acceleration infor-

¹B&K - <http://www.bksv.com>, LMS - <http://www.lmsintl.com/> and NI - <http://www.ni.com/nvh>

²<http://www.vibetech.com>

5.3 Experimental Setup and Equipment

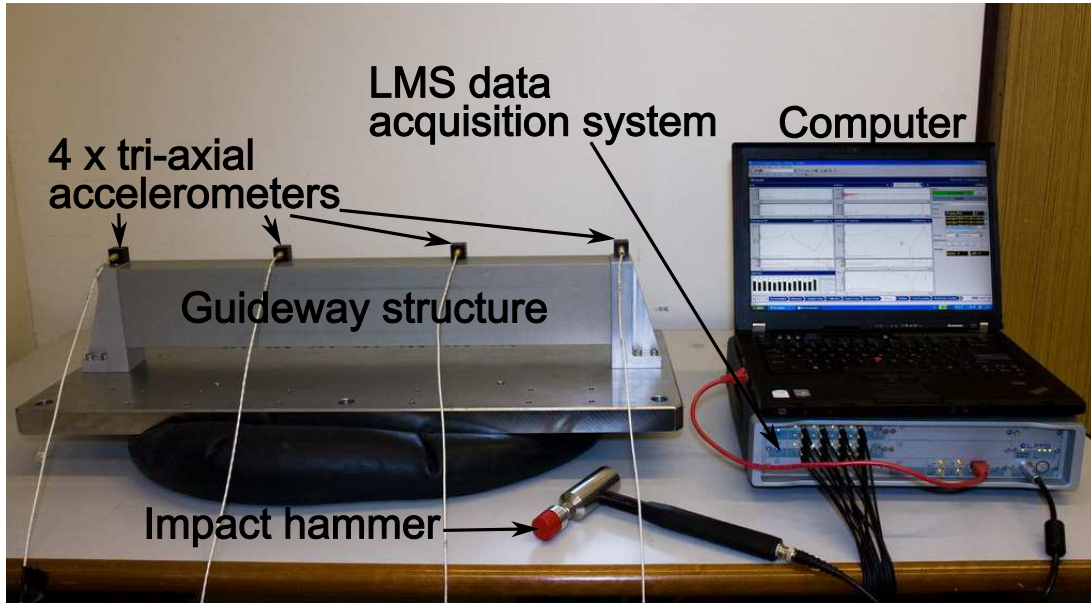


Figure 5.9: Modal Testing Setup of Guideway Structure

Device	Model	Datasheet
Data Acquisition System	LMS 16 channels SCADA Mobile SCM05	[113]
Modal Analysis Software	LMS Test.Lab	[114]
Accelerometers	Kistler PiezoBeam® Triaxial Accelerometer, 50g	[115]
Impact Hammer	Kistler Impulse Force Hammer	[116]
Computer	Lenovo Thinkpad T61 Laptop	

Table 5.1: Equipment used for Modal Testing

mation simultaneously. The impact hammer shown in Figure 5.9 is used to introduce the impulse force excitation to the system. Due to the limitation of 4 accelerometers available, several sets of force-response measurement were required to cover all the measurement points. In the case of the above guideway structure test, 16 measurement points were determined (refer to Figure 4.6), hence 4 sets of force-response measurement were required.

5.3.2 Stiffness Testing Equipments

Experiments to obtain the static stiffnesses of the air bearing mounting were proposed. The experiments were carried out using an Instron (4505) Mechanical Testing Ma-

Chapter 5. Experimental Methodology, Procedure and Equipment

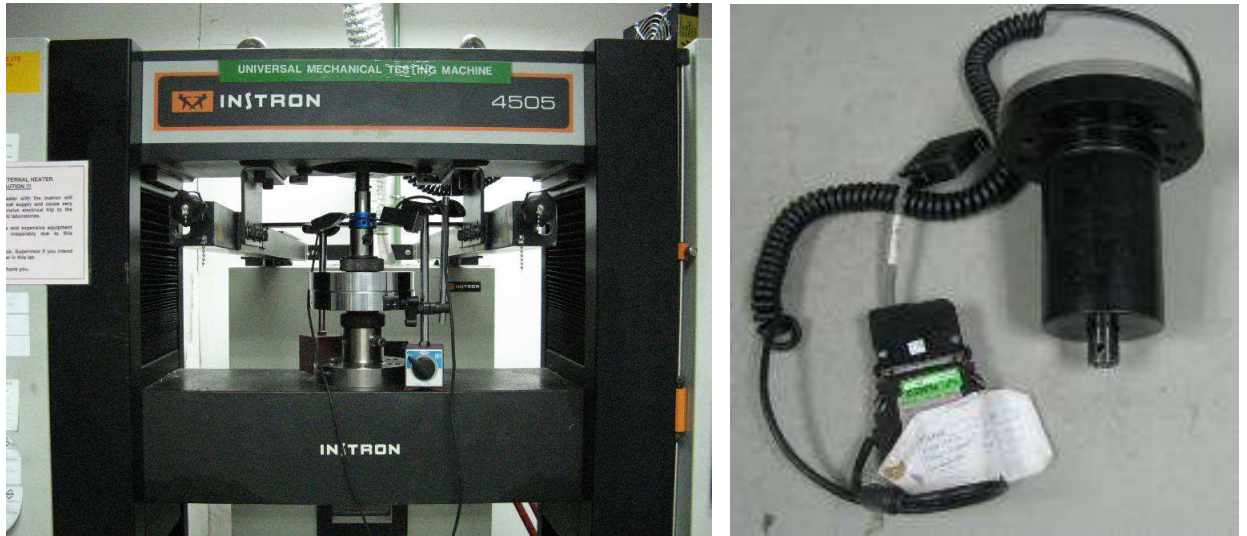


Figure 5.10: Instron 4505 with 1 kN load cell

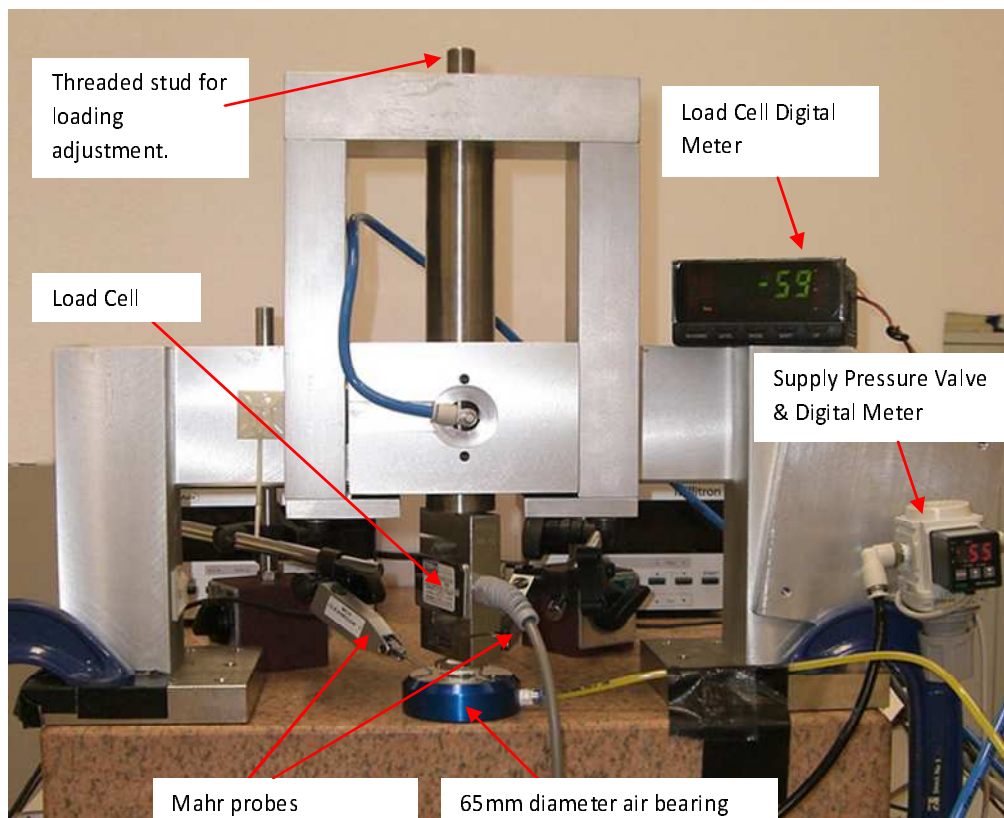


Figure 5.11: Test setup for air film stiffness

5.4 Dedicated Air Bearing Test Rig

chine, with a 1 kN load cell (as shown in Figure 5.10) and two sets of Mahr Linear variable differential transformer (LVDT) probes (1318 Mahr-LVDT [117]) for displacement measurement.

Despite the fact that a load-lift curve of the air bearing was provided in the manufacturer's datasheet, a verification of the actual static stiffness of the air bearing was desirable to increase the confidence of the entire investigation. A similar experiment was set up to obtain the load versus air gap displacement relationship. Figure 5.11 shows the setup of this experiment. Besides evaluating the static stiffness of the air film, more experiments were required to acquire insight to the dynamic behaviour of the air film.

5.4 Dedicated Air Bearing Test Rig

5.4.1 Design Consideration of the Air Bearing Test Rig

Dynamic (modal testing) and static experiments using the various test setups provided understanding to the various aspects of interfaces within the aerostatic guideway system. Despite the fact that dynamic analysis was performed on the guideway, many issues and limitations exist. These issues create uncertainties that hindered the research work. A much customised test rig was required to acquire further understanding of an isolated dynamic system, in particular the air film. An accurate air film model was needed to be developed in order to construct a realistic dynamic model for the entire guideway system.

Before the design of this test rig, it would be valuable to list a few criteria of the test rig:

- The test rig has to be able to maintain an accurate and parallel air gap of an air bearing to 1 μm accuracy.
- The air bearing has to be rigidly mounted, i.e. eliminating 'weak' interfaces such as those discussed in Section 5.2.2.1.

Chapter 5. Experimental Methodology, Procedure and Equipment

- The air gap must be measurable and deterministic.
- The test rig structure has to be relatively rigid as compared to the air film.
- For simplicity seek, the degree-of-freedom (DOFs) for the key measured components has to be kept minimum, preferably not more than three DOFs.

5.4.2 Design of the Opposing Air Bearing Test Rig

A dedicated air bearing test rig was designed. Figure 5.12 shows the CAD assembly of the test rig and the major components of the assembly are annotated. An opposing air bearing system was adopted as the main concept of the test rig. This would provide a closer yet isolated representation of the current guideway system. Furthermore, opposing air bearings systems are commonly found in many commercial linear guides and an in-depth understanding of such system will benefit future design of air bearing linear guides.

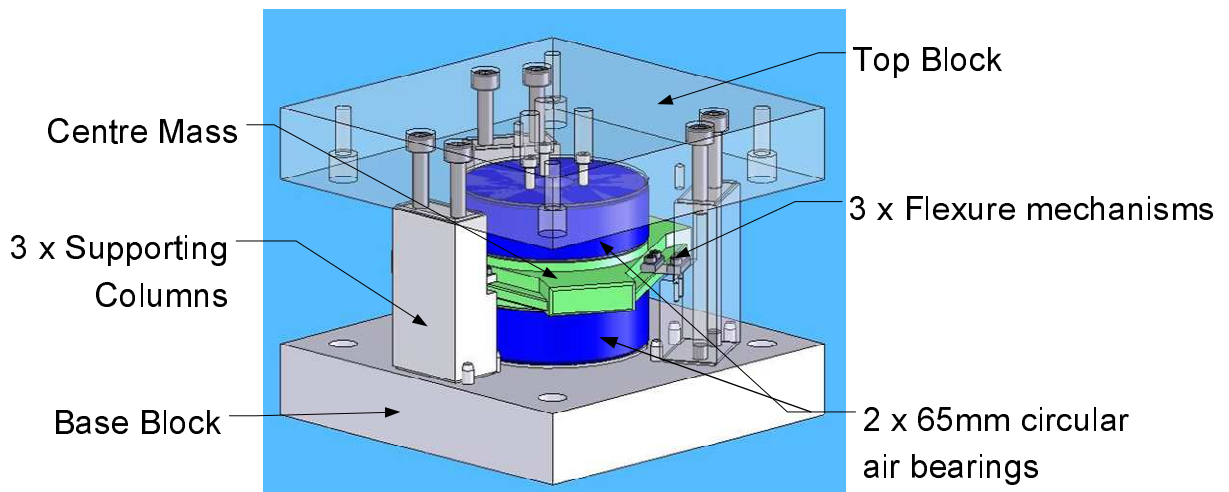


Figure 5.12: Dedicated air bearing test rig

The (green) centre mass shown in Figure 5.12, constrained between the two opposing air bearings is the main component to be investigated. The dynamic behaviour of this centre mass, which is predominantly influenced by the air film dynamics, is measured

5.4 Dedicated Air Bearing Test Rig

in this experimental setup. Ideally, the centre mass should display the first few harmonics of the system. Numerous design and functional aspects of the test rig were incorporated to comply with the criterion, as set in Section 5.4.1. The following are summarised key features in the test rig:

1. Two deterministic air gaps, top and bottom of the mass will be established by the geometry of the structure, as illustrated in Figure 5.13.

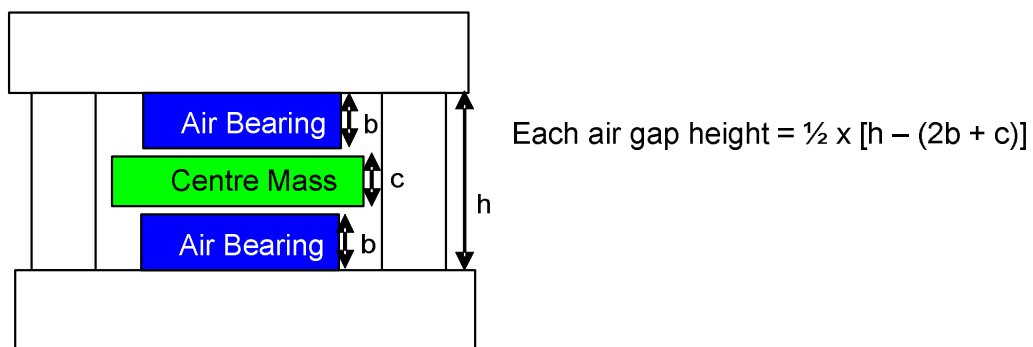


Figure 5.13: Determination of air gap heights

2. The centre mass has three ledges to accommodate the mounting of the accelerometers, as shown in Figure 5.14.

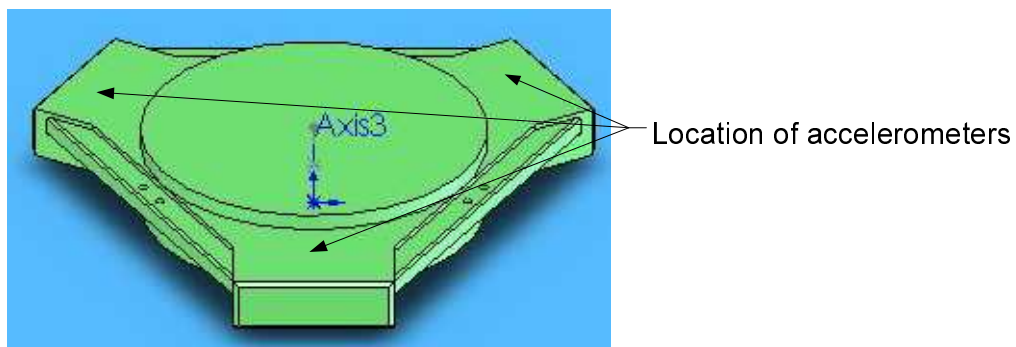


Figure 5.14: Centre Mass

3. Three leaf-spring flexure mechanisms connect the side of the mass to the three supporting columns, as shown in Figure 5.15. The aim is to deter lateral motion of the mass, thus constraining it to only vertical motion and tilting. More detail on the design of the flexure will be given.

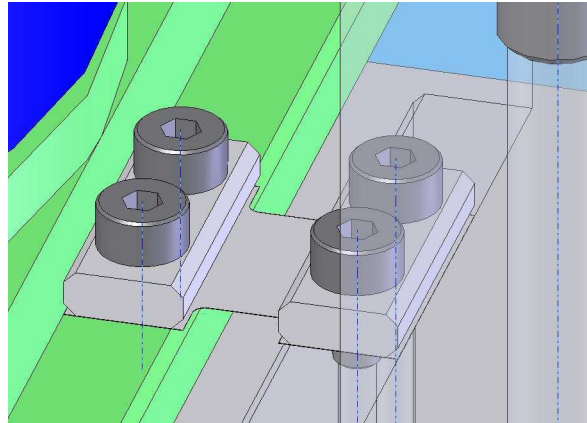


Figure 5.15: Leaf-spring flexure mechanism

4. The critical surfaces such as the interfaces between the supporting column and the two blocks, as well as the air bearings back and the two blocks were diamond turned to ensure precise parallelism and flatness.

5.4.3 Flexure Mechanism

The flexure mechanism was chosen to constrain the lateral motion of the mass, as its static and dynamic characteristics are almost linear and deterministic within the material elastic zone [118, 119]. The flexure is a leaf spring type using a 0.02mm thick shim clamped at both ends, with one end to the mass and the other to the support column. Figure 5.16 shows the schematic drawing of the deflection behaviour of each leaf spring under the loading F , of the mass, when the air supply is off. When the air supply is turned on, there should be minimum deflection, i.e. the mass is 'held in space' by the opposing air bearings.

The stiffness, maximum deflection of the flexure and the first mode natural frequency of the mass can be easily calculated using classical static and dynamic mechanics theory. Since the analysis is focused on the air film dynamics, the dynamic effect of the flexure on the centre mass should be as minimum as possible. The flexure should not exert too much constraint on the vertical motion of the mass, i.e. the stiffness and the natural frequency caused by the flexure mechanism ought to be as low as possible. A 0.02mm thick x 12.7mm wide shim was used. The distance L between the clamping

5.4 Dedicated Air Bearing Test Rig

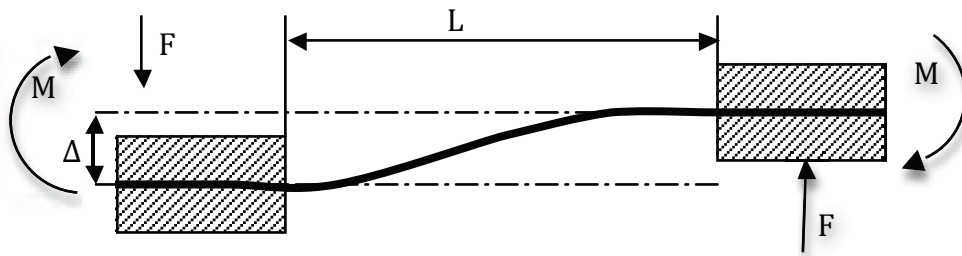


Figure 5.16: Schematic of a leaf spring flexure mechanism

blocks need to be determined to ensure a low stiffness of the flexure mechanism which meets the above requirement.

Based on initial dynamic assessment of the aerostatic guideway and previous works [79, 108, 120], an aerostatic carriage of approximately 3 kg under normal air bearing operating conditions should exhibit a first mode frequency above 100 Hz. In the case of this dedicated test rig, the estimated stiffness (of air films) to mass (of centre mass) ratio is relatively high, thus the natural frequencies are expected to be much higher than the aerostatic guideway (approximately in the magnitude of a thousand Hz). To ensure that the flexure mechanisms contribute minimum dynamic effects on the centre mass, the estimated natural frequencies for the mass held only by the flexure mechanisms should be less than 20 Hz. This is a rather crude but safe target. Based on the 20 Hz natural frequency target, a suitable length, L of the flexure is approximated to be 4 mm. Using the 4 mm flexure length, a brief calculation was carried out to estimate the natural frequencies of the centre mass held by only the flexure mechanism (without the air bearings).

Since the three flexure mechanisms constrain the lateral motion of the centre mass, the expected mode shapes of the mass under the influence of the flexures are the tilt and vertical translation. Figure 5.17 shows a schematic mass spring system which illustrates the potential modal behaviour of the 0.18 kg centre mass under the constraint of three flexure with stiffness, K_{flex} .

Using the beam deflection equation, the deflection of a fixed-fixed end beam system

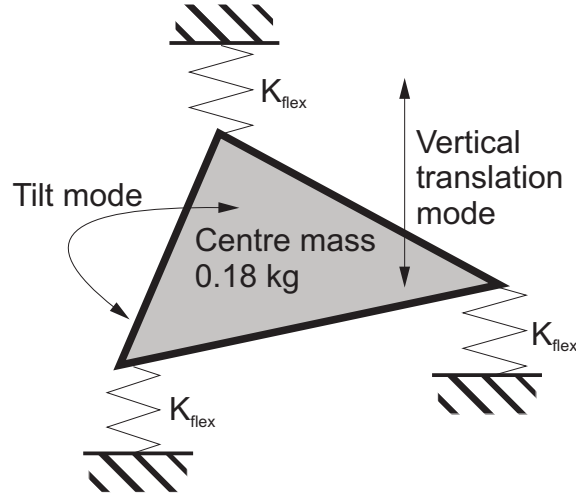


Figure 5.17: Schematic mass spring model of the centre mass held by three flexure mechanisms

like the flexure shown in Figure 5.16 can be obtained by the following equation [118].

$$\Delta = \frac{FL^3}{12EI} \quad (5.1)$$

and therefore the stiffness of each flexure K_{flex} can be expressed as

$$K = \frac{12EI}{L^3} \quad (5.2)$$

The shim is a grade304 stainless steel with Young's Modulus, E of 200GPa, and based on its cross section of 0.02 mm by 12.7 mm, the second moment of inertia, I is computed as $8.5 \times 10^{-6} \text{ mm}^4$. Using Equation (5.2), each flexure would have a stiffness value, K_{flex} of 319 N/m. The natural frequencies of the vertical translation, f_{trans} and tilt, f_{tilt} modes can be calculated by classical undamped vibration equation, as shown below, respectively.

$$f_{trans} = \sqrt{\frac{3K_{flex}}{M}}/2\pi \quad \text{and} \quad f_{tilt} = \sqrt{\frac{3K_{flex}l^2}{I_m}}/2\pi \quad (5.3)$$

where $l = 37 \text{ mm}$, is the distance between the centre of the mass to the centre of the flexure mechanism. $I_m = 1 \times 10^{-4} \text{ mm}$, is the mass moment of inertia for the centre mass and should not be confused with the above second moment of inertia, I . M is the mass weighing at 180 grams. Thus, the vertical translational and tilt modal frequencies

5.4 Dedicated Air Bearing Test Rig

(f_{trans} and f_{tilt}) are 12 and 18 Hz, which are both less than 20 Hz. This verified the appropriateness of the flexure dimension chosen, and its stiffness properties (for the requirement of the dedicated test rig).

5.4.4 Fabrication, Assembly and Other Practical Issues

The critical surface flatness of the joints for the test rig were diamond fly cut to less than $1\ \mu\text{m}$ accuracy to ensure the determinism of its geometry. These include the back of the air bearing pad. These components are shown in Figure 5.18. Note that all the fly cut surfaces are shinier than the rest of the surfaces. This geometrical accuracy is important, as the two air bearings will be rigidly bolted to the top and bottom plates (refer to Figure 5.18). Any discrepancy in the flatness and parallelism between the critical surfaces may introduce an uneven air gap between the air bearing porous surface and the centre mass surface.

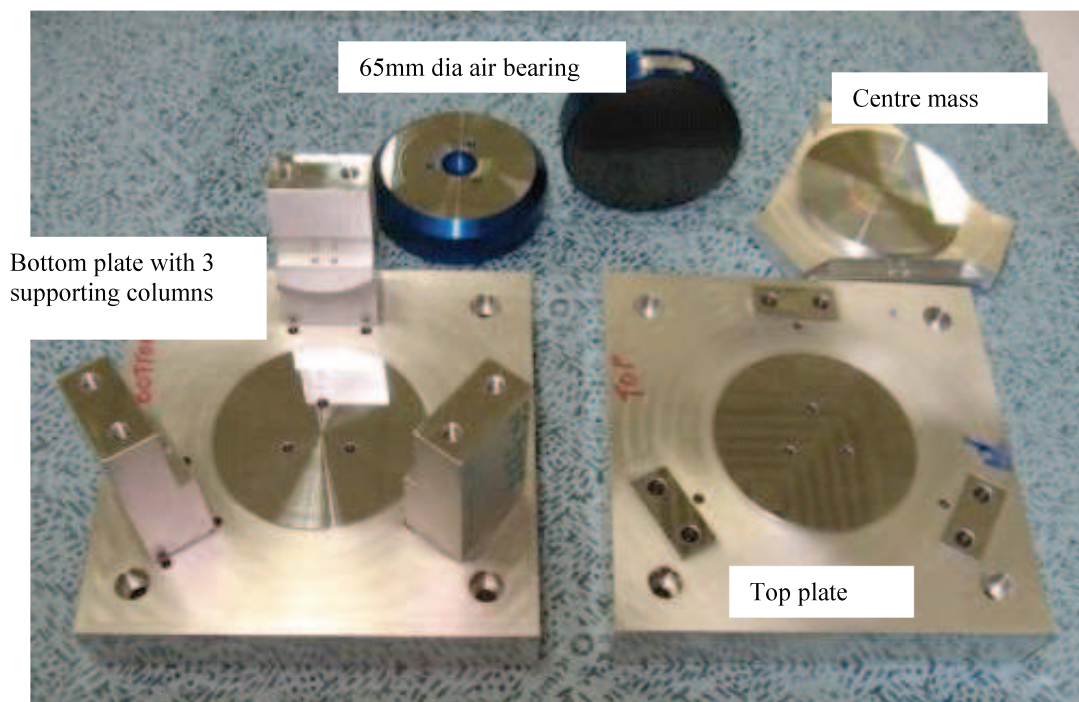


Figure 5.18: Parts and air bearings for the test rig

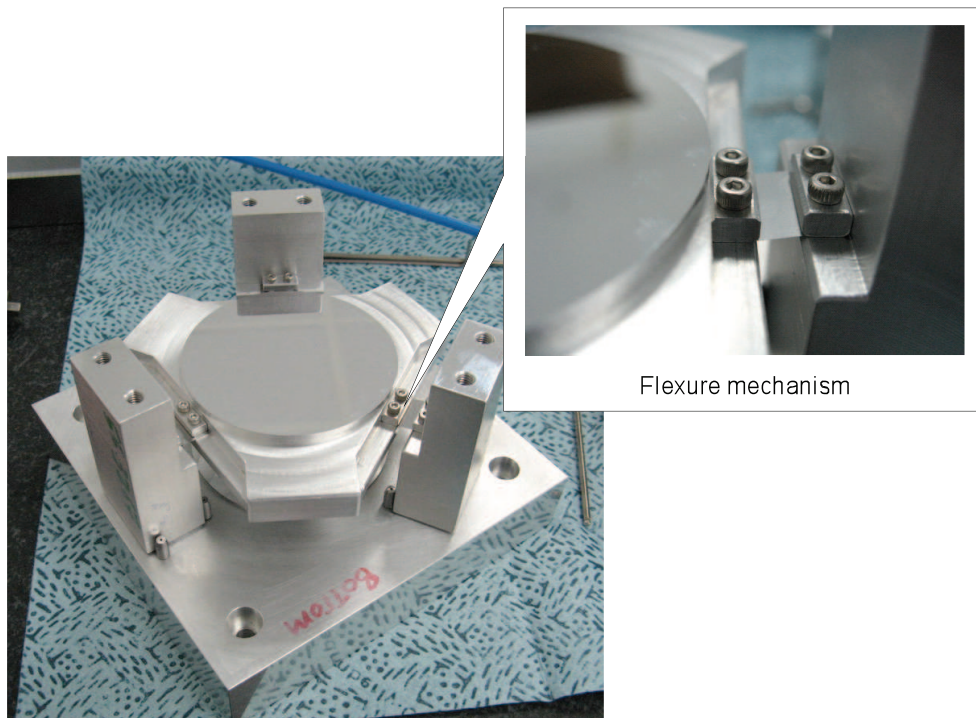


Figure 5.19: Flexure mechanisms on three sides of the centre mass

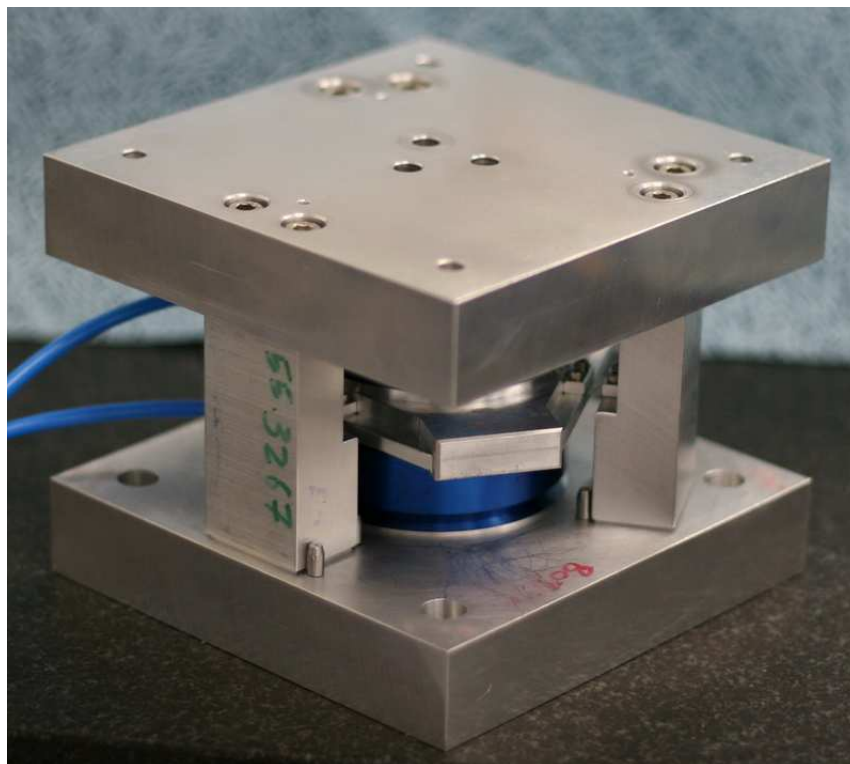


Figure 5.20: Assembled test rig

5.4 Dedicated Air Bearing Test Rig

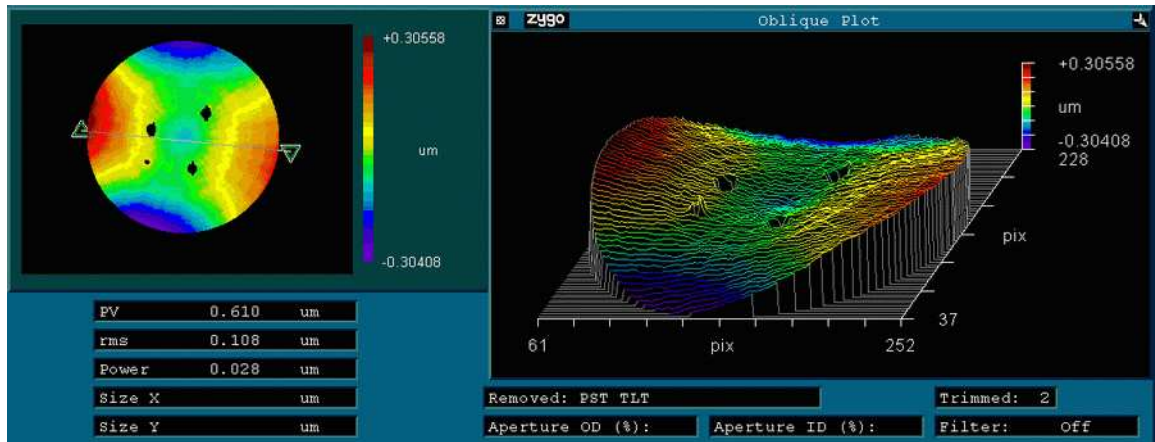


Figure 5.21: Measurement software screen-shot of the top plate surface

The assembly of the flexure mechanism is shown in Figure 5.19. Figure 5.20 shows the complete assembled test rig, with the two opposing 65mm diameter air bearings.

All the critical surfaces were measured using a Zygo GPI Laser Interferometer [121] to verify the machined surface flatness. All the critical surfaces that are diamond fly cut are all within the tolerance of $1 \mu\text{m}$. Figure 5.21 shows one of the software screen-shots of the top plate surface, which shows a peak-to-valley measurement of $0.61 \mu\text{m}$.

5.4.5 Height Measurement of the Air Gaps

In order to investigate the air bearing behaviour under different air gaps conditions, $5 \mu\text{m}$ steel shims were placed in between the structure joints to achieve the desired air gap heights. Ideally, the air gap heights can be worked out by the test rig geometry and taking into consideration the shim thicknesses. This is not a robust way to obtain the true height. Despite the fact that the critical joints of the parts were machined to a precise tolerance, the assembled components may induce geometrical errors of a few micrometre due to different tightness of the screwed joints and the placement of the shims.

The test rig design allows direct measurement of the lift caused by the air bearings. This is done by measuring the vertical displacement of the centre mass when the air

Chapter 5. Experimental Methodology, Procedure and Equipment

supply is turned on and off. Two Mahr LVDT probes were placed on the surfaces of two ledges of the centre mass, as shown in Figure 5.22. The readings of the probes determine the air lift height caused by the bottom air bearing when the air supply is turned off then on. The two probes are shifted to other locations within the three ledges of the centre mass and the displacement measurements are repeated. This step is repeated five times to obtain ten probe readings. The average air gap height caused by the bottom air bearing is computed from these ten readings.

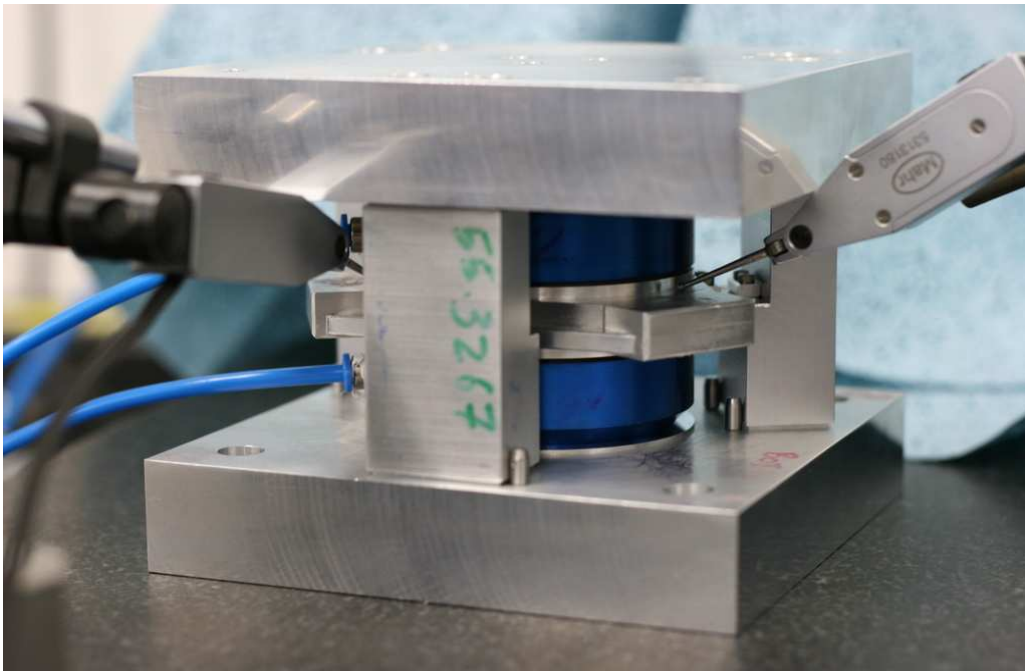


Figure 5.22: Measurement of air gaps using two Mahr LVDT probes

It is important that the mass is held in between the two air bearings by equal upward and downward forces, so that the investigation and analysis will be simpler. That means both the top and bottom air gaps should be approximately identical, thus, the top air gap also has to be measured. To do that, the centre mass was forced upward against the surface of the top air bearing when (both top and bottom) air supply is switch off. This was done by putting three soft springs below the mass to create that upward force, as shown in Figure 5.23. The spring stiffness is much smaller than the air film stiffness, so that they can be neglected from the measurement. Each soft spring has stiffness of approximately 125 N/m, and the combined spring force is just sufficient

5.5 Conclusions

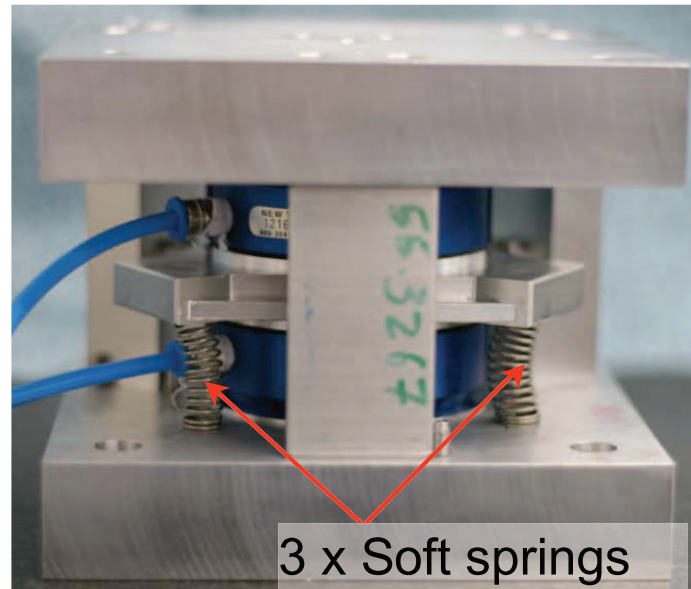


Figure 5.23: Three soft springs were used to push the mass upward when air is turned off to push the 180 g mass upward. The stiffness effects of the springs are negligible to the measurement of the air gap. The downward displacement caused by turning on the air supply is measured by the two Mahr LVDT probes in a similar manner as the upward lift. Both the top and bottom average air gaps were approximately $8 \mu\text{m}$, $\pm 1 \mu\text{m}$.

5.5 Conclusions

In the course of this research the air bearing guideway problem was decomposed into smaller elements to facilitate in-depth investigations of individual interfaces dynamic behaviour. The decomposition of the problem can be carried out in a more systematic approach by adopting the concept of stiffness-chain, as illustrated in Figure 5.7. Stiffness chain approach gives a clear perspective of the separate areas that require more insight. It also allows the individual areas to be viewed as building blocks for the overall motion system, which their static and dynamic model are synthesised to construct the overall air bearing interfaces dynamic model. The eventual aim is to bring together all the experimental findings in a unified manner to construct a more realistic analytical model for the air bearing guideway in FEA.

Chapter 5. Experimental Methodology, Procedure and Equipment

Air film dynamic behaviour remains one of the most complex investigation of this work. The investigation warrants a dedicated test rig to isolate the air film characteristics from the other interfaces dynamics, such as the structure and bearing mounting mechanism. It also serves as a more confident experimental platform, by reducing uncertainties in the air gaps and parallelism between the porous and guideway surfaces. The consideration, design and fabrication of the dedicated air bearing test rig was discussed in detail in the last section of this chapter.

Chapter 6

Dynamic Analysis of Aerostatic Bearing Interfaces

6.1 Introduction

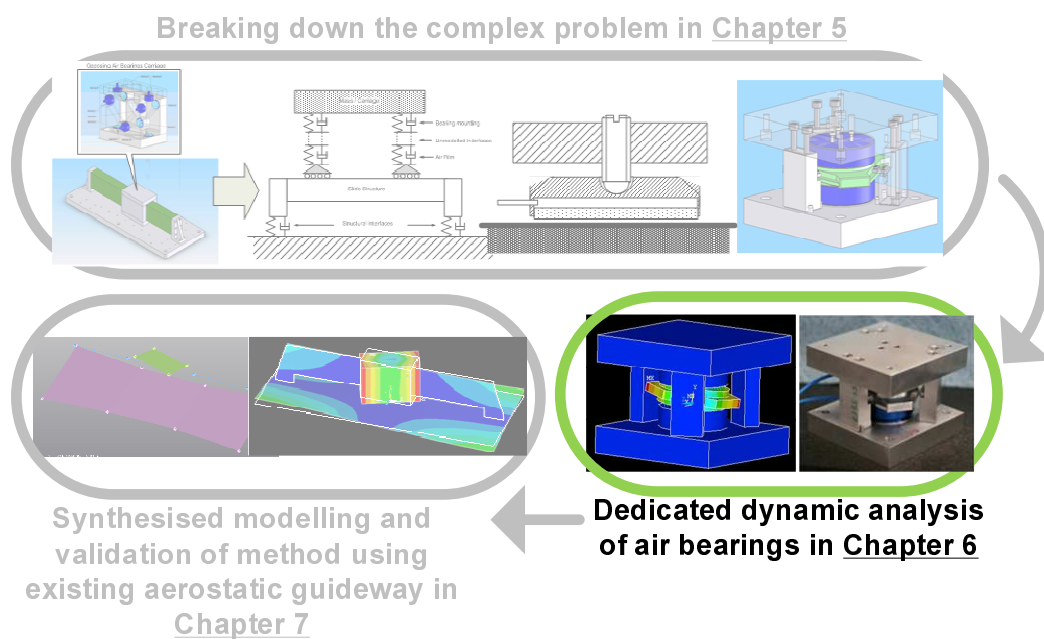


Figure 6.1: Flow of chapters 5 to 7.

This chapter focuses on the dynamic analysis of solely the aerostatic bearing pads. In order to isolate potential dynamic effects of the other interfaces of the air bearing setup, a dedicated air bearing test rig was designed. Insights into the air film dynamics are

Chapter 6. Dynamic Analysis of Aerostatic Bearing Interfaces

gained through the dynamic analysis of the dedicated test rig. A thorough analysis and investigation to identify the air film dynamics parameters is illustrated in this chapter. The subsequent sections will discuss the work to achieve a better understanding of the air film dynamics. The discussions include the following:

1. Analytical modelling of air film.
2. FEA results obtained using the analytical model.
3. Experimental modal testing results of the dedicated test rig.
4. Error estimations of the experimental setup.
5. Discussion of the correlation between the analytical and experimental results, and the error estimates.

6.2 Static Stiffness of Air Film

6.2.1 Stiffness Modelling of Air Film

As mentioned in Chapter 2, Plante et al.'s work [78] was adopted here to model the pressure distribution within the air film. This is due to its faster and more efficient computational performance as compared to the conventional method originally proposed by Majumdar [62, 63]. Figure 6.2 illustrates how a porous air bearing problem can be reduced to a one-dimensional flow and presented as trapezoidal control volume of differential elements.

The generalised one dimensional flow theory is an equation between the derivative of the air flow Mach number, M and selected relevant flow effects, i.e. effect of *area change*, dA/A , *mass flow addition*, $d\dot{m}/\dot{m}$ and *friction*, $4f_c(dr/D_h)$ [122]. The flow equation is expressed as follows:

$$\frac{d(M^2)}{M^2} = \frac{2dM}{M} = C_1 \frac{dA}{A} + C_2 4f_c \frac{dr}{D_h} + C_3 \frac{d\dot{m}}{\dot{m}} \quad (6.1)$$

6.2 Static Stiffness of Air Film

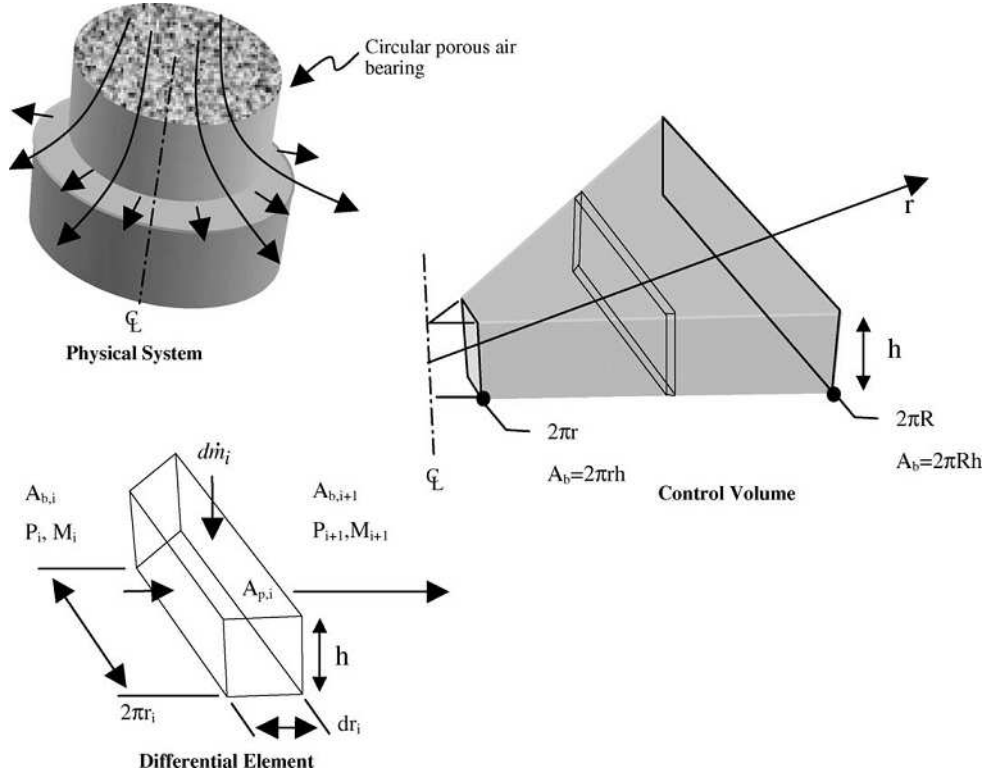


Figure 6.2: 1D generalised air flow from the physical system to the 1D model differential element (Plante et al [78])

and the coefficients C_1 , C_2 and C_3 are given by

$$C_1 = \frac{2 \left(1 + \frac{\gamma-1}{2} M^2\right)}{1 - M^2}, \quad C_2 = \frac{\gamma M^2}{2} C_1, \quad C_3 = (1 + \gamma M^2) C_1 \quad (6.2)$$

Equation 6.1 provides the basis for an iterative process to obtain the Mach number from node i to node $i+1$, as illustrated in Figure 6.2. This leads to an integral relationship to compute each successive pressures, P_i , with the control volume [122]. The relationship between the properties can be expressed as:

$$\frac{P_{i+1}}{P_i} = \frac{\dot{m}_{i+1}}{\dot{m}_i} \frac{A_i}{A_{i+1}} \frac{M_i}{M_{i+1}} \sqrt{\frac{\gamma_{i+1}}{T_i}} \gamma_i \quad (6.3)$$

The load capacity, W and static stiffness, K of a porous aerostatic bearing air film can be expressed in terms of its air film pressure, P , and ambient pressure, P_a [49, 62].

Chapter 6. Dynamic Analysis of Aerostatic Bearing Interfaces

$$W = \int_A (P - P_a) dA \quad (6.4)$$

where A is the surface area of the porous media that is sliding along the guide surface; and

$$K = -\frac{dW}{dh} \quad (6.5)$$

The overall load capacity curve of a 65mm diameter aerostatic porous bearing was computed using the above one dimensional flow method. Figure 6.3 shows the computed curve superimposed on the loading capacity curve provided by the manufacturer's datasheet. The computed curve matches closely with the curve provided by the manufacturer's datasheet. The stiffness of the air bearing at a specified air gap can be computed by numerically differentiating this force versus air gap data. The resulting stiffness versus air gap curve is shown in Figure 6.4

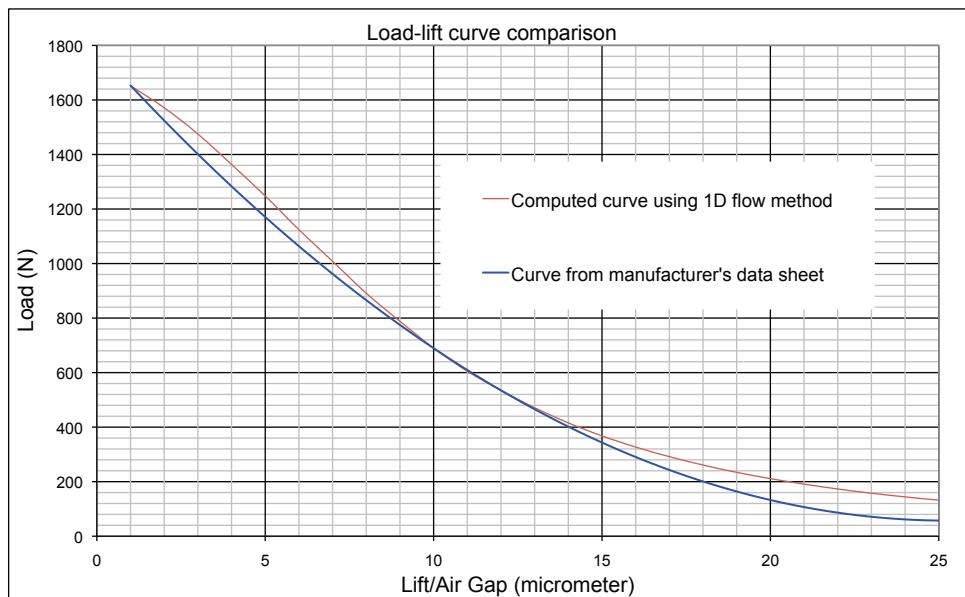


Figure 6.3: Comparison between computed curve and manufacturer data of a 65mm diameter aerostatic porous bearing at 5.5bar

6.2 Static Stiffness of Air Film

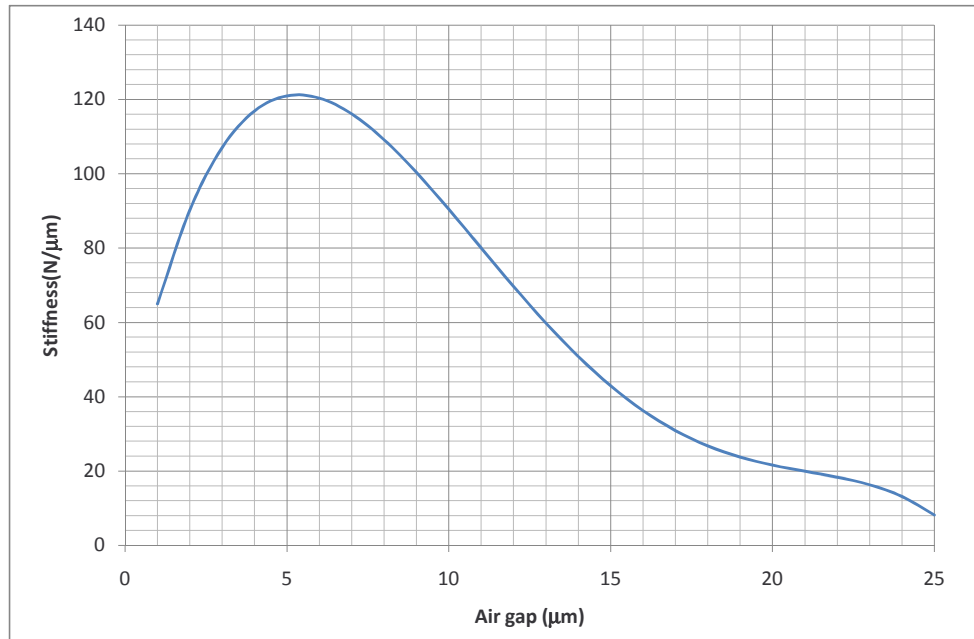


Figure 6.4: Stiffness curve of a 65mm diameter aerostatic porous bearing at 5.5bar

6.2.2 Experimental Results for Air Film Stiffness

Despite the fact that load-lift curves of the aerostatic bearings were provided by the manufacturer, it is still desirable to verify the data with actual measurement, so as to increase the confidence of this investigation. The stiffness test was done on a same 65mm diameter aerostatic bearing. The air film stiffness test setup is mentioned in Chapter 5. Figure 5.11 shows the test setup, which comprised of a load cell, two Mahr LVDT probes, and an adjustable threaded stub to apply the load. To better illustrate the concept of the test, a schematic of the setup is shown in Figure 6.5.

Two stiffness tests were carried out, one at 5.5 bar supply pressure, and the other at 4.5 bar supply pressure. Figure 6.6 shows the raw experimental data collected for the above two tests. This load-lift curve is very different from the 1D formulation computation and the manufacturer's data sheet published before 2008. Revised data sheets were published by the air bearing manufacturer sometime early 2008. The load-lift curves in some of their new data sheets are different from the old ones. Figure 6.7 shows the load-lift curves from the data sheet published before and during 2008, the 1D formulation computed curve, and the average curve obtained from the above stiff-

Chapter 6. Dynamic Analysis of Aerostatic Bearing Interfaces

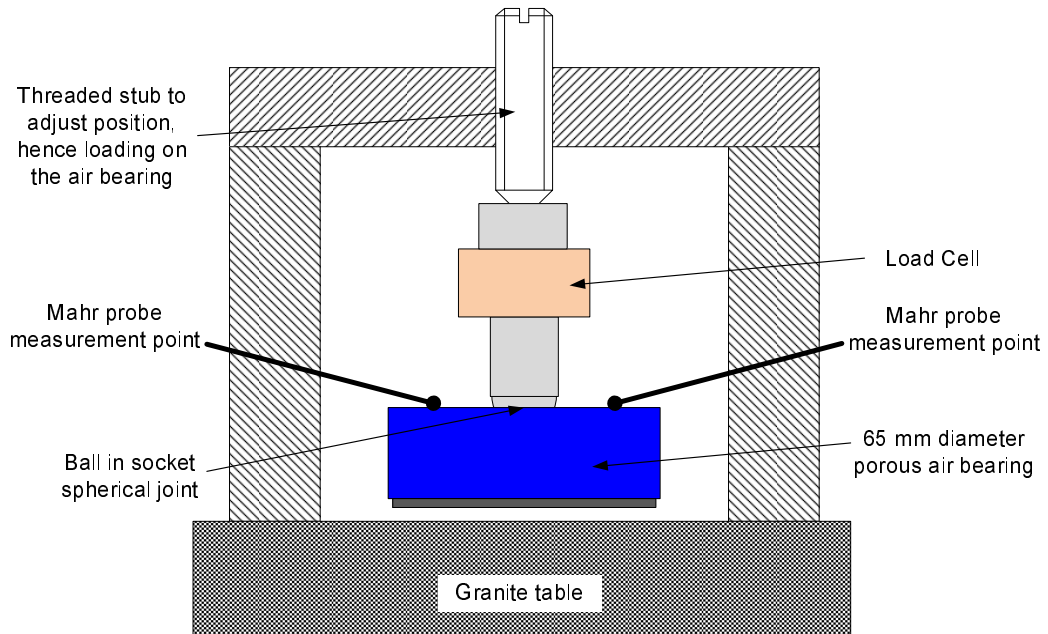


Figure 6.5: Schematic diagram of the air film stiffness test setup

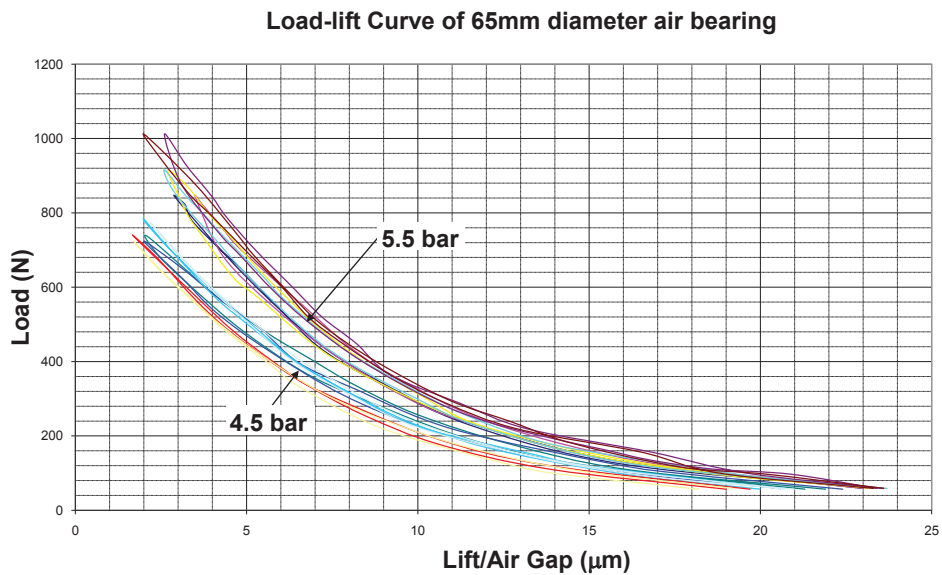


Figure 6.6: Load-lift Curve of 65mm diameter air bearing at 5.5 bar and 4.5 bar supply pressure

6.3 Dynamic Analysis of the Dedicated Air Bearing Test Rig

ness test results, all at 5.5 bar supply pressure. It is observed that the measured load-lift capacity of the air bearing is generally lower than the rest of the curves obtained analytically and from the manufacturer's datasheet.

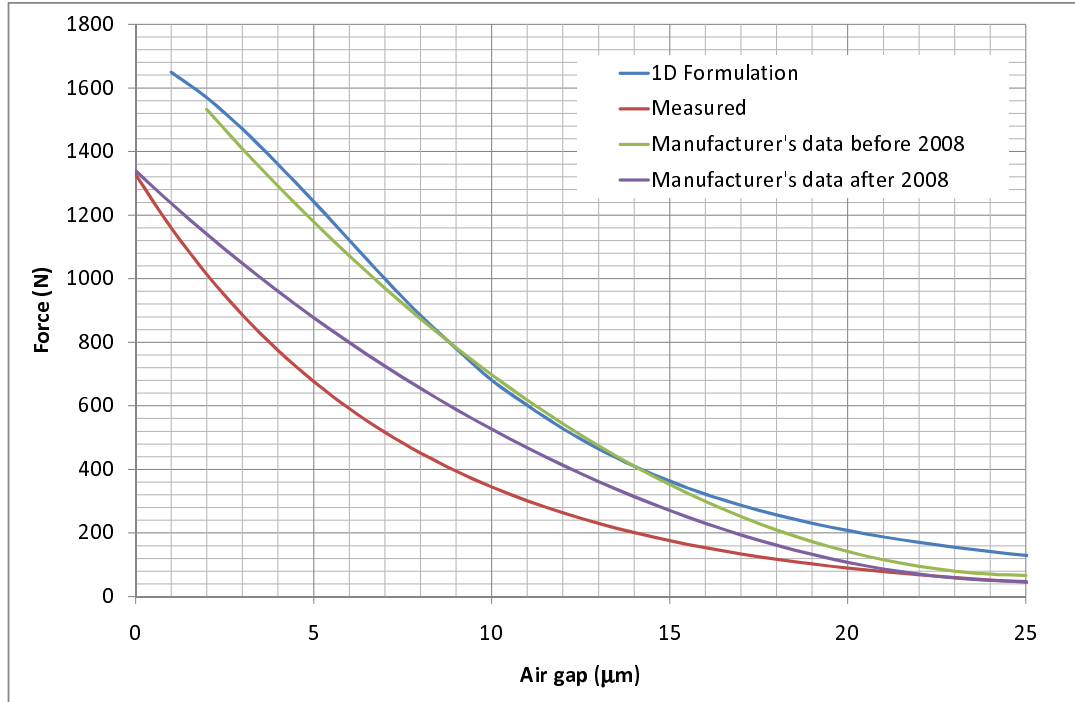


Figure 6.7: Different Load-lift Curves of 65mm diameter air bearing at 5.5 bar supply pressure

6.3 Dynamic Analysis of the Dedicated Air Bearing Test Rig

6.3.1 Dynamic Modelling of Air Film Test Rig Using FEA

A FE model of the air film is constructed based on the air film stiffness computed using the 1D flow formulation. It is more realistic to describe the variation of stiffness due to the pressure profile across the area of the air film. The air film is discretised into 120 non-linear spring elements, 12 slices of 10 segments, as illustrated in Figure 6.8. Each spring element represents a segment of air film. The pressure, P^h_i within each segment is computed numerically based on Equation 6.3 of 1D flow formulation. The superscript h of the pressure, P , denotes the height of the air gap which is used in the pressure computation. Thus, the non-linear springs of segment 1 to 10 can be

Chapter 6. Dynamic Analysis of Aerostatic Bearing Interfaces

represented by load versus displacement relationships expressed in the form of the stiffness Equation 6.5, where the loading capacity, W^h at a specific air gap height, h is expressed as:

$$W^h = \int_A (P_i^h - P_a) dA \quad (6.6)$$

Figure 6.9 shows the 10 load-lift curves computed using the method described above. Each load-lift curve corresponds to each segment of air film. In the FE model, each segment of the air film is modelled as a non-linear spring element with load versus displacement curves of seg-1 to seg-10, as shown in Figure 6.9. Essentially, the air film is made up of 120 non-linear spring elements with 10 different stiffness profiles according to their radial positions in the air gap. The non-linear springs are represented as element COMBIN39 in ANSYS. The element description is in Appendix C.1 [123].

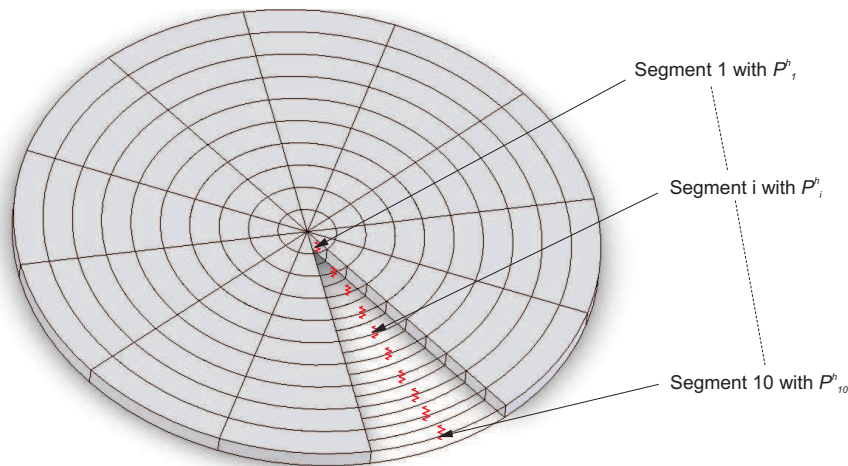


Figure 6.8: Air gap model using 10 different non-linear springs based on their radial positions

The 120 non-linear spring elements connect the structural elements of the top and bottom air bearings to the centre mass top and bottom surfaces, respectively. The modal parameters of the combined FE model for the structural assembly and the air bearings are computed using the FEA modal analysis solver. The FEA modal results is shown in the next section as a comparison against the experimental modal test results. The next section describes the impact modal testing of the dedicated air bearing test rig and presents the experimental results.

6.3 Dynamic Analysis of the Dedicated Air Bearing Test Rig

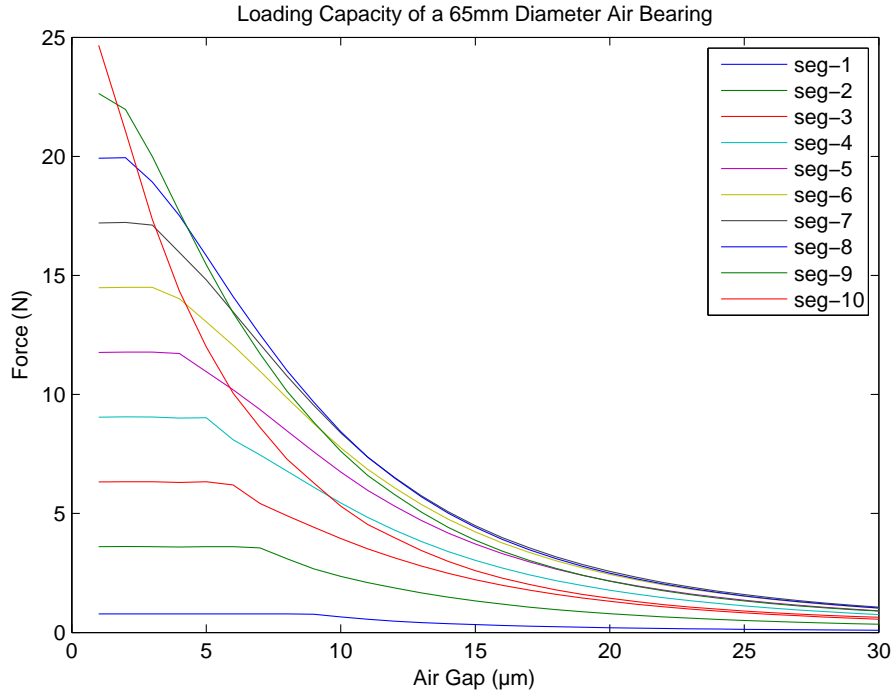
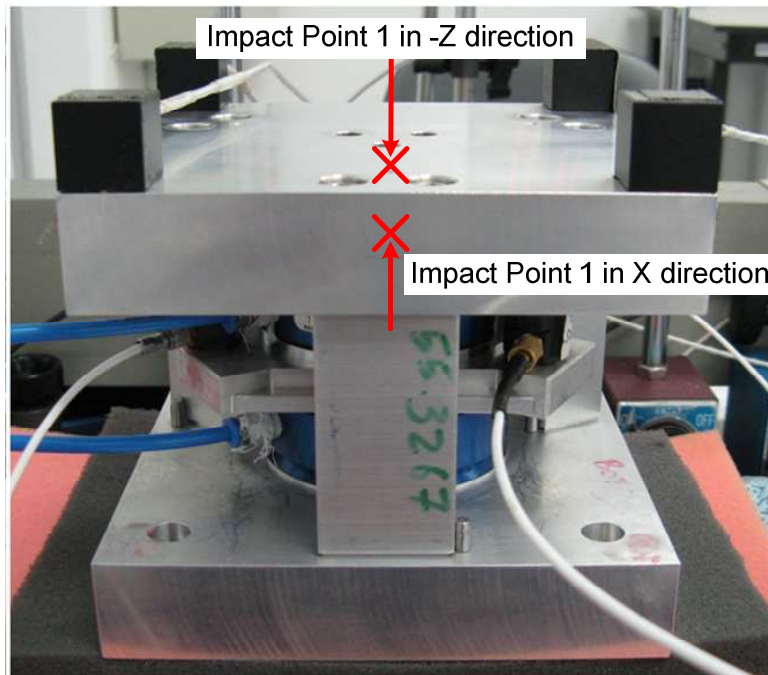


Figure 6.9: Load-lift curves of 10 segments of the air film slice

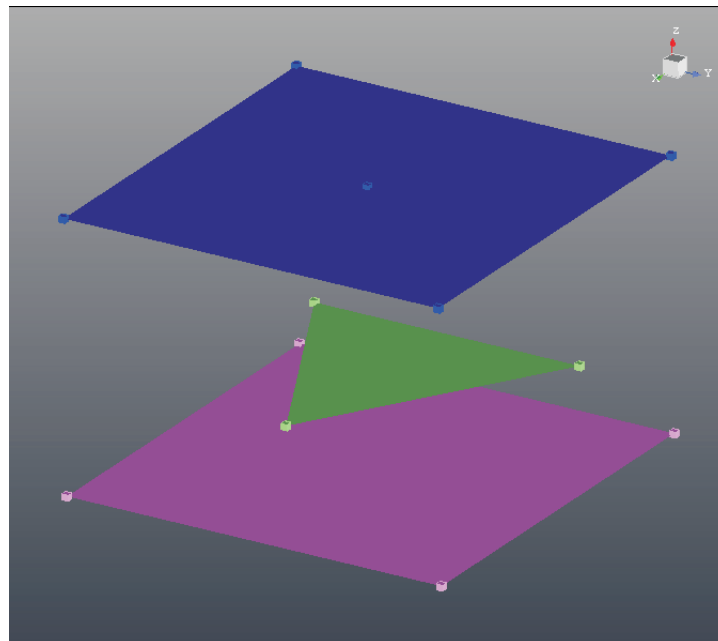
6.3.2 Experimental Modal Testing Results of the Dedicated Test Rig

Three single-axial accelerometers were mounted on the three corners of the centre mass, and four tri-axial accelerometers on the top plate (then bottom plate) of the test rig, as shown in Figure 6.10(a). As shown in Figure 6.10(b), three surfaces were created on the Modal Testing software geometry: one triangular surface representing the centre mass, and two square ones representing the top and bottom plates. A impact point was used as the reference point for the modal testing, impact force was applied in the $-Z$ direction on the tope plate, and in X direction on the side of the top plate (denoted by the red arrow in Figure 6.10(a)). The average FRFs were obtained with four impact forces applied to each impact directions. The average impact force measured was approximately $350 \text{ N}, \pm 70 \text{ N}$.

Two major modal analyses are carried out on the dedicated air bearing test rig: 1) with normal operating air supply and air gaps of most aerostatic guideway system; 2) with a 'less stiff' air film so as to separate the air film dynamics further away from the struc-



(a) Actual modal test setup



(b) Modal test software geometry

Figure 6.10: Sensors setup and impact points for the modal testing

tural dynamics. The former used normal operating parameters, which comprised 11 μm air gap and 5.5 bar air supply. The latter reduces the stiffness of the air film by

6.3 Dynamic Analysis of the Dedicated Air Bearing Test Rig

setting 20 μm air gap and 4.5 bar air supply. FEA computation as described in Section 6.3.1 was also carried out using the above two sets of operating parameters. The comparison of the analytical and experimental results of these two main modal analysis are presented in Tables 6.1 and 6.2.

It can be observed from the results in Table 6.1 and 6.2 that the structural dynamics of the test rig exhibited in Mode 3 and 4 have close agreement between the analytical modelling results and the experimental modal testing results. However, the structural dynamics of the test rig are not the key interest in this investigation. The main concern here is the FE model accuracy of the air film which is displayed in Mode 1 and 2 of the modal results. Mode 1 exhibits a tilting mode shape of the centre mass under the influence of the two opposing air bearings, and Mode 2 shows a vertical oscillation of the centre mass. As shown in Table 6.1, under normal air bearing operating parameters of 11 μm air gaps and 5.5 bar air supply, the FEA modal results for Mode 1 and 2 do not match well with the experimental ones (with Mode 1 having 56 % agreement and Mode 2, 68 % agreement). On the other hand, under the ‘less stiff’ operating parameters of 20 μm air gaps and 4.5 bar air supply, the percentage agreements of Mode 1 and 2 achieve better results. This could be due to the different in sensitivity of the model to error under varying operating parameters. The subsequent sections will investigate the potential geometrical errors and analytical uncertainties involve in the test rig as well as this analysis.

Chapter 6. Dynamic Analysis of Aerostatic Bearing Interfaces

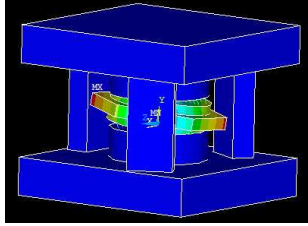
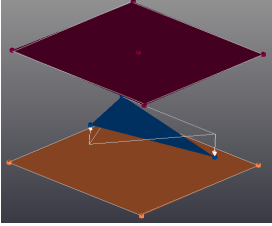
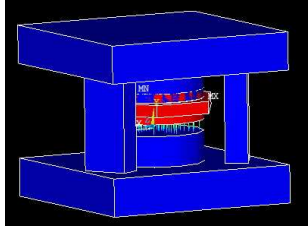
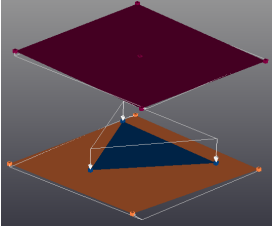
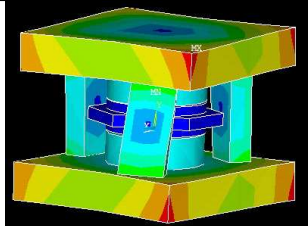
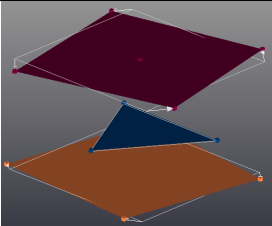
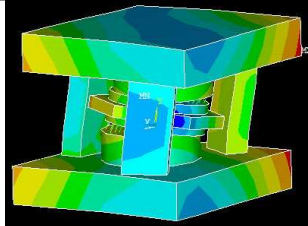
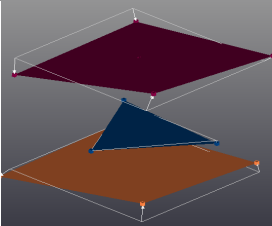
Mode No.	FEA mode shape & frequency	Experimental mode shape & frequency	Percentage agreement
1	 <p>Tilting of centre mass (air film dynamics) at 2257 Hz</p>	 <p>Tilting of centre mass (air film dynamics) at 1260 Hz</p>	56 %
2	 <p>Vertical oscillation of centre mass (air film dynamics) at 3218 Hz</p>	 <p>Vertical oscillation of centre mass (air film dynamics) at 2200 Hz</p>	68 %
3	 <p>Structural assembly deformation at 2483 Hz</p>	 <p>Structural assembly deformation at 2269 Hz</p>	91 %
4	 <p>Structural assembly deformation at 2811 Hz</p>	 <p>Structural assembly deformation) at 2549 Hz</p>	91 %

Table 6.1: Comparison of analytical and experimental modal results for 11 μm air gap and 5.5 bar air supply

6.3 Dynamic Analysis of the Dedicated Air Bearing Test Rig

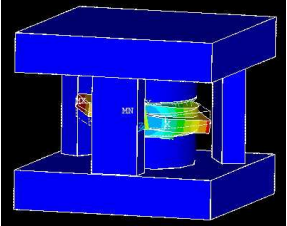
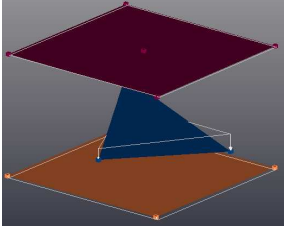
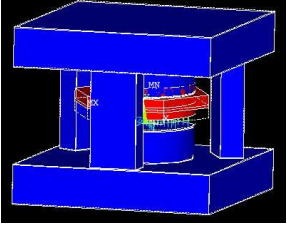
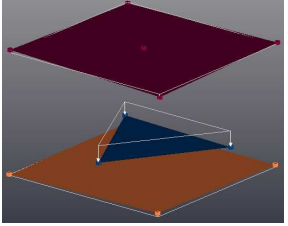
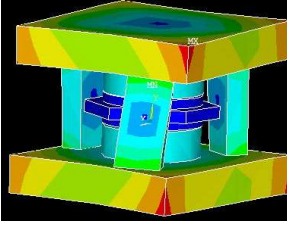
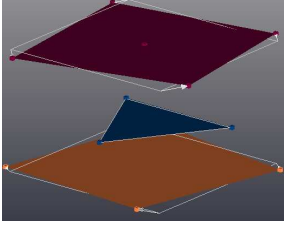
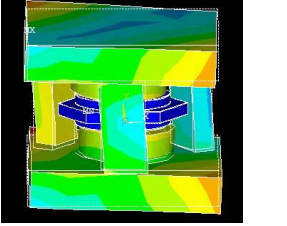
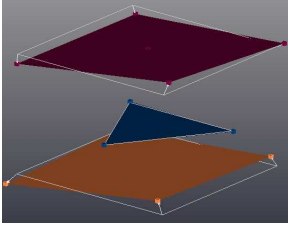
Mode No.	FEA mode shape & frequency	Experimental mode shape & frequency	Percentage agreement
1	 <p>Tilting of centre mass (air film dynamics) at 1067 Hz</p>	 <p>Tilting of centre mass (air film dynamics) at 806 Hz</p>	76 %
2	 <p>Vertical oscillation of centre mass (air film dynamics) at 1577 Hz</p>	 <p>Vertical oscillation of centre mass (air film dynamics) at 1514 Hz</p>	96 %
3	 <p>Structural assembly deformation at 2483 Hz</p>	 <p>Structural assembly deformation at 2262 Hz</p>	91 %
4	 <p>Structural assembly deformation at 2782 Hz</p>	 <p>Structural assembly deformation) at 2533 Hz</p>	91 %

Table 6.2: Comparison of analytical and experimental modal results for 20 μm air gap and 4.5 bar air supply, i.e. lower air film stiffness

6.3.3 Error Estimates of the Test Rig Dynamic Analysis

6.3.3.1 *Potential Errors in Air Gap*

One of the main purposes of the dedicated test rig was to increase the confidence of the air gap height. Section 5.4.5 discussed a method to measure the air gap height. It is therefore realistic to have knowledge of the potential errors associated with the accuracy of the air gaps. The following are four possible error sources that may contribute to the inaccuracy of the air gaps within the **assembled** test rig. The subsequent paragraphs discuss how these errors are determined:

1. Flatness of the top and bottom ‘fly-cut’ surfaces of the centre mass.
2. Flatness of the two air bearing porous surfaces (top and bottom).
3. Parallelism between the top and bottom ‘fly-cut’ surfaces of the centre mass.
4. Parallelism between the two air bearing porous surfaces (top and bottom).

Flatness of the critical surfaces (errors 1 & 2) The flatness measurement of the critical surfaces has been discussed in Section 5.4.4. Using a Zygo GPI Laser Interferometer, all the critical surfaces as mentioned in the error source 1 and 2, i.e. the two porous surfaces of the air bearings and two ‘fly-cut’ surfaces of the centre mass, possess flatness of less than or approximately $1 \mu\text{m}$ peak-to-valley. Screen snapshots of the interferometer measurement software for each surface are included in Appendix D. Table 6.3 shows the results obtained using the interferometer flatness measurement.

Surface	Flatness (peak-to-valley)
Top surface of centre mass	$0.939 \mu\text{m}$
Bottom surface of centre mass	$0.815 \mu\text{m}$
Porous surface of top air bearing	$1.269 \mu\text{m}$
Porous surface of bottom air bearing	$0.888 \mu\text{m}$

Table 6.3: Flatness of critical surfaces

Parallelism between the ‘fly-cut’ surfaces (error 3) Knowledge of the parallelism between the two critical surfaces of the centre mass is essential to determine the extent

6.3 Dynamic Analysis of the Dedicated Air Bearing Test Rig

of non-uniformity in the air gap height over the area of the air film or porous surface. Parallelism measures the tolerance of a plane parallel to a reference plane, as illustrated in Figure 6.11. The parallelism of the centre mass critical surfaces was measured using a coordinate measuring machine (CMM). The CMM¹ has a resolution of $0.05 \mu\text{m}$ with maximum permissible error of $0.95 \mu\text{m}$. A granite block with surface flatness of less than a micrometre was used as the reference plane. Using the CMM, 60 random points are measured on the granite surface over an area of approximately 80 mm by 80 mm. A plane is constructed using the 60 coordinate points. The centre mass was then placed on the above measured area of the granite surface, with the bottom critical surface in contact with the granite. 50 coordinate points were measured on top critical surface of the mass, and a plane is constructed. The CMM software computed the parallelism deviation between the reference plane and top surface plane. The above described measurement was repeated 5 times to obtain an average parallelism error of $2.8 \mu\text{m}$ between the two critical surfaces of the centre mass. It is important to note that this parallelism error between the surfaces includes the flatness errors of each surface as presented in Table 6.3, as illustrated schematically in Figure 6.12.

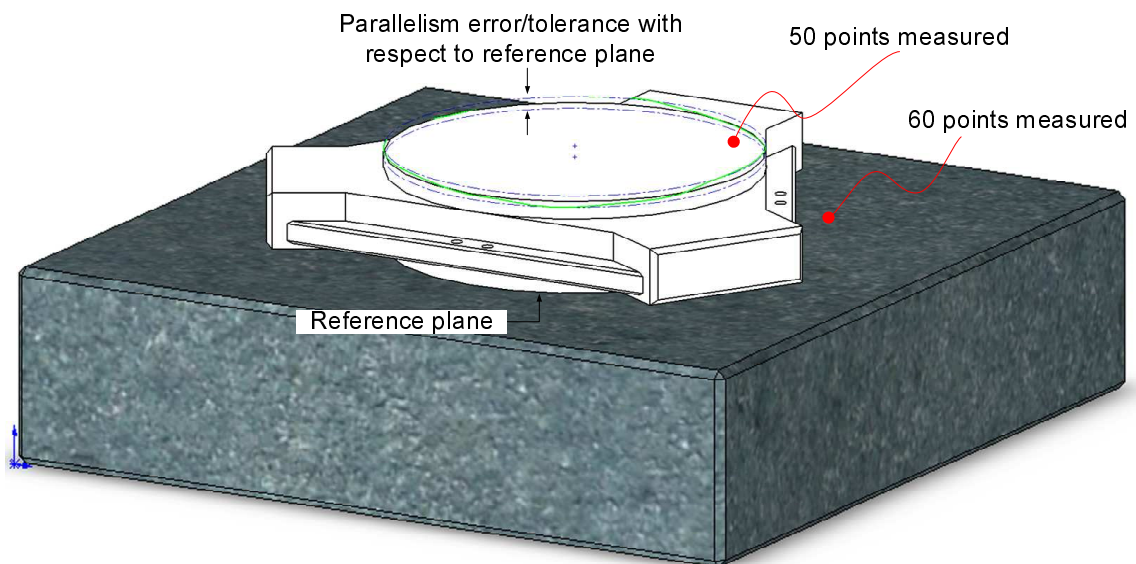


Figure 6.11: Parallelism measurement between the two fly cut surfaces

¹The CMM is a Werth Fixed Bridge VideoCheck[®] IP - <http://www.werthinc.com>

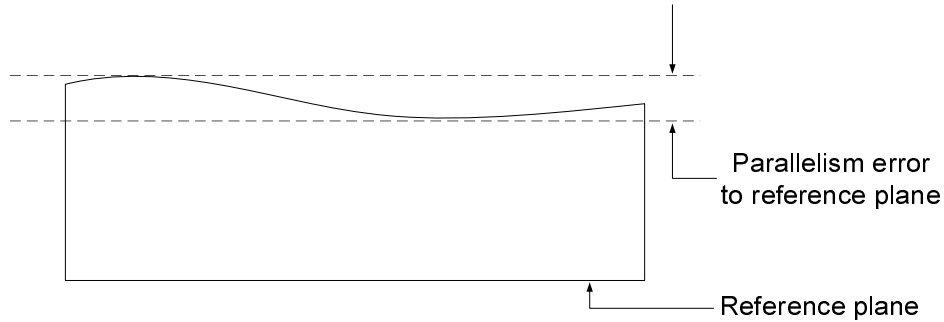


Figure 6.12: The flatness error contributes to the parallelism error.

Parallelism between two air bearing surfaces (error 4) It is not possible to measure the parallelism of the two air bearing surfaces directly using CMM, as done for the centre mass (for error 3). A valid measurement of this parallelism error can only be obtained with the test rig assembled. This poses practical difficulties in measurement. The dedicated air bearing test rig when fully assembled comprises of the centre mass suspended by the three flexure mechanisms as shown in Figure 5.20. Using the shims (as discussed in Section 5.4.5), the top and bottom air gaps were set to approximately $11 \mu\text{m}$ each. The proposed method here is to use the deviation of the air gap measurement as an indication of the parallelism error, as illustrated in Figure 6.13.

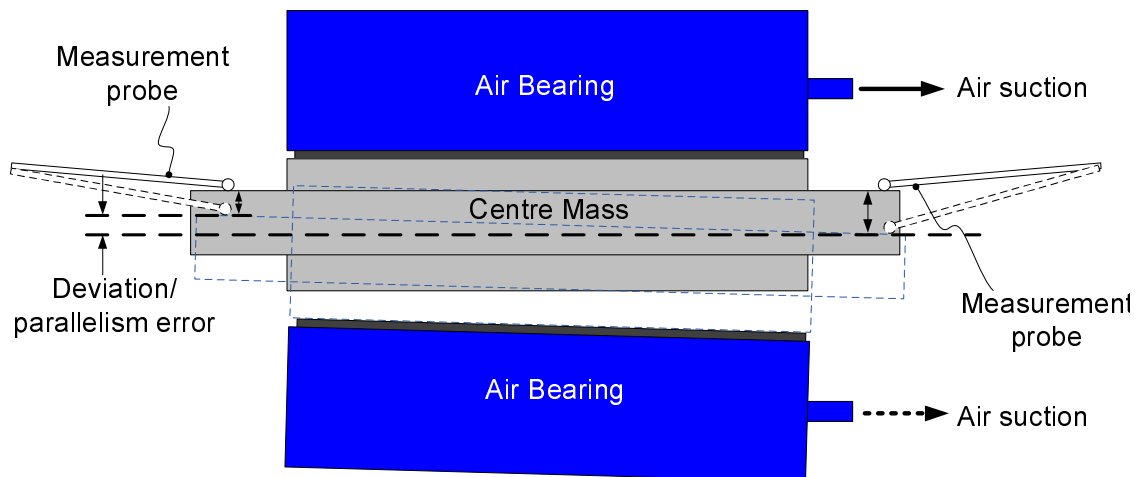


Figure 6.13: Estimating the parallelism error from deviation of air gap measurement

To measure the pre-set gaps between the air bearings and the centre mass, the cen-

6.3 Dynamic Analysis of the Dedicated Air Bearing Test Rig

the mass was forced to displace across the two air bearing porous surfaces. This was done by connecting one of the air supply inlet of the bearings to a vacuum pump. The top and bottom bearings were connect to the vacuum pump via a 3 port, 2 way mechanically-controlled pneumatic valve. Therefore only bearing was connected to the vacuum pump at any one time. For instance, if the 2 way valve links the pump to the top air bearing and when the vacuum pump was switched on, the centre mass would be ‘pulled’ upward by the vacuum suction and in contact with the top air bearing porous surface. The two LVDT measurement probes (1318 Mahr-LVDT [117]) were placed on the ledges of the centre mass in the similar way as described in Section 5.4.5. The control valve was then toggled to switch the vacuum suction to the bottom air bearing and cut off the connection to the top bearing. This forced the centre mass to be displaced downward and in contact with the bottom porous surface. This displacement of the centre mass caused by the switching of the vacuum connection to the air bearings was measured by the LVDT probes. Similar to the air gap measurement discussed in Section 5.4.5, the displacement measurements were repeated 20 times. This was done with the probes placed at different locations on the ledges. From the 20 displacement readings, the maximum deviation of **4.3 μm** was obtained. This was taken as the estimated maximum parallelism error between the two air bearing surfaces. This measurement inevitably encompasses both the parallelism errors of the centre mass as well as the air bearing surfaces.

The various flatness and parallelism errors that directly influence the accuracy of the air gap heights were critically examined. From the above error measurements, the maximum possible error in the (top and bottom) air gap heights were evaluated. Table 6.4 summarises the various potential errors and the maximum possible error of the air gap height. Note that when the air supply for both the top and bottom air bearings were turned on, the centre mass is assumed to maintain at an equilibrium position. The *total maximum error* was assumed to be distributed equally between the top and bottom air gaps, i.e. the *maximum possible error in each air gap* is half of the *total maximum possible error*.

Chapter 6. Dynamic Analysis of Aerostatic Bearing Interfaces

Error source	Potential error
Flatness of top surface of centre mass	0.9 μm
Flatness of bottom surface of centre mass	0.8 μm
Flatness of porous surface of top air bearing	1.3 μm
Flatness of porous surface of bottom air bearing	0.9 μm
Parallelism error between two air bearing surfaces	4.3 μm
Total maximum possible error	8.2 μm
Maximum possible error in each air gap	4.1 μm

Table 6.4: Maximum possible air gap error

6.3.3.2 Potential Errors in Analytical Modal Frequencies

The above air gap errors provide an indication of the discrepancy of the modelled air film, which were initially assumed to be parallel and uniform through the entire air film area. Based on the air gap errors estimation, the possible error in the analytical modal frequencies can be determined. The modal parameters of this air bearing system were computed numerically using FEA. The stiffness of the air film is known to be non-linear, hence it is not easy to compute a unique error value of modal frequency that corresponds directly to the air gap errors shown in Table 6.4. The potential errors in the analytical modal frequencies associated with the above air gap errors can be shown in the form of potential error spans, i.e. with an upper and lower bound frequency value.

To appreciate the potential error in the analytical dynamic modelling of the test rig, the dynamic analysis carried out using 11 μm air gaps (discussed in Section 6.3.2 and shown in Table 6.1) was examined. As presented in Section 5.4.5, the initial measurement condition was by forcing the surface of the centre mass in contact with the air bearing porous surface, then measured the centre mass displacement created by the air pressure. Thus, considering that the LVDT measurements were accurate, it was unlikely that the air gap would be smaller than the measured gap (of 11 μm). Therefore, the lower bound of the frequency error span is computed based on an estimate of 15 μm air gaps, i.e. 11 μm measured gap $+ 4.105 \mu\text{m}$ of possible error; and the lower bound is simply the original analytical results shown in Table 6.1, which is based on zero air gap error. Thus, the FE model is reconstructed based on the maximum potential

6.3 Dynamic Analysis of the Dedicated Air Bearing Test Rig

air gaps of 15 μm , and the upper bound modal frequencies was computed using FEA. Table 6.5 shows the lower and upper bound of the modal frequencies for Modes 1 and 2, caused by the potential air gap errors. Modes 3 and 4, which are mainly dominated by the structural dynamics are not of interest in the investigation here.

Mode No.	Modal Frequency (Lower bound)	Modal Frequency (Upper bound)	Potential error
1	1626 Hz	2257 Hz	631 Hz
2	2357 Hz	3218 Hz	861 Hz

Table 6.5: Potential error range of the modal frequencies based on measured 11 μm air gaps

6.3.3.3 Potential Errors in Experimental Modal Frequencies

Several areas in a experimental modal testing may lower the quality of the measured data, and are worth paying attention to during a modal test. These areas include [40]:

- Signal quality
- Signal fidelity
- Measurement repeatability
- Measurement reliability
- Measured data consistency

These quality issues of measured data have been discussed extensively in (Chapter 3 of) [40], hence will not be reiterated here. However, some of the issues that are more relevant to this work will be assessed and discussed.

All the accelerometers used in this work have been checked using an accelerometer calibrator¹. The calibrator embodies an electromagnetic exciter driven by a crystal oscillator at a frequency of 159.15 Hz. Four triaxial and three uniaxial accelerometers were checked. The acquisition system records the measured acceleration time data

¹Brüel and Kjør Type 4294 accelerometer calibrator [124]

Chapter 6. Dynamic Analysis of Aerostatic Bearing Interfaces

obtained using the accelerometers, and modal analysis software converts the time data into frequency domain data using FFT. These accelerometers were attached to the oscillating head of the calibrator, and the frequency of the oscillation were measured. The error between the measured frequencies of the above sensors and the calibrator's frequency of 159.15Hz were extremely small, with a maximum error of ± 0.03 Hz among the seven accelerometers. The signal and sensory data quality is certainly satisfactory with negligible errors.

One of the problems pertaining to impact excitation test is the difficulties of maintaining the exact same impact force, position and orientation normal to the test rig surface. Another excitation problem is the double impacts or "hammer bounce" commonly happened in impact testing. This produces varying input excitation, resulting in varying FRFs for every measurement. Hence, measurement data consistency and repeatability were also checked during the modal testing. To reduce statistical variance due to varying excitation characteristics, averaging is performed over a set of 5 impact measurements. The modal frequencies percentage errors between two identical measurements (i.e. using the same excitation position/direction and accelerometer reading, but measured at different time) are usually less than 1 %. The measurement data was rejected if a considerable error was observed between two identical measurements, usually resulting from poor impact method.

Another potential measurement reliability error source commonly encountered is the transducer mass loading effect. This effect is more significant with lighter test rigs, where the mass difference between the transducers and test system is small. This is worsened when the transducers are placed at or near the anti-nodal location. There are no established guidelines on mass ratio between the transducers and test system pertaining to the mass loading effects in modal testing. For the modal test carried out in this work, it is worthwhile to evaluate the mass loading effects on the test rig. To appreciate this effect, the same analytical modal FEA of the test rig (as shown in Table 6.1) was repeated with the mass of the accelerometers taken into account. The revised FEA modal analysis produced an approximation of the potential errors due to accelerometers mass loading effect. Table 6.6 shows the modal frequencies comparison of the

6.3 Dynamic Analysis of the Dedicated Air Bearing Test Rig

FEA between the original results (without the accelerometer masses) and the results which included the accelerometer masses. It can be observed from Table 6.6 that the effect of the accelerometers mass is more apparent in mode 1 and 2, where the centre mass is the key component of these two mode shapes. Each uniaxial accelerometer has a mass of 5.5 grams, and each triaxial accelerometer weights 11.2 g. The mass ratio of the three uniaxial accelerometers to centre mass was approximately 7.7 % (16.5 g/214 g), and the ratio of the four triaxial accelerometers to the assembly structure was about 1.8 % (44.8 g/2539 g).

Mode No.	Modal frequencies for FEA w/o accelerometers	Modal frequencies for FEA with accelerometers	Potential error
1	2257 Hz	2088 Hz	169 Hz
2	3218 Hz	3100 Hz	118 Hz
3	2483 Hz	2447 Hz	36 Hz
4	2811 Hz	2766 Hz	45 Hz

Table 6.6: Comparison of modal FEA results between analytical model with and without taking accelerometer masses into account

6.3.4 Corrected Analytical Model of Test Rig

Section 6.3.3 provides a thorough review of the various potential errors that contribute to the discrepancies between the analytical and experimental modal frequencies. The analytical dynamic model discussed in Section 6.3.1 assumed an ideal test rig. The above error analysis of the test rig has ascertained that the ‘ideal test rig’ assumption is inaccurate. In this section, the FE model of the dedicated test rig is reconstructed, which takes into account all the possible errors mentioned in the previous sections.

It is impractical to consider the worst case error of the air gap to be 4 μm (as shown in the maximum possible error in Table 6.4). A more appropriate practice is to use the Root-Mean-Square (RMS) of the air gap error. The RMS of the air gap error cannot be computed using the flatness and parallelism errors shown in Table 6.4, as they do not represent the same statistical data. A more suitable method is to assume evenly

Chapter 6. Dynamic Analysis of Aerostatic Bearing Interfaces

distributed errors within the air gaps and estimate the RMS based on the maximum possible error, i.e. $Error_{max}/\sqrt{2}$, which results in an RMS error of $3 \mu\text{m}$. The accelerometer masses were also placed at the respective locations in the same way as described in Section 6.3.3.3.

The two modal analyses in Section 6.3.2 are reevaluated using the corrected FE model of the test rig. The upper and lower bound of the potential modal frequencies were computed. In this reevaluation, only the relevant modes (Mode 1 and 2) are considered. Table 6.7 shows the comparison between the analytical and experimental modal results using normal air bearing operating parameters of $11 \mu\text{m}$ air gap and 5.5 bar air supply. Table 6.8 shows a similar comparison but with the ‘less stiff’ air film using $20 \mu\text{m}$ air gap and 4.5 bar air supply. In both evaluations, the analytical results are presented in a range of possible modal frequencies due to the potential RMS error in the air gaps as discussed above (i.e. $3 \mu\text{m}$ RMS). Using the lower and upper bound of the range of possible analytical modal frequencies, the uncertainty¹ of the analytical results can be evaluated. Using a Type “B” uncertainty evaluation (which is $a/\sqrt{3}$, where a is the half-width of error) [125], the standard uncertainties for each of the analytical modes are presented in the tables as well.

Mode No.	Range of analytical modal frequency	Standard uncertainty	Experimental modal frequency	Percentage agreement
1	1628 to 2082 Hz	131 Hz	1260 Hz	61 to 78 %
2	2457 to 3096 Hz	184 Hz	2200 Hz	71 to 90 %

Table 6.7: Comparison of analytical and experimental modal frequencies using the normal air bearing operating parameters of $11 \mu\text{m}$ and 5.5 bar air supply

6.3.5 non-linearity of the Air Film Model

The stiffness of the air film varies with air gap, as can be seen in the plot of Figure 6.4. Despite that the air film is modelled as a set of non-linear spring elements, the

¹The definition of uncertainty by UK National Physical Laboratory (NPL), is a quantification of the doubt about the measurement result. It is a parameter, associated with the result of a measurement, that characterises the dispersion of values that could reasonably be attributed to the measurand [125].

6.3 Dynamic Analysis of the Dedicated Air Bearing Test Rig

Mode No.	Range of analytical modal frequency	Standard uncertainty	Experimental modal frequency	Percentage agreement
1	790 to 985 Hz	56 Hz	806 Hz	82 to 98 %
2	1227 to 1522 Hz	85 Hz	1514 Hz	77 to 99 %

Table 6.8: Comparison of analytical and experimental modal frequencies using the ‘less stiff’ air film operating parameters of 20 μm and 4.5 bar air supply

FEA modal analysis solver does not fully utilise the non-linearity. During the computation of the modal parameters, the FEA solver picks the initial displacement values and computes a constant stiffness for each non-linear spring, thus resulting in a set of modal parameters which belongs to a linearised system [123]. The fundamental modal analysis (as presented in Chapter 4) assumes system linearity. This assumption has a few implications [40]:

1. Increasing the input force results in a proportionally increased response in a linear fashion,
2. If two or more excitation patterns are applied simultaneously, the response produced will be equal to the sum of the responses caused by each excitation when applied individually, and
3. The natural frequency of the system is independent of the input force.

Modal analysis for non-linear systems remain a challenging research area. Some promising non-linear modal analysis methods have been proposed [41, 43, 45, 126]. However, this subject is beyond the focus of this research project, thus will not be elaborated in detail. These proposed methods are yet to be well-established, and thus the main reason for its exclusion from FEA software solution.

It is important to recognise that the modal parameters results of the above linearised system may differ from the actual modal behaviour of the non-linear system. To evaluate the non-linearity effect or variation of the resulting analytical modal frequencies, a mathematical simulation of a simplified system was undertaken. The simplified system consists of a centre mass suspended in between two springs, as illustrated in Figure 6.14(a). This simplified model mimics one DOF or Mode 2 of the dedicated test rig.

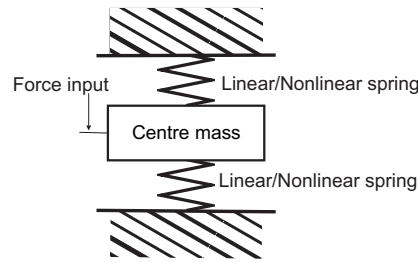
Chapter 6. Dynamic Analysis of Aerostatic Bearing Interfaces

The simulation uses the air bearing condition and stiffness parameters similar to that of the normal air bearing operating parameters of 11 μm and 5.5 bar air supply (see Section 6.3.2). Figure 6.14(b) shows the control block diagram of the simulation. Four sets of transient time data were computed in this simulation, with an impulse force input of 200 N. In the first set, both springs had a constant stiffness corresponding to an 11 μm air gap. The rest of the simulations use the non-linear spring stiffness computed using the 1D flow formulation (in Section 6.2.1) and an initial displacement condition of 11 μm . For the non-linear stiffness simulation, three transient time data were computed with three input forces of increasing magnitude, 200 N, 400 N and 600 N. The centre mass in the simulation has a weight of 0.18 kg. The displacement time data output, $x(t)$ was differentiated twice to obtain the response acceleration, $a(t)$, so as to mimic the test rig dynamic analysis input/output condition. Both the force and response time domain data were transformed into frequency domain, $F e^{i\omega t}$ and $A e^{i\omega t}$ respectively, using a Fast Fourier Transform (FFT) routine written in *MATLAB*. Consequently, the accelerance FRF, $A(\omega)$ of the above simulated system is obtained, which takes the form of

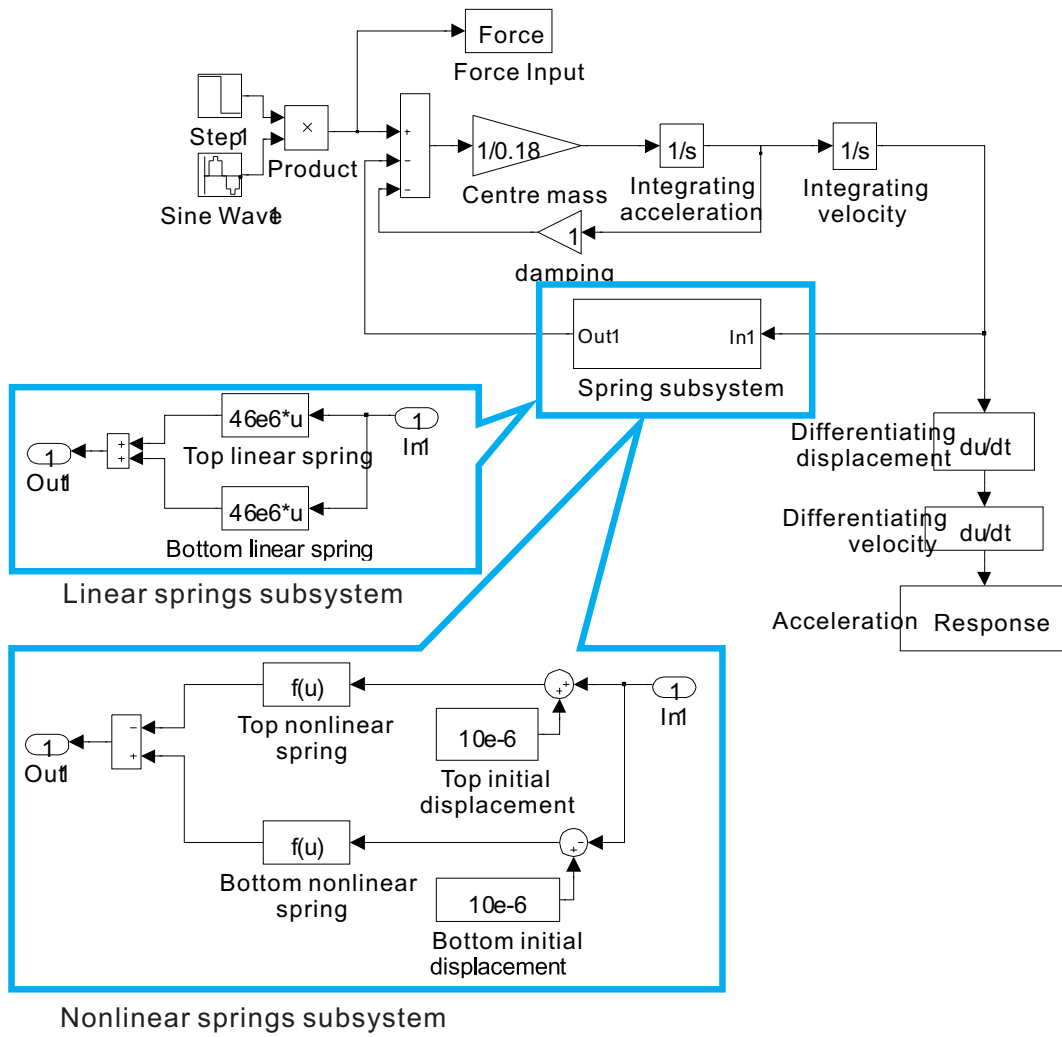
$$A(\omega) = \frac{A}{F} = -\omega^2 \alpha(\omega) \quad (6.7)$$

Figure 6.15 shows the FRFs of the four frequency response accelerances, i.e. the linear stiffness system and the three non-linear stiffness system with increasing input force. It is observed that the natural frequencies of the non-linear system vary with increasing input forces. This further reveals the non-linearity behaviour of the three systems. With smaller excitation force, the non-linear system exhibits modal properties that are closer to a linear system. This can be appreciated by the notion that smaller excitation force induces smaller range of displacement oscillation, thus lower degree of non-linearity within that small range. The experimental modal tests discussed in Section 6.3.2 were subjected to excitation forces of less than 400 N. Therefore, it is worthy to note that the analytical modal frequencies of the non-linear air film model obtained by the FEA possess potential error of approximately 200 Hz or standard uncertainty of 57 Hz, if the maximum input force is assumed to be 400 N. Hence, the analytical uncertainty caused by the non-linearity is considered to be insignificant as compared to the geometrical error.

6.3 Dynamic Analysis of the Dedicated Air Bearing Test Rig



(a) Schematic opposing springs and centre mass system



(b) Control block diagram in *Simulink* for a linear and non-linear opposing spring mass system.

Figure 6.14: Computing transient time data of an opposing springs and centre mass system

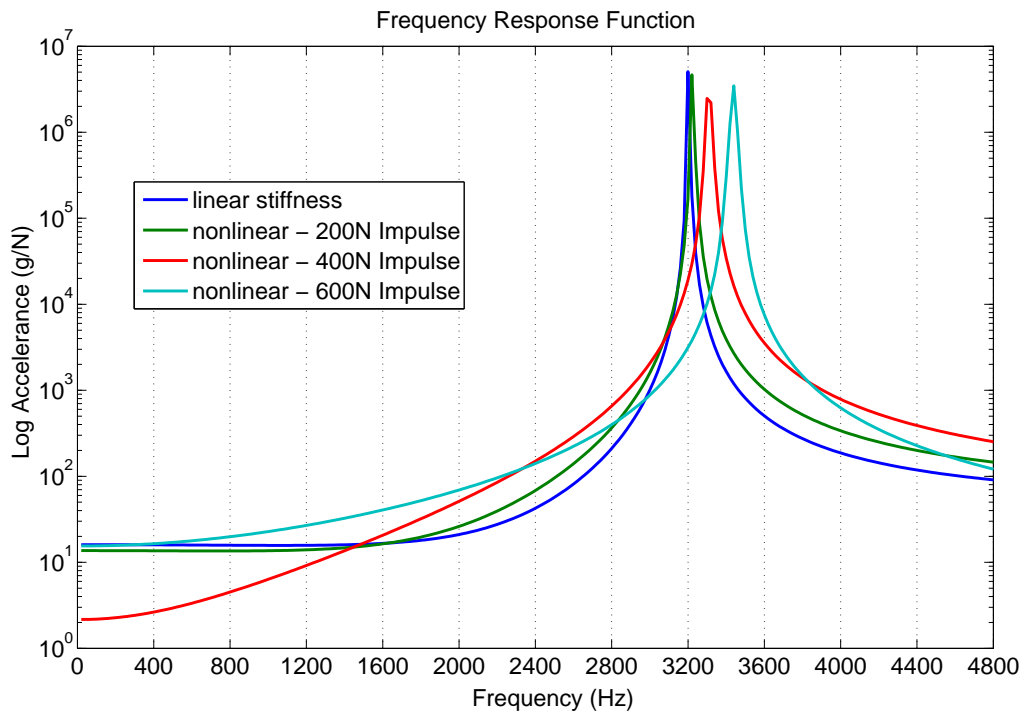


Figure 6.15: FRFs obtained from the linear spring system comparing against the non-linear ones with varying input force

6.4 Discussion on Modal Analysis of the Dedicated Test Rig

6.4.1 Dynamics of the Test Rig

From the dynamic analysis carried out in Section 6.3.1 and 6.3.2, it is clear that the dynamics of the structure can be easily predicted using FEA. The structural dynamics are also decoupled from the air film dynamics, as the modal behaviours of the structure (exhibited in mode 3 and 4) are not affected by the changes of air bearing operating parameters, as shown in Table 6.1 and 6.2. Hence in this discussion the focus will be on mode 1 and 2 which is primarily influenced by the air film dynamics.

The dynamic modelling carried out in Section 6.3.1 assumes the test rig to be 'perfect'. Although employing the same dynamic modelling method, the results of the two analyses (in Table 6.1: normal air bearing operating parameters, and 6.2: 'less stiff air film' setup) shows significant inconsistency. The modal analysis using the 'less stiff

6.4 Discussion on Modal Analysis of the Dedicated Test Rig

air film' setup produced a much better correlation between the analytical and experimental results. The FEA using the computed non-linear springs is able to predict the natural frequencies corresponding to mode 1 of centre mass tilting and mode 2 of vertical motion to an accuracy of 76% and 96%, respectively. However, under normal or higher stiffness air film condition, the prediction of centre mass behaviour is not satisfactory. It is observed that the analytical prediction for the tilting mode is less accurate than the vertical oscillation mode (for both analyses), this may be due to the 'squeeze-out' effect of the air at the edge of the bearing thus weakening the stiffness of the air film at the edge. The achievable prediction accuracy for the tilting mode is dependent on and is worsened by the parallelism error between the air bearing porous surfaces and the centre mass surfaces. This parallelism issue of the air bearing and its tilting modal behaviour will be reiterated in the overall discussion of next chapter, and further understanding is realised.

6.4.2 Errors and Uncertainties of the Analysis

A thorough error analysis was carried out and discussed in Section 6.3.3. Based on the investigation of the various errors and uncertainties, a corrected analytical model was reevaluated in Section 6.3.4. The various errors considered in Section 6.3.3 should not be neglected in the analytical modelling of the test rig. From Table 6.7 and 6.7, it can be seen that the air gap height errors contribute to an approximately 16 to 22% of analysis uncertainties (estimated from the span of percentage agreement column). It is extremely difficult to maintain high precision in the air gap height, especially in an assembled test rig. The dismantling and assembly of the test rig create undesirable parallelism errors that are not repeatable. Although parallelism errors can be reduced with painstaking adjustment of the test rig using steel shim, the flatness of the centre mass critical surfaces and the air bearing porous surfaces are inevitable. The accuracy of analytical model becomes more sensitive to the air gap errors as the air film stiffness increases, i.e. as the operating air gap becomes smaller. This is worsened by the fact that the air film stiffness is non-linear.

7.2 Key Potential Errors in Modelling

platform for the bearing interface analysis has been described. The analysis of the guideway system was broken down into smaller isolated and focused investigations, which also led to a design and analysis of a dedicated air bearing test rig. This Chapter demonstrates the overall dynamic modelling methodology as discussed in Chapter 5 and 6, using this existing aerostatic guideway as a validating case study.

Using the insights obtained from the investigation of the air bearing, as discussed in previous chapter, some of the key potential error and/or uncertainties will be highlighted and quantified. The chapter also presents the FE modelling scheme used to represent the guideway air bearing interfaces. The accuracy of the guideway system FE model is evaluated with modal test results obtained from the actual aerostatic guideway. The chapter concludes with a discussion of the correlation between the analytical and experimental results.

7.2 Key Potential Errors in Modelling

Some aspects of errors and uncertainties in the application of aerostatic bearing pads have been discussed in Chapters 5 and 6, hence the detail may not be reiterated here. Key potential errors which are directly relevant to the aerostatic guideway will be highlighted and quantified in this section.

7.2.1 Errors and Assumptions in the Mounting Mechanism

Besides the air film compliance, there are two other interfaces within the air bearing setup that may ‘weaken’ the overall stiffness of the air bearing. These are the threaded stud which is used to adjusted the air bearing gap and the ball-in-socket spherical joint, which maintains parallelism between the porous surface and the guideway surface, as illustrated in Figure 5.8.

7.2.1.1 *Stiffness of the Threaded Joint*

The threaded stub was machined out of a 15mm diameter steel stub and threaded with a small pitch of 0.5 mm for precise setting of the air gap. The backlash in the threaded

Chapter 7. Dynamic Analysis of an Aerostatic Guideway System

interface generates a complex stiffness behaviour that is difficult to model and incorporate into the overall air bearing stiffness FE model. The backlash is reduced by adding locking nuts at both ends of the threaded stud, to preload them against each other [2]. Figure 7.2 shows the air bearing manufacturer's recommended mounting method, by adding the locking nuts at both ends of the adjusting stud, which provides a preloading effect on the threads. However, these locking nuts are only possible and applicable to certain types of air bearing layout and setup. The existing air bearing setup in the carriage as seen in Figure 5.8 do not allow the use of these locking nuts. This is mainly due to the 'opposing pads' design of the air bearing carriage (as shown in Figure 5.6 and 5.5), and also to permit easy adjustment of each bearing pad's air gap.

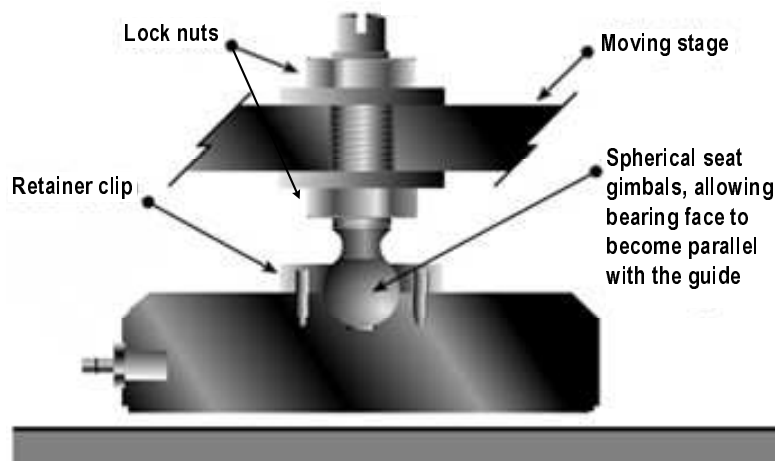


Figure 7.2: Aerostatic Bearing Mounting Mechanism (Source: <http://www.newwayairbearings.com>)

Depending on the machining accuracy of the tapped hole and the threaded stud, a lightly loaded threaded stud will probably have very small contact area within the thread, thus very low stiffness. As the loading increases, the number of contact area increases, and finally the full screw thread is completely in contact after a certain loading threshold. Thus before the threaded joint is completely in contact, the stiffness characteristics of the joint is extremely non-linear and practically challenging to model. Apparently, an ideal threaded joint is one that is well preloaded with all the threaded areas completely in contact. This type of 'perfect' threaded joint theoretically possesses superior stiffness and exhibits dynamic behaviour, which is near structural or bolted

7.2 Key Potential Errors in Modelling

joints dynamics. The stiffness value K_t of such ideal threaded joint can be estimated using a modified bolted joint stiffness equation [28, 29, 127].

$$K_t = \frac{A_t E'}{p} \times n_p \quad (7.1)$$

where A_t is the contacting threaded area, p is the pitch of the thread, and n_p is the number of pitch subjected to the load or in contact with the tapped hole. E' is the elastic modulus of two contacting/interacting elements, commonly known as *effective Young's Modulus* in contact mechanics. In this context, the two elements are the bolt and the tapped part (or nut). The effective Young's Modulus, E' , for the two contacting elements with different materials is defined as:

$$\frac{1}{E'} = \frac{1 - \nu_1^2}{E_1} + \frac{1 - \nu_2^2}{E_2} \quad (7.2)$$

where E_1 and E_2 are the Young's Modulus, and ν_1 and ν_2 are the Poisson ratio for the two contacting elements.

Using the above calculation for bolted joint stiffness, a perfect threaded joint based on the same geometry of the above 15mm threaded stud used in the air bearing mounting mechanism here, produces a stiffness in the magnitude of tens of KN/ μ m. A 25mm air bearing pad has a stiffness ranging from a few N/ μ m to below 30 N/ μ m depending on the air gap height, (which will be discussed later in this chapter). Ideally, the interface behaviour of a preloaded threaded joint will have minimum influence on the dynamic characteristics which is of interest here. **At this stage, the model shall assume that the threaded joint is well preloaded by the forces of the opposing air bearings.** The effect of this assumption will be deliberated and discussed during the validation of the model with the modal test results.

7.2.1.2 Stiffness Modelling of the Spherical Joint

In order to maintain parallelism between the air bearing porous face and the guide-way surface, a ball-in-socket spherical joint was employed in this aerostatic bearing mounting mechanisms. Theoretically, a spherical object when in contact with a sur-

Chapter 7. Dynamic Analysis of an Aerostatic Guideway System

face under no load, forms a point contact. A very small area of contact is created under a finite loading between the two contacting surfaces, where finite deformation of the two contacting objects occur. The stiffness of this contact interface can be modelled using classical Hertzian contact theory. Hertzian contact theory [77, 128] is often used to describe such ‘spherical object to surface’ contact type of mechanical interface.

The Hertzian contacts formulae are derived on the basis of 1) elastic deformation, 2) that the stress distribution below the surface is not affected by finite dimensions of the contacting bodies, and 3) the surfaces are assumed to be frictionless such that the surfaces are only subjected to only a normal force [77, 128].

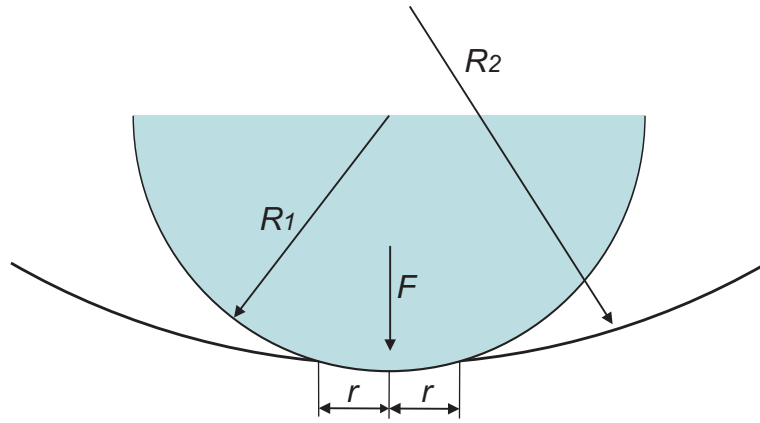


Figure 7.3: Typical Hertzian contact of a sphere on a curve surface

Consider a contact (as shown schematically in Figure 7.3) between a sphere with radius R_1 and a surface with curvature radius R_2 , subjected to a loading force F . The two surfaces form a concentrated contact area with a radius r which can be computed by the following formula [77, 128].

$$r = \left(\frac{3FR'}{4E'} \right)^{1/3} \quad (7.3)$$

where E' is the effective Young Modulus of the two contacting elements and R' the effective radius related to R_1 and R_2 , defined by:

$$\frac{1}{R'} = 2 \frac{R_1 - R_2}{R_1 \times R_2} \quad (7.4)$$

7.2 Key Potential Errors in Modelling

where R_1 and R_2 are the radius of curvature as shown in Figure 7.3. A more general form of the Hertzian contact formulation can be found in [128].

Based on the above equations, the relation between the force F and the contact area indentation δ , i.e. the stiffness K_{mm} of the interface can be derived

$$F = \frac{4}{3}E'\sqrt{R'\delta^3}, \quad K_{mm} = \frac{dF}{d\delta} = 2E'\sqrt{R'\delta} \quad (7.5)$$

Using the above equations, the load versus displacement curve of the contact interface can be computed analytically. The computed curve is plotted in Figure 7.4(b) together with the experimental data. The next subsection presents the work to validate the computed curve against actual measured stiffness of the spherical joint.

7.2.1.3 Experimental Stiffness Results of the Spherical Joint

The stiffness test was carried out using an Instron (4505) Mechanical Testing Machine, as described in Section 5.3.2 and shown in Figure 5.10. In order to isolate all other potential interfaces within the mounting mechanism and achieve a more practical evaluation, the following two experimental setups were employed.

Test Setup 1: Solely ball and socket interface Two circular air bearings were placed back to back, and a steel ball was ‘sandwiched’ in between two sockets, as shown in Figure 7.4(a). Slots were milled away from the aluminium case of the two air bearings to provide access for the Mahr LVDT probes. One probe was placed in contact with the bottom air bearing and the other in contact with the top air bearing. The setup was subjected with a increasing compressive force. The difference obtained from the two LVDT probes readings was the displacement of the two ball-socket interfaces. This measured displacement was solely contributed to by the compliance of the two assumedly identical top and bottom ball-socket (spherical) joint interfaces. The increasing compressive force with the corresponding displacement was recorded. If based on this assumption that both top and bottom interfaces are having identical stiffness characteristics, then it is equivalent to a system with two equal stiffness springs in

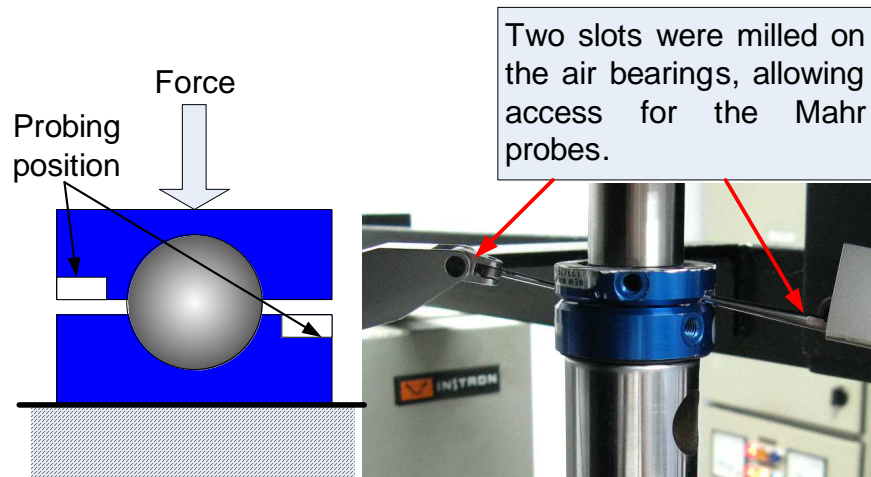
Chapter 7. Dynamic Analysis of an Aerostatic Guideway System

series. Hence, a single spherical joint interface (either top or bottom) will have double the stiffness of the above measured load and displacement relationship. Figure 7.4(b) shows the comparison of three load versus displacement curves for test Setup 1. The red curve shows the actual measured load and displacement relationship of the above ‘sandwiched ball’ experiment, i.e. effect of two spherical joint in series. Thus, for a single spherical joint, the stiffness is doubled. The blue curve shows a modified curve from the original measured data with the load increased to twice the original value. This should be a good approximation of how a single spherical joint will behave under static loading. Finally, the green curve is a computed curve based on the Hertzian formulation presented in the previous subsection.

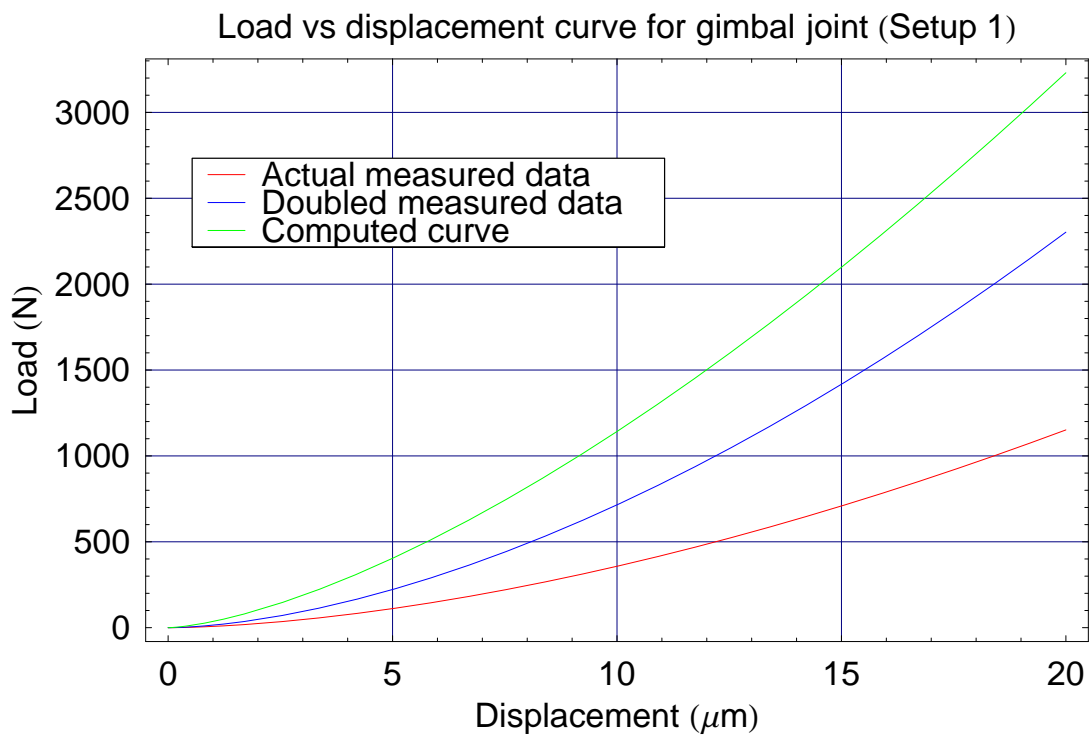
Test Setup 2: Ball in threaded stud interface The threaded ball-end stud used in the mounting mechanism here is made up of a steel thread stud with a conical cavity at the end, and a steel ball (same as the one used in Test Setup 1) attached inside the cavity by epoxy adhesive¹. One may assume that this spherical joint have similar stiffness properties as the one evaluated in Test Setup 1. Test Setup 2 is designed to verify this assumption. This experimental setup uses the same threaded ball-end stud as those used for the actual mounting mechanism in the aerostatic guideway. A washer is rigidly attached to the stud to allow placement of the LVDT displacement probe, as shown in Figure 7.5(a). The force applied on the top of the stud and the corresponding displacement between the washer and the top of the air bearing are measured. The red curve in Figure 7.5(b) shows the plot of the above measured force and displacement relationship. The green curve is the same computed curve as the plot in Figure 7.4(b), i.e. based on a single ball and socket Hertzian contact. The considerable difference in the experimental (red) curve and the computed (green) curve invalidates the above assumption of the stiffness similarity between spherical joint in Setup 1 and 2. Note that the steel ball in the actual spherical joint is attached to the threaded stud by epoxy adhesive. This implies that potentially there is a thin film of epoxy between the ball and the conical cavity at the end of the stud. If the same Hertzian contact formulation

¹Loctite Hysol 3430 structural adhesive

7.2 Key Potential Errors in Modelling



(a) Stiffness testing setup of a steel ball sandwiched in between two air bearing mounting sockets

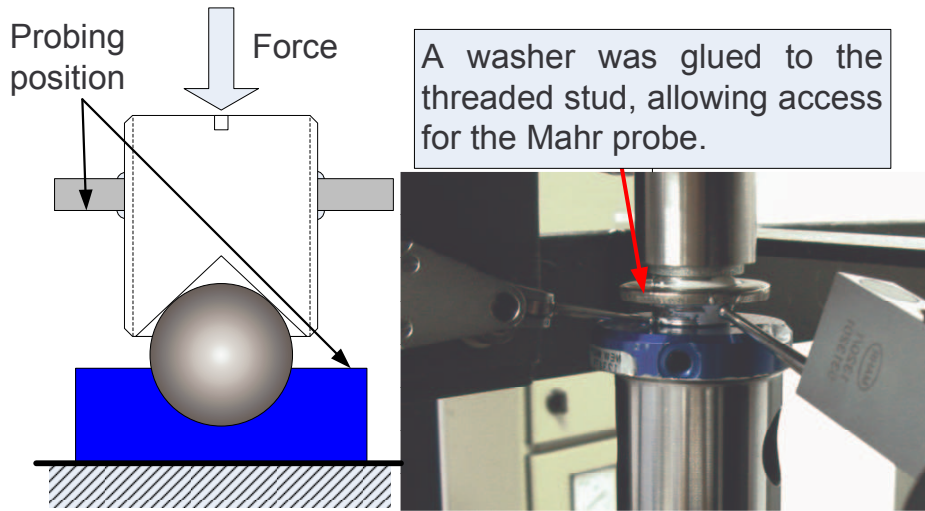


(b) Comparison of force vs displacement curves

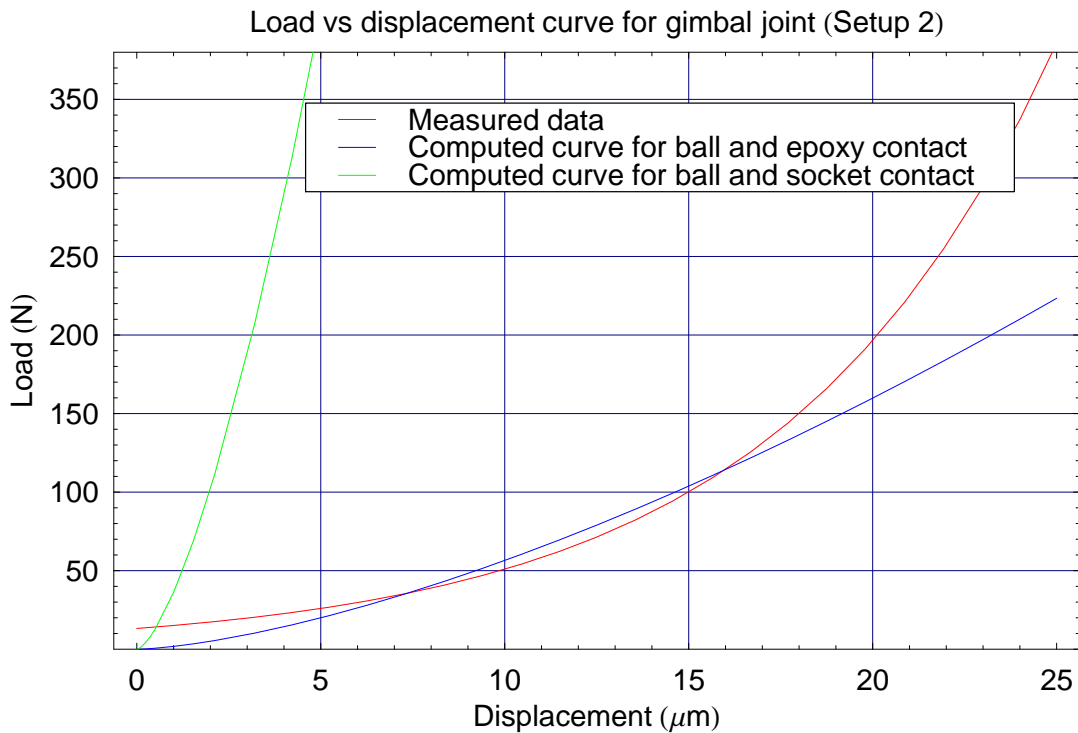
Figure 7.4: Stiffness testing for Test Setup 1

is used to approximate the stiffness of the contact interface between the steel ball and the epoxy 'socket', a force-displacement relationship can be obtained, and shown as the blue curve in Figure 7.4(b). It can be observed from the plot that if the computed

Chapter 7. Dynamic Analysis of an Aerostatic Guideway System



(a) Stiffness testing setup of the steel ball stud in an air bearing mounting sockets



(b) Comparison of force vs displacement curves

Figure 7.5: Stiffness testing for Test Setup 2

(green) curve for the single ball and socket interface is shifted to the right by approximately $20 \mu\text{m}$, the measured curve matches relatively closely to a combination of the shifted green and the blue curve.

7.2 Key Potential Errors in Modelling

7.2.2 Discussion on Errors Contributed by the Mounting Mechanism

The characteristics of air bearing mounting mechanism are neglected in most work involving aerostatic guideway modelling [79, 108, 120]. The above analysis realised that the mounting mechanism may contribute to the dynamic behaviour of the entire aerostatic guideway system. This is due to the relatively ‘weak’ and non-linear stiffness, particularly in the spherical joint, which ranges from approximately 2 to 30 of $\text{N}/\mu\text{m}$, depending on the force applied. The stiffness characteristics of a single spherical joint can be estimated using the classical Hertzian contact equation. However, the stiffness prediction accuracy may vary according to the surface and machining quality of the steel ball and the aluminium socket of the air bearing.

Due to the design of the air bearing carriage of the guideway system investigated here, the spherical joint uses a threaded stud with a steel ball attached at the end. This design has added an undesirable interface within the mounting mechanism, i.e. the cured epoxy film used to bond the ball to the stud. However, the stiffness characteristics can also be estimated using a similar contact equation between the steel ball and the epoxy film. It is important to note that the estimation method assumes a finite thin film of epoxy between the ball and the conical cavity of the stud. For the case of the ball stud used in Test Setup 2, one can nearly deduce from the plot shown in Figure 7.5(b) that the film of epoxy is approximately $20 \mu\text{m}$ thick. Beyond the $20 \mu\text{m}$ point, the measured curve begins to follow the stiffness trend of the computed curve for ball and socket contact. Realistically, the thickness of the epoxy film may vary among the 10 ball studs used in this aerostatic guideway system, inevitably varying individual load versus displacement curve. It is not practical to identify and model each of the individual ball studs within the guideway system.

This work shall assume that all the spherical joint of the air bearing mounting mechanism within this system possess similar stiffness characteristics as the one identified in Test Setup 2. The effect or consequence of the above assumption shall be discussed during the validation of the dynamic modelling for the entire guideway system.

7.2.3 Potential Geometrical Error in the Air Bearing

Flatness error of the bearing porous surface From the work carried out on the dedicated air bearing test rig, it is known that the flatness of the porous surface may not be of very high tolerance relative to the normal operating air gap height ranging from 5 to 8 μm . Hence, it is useful to quantify the porous surface flatness quality of these 25 mm diameter air bearings. Using the same Zygo GPI Laser Interferometer as mentioned in Section 6.3.3, the surface flatness for the air bearings are obtained. The flatness errors range from **0.8 to 1.7 μm peak-to-valley**. Figure 7.6 shows one of the measurement screenshots of a 25 mm diameter air bearing porous surface.

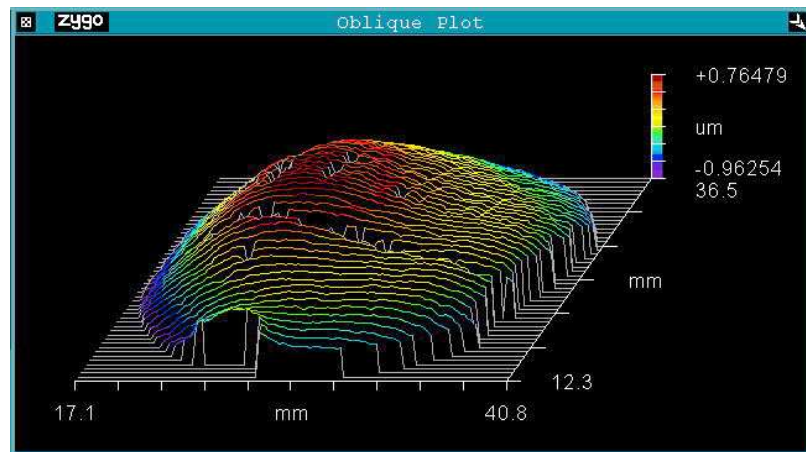


Figure 7.6: Interferometer flatness measurement of a 25mm diameter air bearing porous surface

Parallelism between the porous surface and the guideway surface Unlike the dedicated air bearing test rig, whereby the air bearings are rigidly mounted to establish geometric certainty, the air bearing pads in this guideway system are installed using the mounting mechanism discussed. Although the spherical joint enables a self-parallelism feature, it is practically difficult to have a realisable measurement of the parallelism errors for each bearing porous surface with respect to the guideway surface. **Another assumption of the air bearing is that the spherical joint is perfectly smooth, and when the air supply for the bearing is switched on, the joint ensures perfect parallelism between the porous surface and the guideway surface.**

7.2 Key Potential Errors in Modelling

7.2.4 Air Gap Height Measurement and Estimation

Appendix B describes the procedure to adjust the bearings' air gap height. However, the procedure presented in Appendix B does not consider any potential errors that may produce an inaccurate or misleading height reading. It provides an indirect measurement of the air gap, which assumes perfectly rigid connecting components/structures between the threaded stud and the air bearing, and strictly speaking, the air film. It is practically difficult to measure the actual air film height. Probably the most reliable indirect measurement of the air gap is to position the displacement probe on top of the air bearing itself, and as near to the centre as possible, as illustrated by Probe B in Figure 7.7. This probing position is only possible for other air bearing setup, but not applicable for the carriage design used in this work. Thus the only practical probing position for this aerostatic guideway is position Probe A as illustrated in Figure 7.7.

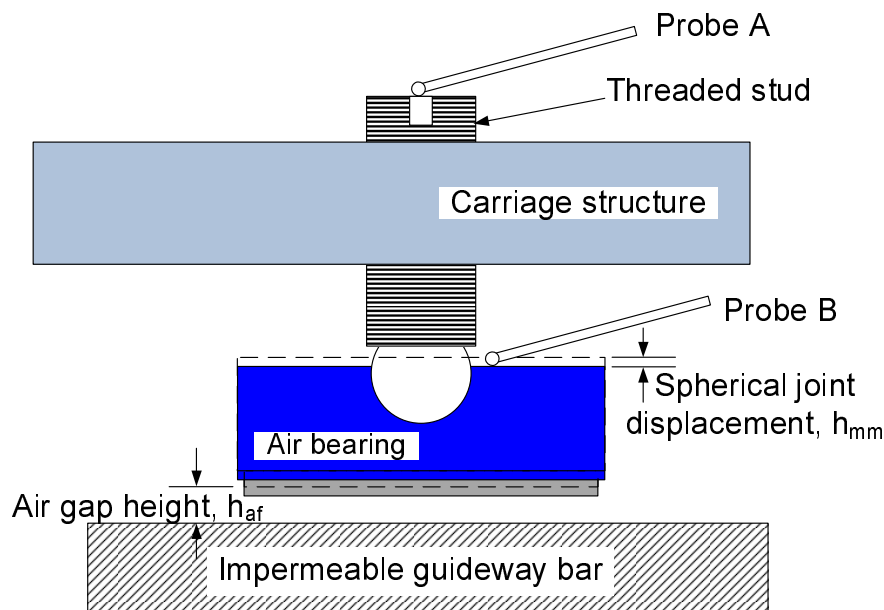


Figure 7.7: Schematic illustration of air gap measurement methods

Theoretically, if the mounting mechanism is perfectly rigid, Probes A and B should obtain the same displacement reading when the air supply is switched on. From Section 7.2.1, it is identified by the analytical and experimental work that the mounting mechanism possesses relatively low stiffness (in the same magnitude as air film stiff-

Chapter 7. Dynamic Analysis of an Aerostatic Guideway System

ness). This creates a deceiving measurement of the actual air gap height if the reading is obtained by Probe A. Probe A measures the resultant displacement contributed by the carriage, mounting mechanism as well as the air bearing lift due to the air supply pressure. However, the actual air bearing displacement within the carriage may differ considerably from the probe reading, as illustrated by the dashed line in Figure 7.7. This ‘internal’ displacement of the air bearing is a function of the compliance from the various interfaces within the mounting mechanism (as discussed in Section 7.2.1).

It is possible to estimate the actual displacement of the air bearing (or Probe B displacement) based on the stiffness characteristics of the spherical joint (from Section 7.2.1.2 and 7.2.1.3) as well as the air film (from Section 6.2.1). Conceptually, by adjusting smaller air gaps using Probe A, larger ‘internal’ displacement of the mounting mechanism/air bearing socket may occur, and vice-versa. This is due to the force exerted by the air film pressure. This force is transferred to the interfaces within the mounting mechanism, causing displacement which is not picked up by Probe A. If the mounting mechanism and the air film stiffnesses are linear, the air bearing displacement can be easily approximated by the ratio of the two stiffnesses. Since, these interfaces have non-linear stiffnesses (furthermore, the air film stiffness is computed numerically), the actual air bearing displacement can only be estimated graphically.

The following explanation of the graphical air gap estimation uses a $5\ \mu\text{m}$ Probe A reading as an example, i.e. the threaded stud is adjusted to produce a displacement reading of $5\ \mu\text{m}$ from Probe A. The plot in Figure 7.8 shows the interaction between the stiffness of the spherical joint and the force induced by the air film with varying air gap. The black dashed curve is the computed load versus air gap curve (based on the method discussed in Section 6.2.1) for a 25 mm diameter air bearing. The red curve shows a computed relationship between the load and displacement of a spherical joint, which assumes the first $20\ \mu\text{m}$ of the joint compliance is mainly contributed by the ball and epoxy film contact. Note that the plot for the spherical joint curve is offset to the right and aligned with the $5\ \mu\text{m}$ air gap. As mentioned, if the mounting mechanism is perfectly rigid, the air gap will be $5\ \mu\text{m}$ when the threaded stud is adjusted to produce a $5\ \mu\text{m}$ displacement. The $5\ \mu\text{m}$ air gap location can be perceived as the initial

7.3 Analytical Dynamic Modelling and Results

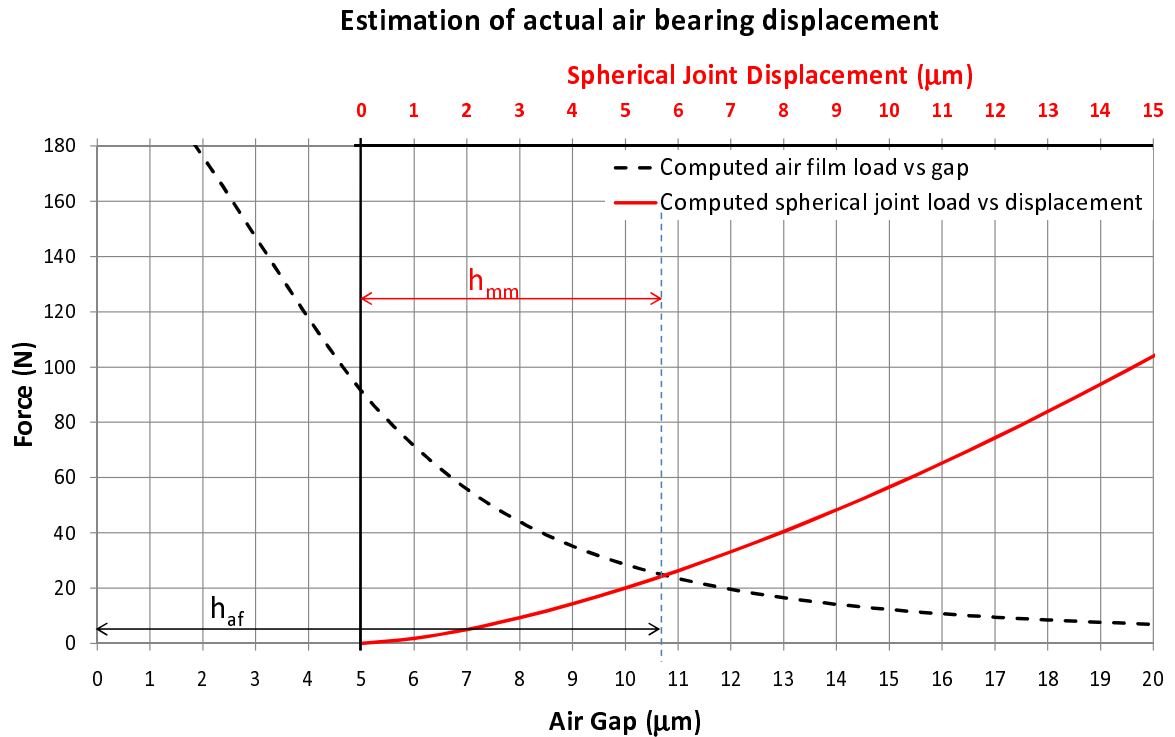


Figure 7.8: Graphical method for estimation of actual air bearing displacement

condition or location of the spherical joint, thus the offset. The air film creates an upward/outward thrust force which causes a corresponding displacement in the spherical joint interfaces. This interaction between the spherical joint and the air film is expressed by the intersection of the red and black dashed curves. The vertical axis value at the intersection gives the estimated air gap, h_{af} . The spherical joint is subjected to a corresponding displacement of h_{mm} . The intersection point can be understood as an interaction equilibrium between the air film force and spherical joint stiffness. Figure 7.7 also show these displacements, h_{af} and h_{mm} , using the air bearing setup.

7.3 Analytical Dynamic Modelling and Results

The FE model for the aerostatic guideway system incorporates all the findings discussed in the previous section. The analytical model for the guideway is also broken down to separate the dynamic behaviour of the air bearing interface and the structural dynamics. This will enhance the understanding of the combined dynamics, which will

Chapter 7. Dynamic Analysis of an Aerostatic Guideway System

be discussed. Before discussing the dynamic FE modelling of the aerostatic guideway, it is useful to recap some of the assumptions established in Section 7.2. The following are the summarised assumptions:

1. The threaded joint of the air bearing mounting mechanism is well preloaded by the forces of the opposing bearings configuration, thus is considered to be substantially stiff and is assumed to be a rigid connection within the model.
2. All the threaded ball studs have a thin film of epoxy between the steel ball and the conical cavity of the studs. The film of epoxy has a thickness of approximately 15 to 20 μm .
3. All the spherical joints of the mounting mechanism have small variation in their stiffness properties. The stiffness characteristics computed using the method discussed in Sections 7.2.1.2 and 7.2.1.3 are representative of average stiffness characteristics of the 10 air bearings used in this guideway.
4. The flatness of the air bearing porous surfaces vary from 0.8 to 1.7 μm . It is not practical and efficient to map this flatness errors to the individual air bearing during modelling, thus an average of 1.2 μm flatness error is considered for all the bearing used in this guideway modelling.
5. It is assumed that the spherical joints enable perfect parallelism between the bearings' porous surfaces and the guideway surface.
6. The method developed to estimate the actual air gap as discussed in Section 7.2.4 is assumed to be adequately robust in estimating the air gap for the FE model.

The following discussion will be centred around the modal behaviour of the carriage and the entire guideway system. Hence, it is useful to adopt a consistent coordinate and orientation convention to describe the various degrees of freedom of the system. Figure 7.9 presents the 3D CAD drawing of the guideway and carriage, as well as a schematic 2D representation of the 10 air bearings layout within the carriage. Note that when the air supply is switch on, the aerostatic carriage is able to slide along the X axis freely. The carriage is constrained by the 10 air bearings in 5 degrees of freedom, namely, Z translation, Y translation, roll, pitch and yaw, as illustrated in the 2D

7.3 Analytical Dynamic Modelling and Results

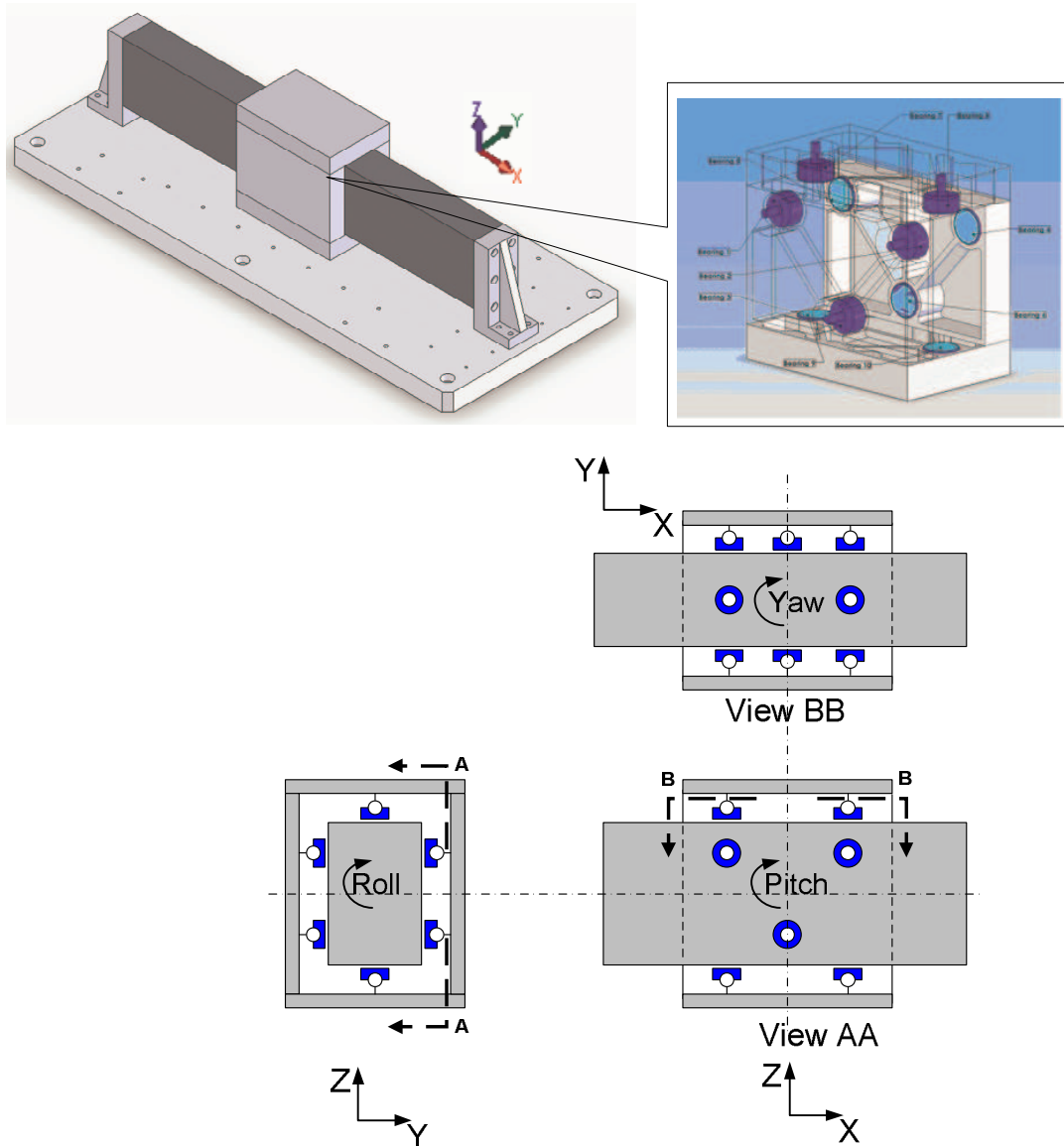


Figure 7.9: Carriage coordinate and orientation convention

schematic.

In the following analysis, two setups are used in the evaluation. Setup 1 set the 10 air bearings to $5 \mu\text{m}$ air gap, and Setup 2 to $9 \mu\text{m}$ air gap. Both setups use air supply pressure of 5 bar.

7.3.1 Stiffness Model of the Air Bearing

Using the same 1D formulation for air flow as discussed in Section 6.2.1, the stiffness model for the 25 mm diameter air bearing was computed. The 1D formulation assumes the following air bearing and operating parameters:

- Air supply pressure: 5.5 bar
- Porous media permeability: $1.25 \times 10^{15} \text{ m}^2$
- Porous media thickness: 5 mm

The static test to verify the actual air film stiffness for the 25 mm diameter air bearing was carried out using the same experimental setup in Figure 6.5 and as discussed in Section 6.2.2. Figure 7.10 shows the comparison between the load versus air gap curve obtained from the 1D formulation method, the manufacturer's data and the experimental results from the static stiffness test. Though some discrepancies are observed between the three curves, these stiffness characteristics for the 25 mm diameter air bearing are relatively close to each other, unlike those obtained for the 65 mm diameter bearing as shown in Figure 6.7.

7.3.2 Dynamic FE Model of the Air Bearing

The stiffness of the overall air bearing setup comprises not only of its air film, but also its mounting mechanism. Thus, the FE model of a single air bearing is represented by a set of 40 non-linear springs corresponding to the air film (similar to those in Section 6.3.1) and a single non-linear spring in series, representing the mounting mechanism stiffness. The FE model the air bearing setup is illustrated in Figure 7.11. The non-linear spring elements represented in *ANSYS* is *COMBIN39* (Appendix C.1). The single blue spring as illustrated in Figure 7.11 is connected to the set of 40 black springs by a 3 DOFs rotary joint, which mimics the behaviour of the actual spherical joint in the mounting mechanism. The force and displacement relationship of the air film, K_{af} and mounting mechanism, K_{mm} is used as the input for element *COMBIN39*. Note that both K_{af} and K_{mm} are not constant values, they are a function of

7.3 Analytical Dynamic Modelling and Results

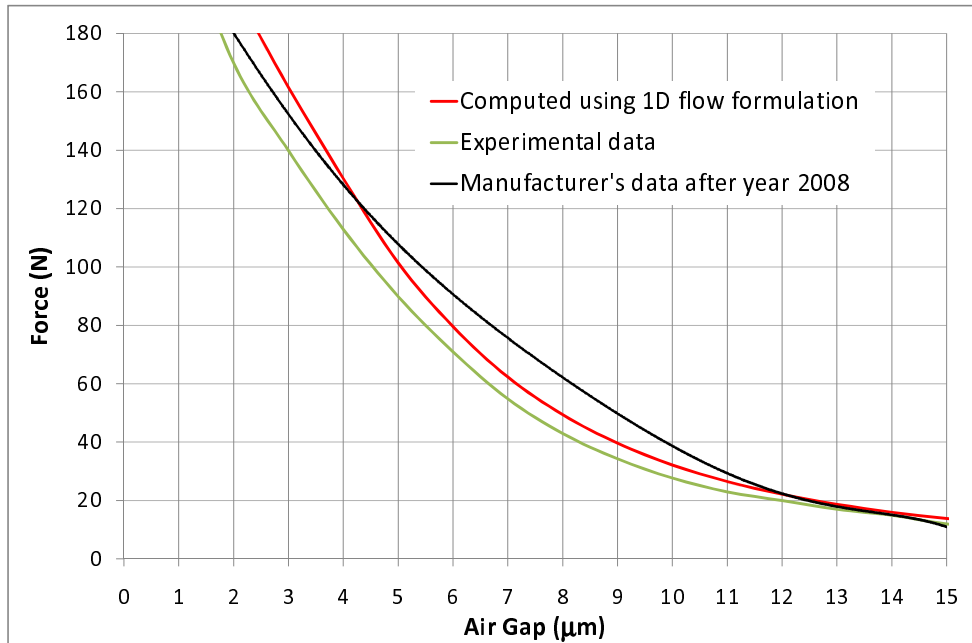


Figure 7.10: Comparison of the computed, experimental and manufacturer's load versus air gap curve for 25 mm diameter air bearing

the air gap and contact displacement, respectively. The relationship of these two stiffnesses are depicted in Equations (2.4) and (7.5), respectively.

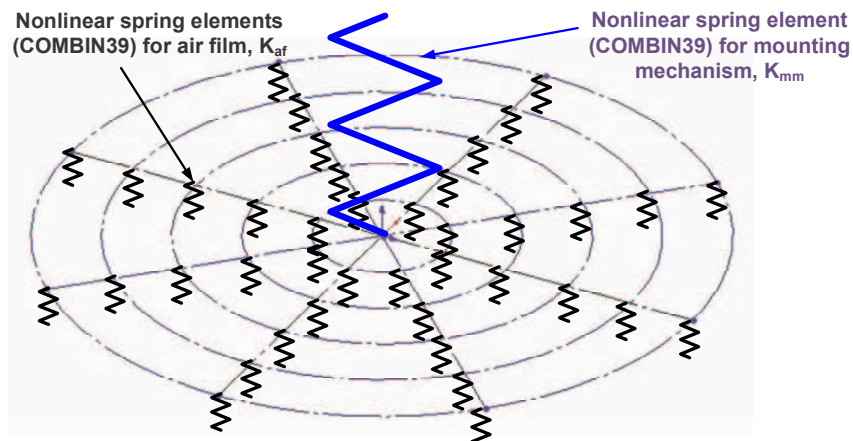
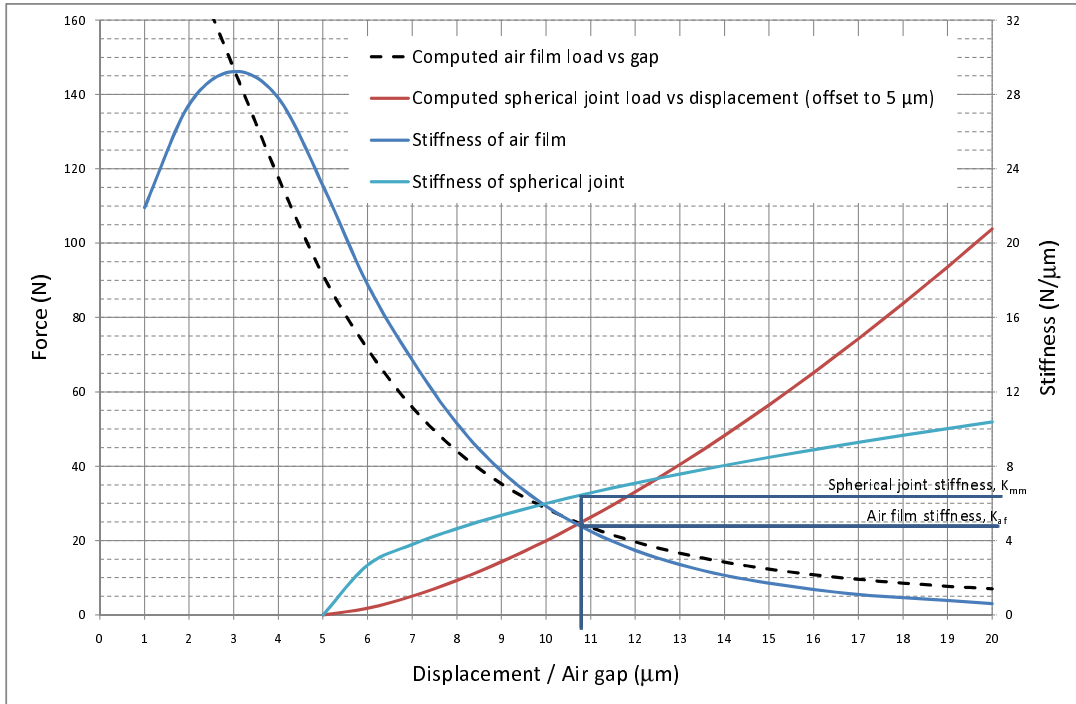


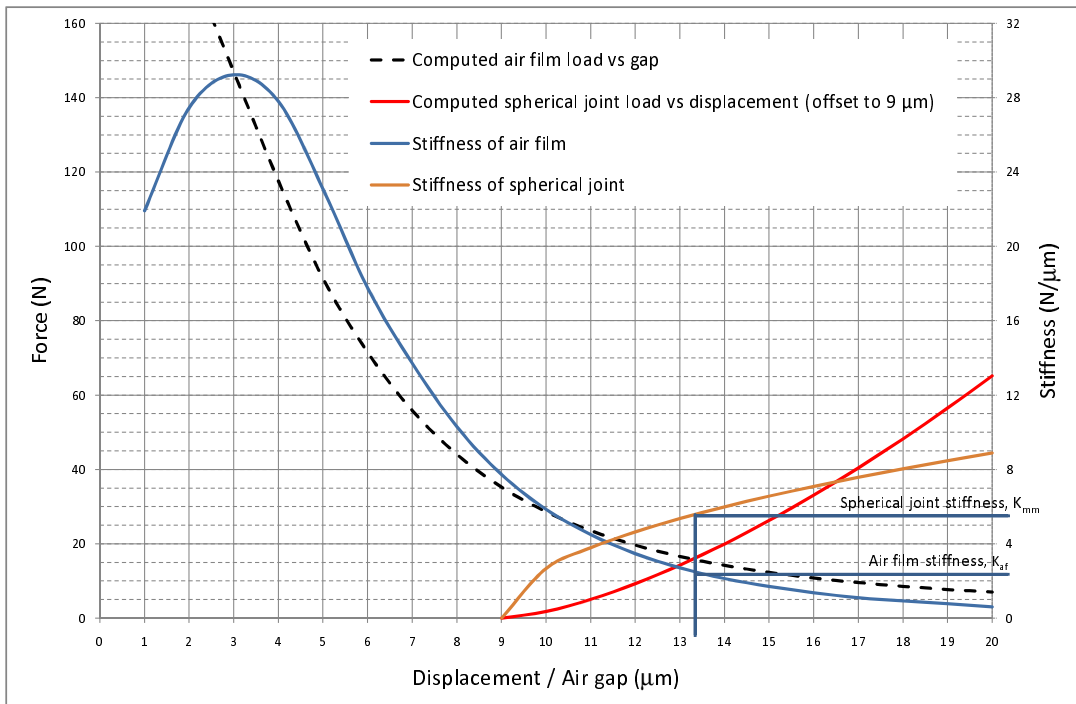
Figure 7.11: FE Model of a single air bearing pad

As discussed in Section 7.2.4, adjustment of the mounting mechanism's threaded stud for each air bearing creates a displacement in the spherical joint and a 'true' air gap height. The air gap height can be estimated by the above stiffness models, K_{af} and

Chapter 7. Dynamic Analysis of an Aerostatic Guideway System



(a) Actual air gap and joint displacement estimation for 5 μm stud setting



(b) Actual air gap and joint displacement estimation for 9 μm stud setting

Figure 7.12: Actual air gap and joint displacement estimation

7.3 Analytical Dynamic Modelling and Results

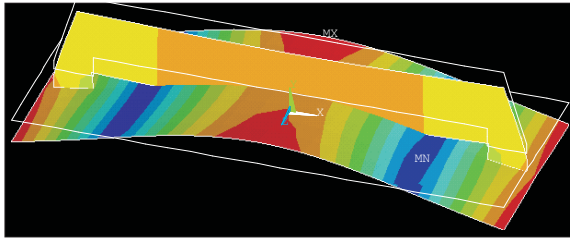
K_{mm} , and the resultant displacement measured at the top of the stud. Figure 7.12 (which are similar to Figure 7.8) shows the graphical estimation of the air gap / displacement and the corresponding air film and spherical joint stiffness for 5 and 9 μm threaded stud settings (Setup 1 and 2, respectively). The air gap and joint displacement obtained from the graphs were used as the initial displacement condition for the non-linear springs in FEA, which can also be understood as an initial compressive condition for both the interfaces. The constant stiffness value obtained from the graph is not applicable to the FE modelling. The FE solver will compute the stiffness value of the interface elements based on the initial condition of the non-linear spring element input (see Appendix C.1). However, the constant stiffness values are useful for the calculation of the undamped modal frequencies, which will be discussed later.

7.3.3 Isolated Dynamics of the Air Bearing Carriage

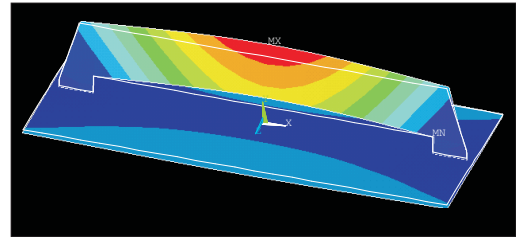
To gain better insight of the overall aerostatic guideway system, it is worthwhile to isolate the air bearings (carriage) dynamics from the structural dynamics. Hence, the analysis can be broken down into the modelling of the air bearing carriage and the structure (which comprises only the base plate and guideway bar). It is simpler and more efficient to analyse structural dynamics using FEA, as most structures are considered to exhibit linear characteristics, and in most cases give better correlation to the real system. As structural dynamics are not the main interest in this investigation, a brief assessment of its modal characteristics was carried out. A FE model of the structure, comprising only of the base plate and guideway bar was constructed. To increase the efficiency of the FE computation in the modal analysis of this structure (and later in the air bearing carriage), the structure elements have been simplified as *SHELL* element, and represented as *SHELL93* element in *ANSYS* (see Appendix C.2). The mode shapes and its modal frequencies results of the structure are presented Figure 7.13. Note the mode names used in the figure (i.e. Mode SB for structure bending, SL for structure lateral and ST for structure twisting), which will be referred to later in the discussion.

The FE model of the air bearing carriage is also constructed in a similar way using the

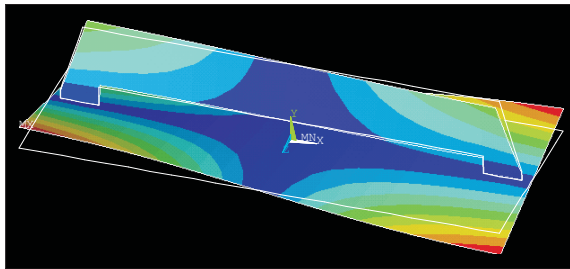
Chapter 7. Dynamic Analysis of an Aerostatic Guideway System



Mode SB - Bending of base plate at 333 Hz



Mode SL - Lateral/Y translation of guideway at 347 Hz



Mode ST - Twisting of base plate at 429 Hz

Figure 7.13: FE computed structural mode shapes

SHELL93 element as the enclosure structure for the 10 air bearing installation. The difference of the air bearing carriage analysis from the above structural one is the addition of the air bearing FE models (as shown in Figure 7.11). Ten of these air bearing FE models were modelled as attached to the respective air bearing locations as illustrated in Figure 7.9. The initial condition or displacement of these air bearing FE models are obtained using the air gap and displacement estimation method discussed above. To confine the modal analysis of the carriage to only the effect of the air bearing dynamics, the set of 40 air film non-linear springs are attached to 2 DOFs-constrained nodes in space (the other unconstrained DOF of the node is along X axis where the carriage slides freely), instead of the guideway bar. The primary interest here is the 5 rigid body modes exhibited by the carriage, as a result of the above boundary conditions. Theoretically, the other 1 DOF rigid body mode of the carriage will have a frequency of 0 Hz [40], thus having no significance in this analysis. Figure 7.14 shows the 5 mode shapes of the carriage, namely: CR, CP, CY, CV and CL for carriage roll, pitch, yaw, vertical translation and lateral translation, respectively, obtained using the above FE model. The corresponding frequencies for these mode shapes are shown later in

7.3 Analytical Dynamic Modelling and Results

Tables 7.1 and 7.2.

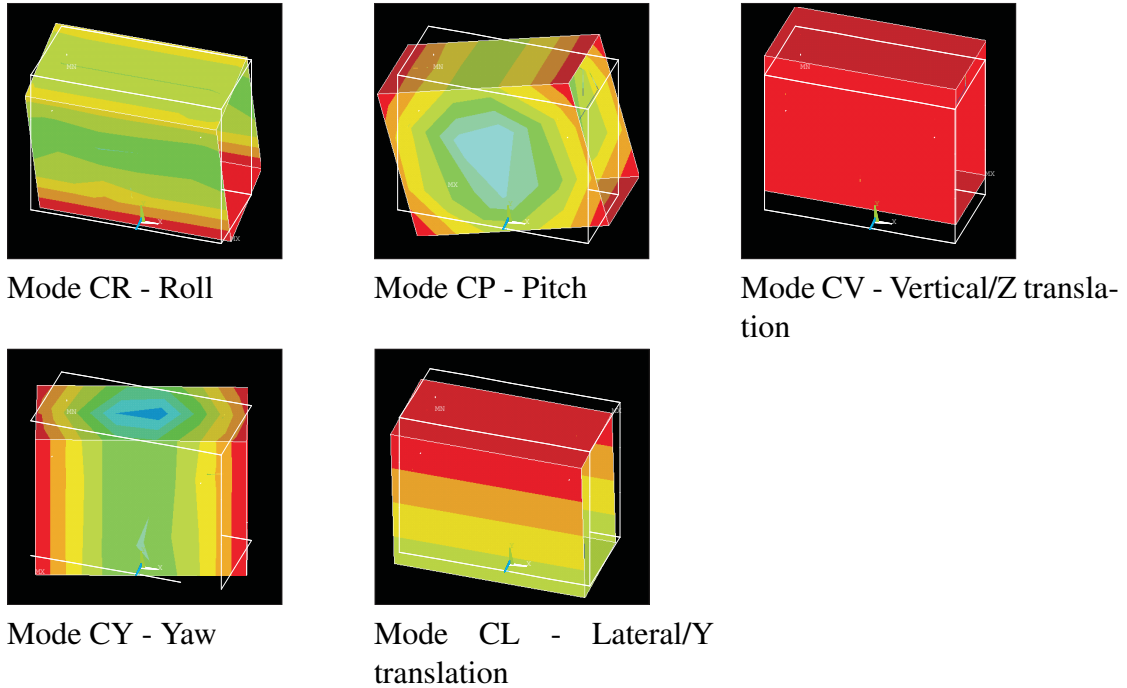


Figure 7.14: Expected isolated carriage mode shapes

Besides obtaining the modal parameters of the carriage using FEA, the undamped natural frequencies of the 5 rigid body modes can also be calculated based on the fundamental of an undamped MDOF system, as presented in Chapter 4. The calculation enables a better understanding of the system modal behaviour. In addition, it acts as a verification of the FEA results before validating it with experimental results. A few assumptions need to be established in order to scale the problem down to a manageable solution. The following are the assumptions.

1. The carriage is assumed to be a rigid and homogeneous lump mass of 2.88 kg.
2. Each air bearing is a point contact, thus the carriage is constrained by 10 springs.
3. The 10 springs are linear with equal and constant stiffness of K_e .
4. The four springs normal to the X-Y plane and the six springs normal to the Z-X plane do not have any interaction (refer to Figure 7.9). Hence, the DOFs of the

Chapter 7. Dynamic Analysis of an Aerostatic Guideway System

carriage can be decoupled into two planes as illustrated in Figure 7.15, and be dealt with separately.

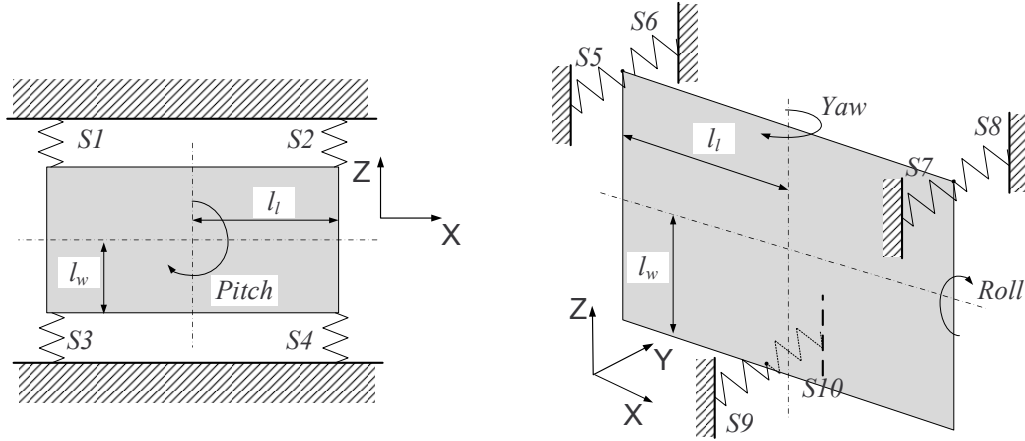


Figure 7.15: Simplified model of air bearing carriage into two decoupled planes

As mentioned, all the springs have a constant effective stiffness, K_e . K_e is a serially combined spring stiffness of the instantaneous K_{af} and K_{mm} obtained using the graphical method shown in Figure 7.12 for the 5 and 9 μm stud setting. Thus, the effective stiffness, K_e for each spring is simply:

$$K_e = \frac{1}{K_{af}^{-1} + K_{mm}^{-1}} \quad (7.6)$$

An undamped MDOF system like the one shown in Figure 7.15 can be described by the equations of motion, in matrix form as

$$[M]\{\ddot{x}(t)\} + [K]\{x(t)\} = \{f(t)\} \quad (7.7)$$

Since it is assumed that there is no coupling between the 5 DOFs, the mass matrix, $[M]$ and stiffness matrix, $[K]$ are both square diagonal matrices in the following DOF sequence: Y, Z, roll, pitch and yaw. Hence, the mass matrix, M can be expressed as:

$$[M] = \text{diag}(m_c, m_c, I_{xx}, I_{yy}, I_{zz}) \quad (7.8)$$

where m_c is the mass of the carriage, and I_{xx} , I_{yy} , and I_{zz} are the moment of inertia

7.3 Analytical Dynamic Modelling and Results

about the X, Y and Z axes, respectively. The stiffness matrix, $[K]$ takes the form of

$$[K] = \text{diag}(6K_e, 4K_e, 6K_e l_w^2, 4K_e l_l^2, 4K_e l_l^2) \quad (7.9)$$

where l_w and l_l are the perpendicular distances of the springs to the centre of the carriage, about where it rotates, as illustrated in Figure 7.15. Note that the translational stiffness when multiply by the square of the perpendicular distance to the rotational axis gives the rotational stiffness. As mentioned in Section 4.1.2.1, the equation of motion (7.7) can be rewritten as Equation (4.16). Equation (4.16) is assumed a homogeneous system and its solution is considered *non-trivial*. Based on linear algebra, a non-trivial solution exists if and only if its determinant is zero, whereby

$$\det|[K] - \omega^2[M]| = 0 \quad (7.10)$$

Substituting Equations (7.8) and (7.9) into Equation (7.10), produces the following 5 eigenvalues, or the square of natural frequencies, $\bar{\omega}_r$, which can be also be expressed as a 5×5 diagonal matrix.

$$[\bar{\omega}_r^2] = \text{diag} \left(\frac{6K_e}{m_c}, \frac{4K_e}{m_c}, \frac{6K_e l_w^2}{I_{xx}}, \frac{4K_e l_l^2}{I_{yy}}, \frac{4K_e l_l^2}{I_{zz}} \right) \quad (7.11)$$

Note that frequency in Hz is $\omega/2\pi$.

The air bearing carriage has the following mass properties.

$$m_c = 2.88 \text{ kg}$$

$$I_{xx} = 0.0117763 \text{ kgm}^2$$

$$I_{yy} = 0.0151621 \text{ kgm}^2$$

$$I_{zz} = 0.0104617 \text{ kgm}^2$$

As mentioned above, two setups are analysed here, 5 and 9 μm threaded stud setting. For Setup 1 with 5 μm stud setting and based on the graphical estimation in Figure 7.12(a), each air bearing has stiffness properties of

$$K_{af} = 4.9 \text{ N}/\mu\text{m}$$

$$K_{mm} = 6.5 \text{ N}/\mu\text{m}$$

Chapter 7. Dynamic Analysis of an Aerostatic Guideway System

which results in an effective stiffness, $K_e = 2.8 \text{ N}/\mu\text{m}$. Table 7.1 shows the modal frequencies results obtained using Equation (7.11) against the FEA results for the 5 μm stud setting.

Mode Shapes	Calculated frequencies	FEA computed frequencies
Mode CR	198 Hz	200 Hz
Mode CP	270 Hz	298 Hz
Mode CV	314 Hz	316 Hz
Mode CY	325 Hz	349 Hz
Mode CL	384 Hz	395 Hz

Table 7.1: Manually calculated and FEA computed modal frequencies results of the isolated air bearing carriage for 5 μm setting

For Setup 2 with 9 μm stud setting and based on the graphical estimation in Figure 7.12(b), each air bearing has stiffness properties of

$$K_{af} = 2.5 \text{ N}/\mu\text{m}$$

$$K_{mm} = 5.5 \text{ N}/\mu\text{m}$$

which results in an effective stiffness, $K_e = 1.7 \text{ N}/\mu\text{m}$. Table 7.2 shows the modal frequencies results obtained using Equation (7.11) against the FEA results for the 9 μm stud setting.

Mode Shapes	Calculated frequencies	FEA computed frequencies
Mode CR	154 Hz	155 Hz
Mode CP	211 Hz	234 Hz
Mode CV	245 Hz	246 Hz
Mode CY	254 Hz	273 Hz
Mode CL	299 Hz	308 Hz

Table 7.2: Manually calculated and FEA computed modal frequencies results of the isolated air bearing carriage for 9 μm setting

The above results demonstrate the close match between the manually calculated and the FEA computed modal frequencies. Minor discrepancies are observed in the pitch and yaw modes of the carriage. This is considered to be due to assumption (2). The manually calculated scheme assumes that each bearing is a single spring or contact point. This implies that the dynamics contributed by the tilting modes of individual air

7.3 Analytical Dynamic Modelling and Results

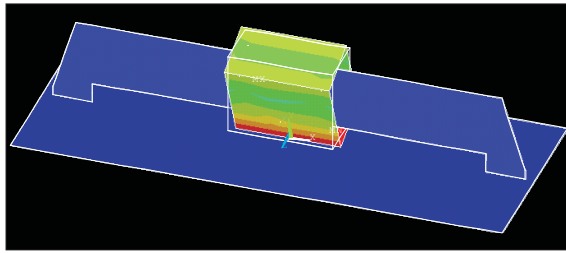
bearings are neglected. As seen in Section 6.3, Mode 1 (tilting of the centre mass) exhibit more compliance in the air film than Mode 2 (vertical translation of centre mass). The FEA models the air film as a set of non-linear springs across the area of the air bearing pad, thus enable the computation of the tilting dynamics of an individual air bearing. This results in slightly higher modal frequencies computed by the FEA than the calculated values in the pitch and yaw mode shapes. This is particularly apparent in yaw mode, which the calculation scheme totally ignore the air bearings or springs S9 and S10 illustrated in Figure 7.15. However, the discrepancies are considered to be minor, as the overall shows very closely agreed results. In general, the FEA achieves a more realistic results, as it accounts for all the bearings characteristics (without neglecting any) when computing the entire system dynamics, as discussed above. The next subsection presents the FEA modal results of the entire aerostatic guideway. The FE model of the aerostatic guideway is constructed with the air bearing carriage attached to the guideway bar structure via the air film non-linear springs.

7.3.4 Analytical Modal Results of the Overall Aerostatic Guideway

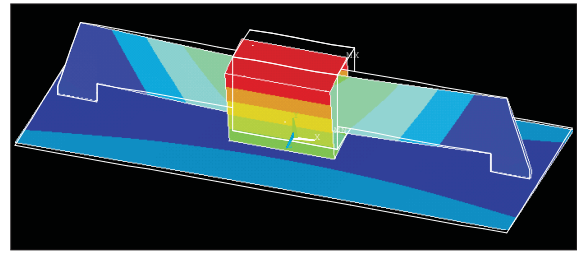
To be more realistic, the FE model should comprise of the air bearing carriage attached to the guideway structure. To compute the system dynamics, the set of 10 non-linear springs that represent the air film of the air bearing are now linked to the structural elements of the guideway bar. Modal analysis using FEA was performed on the reconstructed FE model of the ‘entire’ aerostatic guideway. As in the previous analysis, the FEA used two setups: 5 and 9 μm threaded stud setting. Figures 7.16 and 7.17 show the FEA results for the 5 μm and 9 μm stud settings, respectively.

Note that only the first 7 modes are selected for the discussion here, as the higher harmonics (beyond Mode 7) are mainly structural dynamic in nature, which are not the interest of this analysis. For Setup 1 (in Figure 7.16), it can be observed that Modes 1, 4 and 5 correlate very closely with Modes CR, CP and CY, respectively, in the isolated analysis of the carriage (refer to Table 7.1), in terms of their mode shapes and modal frequencies. This computed results imply that the above three modes have minimum coupling or interaction between the air bearing interfaces and the structure. On the

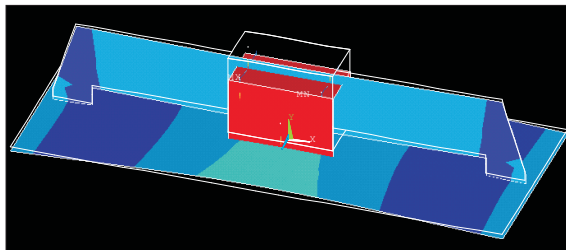
Chapter 7. Dynamic Analysis of an Aerostatic Guideway System



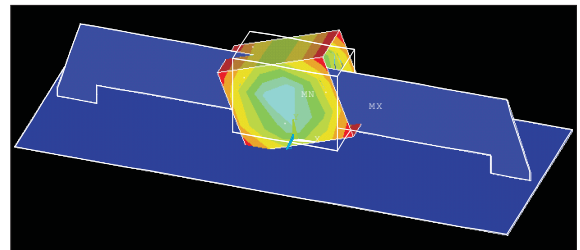
Mode 1 at 194 Hz



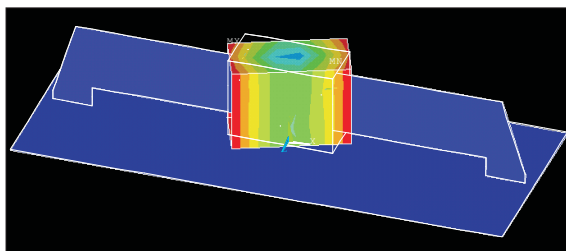
Mode 2 at 261 Hz



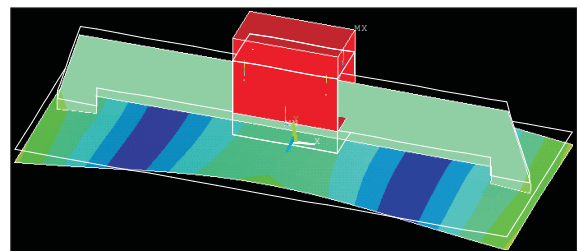
Mode 3 at 281 Hz



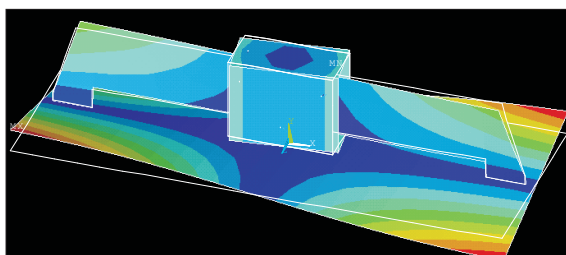
Mode 4 at 297 Hz



Mode 5 at 343 Hz



Mode 6 at 369 Hz

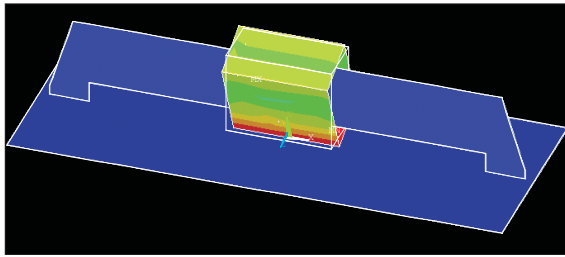


Mode 7 at 430 Hz

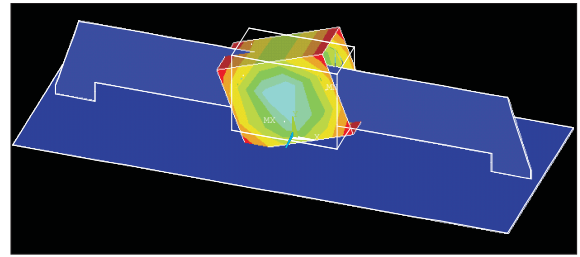
Figure 7.16: FEA results of overall aerostatic guideway for Setup 1: 5 μm stud setting

other hand, the other modes (2, 3, 6 and 7) exhibit various levels of interaction between the air bearing interfaces and the structure. These are known as coupled DOFs or coordinates in modal analysis of coupled structure [40]. It can be observed that Mode 2 is a combination of Mode SL and CL of the isolated structure and air bearing

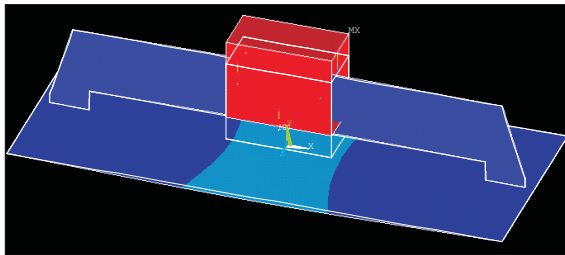
7.3 Analytical Dynamic Modelling and Results



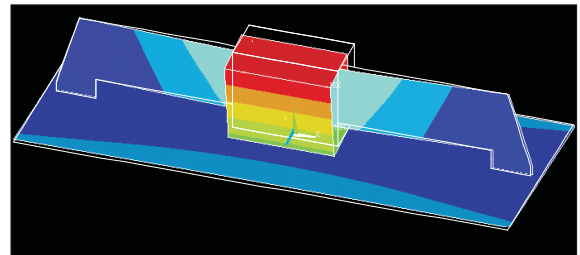
Mode 1 at 153 Hz



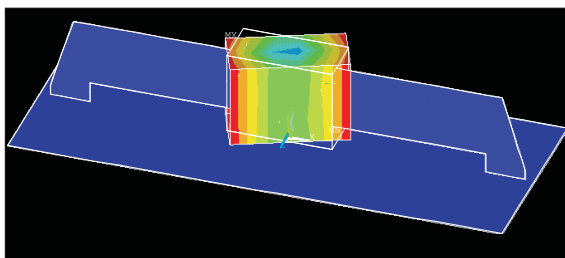
Mode 2 at 234 Hz



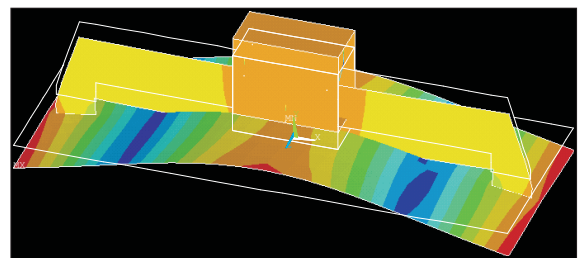
Mode 3 at 237 Hz



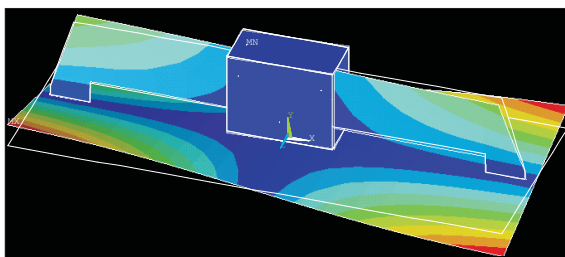
Mode 4 at 242 Hz



Mode 5 at 271 Hz



Mode 6 at 347 Hz



Mode 7 at 429 Hz

Figure 7.17: FEA results of overall aerostatic guideway for Setup 2: 9 μm stud setting

carriage. Both the base plate bending mode (Mode SB) and the vertical oscillation of carriage (Mode CV) are excited in Modes 3 and 6, with varying degree of dynamics contribution from the structure and the air bearing interfaces. Although Mode 7 exhibits mostly structural twisting of the base plate, a slight yaw rotation can be ob-

Chapter 7. Dynamic Analysis of an Aerostatic Guideway System

served in the carriage. A general observation is that the coupled DOFs modes occur when the natural frequencies of the two isolated systems are near to each other and they share the same DOFs of mode shapes.

For Setup 2 (in Figure 7.17), similar modal behaviour to Setup 1 can be seen. A notable difference observed is the marginally less interaction between the structure and the air bearing carriage, in particular, Modes 3, 6 and 7 of Setup 2. This is mainly due to the less stiff air bearing interface at $9\ \mu\text{m}$ stud setting. The proximity of the natural frequencies between the isolated air bearing carriage and structure are relatively larger than the previous case in Setup 1, hence coupled DOFs modes are less prominent in this case.

The above isolated and combined analytical modelling of the aerostatic guideway give a comprehensive understanding of the dynamic behaviour of the guideway in terms of its structure and interface interactions. This modelling scheme allows machine designers to identify and quantify the weaknesses in the stiffness chain of a machine before fabrication/building. The next section shall validate the robustness of the modelling scheme discussed in this section against experimental modal testing results.

7.3.5 Uncertainties in Analytical Modal Results of the Guideway

The modal behaviour can be computed using FEA with the estimated air bearing parameters which are assumed to be accurately acquired. Realistically, uncertainties exist in these parameters, thus the computed results. The parameters used in the FEA possess potential errors. The following section discuss a summarised error estimation from the error sources mentioned in Section 7.2 and 6.3.3.

Geometrical error in air gap height It is seen that the accuracy of the air gap height is crucial in predicting the air film stiffness, thus its dynamic behaviour. The main error sources that contribute to the accuracy of the air gap height has been discussed in Section 7.2. These errors include the flatness of the air bearing porous and guideway surfaces, the parallelism between the bearing porous surface and the guideway surface,

7.3 Analytical Dynamic Modelling and Results

and the accuracy of the LVDT displacement probe used to measure the displacement of the stud. The error values are summarised in Table 7.3. Note that it is assumed that the spherical joints enable perfect parallelism between the bearing porous surfaces and the guideway surface, as mentioned in the beginning of this section, thus the parallelism error is considered to be near $0 \mu\text{m}$. The total potential error in the air gap height is $3.2\mu\text{m}$.

Potential error sources	Error
Maximum flatness of each porous surface	$1.7 \mu\text{m}$
Maximum flatness of guide surface over a $50 \times 50 \text{ mm}$ area	$0.5 \mu\text{m}$
Maximum parallelism	$\sim 0 \mu\text{m}$
LVDT displacement probe accuracy	$1 \mu\text{m}$
Total potential geometrical error for each air bearing	$3.2 \mu\text{m}$

Table 7.3: Potential geometrical error for each air bearing

Other modelling parameters There are other parameters that may also affect the accuracy of the FE model. The major errors include the mass of the accelerometers that are not considered in the analytical model and the accuracy of the air supply pressure. 4 triaxial accelerometers are used for the experimental modal testing. The triaxial accelerometers used are the same as those used for the dedicated test rig modal testing (in Chapter 6), which weigh 11.2 g each. The air supply pressure regulator¹ has an accuracy of $\pm 0.5 \%$. The uncertainty in the air supply pressure accuracy is considered to be negligible.

Another FE model of the aerostatic guideway is constructed using the above potential maximum errors, and the modal parameters are computed using FEA. Tables 7.4 and 7.5 show the comparison of the modal results between a ‘perfect’ FE model and one which account for the maximum potential errors for Setup 1 and 2, respectively. Based on Type “B” uncertainty evaluation [125], the standard uncertainties for each of the modes are presented in the tables as well.

¹CKD R1000 pneumatic pressure regulator

Chapter 7. Dynamic Analysis of an Aerostatic Guideway System

Mode Shape	Modal frequency with perfect measurement	Modal frequency with error	Maximum error	Standard uncertainty
Mode 1	194 Hz	170 Hz	24 Hz	6.9 Hz
Mode 2	261 Hz	251 Hz	10 Hz	2.9 Hz
Mode 3	281 Hz	255 Hz	26 Hz	7.5 Hz
Mode 4	297 Hz	256 Hz	41 Hz	11.8 Hz
Mode 5	343 Hz	300 Hz	43 Hz	12.4 Hz
Mode 6	369 Hz	353 Hz	16 Hz	4.6 Hz
Mode 7	430 Hz	428 Hz	2 Hz	0.6 Hz

Table 7.4: Analytical modal results uncertainties for Setup 1: 5 μm stud setting

Mode Shape	Modal frequency with perfect measurement	Modal frequency with error	Maximum error	Standard uncertainty
Mode 1	153 Hz	126 Hz	27 Hz	7.8 Hz
Mode 2	234 Hz	190 Hz	44 Hz	12.7 Hz
Mode 3	237 Hz	198 Hz	39 Hz	11.3 Hz
Mode 4	242 Hz	219 Hz	23 Hz	6.6 Hz
Mode 5	271 Hz	223 Hz	48 Hz	13.8 Hz
Mode 6	347 Hz	339 Hz	8 Hz	2.3 Hz
Mode 7	429 Hz	427 Hz	2 Hz	0.6 Hz

Table 7.5: Analytical modal results uncertainties for Setup 2: 9 μm stud setting

It can be seen that the standard uncertainty values are inevitably smaller for those modes that are mainly dominated by the structural dynamics, whereby the above discussed potential errors have less significance in their dynamic properties. On the other hand, those modes that exhibit isolated carriage mode shapes, influenced mainly by the air bearings (see Figure 7.16 and 7.17) experience higher uncertainties.

7.4 Validation using Experimental Modal Testing Results

7.4.1 Experimental Modal Testing Setup for the Aerostatic Guideway

This subsection will provide a brief overview of the modal test carried out on the overall aerostatic guideway. Previous chapters have sufficient discussion on the modal testing equipment and procedure, thus the general information of modal testing will no

7.4 Validation using Experimental Modal Testing Results

be reiterated here. The section shall focus on discussion directly related to the test on the guideway system.

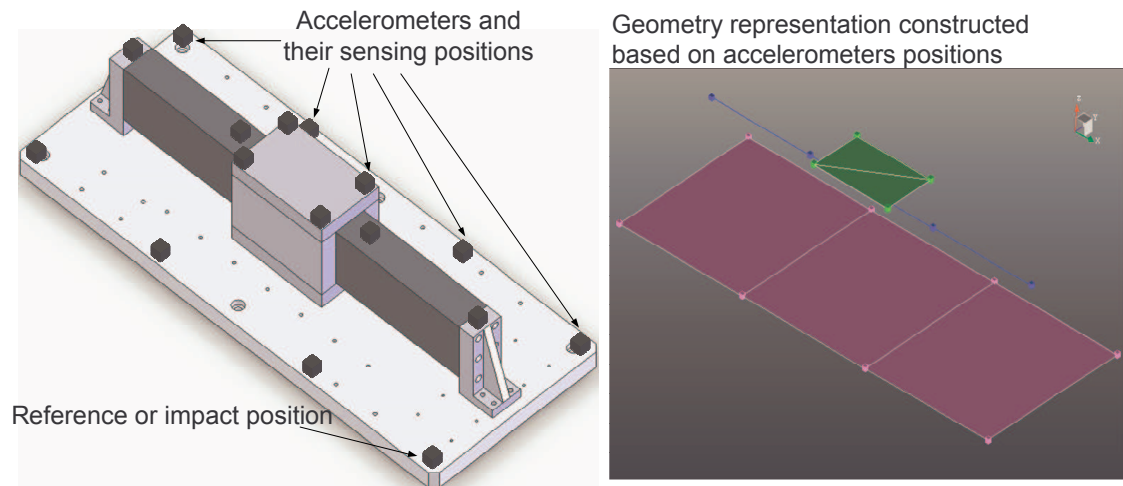


Figure 7.18: Accelerometers positions

Sixteen response or accelerometer positions are selected on the entire aerostatic carriage. These response positions are considered to give sufficient modal information of the system to visualise the mode shapes that are of interest in this analysis. Figure 7.18 shows the sixteen positions of the responses to be measured. The left diagrams shows the 3D CAD model of the aerostatic guideway and the right shows the geometrical representation in the modal testing software, constructed using the identified accelerometers positions. As mentioned in previous chapters, since there are only four triaxial accelerometers available, the modal test employs the roving transducers method. Four sets of roving accelerometers readings are obtained in this experiment, i.e. $(16 \text{ response positions}) / (4 \text{ accelerometers})$. The reference or impact location is also shown in Figure 7.18. Three directions (in X, Y and Z axis) of excitation force are applied on the impact position. Each triaxial accelerometer acquires the same three axes of response data.

Mode Shapes	Analytical modal frequencies	Experimental modal frequencies & damping	Percentage agreement
Mode SB	333 Hz	294 Hz, 0.18 %	88 %
Mode SL	347 Hz	324 Hz, 0.15 %	93 %
Mode ST	429 Hz	425 Hz, 0.07 %	99 %

Table 7.6: Comparison of analytical and experimental modal results of the structure

7.4.2 Experimental Results and Validation of the Guideway Structure

It is useful at this stage to first assess the structural modal results (shown in Figure 7.13) before discussing the overall guideway system. In order to validate the structural modal results computed by FEA, the modal test is carried out with the air bearing carriage removed. In this case only twelve response positions are required for this test, instead of sixteen, i.e. the four response positions on top of the carriage are apparently not included. Table 7.6 compares the analytical modal results of the structure obtained by the FEA against the experimental modal testing results. It is unsurprising that the analytical and experimental results are closely correlated. As mentioned in previous chapters, FEA and element models for structural static and dynamic prediction is relatively established and accurate. Slightly lower natural frequencies are computed by the FEA as compared to the experimental results. This is mainly due to the assumption of perfectly rigid joints in modelling the bolted joints of the actual structure assembly.

7.4.3 Experimental Results and Validation of the Overall Guideway

The experimental modal tests are carried out using the same two setups as the analytical modelling, i.e. 5 and 9 μm stud settings. The 10 air bearings were all adjusted to the desired threaded stud setting using the procedure described in Appendix B. The setting of these stud/air bearing heights have an average uncertainty of approximately $\pm 1 \mu\text{m}$. In this modal testing experiment, all the sixteen accelerometer positions are used, thus acquiring a total of 144 FRFs (16 responses \times 3 DOFs \times 3 reference DOFs). Tables 7.7 and 7.8 show the comparison between the analytical modal results and the experimental results obtained in these experiments for the 5 and 9 μm stud settings, respectively.

7.4 Validation using Experimental Modal Testing Results

Mode Shapes	Analytical modal frequencies	Experimental modal frequencies & damping	Percentage agreement	Remarks & similar isolated modes
Mode 1	193 Hz	207 Hz, 1.03 %	93 %	CR @ 200 Hz
Mode 2	261 Hz	254 Hz, 0.16 %	97 %	Coupled DOFs
Mode 3	281 Hz	263 Hz, 0.62 %	94 %	Coupled DOFs
Mode 4	297 Hz	312 Hz, 3.40 %	95 %	CP @ 298 Hz
Mode 5	343 Hz	391 Hz, 3.27 %	86 %	CY @ 349 Hz
Mode 6	369 Hz	-	-	SB @ 333 Hz
Mode 7	430 Hz	429 Hz, 0.53 %	99 %	ST @ 429 Hz

Table 7.7: Comparison of analytical and experimental modal results of the overall guideway system for Setup 1: 5 μm threaded stud setting

Mode Shapes	Analytical modal frequencies	Experimental modal frequencies & damping	Percentage agreement	Remarks & similar isolated modes
Mode 1	153 Hz	137 Hz, 2.93 %	90 %	CR @ 155 Hz
Mode 2	234 Hz	180 Hz, 5.36 %	77 %	CP @ 234 Hz
Mode 3	236 Hz	222 Hz, 1.56 %	94 %	CV @ 246 Hz
Mode 4	242 Hz	244 Hz, 0.46 %	99 %	Coupled DOFs
Mode 5	271 Hz	305 Hz, 3.99 %	87 %	CY @ 273 Hz
Mode 6	347 Hz	319 Hz, 1.17 %	92 %	SB @ 333 Hz (Coupled DOFs)
Mode 7	429 Hz	425 Hz, 0.10 %	99 %	ST @ 429 Hz

Table 7.8: Comparison of analytical and experimental modal results of the overall guideway system for Setup 2: 9 μm threaded stud setting

Besides showing the analytical and experimental comparisons in Tables 7.7 and 7.8, the last column of the tables also provide some remarks pertaining to the similarity of modes to the isolated structure and carriage analysed in the previous section. Damping ratios for the individual modes obtained through the modal testing are also shown in the experimental results. From the large number of FRFs obtained from the modal testing, Figure 7.19 presents three of the more relevant FRFs of Setup 2: one Z and one Y axis FRFs from a corner on the carriage, and one Z axis FRF from a corner of the base plate (refer to Figure 7.18 for accelerometer positions). The vertical axis of the

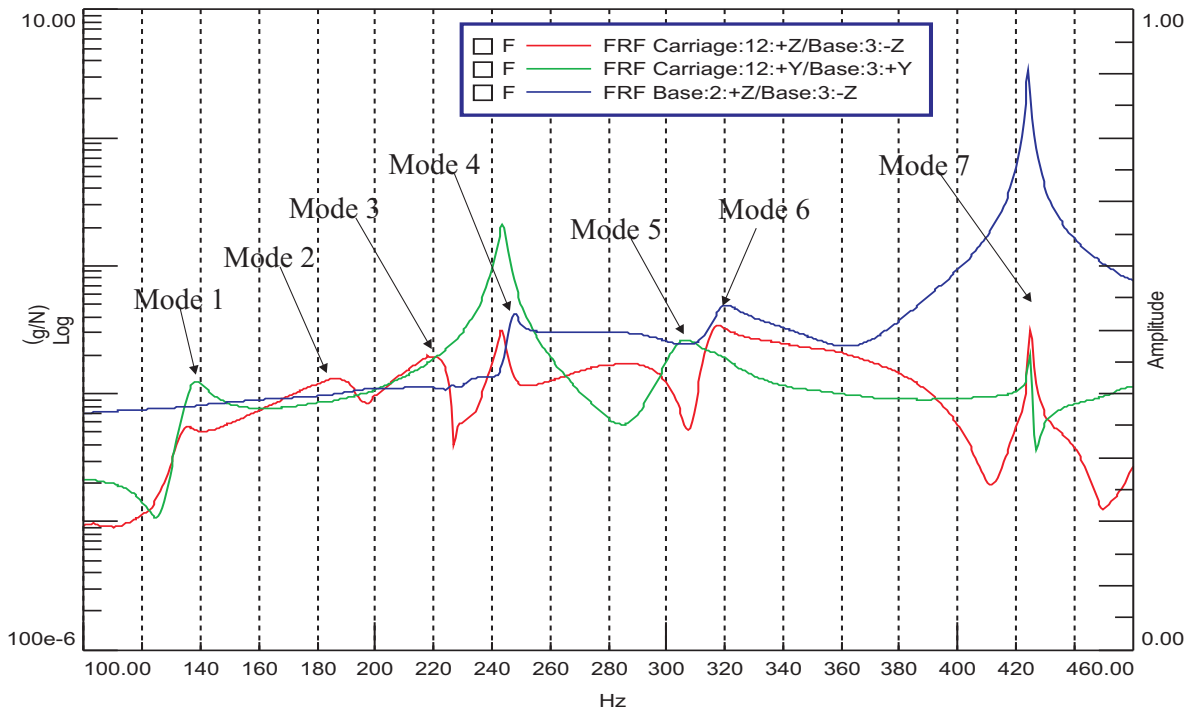


Figure 7.19: FRFs from two carriage responses in Z and Y axis, and one base plate response in Z axis

FRFs plotted here shows the Response Function in terms of acceleration response over force input. The 7 modes as presented in Table 7.8, are also indicated on the FRFs. The mode shapes screenshots of the experimental modal test are shown in Appendix E.

7.5 Discussion on Experimental Results and Validation

The aim of the experimental modal testing on the aerostatic guideway system is to validate the robustness and accuracy of the FE dynamic model for air bearings developed in this work. This section discusses the experimental results presented in the previous section, as well as the validation of the FE dynamic model. A brief assessment of the percentage agreements for both setups shows promising results in the correlation of the analytical and experimental modal characteristics. The air gap height and spherical joint displacement estimation method discussed in Section 7.2.4 enables a more accu-

7.5 Discussion on Experimental Results and Validation

rate FE model of the air bearing interfaces.

Most of the mode shapes computed by the FEA can be found in the experimental results, with one exception in Setup 1. The dynamics exhibited by Mode 6 of Setup 1 does not exist in the actual aerostatic guideway. The coupled DOFs effects in some of the guideway dynamics observed in the analytical results also occur in the experimental results. It is not easy to quantify the dynamic interaction between the structure and the air bearing interfaces (or the carriage). However, using the natural frequencies found in the isolated system, one can have a good indication on the dynamic coupling effect between the structure and the air bearings. For instance in Setup 1, Modes 1, 4 and 5 of the experimental results possess comparable modal frequencies as those computed for Modes CR, CP and CY of the analytically isolated carriage.

The damping of machine interfaces and joints are known to be relatively higher as compared to structural damping [29]. The squeeze film damping ratio of a air film can be as high as 20 % (of the critically damping value) depending on the air gap and air pressure [63, 66, 129]. Thus, a check on the modal damping ratio suggests whether a mode shape has more contribution from the machine interfaces (i.e. the air bearings) or the structure. Modes with damping ratio less than 1 % are mostly dominated by structural dynamics, as observed in Modes 2, 3 and 7 of Setup 1, and Modes 4 and 7 of Setup 2.

In general, the FE model developed in this work is able to predict the dynamic behaviour of the air bearing interfaces, in terms of mode shapes and modal frequencies, within 77 % accuracy, and an average accuracy of above 85 %. These results are considered to be significantly promising taking into account the various uncertainties in the experimental setup, as discussed in Section 7.2.

The dynamic prediction of the dedicated air bearing test rig presented in the previous chapter appears to be less accurate than those achieved in the analysis of a more complicated aerostatic guideway. This results seem to be counterintuitive. However, this outcome can be comprehended by a few factors.

Chapter 7. Dynamic Analysis of an Aerostatic Guideway System

Parallelism The issue of parallelism between the air bearing porous surface and the guideway surface has been substantially reduced with the self-aligning capability of the air bearing mount mechanism's spherical joint. As mentioned in the beginning of this modelling discussion, the parallelism error of the air bearing within the guideway setup is assumed to be negligible. On the other hand, the dedicated test rig is subjected to a known parallelism error of approximately 2 to 3 μm . In the dedicated test rig, it is an important feature to rigidly mount the air bearing to the structure to eliminate undesirable effects from other interfaces compliance (like the mounting mechanism as discussed). Nevertheless, this consideration creates an inevitable geometrical error in the dedicated test rig.

Constraint of air bearing tilt mode There are two major modes of the centre mass under the influence of the opposing air bearings: the tilt and vertical oscillation. From the analysis of the aerostatic guideway, it is observed that the individual air bearing tilt mode is essentially absent. All the five mode shapes of the carriage (which include the rotational types) are mainly dominated by linear displacement of the air bearing compliances. Using a simple schematic representation of one of the carriage rotational mode, Figure 7.20 illustrates this argument. Due to the layout as well as the mounting mechanism of the air bearings within the guideway carriage, the tilting mode of individual air bearings are constrained. From Chapter 6, the analytical results of the vertical translation modal behaviour correlate better with the experimental results, as compared to the tilting mode. It is also found that the analytical prediction accuracy of the tilting mode properties of the air bearing is highly dependent on the parallelism error between the air bearing porous surface and the guide surface (in the case of the dedicated test rig, the centre mass surface). Thus, with minimised parallelism errors as mentioned above and constrained air bearing tilt mode, the entire dynamic behaviour of the carriage encompasses mainly the linear translation of individual air bearing setup. Consequently, this condition increases the accuracy of the FEA prediction by reducing the sensitivity of the model caused by a difficult to model modal characteristic. This can also be appreciated from the analytical model of the isolated carriage illustrated in Figure 7.15, and further verified by the correlation between the dynamic characteristics of the isolated carriage and the entire guideway.

7.5 Discussion on Experimental Results and Validation

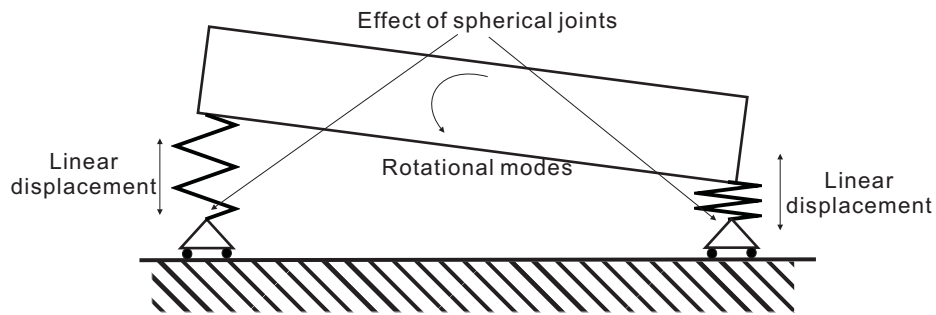


Figure 7.20: Schematic representation of a rotational mode of the guideway carriage

Averaging effect The dedicated test rig has two rigidly mounted opposing air bearings. The two (top and bottom) air gaps of the test rig were subjected to the inherent potential errors due to fabrication and assembly, thus leading to the achievable accuracy of the analytical modal results. The carriage of the aerostatic guideway is held by a configuration of 10 air bearings. Despite the fact that the aerostatic guideway is subjected to similar errors, the higher number of air bearings reduces the significance of individual errors based on averaging effect among the bearings.

Chapter 8

Overall Discussion

8.1 Breaking Down the Problem

The concept of a stiffness chain is essential in the decomposition of a complex machine interface problem. A stiffness chain is commonly used in evaluating the errors of end mills which are held by the tool holder and spindle [105, 106]. The work here extends the application of this concept in the evaluation of machine interfaces, in particular, aerostatic bearings/guideways, as shown in Figures 5.7 and 5.8.

In this research, some form of initial hypothesis was needed to identify the key interfaces within the stiffness chains that are significant to the dynamics of an aerostatic guideway. The structure and mechanical contact interfaces (discussed in Section 2.3), which possess relatively high stiffnesses are not considered to be of interest here. The key interfaces within the aerostatic bearing are identified, namely the air film, the spherical joint and the threaded stud to set the air gap. The static stiffness of each of these interfaces were computed using their respective stiffness models (as discussed in Sections 5.2.2.4, 7.2.1.1 and 7.2.1.2). The computed stiffnesses were validated with experiments, except for the threaded joint, which was assumed to have relatively high stiffness under proper preloading. The model and assumption prove to be valid as the dynamic modelling of the aerostatic guideway achieved good correlation with experimental results.

8.2 Dedicated Air Film Dynamic Analysis

This work demonstrated a systematic and comprehensive methodology that breaks down a complex aerostatic guideway into key interface elements, and identifies their parameters which contribute to the system dynamic behaviour. The practice of this machine dynamic modelling approach in the precision engineering industry will enhance the design process and address some of the issues discussed in Section 3.2.1. However, this may require further work in this area in order to increase the adoption of this approach in the industry, i.e. automation of this design approach through software module.

8.2 Dedicated Air Film Dynamic Analysis

The breaking down of the various stiffness elements within the aerostatic guideway leads to a dedicated and in-depth investigation of the air film dynamic effects. Most of the earlier work in air bearing analysis has focused on the static characteristics of the air film [49, 59, 61–66]. Some recent modal analysis work was carried out on aerostatic guideway system, as a whole, [79, 120], which lacks the insight into the individual air bearing dynamic behaviour.

In this research, **a dedicated air bearing test rig, which allowed in-depth and isolated analysis into the bearing dynamic characteristics was designed.** The test rig (which comprised of two rigidly mounted opposing air bearings and a centre mass suspended in between the bearings by flexure mechanisms) enabled the study of the air film dynamic effect on the centre mass in a controlled and deterministic environment, as opposed to a guideway system with various interfaces and uncertainties. Using the dedicated test rig, a comprehensive study on the dynamic characteristics of the air film, the non-linearity effect as well as the impact of the air gap geometry on the accuracy of the analytical modal parameters was carried out. Due to the non-linear stiffness of the air film, the air gap height accuracy is found to be crucial in achieving an accurate modal behaviour of the centre mass (which was held in between two air films).

Although the dedicated air film test rig provides a good platform to investigate the air film dynamics, it is important to note that the operating condition (in terms of

bearing mounting method, mass loading and thus range of natural frequencies) may not correspond to most practical situations. Hence, it was essential to validate the findings in Chapter 6 with actual aerostatic guideway system, as discussed in Chapter 7.

8.3 Minimising the Uncertainties

Due to the non-linearity of the air film stiffness and the mounting mechanism, the accuracy of the FE model which leads to the results of the dynamic behaviour is highly dependent on the accuracy of the air gap height. A substantial amount of attention was placed in achieving accurate information about the air gap parameters in this thesis. Few papers place emphasis on determining the error within an aerostatic guideway. One relevant work found in the investigation of error within aerostatic guideways is by Ekinici et al [130]. Ekinici et al gave a detail account of how the stiffness of an orifice type of aerostatic bearings guideway are modelled and validated the model experimentally. However, their work considered the stiffnesses of the air bearing setup to be constant, which differs to the findings in this thesis and many other references.

Section 6.3.3 provides an in-depth understanding of the typical errors that are expected from a porous air bearing. One of the key geometrical errors of an air bearing is the flatness of the porous surface which range from a fraction of a micrometre to approximately $1.7 \mu\text{m}$ peak-to-valley. The parallelism of the porous surface to the guideway surface which is greatly associated to the quality/smoothness of the spherical joint also contributes to the air gap height accuracy. For practical reasons, these errors are often assumed to be negligible. This may be acceptable when a number of air bearings is used within one setup or one axis of guideway, whereby the above geometrical errors are considered to be averaged out among the air bearings. However, this error averaging hypothesis is not applicable to the dedicated test rig which only comprises of a set of (two) rigidly mounted opposing air bearings, thus a comprehensive error analysis was needed. This error analysis for the dedicated test rig also examined the analytical shortcoming in terms of accounting for the accelerometers mass loading on the test rig during modal testing. **The above error analysis established in this research allowed**

8.4 Accurate FE Model for Dynamic Simulation

understanding of the various errors that impact the achievable accuracy of its analytical dynamic prediction.

8.4 Accurate FE Model for Dynamic Simulation

As mentioned, static stiffness modelling of air film is well established with several variants from the original proposed method [49, 62, 63]. Most use iterative methods to obtain the air film pressure profile, which can be used to compute the overall loading capacity of the bearing, thus its stiffness. A 1D flow formulation method [78], which can be computed numerically is employed in this research to calculate the stiffness model of the air bearing. This method was chosen for its ease and flexibility in implementation using Mathematical programs, such as *MATLAB*, and its efficiency in computation as compared to other modelling methods. The air film forms a pressure profile across the area of the air bearing porous surface, thus a variation of stiffness across the area of the air film. A single spring element, which is commonly used to model the air bearing within a guideway [79, 120] may not be adequate to describe the air film dynamic behaviour accurately in this test rig setup. Hence, a set of non-linear spring elements to form the FE model of the air film was proposed in Section 6.3.1.

When air bearings were setup in a guideway system and installed with mounting mechanisms that facilitate parallelism of the porous surface to the guideway surface, more elements of uncertainty were introduced. The common opposing air bearings layout often encloses the bearings within the carriage or some supporting structure. This often hinders the possibility for direct measurement of the air bearing lift or actual air gap created by the air supply pressure and/or through some gap presetting mounting mechanisms. Nevertheless, some of these uncertainties can be modelled and estimated. One of the main contributions in Section 7.2, is the estimation of the air gap and spherical joint displacement. Through the stiffness model and the force interactions between the air film and the spherical joint, the ‘actual’ air gap height can be estimated based on displacement measurement of the threaded stud. This is favourable to the accuracy of the air film model as the misinterpreted air gap by the stud displacement measurement can be notably different from the ‘actual’ air gap, as shown in the plot of Figure

Chapter 8. Overall Discussion

7.12. This estimation of air gap height through joint and air film stiffnesses for unaccessible air bearing mounting setup increases the robustness and accuracy of aerostatic guideway dynamic model.

To illustrate the significance of this air gap height estimation and using the case of Setup 1 of Section 7.3.2 (5 μm stud setting) as an example, Table 8.1 presents the computed stiffnesses of a single air bearing setup within the guideway using three different schemes, as described below.

1. *Scheme A*: Stiffness obtained merely from the air bearing load-lift curve and considering the stud displacement as the air gap height.
2. *Scheme B*: Stiffness calculated based on the combined compliances of the air film in series with the mounting mechanism and considering the stud displacement as the air gap height.
3. *Scheme C*: Effective stiffness, K_e computed based on the proposed air gap estimation method, as discussed in Section 7.2.4

A single air bearing stiffness based on		
Scheme A	Scheme B	Scheme C
23 N/ μm	6.9 N/ μm	2.8 N/ μm

Table 8.1: Computed air bearing stiffnesses based on three different schemes

From Table 8.1, it can be seen that the method used in obtaining the air bearing stiffness will result in a substantially different dynamic characteristic prediction of an aerostatic guideway system. If a design engineer is to take it for granted that the mounting mechanism of an air bearing setup is sufficiently rigid such that it can be ignored, and chooses to employ Scheme A to obtain the air bearing stiffness, an erroneous FE model will be constructed. The resulting dynamic characteristics of his/her aerostatic guideway design will be severely misled. As discussed in Section 3.2.1, *time-to-market* is critical to ensure the manufacturer/company stays above the competition. The ‘first time right’ mindset in precision machine development is important to warrant the company sustainability in this ever demanding knowledge-based economy. In this thesis, **the significant dynamic effect of air bearing mounting interfaces has been reviewed.**

8.4 Accurate FE Model for Dynamic Simulation

A comprehensive air bearing FE model has been developed that take into consideration the non-linearity in the air film as well as its mounting mechanism.

non-linear modal analysis remains a challenging research area. Many positive research outcome has been proposed by [41, 43, 45, 126], which are mathematically and computationally challenging. The implementation of non-linear modal analysis in an FEA environment is still a technology gap. The non-linear air film FE model proposed in Section 6.3.1 provides a more accurate representation of the air film behaviour. However, in order to fully exploit this FE model, the FEA software package should incorporate non-linear modal analysis capabilities, which is currently lacking. Although the non-linear modal parameters of this air film model can be computed using the time-domain method, either in FEA environment or numerically using *MATLAB* (as shown in Section 6.3.5), it is computationally inefficient, especially when the system becomes more complex and with more DOFs. Potentially, this becomes a motivation for further work of this research, which will be discussed in the next chapter.

Chapter 9

Conclusion and Further Work

9.1 Research Overview and Contributions

The Engineering Doctorate (EngD) programme aims to equip research engineers with rigorous research capabilities in an industrial or business context. This EngD research project identified the weaknesses in current industrial practice of precision machine design, in particular, the robustness of dynamic modelling of machine interfaces during the design phase. With this motivation, the main aim of this research was to accurately describe the non-linear dynamics of a non-contact (in this case, an aerostatic) guideway system in order to achieve a good FEA model in the design stage. The main aim was broken down into sub-objectives as follow:

1. Identification of key interfaces in the guideway system
2. Formulate a systematic identification method to obtain an accurate set of dynamic model parameters
3. Validation of design methodology that incorporates interfaces dynamics

The research has fulfilled the above objectives, which were established at the beginning of the programme. Chapter 8 gives a broad overview on how a complex aerostatic guideway is broken down into key interface elements using the concept of stiffness chain, and the methodology to identify the various interface parameters that lead to an accurate dynamic model of the guideway. The identification of the aerostatic guideway characteristics leads to in-depth studies of the air bearing's air film behaviour as well

9.1 Research Overview and Contributions

as its mounting mechanism. The findings of the air bearing dynamic characteristics were validated using the aerostatic guideway system. Good correlation between the analytical modelling and the experimental modal testing was achieved. The case study on the guideway gives further insight into the stiffness interaction between the air film and the bearing mounting mechanism.

The contributions of this research are consciously entrenched (in bold) within the discussion of Chapter 8. They can be summarised as follows:

1. Development of a systematic and comprehensive methodology that breaks down a complex aerostatic guideway into key interface elements, and identifies their parameters which contribute to the system dynamic behaviour.
2. Design of a dedicated air bearing test rig which allows in-depth and isolated analysis into the bearing dynamic characteristics.
3. Understanding of the various errors that impact the achievable accuracy of an analytical dynamic prediction through an error budget of the dedicated air bearing test rig and aerostatic guideway.
4. An estimation method for air gap height for inaccessible air bearing mounting setups which increases the robustness and accuracy of the overall aerostatic guideway dynamic model.
5. The significant dynamic effect of air bearing mounting interfaces has been reviewed. A comprehensive air bearing FE model has been developed that take into consideration the non-linearity in the air film as well as its mounting mechanism.

This research project set out to develop a solution to improve precision machine design in the industry. The thesis marks a milestone in the understanding of aerostatic guideway dynamic behaviour. However, to produce a design tool ready for industrial adoption, findings from this research required further development and close collaboration with FEA software manufacturers to increase its *Technology Readiness Level* (TRL, as discussed in Section 3.3.3). The above contributions shall lay the foundation

Chapter 9. Conclusion and Further Work

and enable a design tool for analysing complex precision systems. The next section suggests some further work to increase the TRL of this research work.

9.2 Further work

The following summarises some of the potential further work for this research.

non-linear modal analysis for FEA Not all commercial FEA software packages consider non-linearity in their modal analysis solver. Fundamental modal analysis theory assumes linearity of system. Most machine interfaces exhibit non-linearity in different extent. Although linearisation and assumption of linear behaviour within an operating region enable the the non-linear system to be predicted with certain level of accuracy, the solution is usually not generic and unified enough to easily implemented on different system. Research outcome in the field of non-linear modal analysis proposed by [41, 43, 45, 126] are mostly mathematically and computationally challenging. As the proposed methods are not yet well-established, implementation of such methods in FEA is still a research gap.

Squeeze film damping and its effect on air bearing dynamics In this research, the modelling focus has been directed to the stiffness of the air bearing interfaces. The key interest here is to achieve accurate modal parameters, i.e. mode shapes and its corresponding natural frequencies, using the modal analysis solver in FEA. It is considered that modal frequency is mainly dependent on the system stiffness property. The damping property generally influences the magnitude of the response. The thin air film produced by aerostatic bearings is known to exhibit significant squeeze film damping [70]. This damping property of the air film may reduce the significance of some of the mode shapes by lowering its vibration magnitude. Hence, the next step to acquire a complete picture of air bearing dynamic behaviour, is to study the squeeze film damping and its effect on air bearing dynamics.

Mechanism or method for efficient and accurate setting of air gap height From the work discussed in Chapter 5 to 7, one would realise the difficulties and issues

9.2 Further work

related to the current method in setting the air gap height of an aerostatic bearing. There may be a potential for a radical mechanism design or method for air bearing installation, such that air gap height setting can be performed more efficiently and accurately.

Integrating dynamic model of guideway with controller design The ultimate aim for a robust dynamic modelling using FEA is to develop a dynamically optimal precision machine or motion system. Dynamic modelling and prediction of the motion system forms a portion of the design process. Incorporating the dynamic characteristics of the guideway or the whole motion system into a simulated control scheme forms a more holistic design approach. This is the concept of Mechatronic design or “Design-for-Control” approach, discussed in Section 2.2. The work here shall benefit the advancement of this design approach by providing a more comprehensive and robust dynamic modelling methodology for aerostatic guideway.

References

- [1] Weck, M., Kruger, P. and Brecher, C., Limits for controller settings with electric linear direct drives. *International Journal of Machine Tools and Manufacture*, vol. 41, no. 1, pp. 65–88, 2001.
- [2] Chen, C. L., Jang, M. J. and Lin, K. C., Modeling and high-precision control of a ball-screw-driven stage. *Precision Engineering*, vol. 28, no. 4, pp. 483–495, 2004.
- [3] Mao, J., Tachikawa, H. and Shimokohbe, A., Precision positioning of a dc-motor-driven aerostatic slide system. *Precision Engineering*, vol. 27, no. 1, pp. 32–41, 2003.
- [4] Wang, J., *Robust Tracking Controller Design with Application to the Motion Control of an X-Y Feed Table for High-Speed Machining*. PhD thesis, Katholieke Universiteit Leuven, Faculty of Engineering, Department of Mechanical Engineering, Belgium, 2004.
- [5] Dejima, S., Gao, W., Katakura, K., Kiyono, S. and Tomita, Y., Dynamic modeling, controller design and experimental validation of a planar motion stage for precision positioning. *Precision Engineering*, vol. In Press, Corrected Proof, 2005.
- [6] Brecher, C., Weck, M. and Yamasaki, T., Controller-integrated predictive oscillation compensation for machine tools with parallel kinematics. *International Journal of Machine Tools and Manufacture*, vol. 46, no. 2, pp. 142–150, 2006.
- [7] Liaw, H. C., Lim, S. Y., Lin, W. and Tan, K. K., Robust model-reaching control of high-precision linear motion systems. in *Industrial Electronics Society*,

REFERENCES

- 2003.*IECON '03.The 29th Annual Conference of the IEEE*, vol. 3, pp. 2794–2799, 2003.
- [8] Tan, K. K., Huang, S. N. and Lee, T. H., Geometrical error compensation and control of an xy table using neural networks. *Control Engineering Practice*, vol. 14, no. 1, pp. 59–69, 2006.
- [9] Tang, K. Z., Huang, S. N., Tan, K. K. and Lee, T. H., Combined pid and adaptive non-linear control for servo mechanical systems. *Mechatronics*, vol. 14, no. 6, pp. 701–714, 2004.
- [10] van Amerongen, J. and Breedveld, P., Modelling of physical systems for the design and control of mechatronic systems. *IFAC Professional Brief, Annual Review in Control* 27, pp. 87–117, 2003.
- [11] Brussel, H. M. J. V., Mechatronics-a powerful concurrent engineering framework. *Mechatronics, IEEE/ASME.Transactions on*, vol. 1, no. 2, pp. 127–136, 1996.
- [12] van Amerongen, J., The role of control in mechatronics. *Engineering Science and Education.Journal*, vol. 9, no. 3, pp. 105–112, 2000.
- [13] Breedveld, P. C., Rosenberg, R. C. and Zhou, T., Bibliography of bond graph theory and application. *Journal of the Franklin Institute*, vol. 328, no. 5-6, pp. 1067–1109, 1991.
- [14] de Vries, T. J., *Conceptual design of controlled electro-mechanical systems - a modeling perspective*. PhD thesis, University of Twente, Enschede, Netherlands, 1994.
- [15] Coelingh, H. J., *Design support for motion control systems, A Mechatronic Approach*. PhD thesis, University of Twente, Enschede, The Netherlands,, 2000.
- [16] de Vries, T. J., Breedveld, P. and Meindertsma, P., Polymorphic modelling of engineering systems. in *Proc.Int.Conf.on Bond Graph Modeling and Simulation*, vol. 25(2), (San Diego, California, U.S.A.), pp. 17–22, 1993.

REFERENCES

- [17] de Vries, T. J., Breunese, A. P. and Breedveld, P. C., Max: a mechatronic model building environment. in *Proc.Lancaster Int.Workshop on Engineering Design CACD '94*, (Lancaster, U.K.), pp. 299–318, 1994.
- [18] Weck, M., Q. M. and Brecher, C., Coupled simulation of control loop and structural dynamics. in *WGP, Production Engineering*, vol. X/2, pp. 105–110, 2003.
- [19] Killat, U., Duijsen, P. J. and Bauer, P., Integrated simulation of mechanics, electronics and control. in *Mechatronics*, vol. 4 (1), pp. 223–227, 2006.
- [20] Altintas, Y., Brecher, C., Weck, M. and Witt, S., Virtual machine tool. *CIRP. Annals.- Manufacturing Technology*, vol. 54, no. 2, pp. 115–138, 2005.
- [21] Bianchi, G., Paolucci, F., den Braembussche, P. V., Brussel, H. V. and Jovane, F., Towards virtual engineering in machine tool design. *CIRP. Annals.- Manufacturing Technology*, vol. 45, no. 1, pp. 381–384, 1996.
- [22] Brussel, H. V., Sas, P., Nemeth, I., Fonseca, P. D. and den Braembussche, P., Towards a mechatronic compiler. *Mechatronics, IEEE/ASME. Transactions on*, vol. 6, no. 1, pp. 90–105, 2001.
- [23] Rankers, A. M., *Machine Dynamics in Mechatronics Systems, An engineering approach*. PhD thesis, Twente University, The Netherlands, 1997.
- [24] Brecher, C., Schauerte, G. and Merz, M., Modeling and simulation of adaptronic drilling tool axes as the basis of control design. *Production Engineering*, vol. 1, no. 3, pp. 297–301, 2007.
- [25] Brecher, C., Witt, S. and Queins, M., Coupled simulation of structural dynamics and control loops for the development of high-dynamic machine tool. in *NAFEMS Seminar: Mechatronics in Structural Analysis*, (Wiesbaden, Germany), 2004.
- [26] Brecher, C., Manohran, D. and Witt, E. S., Structure integrated adaptronic systems for machine tools. *Production Engineering*, vol. 2, no. 2, pp. 219–223, 2008.

REFERENCES

- [27] Yoshimura, M. and Okushima, K., Computer-aided design improvement of machine tool structure incorporating joint dynamics data. in *CIRP Annals*, vol. 28, pp. 241–246, 1979.
- [28] Blake, A., *Design of mechanical joints*. New York: Marcell Dekker, 1 ed., October 1985.
- [29] Slocum, A. H., *Precision Machine Design*. Englewood Cliffs, New Jersey: Prentice-Hall, 1992.
- [30] Lee, J., A study on the dynamic modelling of structures with bolted and bearing joints. *CIRP Annals - Manufacturing Technology*, vol. 37, no. 1, pp. 343–346, 1988.
- [31] Chlebus, E. and Dybala, B., Modelling and calculation of properties of sliding guideways. *International Journal of Machine Tools and Manufacture*, vol. 39, pp. 1823–1839, Dec. 1999.
- [32] Zhang, G. P., Huang, Y. M., Shi, W. H. and Fu, W. P., Predicting dynamic behaviours of a whole machine tool structure based on computer-aided engineering. *International Journal of Machine Tools and Manufacture*, vol. 43, pp. 699–706, May 2003.
- [33] Fu, W. P., Huang, Y. M., Zhang, X. L. and Guo, Q., Experimental investigation of dynamic normal characteristics of machined joint surfaces. *Journal of Vibration and Acoustics*, vol. 122, no. 4, pp. 393–398, 2000.
- [34] Gupta, P. K., *Advanced dynamics of rolling elements*. New York: Springer-Verlag, 1984.
- [35] Stacke, L.-E., Fritzon, D. and Nordling, P., Beasts - a rolling bearing simulation tool. *Proceedings of the Institution of Mechanical Engineers, Part K: Journal of Multi-body Dynamics*, vol. 213, pp. 63–71, Jan. 1999.
- [36] Shamane, D. M., Hong, S. W. and Shin, Y. C., Experimental identification of dynamic parameters of rolling element bearings in machine tools. *Journal of Dynamic Systems, Measurement, and Control*, vol. 122, no. 1, pp. 95–101, 2000.

REFERENCES

- [37] Ohta, H. and Hayashi, E., Vibration of linear guideway type recirculating linear ball bearings. *Journal of Sound and Vibration*, vol. 235, pp. 847–861, Aug. 2000.
- [38] Sapanen, J. and Mikkola, A., Dynamic model of a deep-groove ball bearing including localized and distributed defects. part 1: theory. *Proceedings of the Institution of Mechanical Engineers, Part K: Journal of Multi-body Dynamics*, vol. 217, pp. 201–211, Jan. 2003.
- [39] Ni, J. and Zhu, Z., Elastic deflection of the sliding bearing interface in the tangential direction. *Proceedings of the Institution of Mechanical Engineers, Part C: Journal of Mechanical Engineering Science*, vol. 216, pp. 235–242, Jan. 2002.
- [40] Ewins, D. J., *Modal Testing: Theory, Practice and Application*. London: Research Studies Press Ltd., 2000.
- [41] Worden, K. and Tomlinson, G. R., non-linearity in experimental modal analysis. *Philosophical Transactions: Mathematical, Physical and Engineering Sciences*, vol. 359, no. 1778, pp. 113–130, 2001.
- [42] Ferreira, J. V., *Dynamic Response Analysis of Structures with non-linear Components*. PhD thesis, University of London, Imperial College of Science, Technology and Medicine, London, 1998.
- [43] Lin, R., *Identification of the Dynamic Characteristics of non-linear Structures*. PhD thesis, Imperial College London, 1990.
- [44] Liu, W., *Structural Dynamic Analysis and Testing of Coupled Structures*. PhD thesis, University of London, Imperial College of Science, Technology and Medicine, London, 2000.
- [45] Siller, H. R. E., *Non-Linear Modal Analysis Methods for Engineering Structures*. PhD thesis, Imperial College London, 2004.
- [46] Stansfield, F. M., *Hydrostatic Bearings For Machine Tools and Similar Applications*. Machinery Publishing, 1970.

REFERENCES

- [47] Guo, Z., Hirano, T. and Kirk, R. G., Application of cfd analysis for rotating machinery—part i: Hydrodynamic, hydrostatic bearings and squeeze film damper. *Journal of Engineering for Gas Turbines and Power*, vol. 127, no. 2, pp. 445–451, 2005.
- [48] Jeon, S. and Kim, K., A fluid film model for finite element analysis of structures with linear hydrostatic bearings. *Proceedings of the Institution of Mechanical Engineers, Part C: Journal of Mechanical Engineering Science*, vol. 218, pp. 309–316, Jan. 2004.
- [49] Powell, J., *Design of aerostatic bearings*. Brighton: Machinery Publishing, 1970.
- [50] Moore, D. F., A review of squeeze films. *Wear*, vol. 8, no. 4, pp. 245–263, 1965.
- [51] Bao, M. and Yang, H., Squeeze film air damping in mems. *Sensors and Actuators A: Physical*, vol. 136, pp. 3–27, May 2007.
- [52] Andrews, M. K., Turner, G. C., Harris, P. D. and Harris, I. M., A resonant pressure sensor based on a squeezed film of gas. *Sensors and Actuators A: Physical*, vol. 36, pp. 219–226, May 1993.
- [53] Thornton, B. H. and Bogoy, D. B., non-linear aspects of air-bearing modeling and dynamic spacing modulation in sub-5-nm air bearings for hard disk drives. *Magnetics, IEEE Transactions on*, vol. 39, no. 2, pp. 722–728, 2003.
- [54] Minikes, A. and Bucher, I., Coupled dynamics of a squeeze-film levitated mass and a vibrating piezoelectric disc: numerical analysis and experimental study. *Journal of Sound and Vibration*, vol. 263, no. 2, pp. 241–268, 2003.
- [55] Stolarski, T. and Chai, W., Load-carrying capacity generation in squeeze film action. *International Journal of Mechanical Sciences*, vol. 48, pp. 736–741, July 2006.
- [56] Yoshimoto, S., Kobayashi, H. and Miyatake, M., Float characteristics of a squeeze-film air bearing for a linear motion guide using ultrasonic vibration. *Tribology International*, vol. 40, pp. 503–511, Mar. 2007.

REFERENCES

- [57] Abdel-Rahman, G. M., Studying fluid squeeze characteristics for aerostatic journal bearing. *Physica B: Condensed Matter*, vol. 403, pp. 2390–2393, Jul 2008.
- [58] Puri, V. K. and Patel, C. M., The squeeze film in a porous composite slider bearing. *Wear*, vol. 70, pp. 197–206, Aug. 1981.
- [59] Boffey, D. A., Barrow, A. A. and Dearden, J. K., Experimental investigation into the performance of an aerostatic industrial thrust bearing. *Tribology International*, vol. 18, no. 3, pp. 165–168, 1985.
- [60] Boffey, D. A., Waddell, M. and Dearden, J. K., A theoretical and experimental study into the steady-state performance characteristics of industrial air lubricated thrust bearings. *Tribology International*, vol. 18, no. 4, pp. 229–233, 1985.
- [61] Stout, K. J., Design of aerostatic flat pad bearings using annular orifice restrictors. *Tribology International*, vol. 18, no. 4, pp. 209–214, 1985.
- [62] Majumdar, B., The numerical solution of aerostatic journal bearings with several supply ports. *Wear*, vol. 15, no. 5, pp. 331 – 340, 1970.
- [63] Raman, K. V. and Majumdar, B. C., Experimental investigation of the stiffness and damping characteristics of aerostatic rectangular thrust bearings. *Wear*, vol. 52, no. 1, pp. 71–78, 1979.
- [64] Stout, K. J., El-Ashkar, S., Ghasi, V. and Tawfik, M., Theoretical analysis of two configurations of aerostatic flat pad bearings using pocketed orifice restrictors. *Tribology International*, vol. 26, no. 4, pp. 265–273, 1993.
- [65] Stout, K. J. and Sweeney, F., Design of aerostatic flat pad bearings using pocketed orifice restrictors. *Tribology International*, vol. 17, no. 4, pp. 191–198, 1984.
- [66] Mukai, T., Analysis of dynamic characteristics of air bearing. Tech. Rep. 93, Nippon Steel Corporation, January 2006.

REFERENCES

- [67] Devitt, A. J., Orifice vs. porous media air bearings. tech. rep., New Way Air Bearings, 1999.
- [68] Sneck, H. J., A survey of gas-lubricated porous bearings. *ASME Journal of Lubrication Technology*, vol. 90, pp. 804–809, 1968.
- [69] Kwan, Y. B. P. and Corbett, J., Porous aerostatic bearings-an updated review. *Wear*, vol. 222, no. 2, pp. 69–73, 1998.
- [70] Devitt, A. J., Air bearings with a damping function for metal-cutting machine tools. tech. rep., New Way Air Bearings, 1994.
- [71] Rao, N. S., Analysis of externally pressurized porous gas bearings: Rectangular thrust bearings. *International Journal of Machine Tool Design and Research*, vol. 19, no. 2, pp. 87–93, 1979.
- [72] Rao, N. S. and Majumdar, B. C., An approximate method for the calculation of dynamic stiffness and damping coefficients of externally pressurized porous gas journal bearings. *Wear*, vol. 61, no. 2, pp. 375–379, 1980.
- [73] Singh, K. C. and Rao, N. S., Static characteristics of aerostatic porous rectangular thrust bearings. *Wear*, vol. 77, no. 2, pp. 229–236, 1982.
- [74] Tian, Y., Static study of the porous bearings by the simplified finite element analysis. *Wear*, vol. 218, no. 2, pp. 203–209, 1998.
- [75] Yoshimoto, S. and Kohno, K., Static and dynamic characteristics of aerostatic circular porous thrust bearings (effect of the shape of the air supply area). *Journal of Tribology*, vol. 123, no. 3, pp. 501–508, 2001.
- [76] Su, J. C., You, H.-I. and Lai, J.-X., Numerical analysis on externally pressurized high-speed gas-lubricated porous journal bearings. in *Industrial Lubrication and Tribology*, vol. 55, pp. 244–250, 2003.
- [77] Beek, A. V., *Design of aerostatic bearings*, ch. 12, pp. 411–436. 2nd ed., 2006.

REFERENCES

- [78] Plante, J. S., Vogan, J., El-Aguizy, T. and Slocum, A. H., A design model for circular porous air bearings using the 1d generalized flow method. *Precision Engineering*, vol. 29, no. 3, pp. 336–346, 2005.
- [79] Cortesi, R., An easy to manufacture non-contact precision linear motion system and its applications. Master's thesis, Massachusetts Institute of Technology, 2006.
- [80] “Science & technology 2010 plan.” Singapore Ministry of Trade & Industry, 2006.
- [81] Hill, T., *Manufacturing strategy : the strategic management of the manufacturing function / Terry Hill*. Macmillan, Basingstoke, Hampshire :, 2nd ed. ed., 1993.
- [82] Ward, J. M. and Murray, P., *Benefits Management: Best Practice Guidelines*. Information Systems Research Centre, Cranfield School of Management, Cranfield, 2000.
- [83] Ward, J. and Daniel, E., *Benefits Management: Delivering Value from IS & IT Investments*. Wiley Series, January 2006.
- [84] Farrukh, C., Phaal, R. and Probert, D., Technology roadmapping - linking technology resources into business planning. in *4th International Conference on Management Innovative Manufacturing (MIM2000)*, Aston Business School, UK, July 2000.
- [85] Lanctot, A. and Swan, K. S., Technology acquisition strategy in an internationally competitive environment. *Journal of International Management*, vol. 6, no. 3, pp. 187–215, 2000.
- [86] Cho, D.-H. and Yu, P.-I., Influential factors in the choice of technology acquisition mode: an empirical analysis of small and medium size firms in the korean telecommunication industry. *Technovation*, vol. 20, pp. 691–704, Dec. 2000.

REFERENCES

- [87] Baines, T., An integrated process for forming manufacturing technology acquisition decisions. *International Journal of Operations & Production Management*, vol. 24, no. 5, pp. 447–467, 2004.
- [88] Mankins, J. C., Technology readiness levels. a white paper, Advanced Concepts Office, Office of Space Access and Technology, NASA, April 1995.
- [89] Speser, P. L., *The Art and Science of Technology Transfer*. Hoboken, New Jersey, USA: John Wiley & Sons, Inc., 2006.
- [90] He, J. and Fu, Z.-F., *Modal Analysis*. Butterworth-Heinemann, 2001.
- [91] Kelly, S. G., *Schaum's Outline of Theory and Problems of Mechanical Vibrations*. McGraw-Hill Professional, 1996.
- [92] Thomson, W. T., *Theory of Vibration With Application*. Kluwer Academic Pub, 4th ed., 1993.
- [93] Sondipon, A., *Damping Models for Structural Vibration*. Phd, Cambridge University, Engineering Department, Trinity College, Cambridge, September 2000.
- [94] Varanasi, K., On the design of a precision machine for closed-loop performance. Master's thesis, Massachusetts Institute of Technology, Cambridge, Massachusetts, 2002.
- [95] Varanasi, K., *Vibration Damping using Low-Wave-Speed Media with Applications to Precision Machines*. PhD thesis, Massachusetts Institute of Technology, Cambridge, Massachusetts 2004.
- [96] Pilkey, D. F., *Computation of a Damping Matrix for Finite Element Model Updating*. PhD thesis, Virginia Polytechnic Institute and State University, 1998.
- [97] Adhikari, S., Damping modelling and identification using generalized proportional damping. in *Proceedings of the 23rd International Modal Analysis Conference (IMAC - XXIII)*, (Orlando, Florida, USA), Society of Experimental Mechanics (SEM), February 2005.

REFERENCES

- [98] Adhikari, S., Damping modelling using generalized proportional damping. *Journal of Sound and Vibration*, vol. 293, pp. 156–170, May 2006.
- [99] Rayleigh, J. W. S., *The Theory of Sound*, vol. 1. Macmillan and Co., 1877.
- [100] Lankarani, H. M. and Nikraves, P. E., A contact force model with hysteresis damping for impact analysis of multibody systems. *Journal of Mechanical Design*, vol. 112, no. 3, pp. 369–376, 1990.
- [101] Al-Bender, F. and Symens, W., Characterization of frictional hysteresis in ball-bearing guideways. *Wear*, vol. 258, pp. 1630–1642, June 2005.
- [102] Yong-Sub, Y., Kim, Y., Choi, J., Yoo, J., Lee, D., Lee, S. and Lee, S., Dynamic analysis of a linear motion guide having rolling elements for precision positioning devices. *Journal of Mechanical Science and Technology*, vol. 22, pp. 50–60, Jan. 2008.
- [103] Avitabile, P., Experimental modal analysis: A simple non-mathematical presentation. *Sound & Vibration*, pp. 1–11, 2001.
- [104] New Way Air Bearings, 50 McDonald Blvd., Aston, PA 19014 USA, *New Way Application and Design Guide, Rev. E*, January 2006.
- [105] Uriarte, L., Herrero, A., Zatarain, M., Santiso, G., de Lacalle, L. N. L., Lamikiz, A. and Albizuri, J., Error budget and stiffness chain assessment in a micromilling machine equipped with tools less than 0.3 mm in diameter. *Precision Engineering*, vol. 31, no. 1, pp. 1–12, 2007.
- [106] Salgado, M. A., de Lacalle, L. N. L., Lamikiz, A., Munoa, J. and Sanchez, J. A., Evaluation of the stiffness chain on the deflection of end-mills under cutting forces. *International Journal of Machine Tools and Manufacture*, vol. 45, no. 6, pp. 727–739, 2005.
- [107] Teo, C. S.; Tan, K. K. H. and Lim, S. Y., Dynamic modeling and adaptive control of a multi-axial gantry stage. in *Systems, Man and Cybernetics, 2005 IEEE International Conference on*, vol. 4, pp. 3374–3379, 2005.

REFERENCES

- [108] Slocum, A., Basaran, M., Cortesi, R. and Hart, A. J., Linear motion carriage with aerostatic bearings preloaded by inclined iron core linear electric motor. *Precision Engineering*, vol. 27, no. 4, pp. 382–394, 2003.
- [109] Yoshimoto, S., Tamura, J. and Nakamura, T., Dynamic tilt characteristics of aerostatic rectangular double-pad thrust bearings with compound restrictors. *Tribology International*, vol. 32, no. 12, pp. 731–738, 1999.
- [110] Mekid, S. and Bonis, M., Conceptual design and study of high precision translational stages: application to an optical delay line. *Precision Engineering*, vol. 21, no. 1, pp. 29–35, 1997.
- [111] Frost&Sullivan, “World noise vibration and harshness (nvh) test equipment market.” Frost & Sullivan Market Engineering Research, Nov 2008.
- [112] Peeters, B., der Auweraer, H. V., Guillaume, P. and Leuridan, J., The polymax frequency-domain method: a new standard for modal parameter estimation?. *Shock and Vibration*, vol. 11, pp. 395–409, Jan. 2004.
- [113] LMS, *LMS Product Information - LMS SCADAS Mobile*. LMS International, LMS/TL/SCM/SCM05/150606, 2006.
- [114] LMS, *LMS Solutions Guide - LMS Test.Lab Overview*. LMS International.
- [115] Kistler, *Kistler PiezoBEAM Triaxial Accelerometer - Type 8690C*. Kistler.
- [116] Kistler, Type 9726A, *Kistler Quartz - Impulse Force Hammer*.
- [117] Mahr, *Mahr Inductive Probe Millimar 1301 / 1303 / 1304 K / 1318*. Mahr GmbH.
- [118] Vehar, C., *Flexure design for precision and control*. 2004.
- [119] Howell, L. L., *Compliant Mechanisms*. New York: John Wiley & Sons, Inc., 2001.
- [120] O’Connor, B., *Modeling and analysis of porous graphite air bearings*. Master’s thesis, The Pennsylvania State University, 2000.

REFERENCES

- [121] Zygo, *GPI FlashPhase™ Specifications*. Zygo Corporation, Middlefield, CT 06455, 2005.
- [122] Shapiro, A. H., *The Dynamics and Thermodynamics of Compressible Fluid Flow*, vol. 1. New York, NY: John Wiley & Sons, 1953.
- [123] ANSYS, *Release 10.0 Documentation for ANSYS*. ANSYS Inc.
- [124] Brüel and Kjær, *Calibration Exciter - Type 4294 and Type 4294-002*. Brüel & Kjær, DK-2850 Nærum.
- [125] Bell, S., Measurement good practice guide no. 11 (issue 2) - a beginners guide to uncertainty of measurement. tech. rep., Centre for Basic, Thermal and Length Metrology National Physical Laboratory, 2001.
- [126] Pierre, C., Jiang, D. and Shaw, S., non-linear normal modes and their application in structural dynamics. *Mathematical Problems in Engineering*, vol. 2006, 2006.
- [127] Bickford, J. H. and Nassar, S., *Handbook of bolts and bolted joints*, vol. 911. CRC Press, 1998.
- [128] Johnson, K., *Contact Mechanics*. Cambridge University Press, 1985.
- [129] Roblee, J. W. and Mote, C. D., Design of externally pressurized gas bearings for stiffness and damping. *Tribology International*, vol. 23, no. 5, pp. 333–345, 1990.
- [130] Ekinci, T. O., Mayer, J. and Cloutier, G. M., Investigation of accuracy of aerostatic guideways. *International Journal of Machine Tools and Manufacture*, vol. 49, no. 6, pp. 478 – 487, 2009.

Appendix A

Technical data of New Way Air Bearing

Appendix A. Technical data of New Way Air Bearing

A.1 Specifications of 25 mm Diameter Air Bearing

SPECIFICATIONS: 25mm #S102501	
Input Pressure	.41 MPa (60psi)
Ideal Load N (lbs)	80 (18)
Stiffness N/micron (lbs/u in) ¹	18 (0.10)
Flow NLPM (SCFH) ¹	0.53 (1.2)
Fly Height ¹	5 microns
Bearing Size	25mm
Bearing Height mm (in)	13 (0.52)
Bearing Weight grams (oz.)	14 (0.5)
Housing Material/Finish	Aluminum/Anodized
Porous Media Material	Carbon
Bearing Face Surface Size - Carbon mm (in)	24mm (0.940) ϕ
Flatness mm (in)	0.0005 (0.00002)
Ball Socket Size	13mm
Pressure Port Thread	M3 X 0.5
Viable Pressure Range	.414-.552MPa (60psi - 80psi)
Maximum Allowable Pressure Supply	.689 MPa (100psi)
Resolution ³	Infinite
Maximum Speed ⁴	50m/sec
Common Guide Surfaces	Granite, hard-coated aluminum, ceramics, glass, stainless steel, plated steel
Suggested Guide Surface Finish ⁵	16 RMS

Figure A.1: New Way air bearing 25 mm diameter specification (Source: <http://www.newwayairbearings.com>)

A.2 Load lift curves of 25 mm Diameter Air Bearing

A.2 Load lift curves of 25 mm Diameter Air Bearing

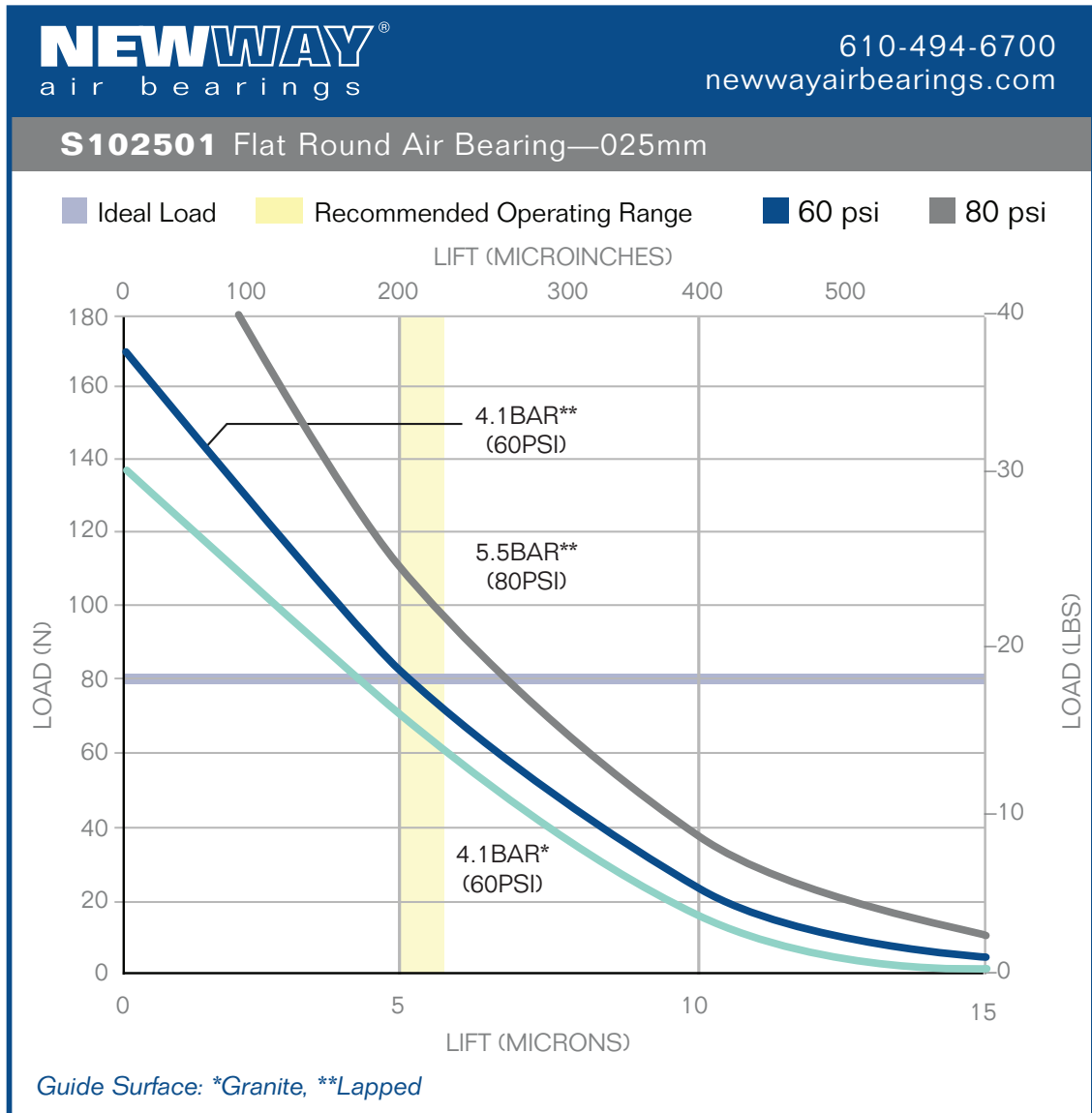


Figure A.2: New Way air bearing 25 mm diameter manufacturer's load-lift curve (Source: <http://www.newwayairbearings.com>)

A.4 Specifications of 65 mm Diameter Air Bearing

A.4 Specifications of 65 mm Diameter Air Bearing

SPECIFICATIONS: 65mm #S106501	
Input Pressure	.41 MPa (60psi)
Ideal Load N (lbs)	666 (150)
Stiffness N/micron (lbs/u in)¹	87 (0.50)
Flow NLPM (SCFH)¹	1.4 (2.9)
Fly Height¹	5 microns
Bearing Size	65mm
Bearing Height mm (in)	20 (0.79)
Bearing Weight grams (oz.)	151 (5.3)
Housing Material/Finish	Aluminum/Anodized
Porous Media Material	Carbon
Bearing Face Surface Size - Carbon mm (in)	63 (2.48) ϕ
Flatness mm (in)	0.0005 (0.00002)
Ball Socket Size	13mm
Pressure Port Thread	M5 X 0.8
Viable Pressure Range	.414-.552MPa (60psi - 80psi)
Maximum Allowable Pressure Supply	.689 MPa (100psi)
Resolution³	Infinite
Maximum Speed⁴	50m/sec
Common Guide Surfaces	Granite, hard-coated aluminum, ceramics, glass, stainless steel, plated steel
Suggested Guide Surface Finish⁵	16 RMS

Figure A.4: New Way air bearing 65 mm diameter specification (Source: <http://www.newwayairbearings.com>)

Appendix A. Technical data of New Way Air Bearing

A.5 Load lift curves of 65 mm Diameter Air Bearing

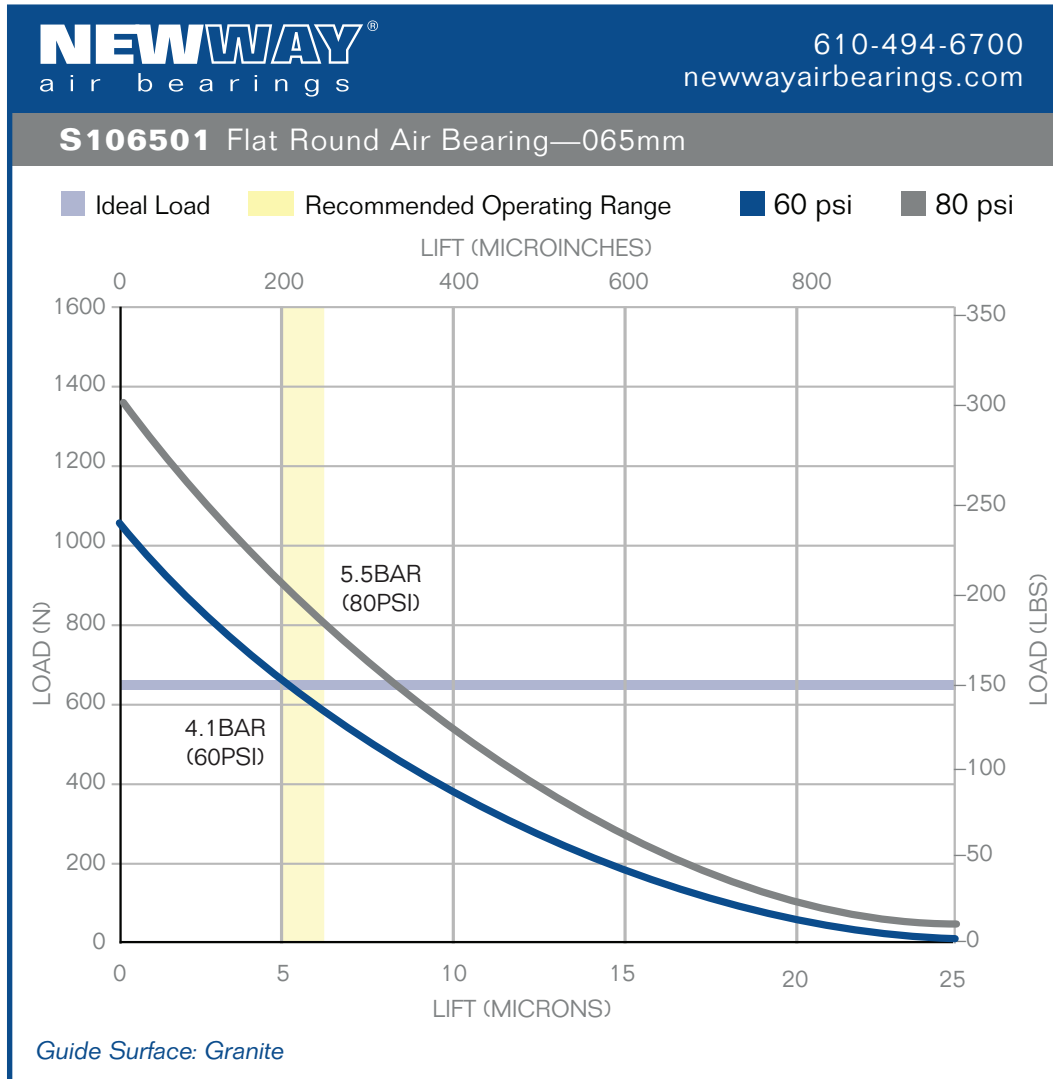


Figure A.5: New Way air bearing 65 mm diameter manufacturer's load-lift curve (Source: <http://www.newwayairbearings.com>)

A.6 Engineering drawings of 65 mm Diameter Air Bearing

A.6 Engineering drawings of 65 mm Diameter Air Bearing

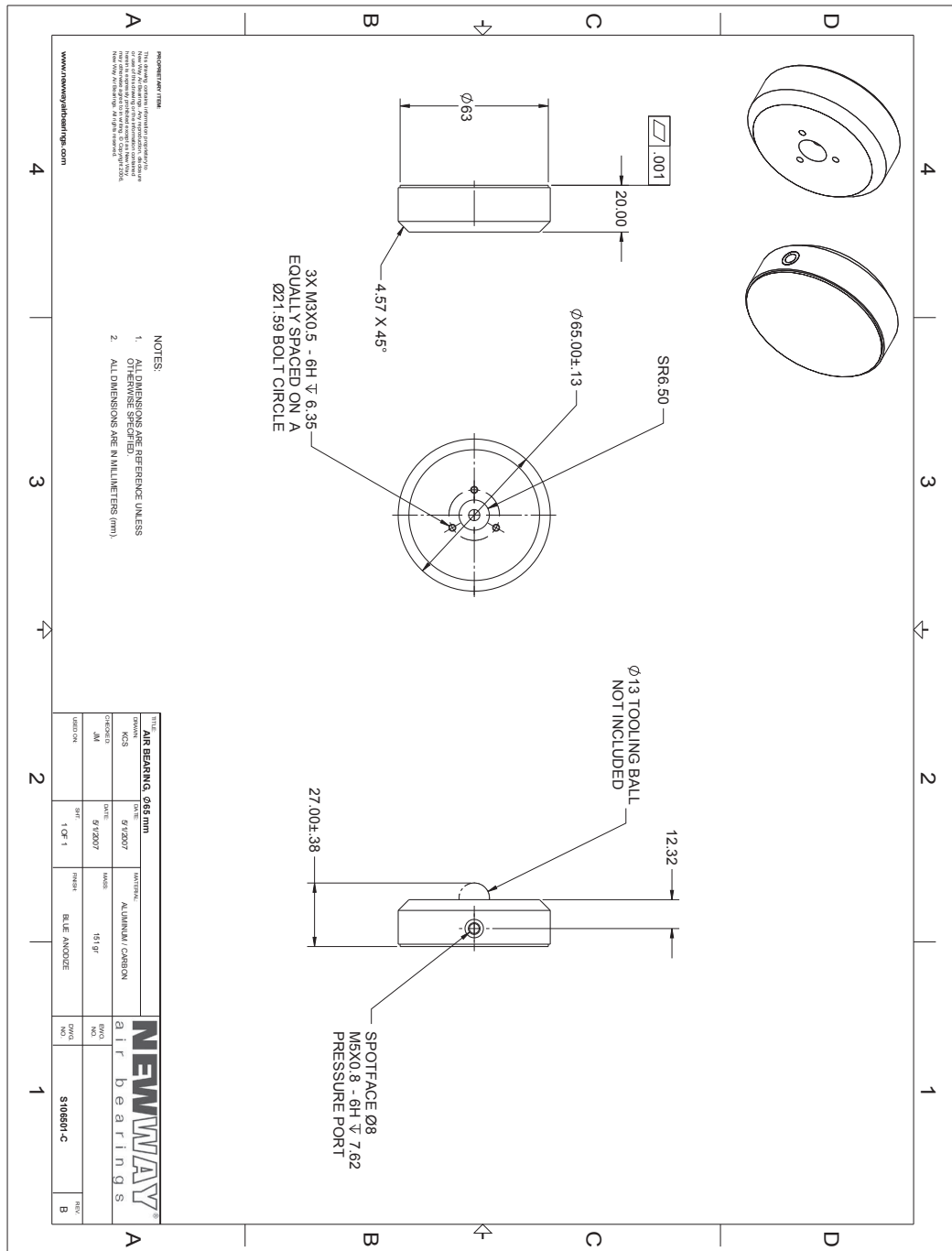


Figure A.6: New Way air bearing 65 mm diameter engineering drawing (Source: <http://www.newwayairbearings.com>)

Appendix B

Air gap height measurement procedure

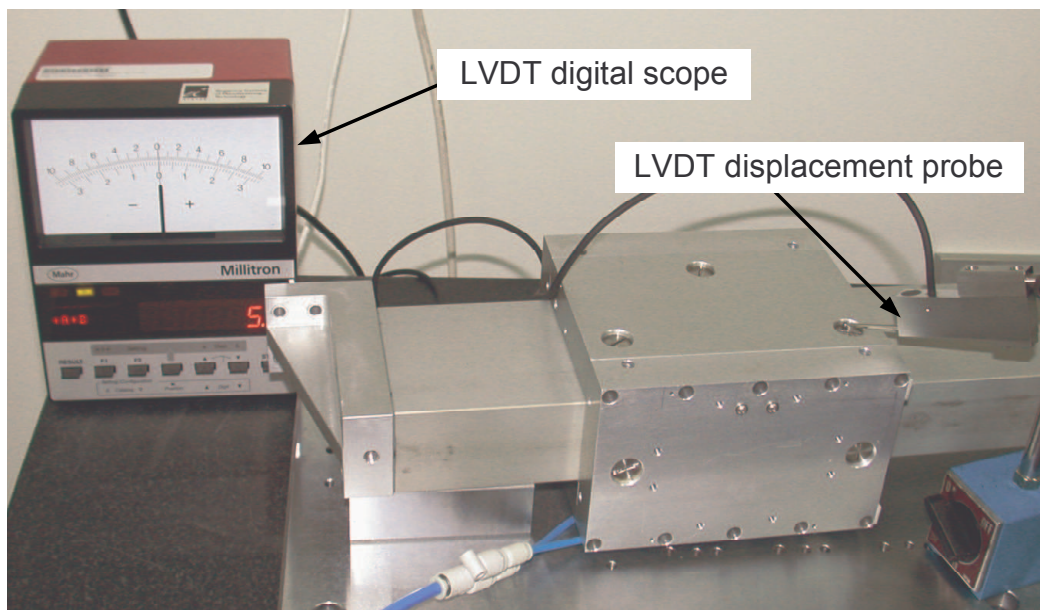


Figure B.1: Air Gap Measurement Setup

Figure B.1 shows the measurement setup of the air bearings carriage. The guideway bar was removed from the base plate, so that the carriage's surface with the air bearings to be measured can be orientated facing up. The steps to obtain the air gap measurement of each air bearing are as follow.

1. Make sure the air supply to all the air bearings are turned on to the desired

Appendix B. Air gap height measurement procedure

operating pressure.

2. Adjust all the air bearing gap via the threaded stud to random height, so long as the carriage can be moved effortlessly.
3. Choose one bearing to start with, and place the carriage in an orientation whereby the screw slot for the measuring bearing is facing up, as shown in Figure B.1. Ensure that the carriage can still slide freely.
4. Turn off the air supply to the bearing and let the bearing settle such that it is in contact with the guide bar surface. Make sure the carriage cannot be moved, i.e. the air bearing is pressing on the bar surface.
5. Place the tip of the measuring probe on the threaded stud setting screw of the bearing mounting mechanism, and zero the probe.
6. Turn the air supply back on to the operating pressure.
7. The measurement reading should indicate the lift of the air bearing in micrometre scale.
8. Redo step 1 to 4 for about five times to obtain the average.
9. Slide the carriage to other position on the bar and perform step 1 to 4 again to make sure that the air gap is consistent throughout the length of the guideway.
10. Repeat step 2 to 10 on all the air bearings until all have been adjusted to the desired air gap height.

Appendix C

ANSYS Element Description

The information in this appendix is extracted from ANSYS reference manual [123].

C.1 COMBIN39 Element Description

COMBIN39 is a unidirectional element with non-linear generalized force-deflection capability that can be used in any analysis. The element has longitudinal or torsional capability in 1-D, 2-D, or 3-D applications. The longitudinal option is a uniaxial tension-compression element with up to three degrees of freedom at each node: translations in the nodal x, y, and z directions. No bending or torsion is considered. The torsional option is a purely rotational element with three degrees of freedom at each node: rotations about the nodal x, y, and z axes. No bending or axial loads are considered.

The element has large displacement capability for which there can be two or three degrees of freedom at each node.

See COMBIN39 in the ANSYS, Inc. Theory Reference for more details about this element. The element has no mass or thermal capacitance. These may be added by using the appropriate elements (see MASS21 and MASS71). A bilinear force-deflection element with damping and gaps is also available (COMBIN40).

C.2 SHELL93 Element Description

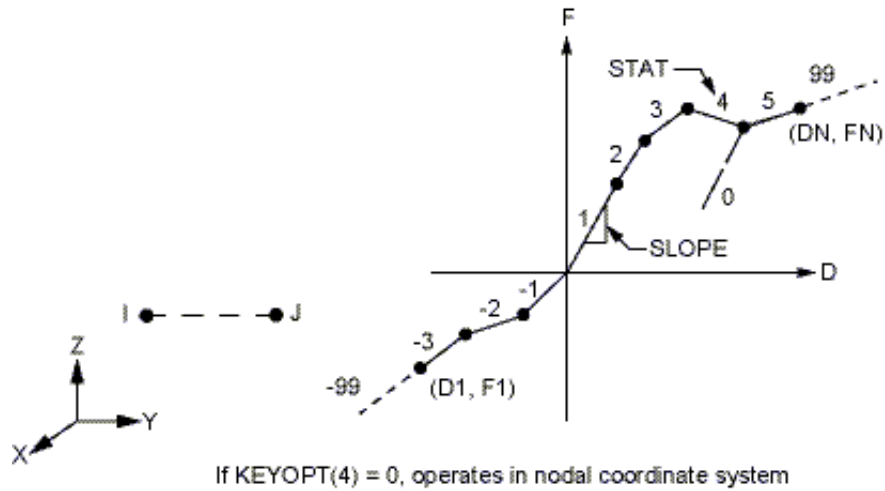


Figure C.1: COMBIN39 Geometry

The geometry, node locations, and the coordinate system for this element are shown in Figure 39.1: "COMBIN39 Geometry". The element is defined by two (preferably coincident) node points and a generalized force-deflection curve. The points on this curve (D1, F1, etc.) represent force (or moment) versus relative translation (or rotation) for structural analyses, and heat (or flow) rate versus temperature (or pressure) difference for a thermal analyses. The loads should be defined on a full 360 basis for an axisymmetric analysis.

C.2 SHELL93 Element Description

Shell elements are a special class of elements that are designed to efficiently model thin structures. They take advantage of the fact that the only shear on the free surfaces is in-plane. Normals to the shell middle surface stay straight, but not necessarily normal. As a result, the in-plane strain variation through the thickness cannot be more complex than linear.

SHELL93 is particularly well suited to model curved shells. The element has six degrees of freedom at each node: translations in the nodal x, y, and z directions and rotations about the nodal x, y, and z-axes. The deformation shapes are quadratic in both in-plane directions. The element has plasticity, stress stiffening, large deflection,

Appendix C. ANSYS Element Description

and large strain capabilities. See SHELL93 in the ANSYS, Inc. Theory Reference for more details about this element.

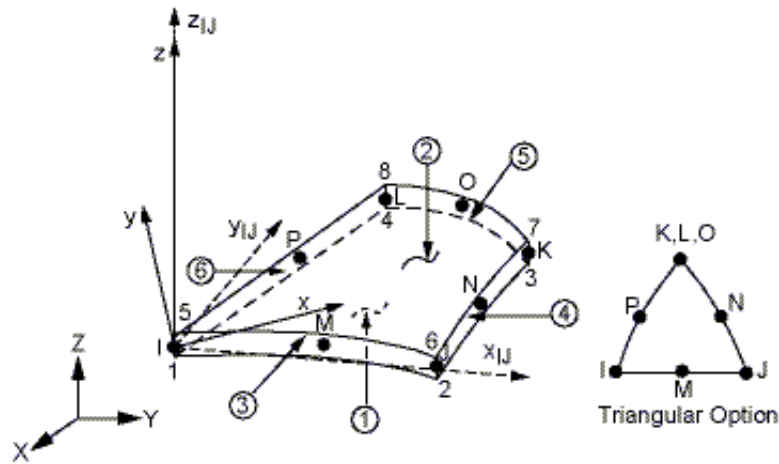


Figure C.2: SHELL93 Geometry

x_{IJ} = Element x-axis if ESYS is not supplied.

x = Element x-axis if ESYS is supplied.

The geometry, node locations, and the coordinate system for this element are shown in Figure C.2. The element is defined by eight nodes, four thicknesses, and the orthotropic material properties. Midside nodes may not be removed from this element. A triangular-shaped element may be formed by defining the same node number for nodes K, L and O.

Appendix D

Flatness Measurement of Critical Surfaces using Interferometer

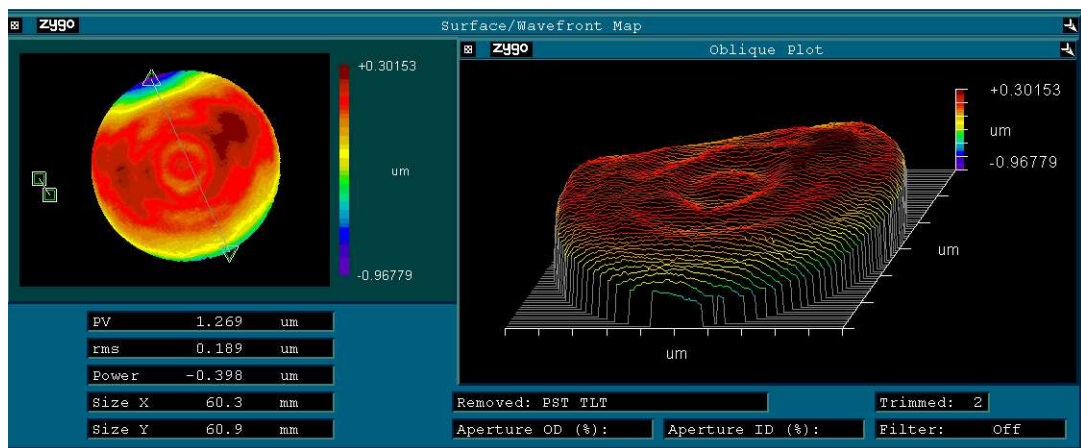


Figure D.1: Flatness of Top Air Bearing Porous Surface

Appendix D. Flatness Measurement of Critical Surfaces using Interferometer

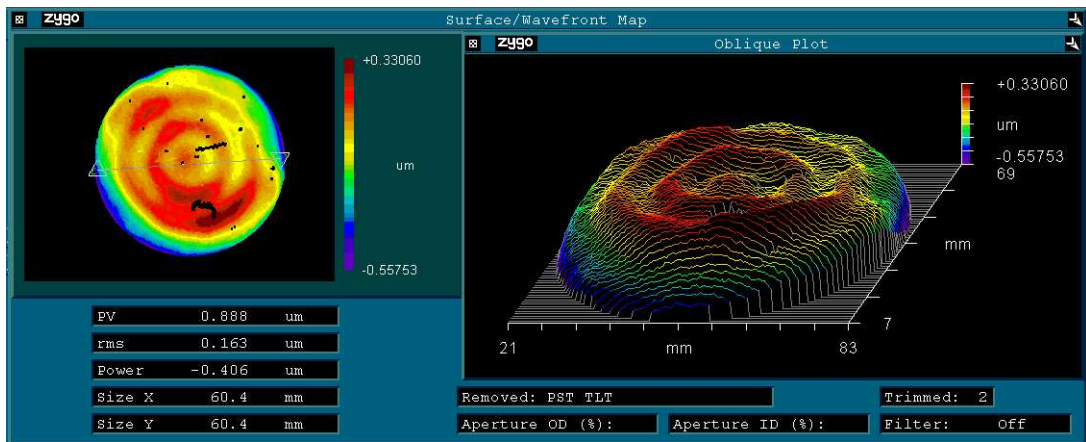


Figure D.2: Flatness of Bottom Air Bearing Porous Surface

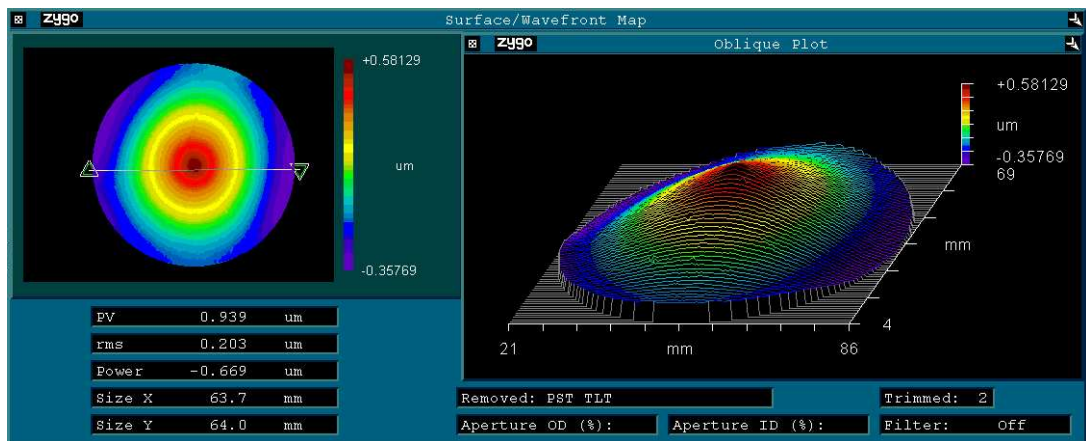


Figure D.3: Flatness of Centre Mass Top 'Fly-cut' Surface

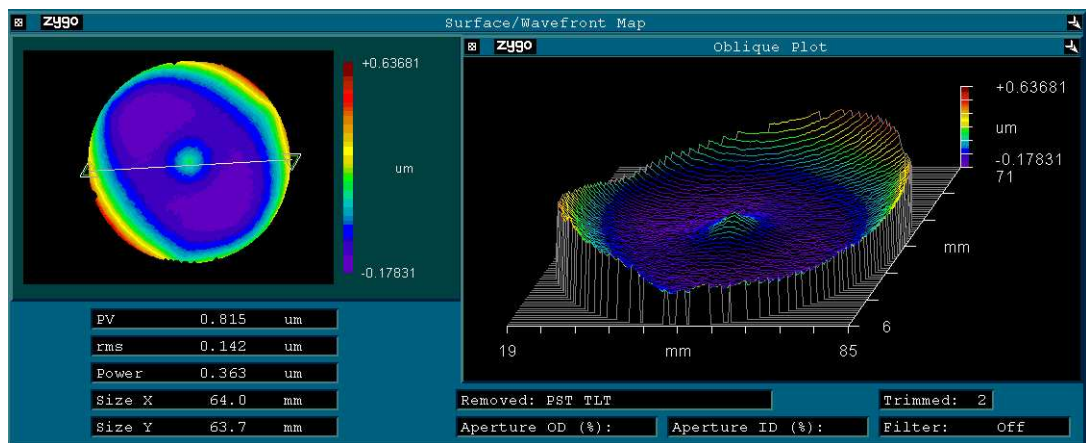
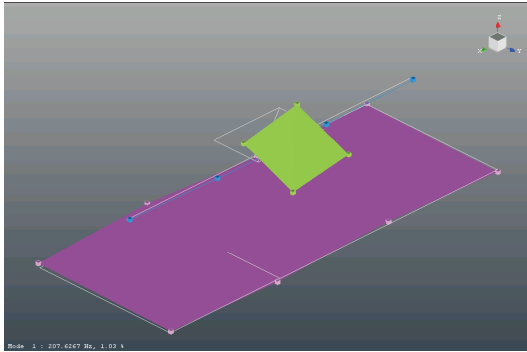


Figure D.4: Flatness of Centre Mass Bottom 'Fly-cut' Surface

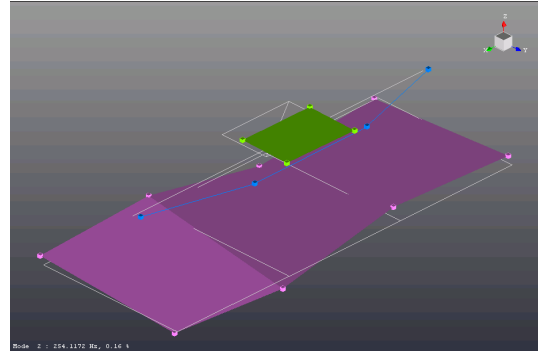
Appendix E

Experimental results of guideway modal testing

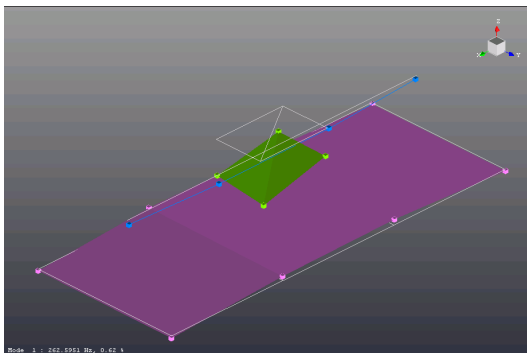
Appendix E. Experimental results of guideway modal testing



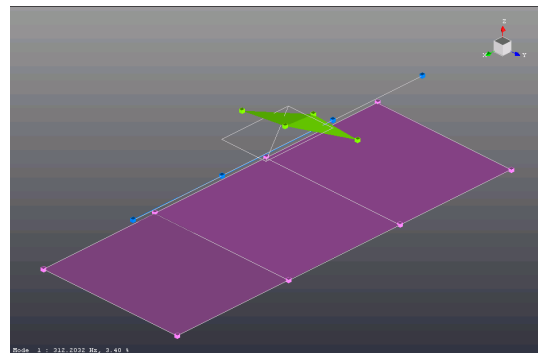
Mode 1 at 207 Hz



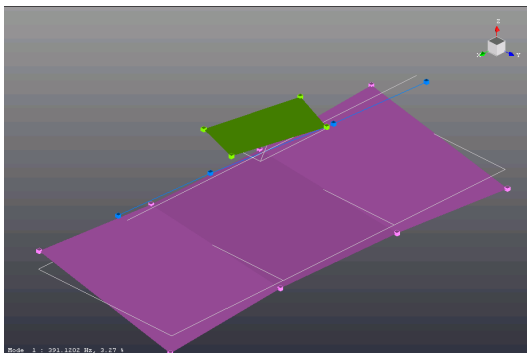
Mode 2 at 254 Hz



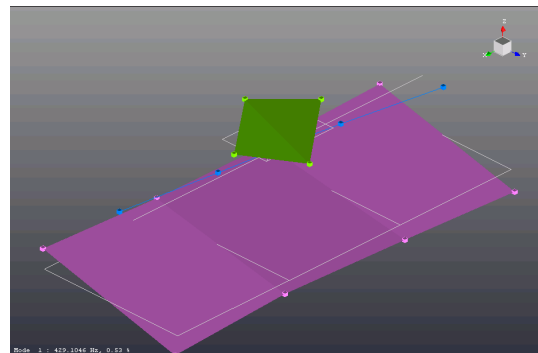
Mode 3 at 263 Hz



Mode 4 at 312 Hz



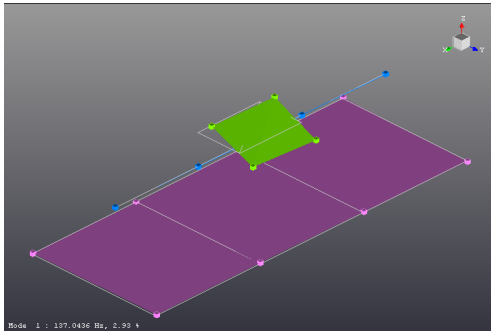
Mode 5 at 391 Hz



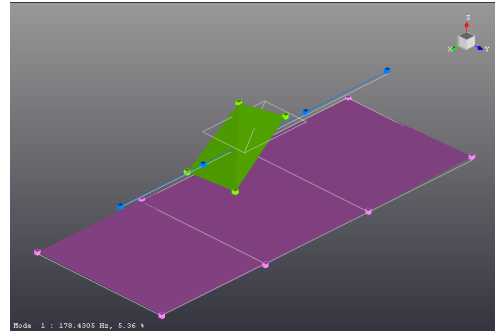
Mode 7 at 429 Hz

Figure E.1: Experimental modal testing results of overall aerostatic guideway for Setup 1: 5 μm stud setting

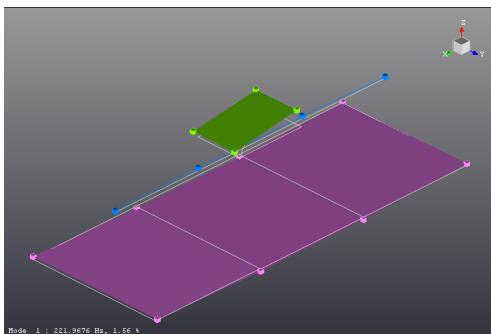
Appendix E. Experimental results of guideway modal testing



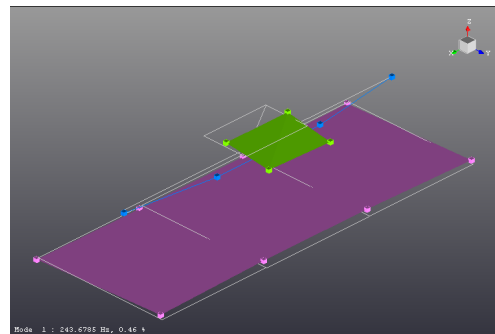
Mode 1 at 137 Hz



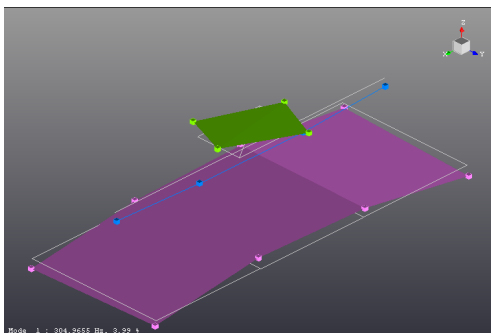
Mode 2 at 180 Hz



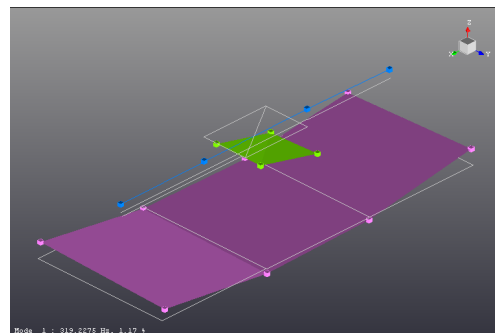
Mode 3 at 221 Hz



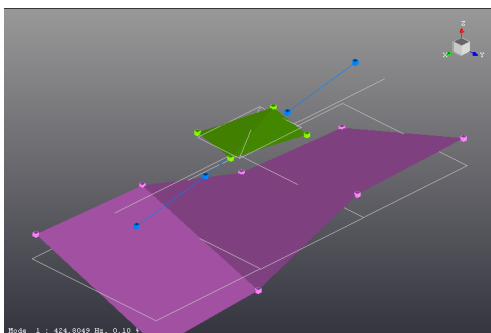
Mode 4 at 244 Hz



Mode 5 at 305 Hz



Mode 6 at 319 Hz



Mode 7 at 425 Hz

Figure E.2: Experimental modal testing results of overall aerostatic guideway for Setup 2: 9 μm stud setting